

Multichannel Image Detectors

Volume 2

ACS SYMPOSIUM SERIES 236

Multichannel Image Detectors

Volume 2

Yair Talmi, EDITOR
Princeton Instruments, Inc.

Based on a symposium cosponsored by
the Division of Analytical Chemistry
and the Division of Physical Chemistry
at the 184th Meeting
of the American Chemical Society,
Kansas City, Missouri,
September 12–17, 1982



American Chemical Society, Washington, D.C. 1983



Library of Congress Cataloging in Publication Data

(Revised for vol. 2)

Multichannel image detectors.

(ACS symposium series, ISSN 0097-6156; 236)

"Based on symposia sponsored by the Divisions of Analytical and Physical Chemistry of the American Chemical Society; v. 1, 176th meeting, Miami Beach, Fla., Sept. 11-12, 1978; v. 2, 184th meeting, Kansas City, Mo., Sept. 12-17, 1982."

Includes bibliographies and index.

1. Spectrum analysis—Congresses. 2. Spectrum analysis—Instruments—Congresses. 3. Image processing—Equipment and supplies—Congresses.

I. Talmi, Yair, 1942- . II. American Chemical Society. Division of Analytical Chemistry. III. American Chemical Society. Division of Physical Chemistry. IV. American Chemical Society. Meeting (176th: 1978: Miami Beach, Fla.) V. American Chemical Society. Meeting (184th: 1982: Kansas City, Mo.) VI. Series: ACS symposium series; 102, etc.

QD95.M975 1983 543'.0858 79-12441
ISBN 0-8412-0814-X

Copyright © 1983

American Chemical Society

All Rights Reserved. The appearance of the code at the bottom of the first page of each article in this volume indicates the copyright owner's consent that reprographic copies of the article may be made for personal or internal use or for the personal or internal use of specific clients. This consent is given on the condition, however, that the copier pay the stated per copy fee through the Copyright Clearance Center, Inc. for copying beyond that permitted by Sections 107 or 108 of the U.S. Copyright Law. This consent does not extend to copying or transmission by any means—graphic or electronic—for any other purpose, such as for general distribution, for advertising or promotional purposes, for creating a new collective work, for resale, or for information storage and retrieval systems. The copying fee for each chapter is indicated in the code at the bottom of the first page of the chapter.

The citation of trade names and/or names of manufacturers in this publication is not to be construed as an endorsement or as approval by ACS of the commercial products or services referenced herein; nor should the mere reference herein to any drawing, specification, chemical process, or other data be regarded as a license or as a conveyance of any right or permission, to the holder, reader, or any other person or corporation, to manufacture, reproduce, use, or sell any patented invention or copyrighted work that may in any way be related thereto.

PRINTED IN THE UNITED STATES OF AMERICA

ACS Symposium Series

M. Joan Comstock, *Series Editor*

Advisory Board

David L. Allara

Robert Baker

Donald D. Dollberg

Brian M. Harney

W. Jeffrey Howe

Herbert D. Kaesz

Marvin Margoshes

Donald E. Moreland

Robert Ory

Geoffrey D. Parfitt

Theodore Provder

Charles N. Satterfield

Dennis Schuetzle

Davis L. Temple, Jr.

Charles S. Tuesday

C. Grant Willson

FOREWORD

The ACS SYMPOSIUM SERIES was founded in 1974 to provide a medium for publishing symposia quickly in book form. The format of the Series parallels that of the continuing ADVANCES IN CHEMISTRY SERIES except that in order to save time the papers are not typeset but are reproduced as they are submitted by the authors in camera-ready form. Papers are reviewed under the supervision of the Editors with the assistance of the Series Advisory Board and are selected to maintain the integrity of the symposia; however, verbatim reproductions of previously published papers are not accepted. Both reviews and reports of research are acceptable since symposia may embrace both types of presentation.

PREFACE

IT HAS BEEN FOUR YEARS since the previous ACS symposium on Multichannel Image Devices was held and its proceedings subsequently published (ACS Symposium Series No. 102). A great deal of progress has since been made, both in technology and in the acceptance of multichannel image devices by spectroscopists.

Progress in optoelectronic image detectors (OIDs) has been due predominantly to the rapid advancement in silicon large-scale integrated circuit technology. This progress has enabled the manufacture of large-format self-scanned OIDs with scientific-grade performance in good yields and at a relatively affordable cost and a more reliable delivery schedule.

Self-scanned silicon photodiode arrays with up to 4096 individual light sensing elements have emerged as the linear OID of choice for most spectrometric applications. For two-dimensional area array OIDs, charge-coupled devices and charge-injection devices with element (pixel) packing of up to 800×800 seem to provide a better overall performance. Similar progress has been achieved in microchannel plate (MCP) image intensifier technology, particularly in respect to long-term stability.

As a result, self-scanned solid-state OIDs with and without MCP image intensifications have rapidly replaced OIDs based on vidicon (second generation) television pickup tube technology. Moreover, indications are that in the near future, the progress in silicon-based LSI devices will expand to more exotic materials such as InSb, InAs, HgCdTe, and PbSnTe. This expansion will allow for the development of IR-sensitive OIDs that could eventually replace mechanical multiplex detection systems based on mathematical transformations such as Fourier and Hadamard.

Acceptance of OIDs by scientists has been a direct result of their success in the field, i.e., their unique performance characteristics and long-term reliability. As more instrumentation based on these devices enters the scientific marketplace, a steady improvement in performance can be expected. Even more important, feedback from an ever increasing number of users should help convince OID manufacturers of the commercial viability of the scientific market, which may result in devices specifically designed for, rather than adapted for, scientific usage.

These proceedings are not intended to present a rigorous and expansive analysis of either the fundamental operation or the scientific applicability of

multichannel image devices. Instead, a few selected works are presented in this rapidly growing field. We hope to succeed in demonstrating the potential of this detection technique and to persuade others to probe into its use in their studies.

YAIR TALMI
Princeton Instruments, Inc.
P.O. Box 2318
Princeton, NJ 08540

August 1983

Guidelines for the Selection of Four Optoelectronic Image Detectors for Low-Light Level Applications

YAIR TALMI

Princeton Instruments, Inc., P.O. Box 2318, Princeton, NJ 08540

KENNETH W. BUSCH

Department of Chemistry, Baylor University, Waco, TX 76798

The performance characteristics of four optoelectronic image detectors (OIDs) are discussed. The detectors discussed are the silicon intensified target vidicon (SIT), the intensified SIT, the intensified silicon photodiode array detector (ISPD), and the self-scanned photodiode array detector. The main objective of the paper is to provide research workers interested in applying OIDs to a particular application with comparative performance information so that the best detector for a particular application may be selected.

Optoelectronic image detectors (OIDs) are currently of great interest to a variety of research workers whose work involves the detection of different portions of the electromagnetic spectrum. The great diversity of OIDs makes it difficult for researchers who are not necessarily experts in the area of optoelectronic image detection to select the best image detector for a particular application. For example, a detector whose performance is satisfactory for applications involving high-light levels may be totally unsatisfactory when used to detect low-light levels. The main objective of this paper is to provide a framework for comparison of a number of OIDs which are expected to have a real impact on spectroscopic detection in the foreseeable future.

The scope of this discussion will be limited to those spectroscopic applications where low light levels are involved. It is in these applications where most of the problems occur, and where an in-depth knowledge of detector performance is required in selecting a detector for a particular application. By definition, in this category are included all "photon-starved" areas of spectrometry. It is instructive to consider some of the causes of photon starvation in spectroscopy.

0097-6156/83/0236-0001\$08.50/0
© 1983 American Chemical Society

Low-level signals can result from a variety of causes. Among them are: 1. Inefficiency of the spectrometric phenomena, e.g., various chemiluminescence, bioluminescence, or thermoluminescence processes. 2. Inefficient spectral sources or associated optics as encountered with the fluorescence of microscopic samples or in laser microprobe atomic emission where there is insufficient energy in the excitation source. 3. Loss of light due to high requirements of filtering as in resonance Raman spectroscopy where a high degree of filtering is necessary to exclude the resonance exciting line.

Another common reason for photon starvation involves spectral phenomena of a transient nature. The shorter the measured pulse, the more difficult it is to keep it at a sufficiently high energy level to be measured. In this category belong a great number of laser spectroscopic studies of lifetime, i.e., studies of mechanisms involving various transition states, forbidden states, energy exchange through radiation and radiationless mechanisms, etc. Another example of a spectroscopic technique involving transient signals is picosecond laser spectroscopy which permits differentiation of phenomena that would be otherwise unresolved, e.g., scattering and fluorescence. Ultra-short spectroscopy also allows measurements to be made in the presence of exceedingly high continuous-wave (cw) background levels as encountered in the measurement of plasma temperatures by Thompson scattering, or measurement of fluorescence of oil slicks in daylight. In this case, the discrimination against the high background level is performed by synchronizing data acquisition with pulse timing. The performance of these procedures can be improved by averaging many individual pulses, obtained either synchronously or asynchronously.

Limited periods of illumination or excitation of the sample represent still another cause of photon starvation. Brief periods of illumination are often necessary in a number of spectroscopic applications to avoid deleterious effects. For example, prolonged irradiation of various fluorescing compounds can often result in bleaching. Similarly, microsample analysis by Raman spectrometry can easily cause structural and compositional damage to the sample upon long exposure to the intense excitation radiation.

Finally, the availability of very limited amounts of sample can result in a low radiant flux when samples are analyzed by emission spectroscopy. Clinical analyses involving samples from either children or small animals are an example of a situation where the amount of sample available is often very limited.

Detectors for Low-Light Level Operation

There are a variety of OIDs that are satisfactory for low-light level operation. Here, however we will discuss only the

detectors most available commercially, or those that are expected to have a real impact in the foreseeable future.

Silicon Intensified Target (SIT) Vidicon and Intensified SIT (ISIT)

These are silicon vidicon (generic name) TV-type detectors that have been extensively described in the spectroscopic literature. Basically they consist of a two-dimensional (2D) sensing area made of an array of silicon photodiodes that also serve as temporary storage devices, and an electron beam scanning arrangement to read the signal off this target. The high sensitivity of the SIT is achieved through an image intensification stage with an internal gain of approximately 2500. An image, e.g., a spectrum, is first converted by the photocathode to an equivalent electron image. An electrostatic focusing section, accelerates this electron image, while retaining its fidelity, resulting in incident electrons of approximately 8-9 KeV. Since each photoelectron produces an additional electron/hole pair in the silicon target for each increase of 3.6 eV, the internal gain is approximately 2500 for 9 KeV electrons. If the readout noise is maintained at approximately 2500 electrons/scan/channel, then a $S/N = 1$ should theoretically be achieved for a signal of 1 photoelectron/channel.

The ISIT consists of a first-generation triode image intensifier with an optical gain of 50-100 which is optically coupled to the photocathode of an SIT tube. The main advantages of an ISIT over an SIT are:

Gain. Theoretically, the ISIT can produce a signal of at least 5 digital counts per photoelectron. In fact, most of this assumed advantage is lost in the digitization process and, of course, the maximum S/N for a signal of 1 photoelectron cannot be better than 1. However, by lowering the gain of the preamplifier to obtain a readout noise less than 1 count rms, an improvement in S/N is obtained for low level signals (less than 1 photoelectron/scan) when on-target integration is utilized.

Spectral Response. For reasons stemming from differences in production philosophies, rather than fundamental differences, commercial image intensifiers have more efficient photocathodes, particularly in the red. In the UV, a UV-to-visible chemical converter is still necessary.

Gating Ratio. The on/off gating ratio is higher by approximately 2 orders of magnitude, making the ISIT a better detector for pulse spectroscopy.

Format. Larger format image intensifiers, e.g., 25 and 40 mm in diameter, are more available and affordable than SITs. Such intensifiers can be optically coupled to an SIT through a format reducing optical-fiber coupler, e.g., 40 to 18 mm (SIT standard format). This method will allow a wider spectral coverage with little, if any, loss in resolution.

The main disadvantages of the ISIT are: 1. Substantially costlier. 2. Less reliable; shorter lifetime. 3. More difficult to operate; more operational parameters to control. 4. Less immune to sudden "light" shocks. 5. Worse pin-cushion distortion; worse resolution and more nonlinear wavelength calibration. 6. More difficulties on cooling, i.e., more lag at lower temperatures. Therefore, the ISIT is even less amenable than the SIT to long term signal integration (on-target).

MCP/SPD (ISPD-Intensified Silicon Photodiode Array Detector)

The ISPD or intensified silicon photodiode array detector consists of a microchannel plate (MCP) image intensifier optically coupled to a silicon photodiode array (SPD) as the multichannel readout/storage device. The MCP (1) is a disk-shaped continuous dynode electron multiplier imager. It consists of millions of hollow microchannels formed in a glass substrate, where each channel, which is 12-25 μm in diameter, is semi-conducting. Each channel acts as an individual electron multiplier with an absolute geometric registration between the input and output plates of the device. An optical gain of 10-50 $\times 10^3$ is typical of MCPs. Cascading a few MCPs with channels arranged in a chevron orientation can produce gains of 10^7 , sufficient for multichannel photon counting. An MCP image intensifier consists of an input photocathode followed by an MCP wafer which is in turn followed by a phosphor output. Focusing of the electron image produced by the photocathode can be done by proximity, electrostatic, and magnetic methods. Only the first two are available commercially at an affordable cost. This discussion will concentrate on the MCP/SPD, although other OIDs can be used as readout devices (1).

Self-Scanned Silicon Photodiode Array (SPD)

At this time, the self-scanned silicon photodiode array is the only commercially available device that has been specifically designed as a parallel spectrometric detector. The performance characteristics of this detector and its applicability to spectrophotometric and spectrofluorometric measurements have been rigorously discussed elsewhere (2-4). The self-scanned photodiode array is a monolithic silicon wafer consisting of an array of diodes, each acting as a light-to-charge transducer and a storage device. Two shift registers

read out the charge signals stored in each of the odd and even diodes. Low noise and, consequently, high dynamic range are achieved through an appropriate design of the readout preamplifier and signal processing electronic section. One commercially available device, an S-type silicon photodiode array made by EG&G Reticon, is arranged so that each individual diode is 2.5 mm high and 25 μm wide. This 100:1 aspect ratio is a compromise design corresponding to typical aspect ratios of conventional spectrometer entrance slits.

The Ideal Multichannel (Parallel) Detector

The selection of a particular OID for a given application involves a number of important considerations. In evaluating the performance of these devices, it is instructive to compare their actual performance characteristics with those of a hypothetical ideal OID. In this way, it is possible to determine the extent to which a given detector compares in performance to an "ideal" OID. Table I lists some of the major characteristics of an ideal OID. These criteria are divided into two categories: operation and performance characteristics, and spectrometric performance. In the discussion which follows, each detector under consideration will be evaluated against the criteria listed in Table I. To be most useful to the reader in locating information about a particular performance feature of a given detector, the following discussion will be organized around the format developed in Table I. Thus, the reader who is interested in a particular characteristic-- immunity to light shocks, for example-- can refer to that section for a discussion of this feature for the detectors under consideration.

Operation and Performance Characteristics

Cost and Availability

SIT & ISIT. Commercially available from a variety of manufacturers at a moderate cost.

ISPD. Commercially available in 18, 25, and 40 mm diameters (MCP intensifiers). SPDs are available as 64, 128, 512, 1024, and 4096 element arrays.

SPD. SPDs are commercially available, although due to production yield considerations their price is still relatively high.

Reliability and Repeatability

SIT & ISIT. Reasonably good.

Table I. The Ideal Spectrometric Multichannel
(Parralel) Detector

Operation and Performance Characteristics

1. Low cost and wide commercial availability.
2. High device-to-device performance reliability and repeatability.
3. Long shelf life, long operation life, and long term stability. Day-to-day reproducibility.
4. Availability in a large variety of formats, sizes, pixel (picture cell) dimensions, and array density. Both linear and area arrays are necessary.
5. Simplicity of operation, minimal number of adjustable parameters that affect the performance of the detector.
6. Mechanical and electronic ruggedness. Tolerance to and operability under hostile environments, i.e., heat, humidity, magnetic fields, RF, etc. Minimum microphonic effects, i.e., stability of readout under vibration and other pressure wave oscillations.
7. Immunity to sudden "light shocks," i.e., rapid recovery from sudden exposure to high light levels. Non-destructive under very high light levels as long as exceedingly high temperatures are not reached.
8. Low weight, low power consumption, easy and adjustable cooling.
9. High tolerance flatness across the entire array to avoid loss of resolution at the flat focal place of the spectrometer. Availability of curved arrays to fit curved focal planes.

Spectrometer Performance

1. Wide spectral response: x-ray to IR. At least it is desirable to have detectors covering the UV to NIR, x-ray to UV, and NIR to medium IR.
2. Arrays with a variable spatial (spectral) resolution. This can be achieved by varying electronically the density of the array. Good resolution.
3. Random access readout of individual pixels. Pseudo random access, i.e., fact access, is possible with linear arrays. Real random access is possible with a variety of 2D arrays. To enhance the S/N of low level signals in the presence of high level signals, this access should be possible without a destructive readout.
4. Ultrarapid electronic shuttering (gating) for measurements of very fast transient phenomena. High on/off gating ratios are necessary.

Table I (Continued)

5. Minimum number of blemishes and defects. Most defects belong to either of two categories; severely reduced (or no) response, and unusually high dark charge.
6. Minimum variations in dark-charge and response across the array. Also, minimum variation in spectral response, i.e., constant response (with high efficiency) with wavelength. This excludes, by definition, "photon sensors."
7. Low dark-charge to enable long signal integration and storage periods and for long-term stability. Dark charge noise should be negligible compared with either preamplifier/readout or photon shot noise.
8. Low preamplifier noise, and very high gain (10^7) to detect very low light level signals, ideally through photon-counting techniques. Readout system should have an ultrarapid response time.
9. Very wide dynamic range. Usually a transfer characteristic curve (input-to-output) with a slope () of 1 is ideal. However, a capability to alter this slope electronically can be advantageous when very high dynamic reserves are necessary with pixels of limited capacitance.
10. Long signal integration periods for enhancement of S/N. High flexibility in altering the length of these periods.
11. Long signal storage periods. Particularly useful in 2D OIDs where a large amount of data must be temporarily stored before being transferred to memory.
12. Negligible readout lag, i.e., incomplete readout of signal. This is specifically important for transient spectrometry.
13. Negligible blooming, i.e., pixel-to-pixel crosstalk, mostly due to charge signal overspill to adjacent pixels.
14. Long term electrical, radiometric and geometric stability (wavelength calibration).
15. Minimum distortion of image (spectral lines) across the array. Constant magnification.
16. Equal modulation transfer function (MTF) across the array. This will result in equal resolution characteristics.
17. Capability to vary spectral dimensions either optically (with optical fiber couplers) or electronically (by demagnification) to ensure compatibility with focal plane format.
18. Capability of varying scan time.

ISPD. Reasonably good, although they vary widely with respect to photocathode sensitivity ($\mu\text{A}/\text{lumen}$) and uniformity.

SPD. Device-to-device reliability is generally good, although substantial variations in dark charge are still significant.

Long Term Stability

SIT & ISIT. Reasonably satisfactory.

ISPD. Electrostatically focused MCPs are better in this respect. Proximity-focused MCP intensifiers show an average gain reduction of 40-50% after 2-3,000 hours of non-stop exposure to varying low light levels. This is equivalent to approximately 1-1.5 years of continuous operation (4 hours/day). Also, the gain can be raised again, resulting in a real lifetime of 6,000-8,000 hours.

SPD. The SPD, typical of other integrated circuit devices, has good shelf and operational life. Day-to-day reproducibility of performance is good. A potential problem, not yet thoroughly investigated, is variation in response after prolonged exposure to high level UV radiation. At what energy dose that phenomenon becomes significant and whether or not annealing can be performed is not yet fully understood. However, when used in conventional UV-spectrometric measurements, this problem does not appear to be serious.

Formats

SIT & ISIT. Available in a few formats, e.g., 18- and 25-mm diameter, but non-standard ones are expensive.

ISPD. MCP wafers are available in a variety of formats, shapes, and sizes, e.g., circular wafers of up to 13 cm in diameter and rectangular wafers of up to 8 x 10 cm are routinely fabricated. MCPs are also available with individual channels biased at a specific angle. This is very useful for grazing incidence VUV-X-ray spectroscopy. MCPs can be stacked, in tandem, to achieve high gains, or otherwise the individual channels are bent in either a "J"- or "C"-shape to allow operation at high voltages (2500-3000 V). At these voltages, a single MCP may achieve enough gain for photon counting (1). MCP intensifiers are commercially available only in 18, 25, and 40 mm diameter formats.

SPD. S-type SPDs are available in formats of 64, 128, 512, and 1024 element arrays. A new 4096 element array SPD detector (aspect ratio 40:1) is now available. Area arrays with up to 200 x 200 elements are also available. It is our opinion (as

well as others), however, that charge-coupled devices (CCDs) and charge-injection type imagers (CIDs) hold greater promise for two-dimensional measurements.

Simplicity of Operation

SIT & ISIT. No. Magnetic coil parameters, cathode voltage, and image section must all be carefully controlled.

ISPD. Very simple operation with minimum variable parameters. MCP photocathode voltage is adjustable from approximately 160-240 V, but is typically fixed. Phosphor voltage is adjustable from 5-6 KV, and is also typically fixed. MCP voltage can be varied to adjust the gain. As a rule of thumb, a 50 V increase in voltage will double the gain. With respect to SPDs, the phases and preamplifier gain need usually be adjusted only once. Scan time is usually fixed.

SPD. The SPD is rather simple to operate. Adjustments are mainly those of phases and odd-even preamplifier gain setting. The array does not provide any amplification gain (as SIT or MCP/SPD devices do). Scan rate can also be adjusted from a few KHz to a few MHz.

Ruggedness

SIT & ISIT. Rather good mechanical and electrical ruggedness. These devices are susceptible to magnetic fields, and suffer from microphonic effects.

ISPD. Rather compact and resilient devices. Mechanically and electronically rugged. Magnetic fields have little effect. MCPs and SPDs are non-microphonic, and are designed to operate under high humidity and temperature conditions.

SPD. Electronically and mechanically very rugged. Tolerant of high temperature, humidity, vibration, and electrical or magnetic fields.

Light Shocks

SIT & ISIT. Can tolerate a reasonable light flux without any substantially adverse effects. However, precautions are necessary to avoid actual damage to the photocathode.

ISPD. MCPs should not be exposed to light levels above 4×10^{-5} foot-candle for long periods of time. Precautions should be similar to those taken with PMTs. Exposure to high light levels will temporarily raise the noise level of the detector. To protect the MCP and warn the user, ISPD detectors are usually

equipped with an automatic bright-control circuitry that shuts off the photocathode voltage when photocurrent or phosphor currents above a threshold level are reached. Also, a beeper alarm warns the user of this situation (5).

SPD. High immunity to "light shocks". Recovers rapidly from exposure to very high light levels. Not adversely affected by light except when levels are sufficiently high to heat the silicon wafer above its melting point.

Low Weight and Power Consumption

SIT & ISIT. No.

ISPD. MCP intensifiers, particularly the proximity focused type, are very compact and rugged. They require little power for operation and are easy to cool.

SPD. Small size and low weight. Uses very little power, and can be cooled to liquid nitrogen temperature.

Flatness

SIT & ISIT. Array is flat. Curved formats are not available. Electrostatic focusing causes pin-cushion distortion and a loss of geometric resolution at the detector's edges.

ISPD. Both MCPs and SPDs are very flat and have excellent geometric (wavelength) registration. Electrostatic focusing, however, causes pin-cushion distortion and therefore a loss of geometric registration, particularly at the detector's edges. The proximity MCP produces a near perfect geometric registration and does not suffer from reduced sensitivity at the edges (shading). Concave-shaped MCPs are available for non-photon applications (see below).

SPD. Very flat arrays with excellent geometric resolution, typical of integrated circuit technology.

Spectrometric Performance

Spectral Response

SIT & ISIT. Spectral response depends on the selection of the photocathode and can be optimized for the blue or the near IR. Typical photocathodes are S-20 and S-20R (extended red multi-alkali) which allow an adequate response up to 900 nm. Because the electrostatically focused image section requires a special optical-fiber faceplate window (curved inside to match the focusing field contours) made out of glass, the cut-off

wavelength for SITs is approximately 350 nm. To overcome this problem, a thin layer of a proper organic scintillator (fluorescing agent) is deposited on the optical-fiber faceplate. With such a scintillator an overall quantum efficiency (QE) of 1-2% can be achieved to 100 nm or lower. The effective QE of SIT detectors is lower than that of PMTs because of transmission losses through the fiber faceplate.

ISPD. The MCP intensifier offers an unusually wide spectral response, unmatched by any other OID. Each spectral region will be discussed in turn.

In the UV-Visible, the electrostatic MCP intensifier has the same spectral characteristics as the SIT, i.e., S-20 or S-20R photocathodes, and requires a chemical converter for UV measurements. The proximity focused MCP intensifier has a good response in the 200-850 nm spectral range.

In the VUV, two possibilities exist. First MgF_2 or LiF windows can be used with a variety of photocathodes, mostly of the solar-blind type. Second, the photocathode material can be directly deposited on the input of the MCP. For instance, CsI , KBr , and $CsTe$ photocathodes are good to approximately 100 nm, whereas LiF , BaF_2 , MgF_2 , and CaF_2 respond below 100 nm. Third, the channels themselves respond directly to photons of energies below approximately 100 nm.

MCPs have been used extensively for direct measurement of particles: for example, ions in the 3 eV-20 KeV range, electrons in the 100 eV to 100 KeV range, positrons, and metastables and neutrals such as H_2 , He, Ne, Ar, Kr, Xe, etc. There is a substantial literature on this mode of detection, but its compilation here is beyond the scope of this paper.

SPD. SPDs have good response in the spectral region from 185 (or less) to 1100 nm (2). For use in the VUV and EVUV regions, it is possible to deposit a fluorescing agent directly on the diodes which will act as a wavelength-up converter, thereby ensuring a good response to wavelengths less than 185 nm. In the x-ray spectral region, inorganic phosphors can be deposited on the optical-fiber window coupler (SF-type SPDs). With an appropriate thinning of the protective SiO_2 overcoat, the SPD can directly respond to high energy particles such as electrons. Some adverse side effects, mainly due to an increase in dark-charge under continuous bombardment, have been reported. Also, there is a significant absorption of electrons with energies below 6 KeV, even with an overcoating of SiO_2 that is 1 μm thick. This absorption makes the device insensitive to electrons at these energies.

Resolution

SIT & ISIT. The resolution of SIT detectors can be defined in several ways-- a) position (spatial) resolution, b) Rayleigh resolution, and c) modulation transfer function (MTF).

Spatial resolution is one channel which is typically 25 μm wide. Spectral resolution is the product of the channel width and the reciprocal dispersion of the spectrometer. For example, a spectrometer with a focal length of 0.25 m and grating of 152.5 grooves/mm typically produces a reciprocal linear dispersion of 25 nm/mm. Therefore a 25 μm channel will cover 0.64 nm. A 305 g/mm grating used with the same spectrometer would produce a resolution of 0.32 nm/channel.

Rayleigh resolution is the separation required for two images to be recognized as such. With OIDs this will typically mean that separation is such that cross talk between lines is 50%. If zero cross talk is required, at least one separating channel is necessary between the two lines. Under ideal conditions, cross talk between SIT channels is approximately 40 to 50%, so that Rayleigh resolution is about 50 μm (2 channels). If a narrow slit is used with a high quality spectrometer, Rayleigh resolution in wavelength units becomes 50 μm times the reciprocal dispersion. A simplified version of wavelength resolution which will be used throughout this manuscript is the number of channels (or pixels) at FWHM of a spectral line. For an SIT, this resolution is approximately 2-3 channels. The resolution, however, is not uniform across the detector and worsens when approaching the edges. The reason for this is a pin-cushion geometric distortion, typical of electrostatic image sections. A distortion of 5% is typical and will reduce resolution and cause errors in the wavelength calibration curve of the detector. The latter, however, can be computer-corrected.

Another means of expressing the fidelity of an optical system is in terms of its modulation transfer function. The modulation transfer function describes the ability of the optical system to accurately reproduce an object whose pattern of luminance varies in a sinusoidal manner. An optical system which can precisely duplicate the modulation pattern of the object in the modulation pattern of the image has a modulation transfer function equal to 1.0; this represents the performance of a perfect system. The greater the difference between the modulation pattern in the image compared with that in the object, the lower the modulation transfer function. In practice, the modulation transfer pattern is usually evaluated with a square-wave pattern produced by a periodic array of lines. The modulation transfer function approaches zero as the spatial frequency of the lines increases. The limiting resolution in terms of the modulation transfer function is

determined by the number of line pairs per millimeter which give a modulation transfer function which approaches zero.

When two closely spaced spectral lines of equal intensity satisfy the Rayleigh criterion, the valley between the lines is approximately 19% of the peak intensity. This corresponds to an MTF of about 0.10. Based on the data presented under the discussion of Rayleigh resolution, a MTF of 0.10 would be expected to result from a pattern with about 20 lines/mm.

The resolution of the SIT is definitely variable; any number of adjacent channels can be grouped together and read out as a single resolution element. Also, the number of diodes read out in each channel can be varied from four (approximately 100 μm) to 400 (approximately 10 mm). Thus, the two-dimensional target can be divided into a number of horizontal tracks, each of which can contain any number of resolution elements (max. 512) depending on the grouping setup.

ISPD. With proximity MCP intensifiers the resolution is practically constant across the entire array. By our spectral resolution definition (see SIT), the resolution is 3-4 diodes at FWHM. Near field stray light, however, widens the wings of spectral lines. There are a few phenomena believed to cause this apparent stray radiation energy (veiling glare). These include: (a) Light transmitted through the semi-transparent photocathode is reflected from the MCP wafer back to the photocathode. This process is enhanced by the closeness of the photocathode to the input faceplate of the MCP, i.e., 200 μm . (b) High energy photoelectrons colliding with the dead area between MCP channels (10,000 V/cm field) can produce secondary electrons that are collected by channels within approximately a 200 μm radius (8 diodes). With electrostatic intensifiers this stray energy (estimated at approximately 3% of photoelectron energy) can be collected by a special grid electrode placed between the photocathode and the MCP. This is impossible to do with proximity intensifiers. (c) Secondary electrons are spread during multiplication across the channel. This will reduce the resolution with both types of intensifiers. Since the resolution with the proximity-focused phosphor is approximately inversely proportional to the gap between the phosphor and the output faceplate of the MCP, and square root inversely proportional to the voltage between them, it could be somewhat improved by reducing the gap and/or raising the voltage. However, corona discharge problems set a practical limit on this approach. The effect of near field stray radiation on the spectral line profile is shown in Figure 1.

SPD. The spectral resolution of an SPD is governed by the same factors discussed for the SIT, i.e., it depends on the grating/spectrometer combination. The spatial resolution is degraded by a degree of diode-to-diode cross-talk, i.e., it is

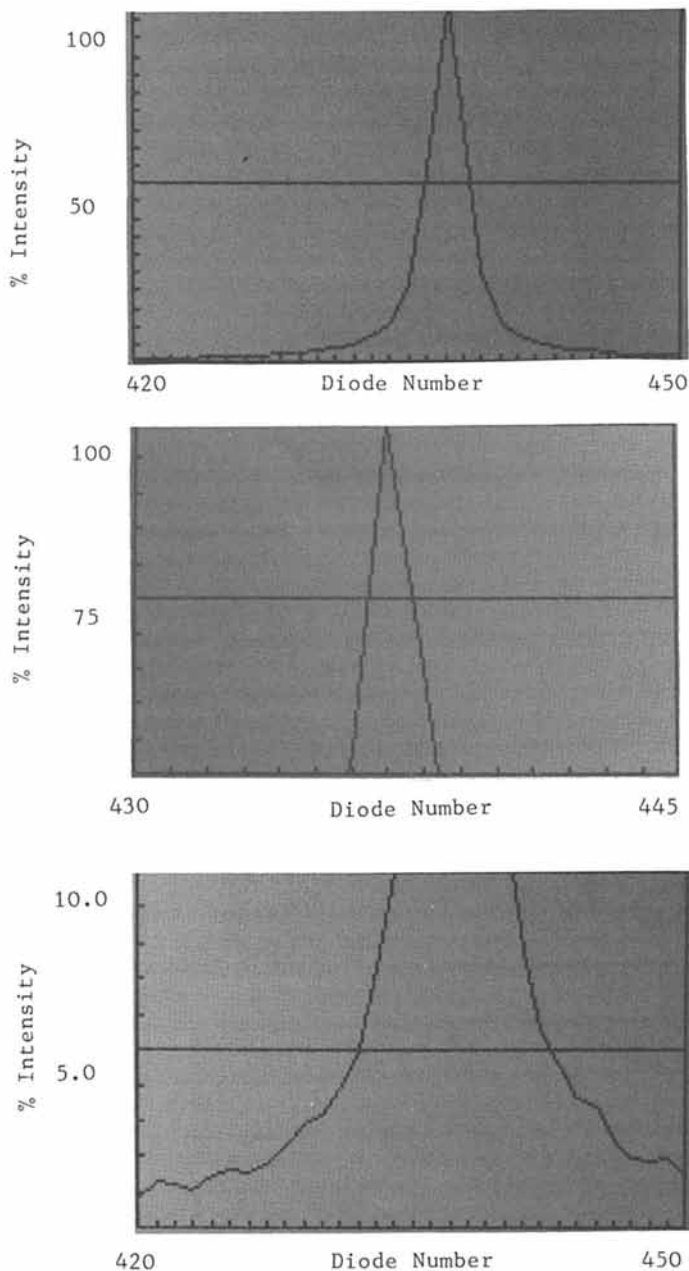


Figure 1. The effect of near field stray radiation on the spectral line profile (546-nm Hg emission line). The detector was a microchannel-plate image intensified diode array (Reticon model RL-512SF, Princeton Instruments, Inc. model IRY-512). Key: a, full line profile; b, upper half (FWHM) of line; and c, lower portion of line, 0-10% relative emission intensity.

very difficult to contain the entire energy of a very narrow line within the boundaries of a single diode. Typically, however, 2 diodes or less can characterize the FWHM of a spectral line. The cross-talk of SPDs is actually an advantage because it reduces aliasing problems (2). This "anti-aliasing" effect of cross-talk is particularly important for high resolution applications. A demonstration of the excellent resolution of SPDs is shown in Figure 2.

The spatial and spectral resolution of the SPD can be electronically varied by summing adjacent diodes in groups of 2,4,6,8, 10 etc. The diodes are read out (recharged) at very high rates, e.g., 2 MHz, but only the group-summed total integrated signal is digitized, and at a regular scan rate, e.g., 60 KHz. Diode grouping is useful in kinetics applications where sequential scans must be rapidly stored, but where spectral resolution can be reduced by grouping without any loss in experimental results. Grouping is also useful in smoothing (low-pass filtering) the odd/even gain variation pattern typical of SPDs, and thus making their real-time display more amenable to user interpretation.

Random Access Capability

SIT & ISIT. Real random-access is possible because the electron readout beam can be randomly directed to any portion of the target, skipping all others. This mode of operation is extremely useful in that it allows a (destructive) readout of very intense spectral lines, thereby avoiding severe blooming problems, while permitting weak signals to integrate for long periods of time, on target, to improve their S/N ratios. The random-access capability of the SIT makes it ideal for a variety of 2D applications, e.g., echelle spectrometry, total luminescence spectrometry, etc. The main limitation on this mode of operation is set by dark charge buildup that, unless reduced by cooling, will limit the time available for on-target signal integration.

ISPD. Random access capability depends only on the properties of the readout device. With the SPD only a pseudo-random, fast-access (skip) readout is possible (2,3).

SPD. The diodes in an SPD must be sequentially scanned by the shift registers and therefore a real random access cannot be accomplished. However, a pseudo-random access (fast access) readout mode is possible. In this mode, diodes that contain no relevant spectral information are skipped (not read) at a high scan rate, e.g., 2 MHz, whereas those containing desired information are digitized at a regular scan rate, e.g., 60 KHz. This operation permits a fast array scan without sacrifice in resolution, as grouping does.

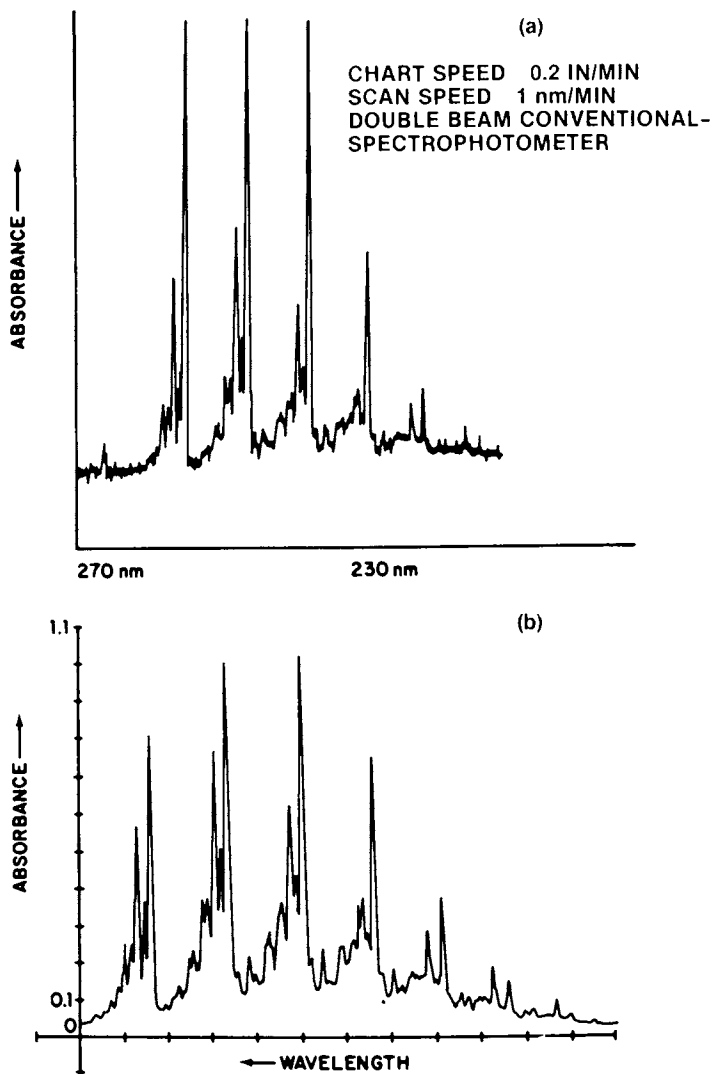


Figure 2. Molecular absorption spectrum of benzene vapor. Key: a, conventional spectrophotometer with a scan time of more than 45 min; and b, SPD detector with a signal integration time of 2 s (detector, Princeton Instruments, Inc. model IRY-512).

Gating

SIT & ISIT. Focusing electrodes in the electrostatic image section can be operated as a grid in a triode tube. By gating the tube off, photoelectrons from the photocathode fail to reach the silicon diode array. Gating allows a highly controlled exposure time on the target from 30 ns time frames to approximately 10 μ s (or longer). Also, precise delay time settings determine exactly when this exposure will occur after the initiation of the measured phenomenon, e.g., laser pulse. The accuracy of gating depends on the on/off gating ratio which is the ratio of the signal when the tube is gated on to that when the tube is gated off. The higher this ratio the better. With SITs this ratio varies from 10^4 :1 to 10^6 :1 and is higher the lower the light level. This occurs because some light transmitted through the semi-transparent photocathode passes through the focus grid pin hole. The gate pulse width is limited mostly by the electrical conductivity of the photocathode.

ISPD. Electrostatic intensifiers are hard to gate. Proximity intensifiers, however, are easy to gate since the photocathode is operated at low voltage, i.e., 160-220 V. To gate these detectors down to the 5 ns pulse width region, careful attention must be paid to the design of the gating power supply and its interface to the photocathode, and to the design and manufacture of the photocathode, particularly its conductivity and the mounting of the photocathode, especially the number and type of contacts. Recently, there are indications that MCPs might be gateable below 1 ns.

SPD. SPDs cannot be gated. Increase in temporal resolution can be performed only through faster scan rates (limited by A/D conversion) or by fast-access or grouping.

Blemishes

SIT & ISIT. Tubes with different blemish specifications are available at different costs.

ISPD. MCPs with good blemish specifications are relatively easy to obtain for use with linear detectors, i.e., where only a strip of the entire array is utilized.

SPD. Arrays differ from one another in the degree and number of blemishes. Arrays of the same type can differ by a factor of 5 or even 10 with respect to their overall average dark charge. Diode-to-diode dark charge variations in acceptable arrays are typically in the 2-10% range. Similarly, response variations

across an array are also within a similar range. Manufacturers can select SPDs with a prespecified blemish and dark charge specification at a higher cost. Response variation and spectral variation across an array can be easily corrected, as described in the SIT section.

Response Variations

SIT & ISIT. When operated at room temperature, each channel has a distinct dark charge signal level. At regular scan rates of 10-60 $\mu\text{s}/\text{channel}$, this level is very small. Channel-to-channel dark variations are very small, 1-2% being typical, but become larger as the number of diodes (vertically) summed in each channel is decreased. For long integration (on-target) periods, the SIT can be cooled to dry-ice temperature where the dark charge level is low enough to permit up to 45 minutes of target exposure without any adverse dark charge effects. At low temperature, however, readout discharge lag becomes more significant (see below). The advantage of on-target integration will also be discussed below.

ISPD. Dark charge levels and their variation across the ISPD are dominated by the dark charge of the SPD (2), typically 30 to 100 counts/second (1 count = 1400 electrons). Figure 3 shows the dark charge level of a 512 element ISPD (Princeton Instruments, Inc., Model IRY/512). Diode-to-diode dark charge variations are very reproducible and therefore easily subtractable. The "width" (band) of the curve is mostly due to odd-even (diode) preamplifier gain differences. There is, however, another source contributing to variations and noise across the array, namely photocathode spontaneous emission. Spontaneous emission is typically specified by manufacturers in terms of Equivalent Background Input (EBI), i.e., the photoelectron spontaneous emission is measured in terms of an equivalent signal due to illumination. EBI is typically 5×10^{-12} to 3×10^{-11} lumen/cm² for MCPs (similar to values of 1st generation image intensifiers as used in ISITs). Measurement of spontaneous emission from a 512 element ISPD with an EBI = 1.2×10^{-11} lumen/cm² showed a level of approximately 11 counts/second/diode which corresponds to approximately 11 photoelectrons/second/diode in this case (1 photoelectron = 1 count). This will amount to approximately 9.2 photoelectrons/diode / second / 1×10^{-11} lumen/cm². Response variations across the array are due to corresponding variations in the MCP and the photocathode, and can be as large as 10-30%, Figure 4. MCPs with abrupt (high spatial frequency) response variations are not used in ISPDs. These variations are easily corrected by flat-field normalization (2,3). Response variations due to wavelength dependency of the transducer (photocathode) are also correctable (6).

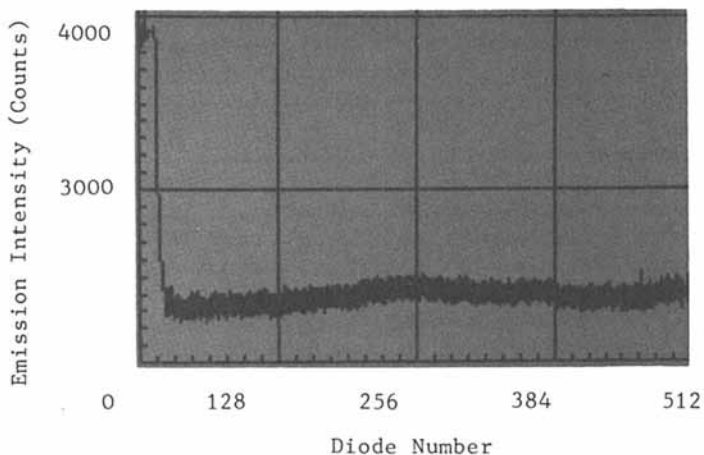


Figure 3. Dark charge pattern of a preselected silicon photodiode array (Reticon RL-512SF). Note that the first 20 diodes of this particular device have significantly higher dark levels. Detector conditions (Princeton Instruments, Inc. model IRY-512): temperature, -20°C ; and integration time, 50 s.

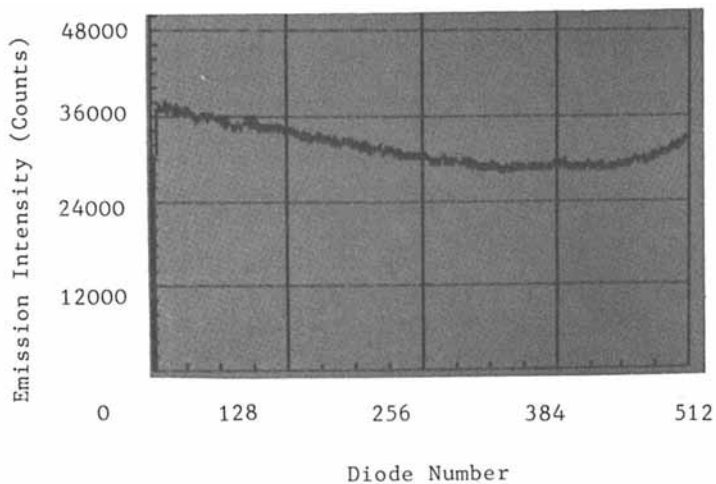


Figure 4. Uniformity of response in the array. The detector (as in Figure 3) was uniformly illuminated by diffused light (tungsten lamp).

SPD. Dark charge is reduced with cooling, i.e., approximately by a factor of 2 for each temperature reduction of 6.7 °C. A good SPD detection system can have a readout noise as low as 1200 rms electrons/diode. The preamplifier gain is then set so that 1 count (A/D converter) equals 1200 electrons. A good SPD will produce dark charge of the following magnitudes for different operating temperatures:

Temperature (°C)	electrons/sec/diode	counts/sec/diode
25	6×10^6	5000
-20	6×10^4	50
-100	15	0.0125

If it is conservatively assumed that 50% of the A/D converter range (14 bits) can be used for dark charge, then possible signal integration times (on-target) are:

1.6 seconds at 25 °C

164 seconds at -20 °C

182 hours at -100 °C

At very low integration times, the limit on integration is set by cosmic radiation. Dark charge does not contribute to the overall noise of the SPD until it reaches a level of approximately 1200 counts/diode/scan or more. The characteristic fixed pattern noise (2) and dark charge of each SPD are very stable and are therefore easily subtractable from any spectrum measured without affecting its accuracy or precision. For this stability to hold, however, stable electronics and high precision thermostating of the cooled SPD are required. Once these conditions are fulfilled the SPD shows excellent long-term stability, as discussed below.

Gain

SIT & ISIT. The gain is adequate to measure analog signals of approximately 2 photoelectrons (approx. 20 photons) / pixel / scan. In principle, if the system is well designed and fully optimized, SIT detection systems could be set at 2 photoelectrons = 1 count or 2500 electrons. The gain is far from adequate to utilize the detector in the digital photon counting mode. "Detection" usually means "certainty of the presence of a signal." With single channel detectors, three times the rms noise is usually considered the detection threshold. With multichannel detectors, this threshold is most

likely insufficient because the probability of "detecting" a 3 x rms deviation in the baseline is about 10^{-3} when 500 trials (channels) are taken in each measurement. With 500 channels, there is a probability of approximately 30% that a 3 x rms noise signal will be falsely detected for one channel. A threshold of 5 x rms will raise the confidence that the event is real to about 70%. This degree of confidence of detection is, of course, just another way to describe the S/N. S/N improves in a square-root fashion with the number of consecutive scans, averaged in memory, or the number of grouped channels that measure the spectral event. This is the same as saying that the confidence level of detecting a real event increases with the square root of the number of averaged scans. For very low light level signals, i.e., below the preamplifier noise level, on-target integration is preferable because the S/N improves almost linearly with time of integration rather than in a square-root fashion. This, of course, requires cooling of the detector. Dark charge reduction is approximately a factor of 2 for each reduction in temperature of 7-8 °C.

ISPD. A straight channel MCP intensifier cannot produce a gain in excess of 50-60,000, and proximity intensifiers usually have a gain of 10-20,000. Nevertheless, with proper design of the electronics, proper cooling, and careful prevention of corona discharge (HV), the readout noise can be maintained at a 1200-1400 electrons rms level. With a gain of 10^4 , it is theoretically possible to obtain approximately 2 counts per photoelectron (1 count = 1200-1400 electrons) or more. Using the previous detection definition (see SIT), the minimum detection is approximately 5 counts which corresponds to 2.5 photoelectrons/scan. As with SITs and SPDs, S/N can be improved with signal integration (2,3). Theoretically, with signal levels above 1 photoelectron both in-memory and on-target integrations will produce the same improvement, since the system is photon shot-noise limited. Below this level, however, on-target signal integration will produce an improvement that is linearly proportional with integration time, compared to square-root proportional with in-memory integration. This is so because the system is readout-noise limited. Figures 5 and 6 show the improvement in S/N with on-target signal integration.

SPD. The SPD provides no signal gain, and its readout noise is limited by its thermodynamic (KTC) noise to approximately 700 to 1200 rms electrons. Considering detection to be at signal = 5 x rms noise (see SIT section) and an average quantum efficiency of 50%, the smallest detectable signal is approximately 10^4 photons/diode/scan. For light signals of short duration (< scan time), this detection, obviously does not allow low light level measurements. When long on-target signal integration times are possible (see below) low light level signals can be detected.

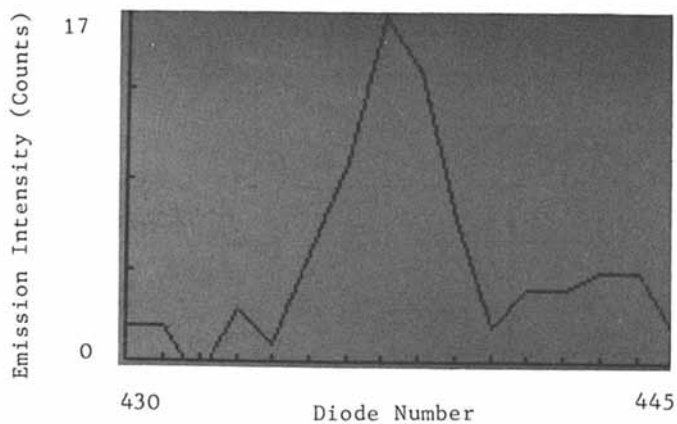


Figure 5. Line profile of the Hg line (546 nm). Detector is the same as in Figure 1. The on-target signal integration was 16.67 ms.

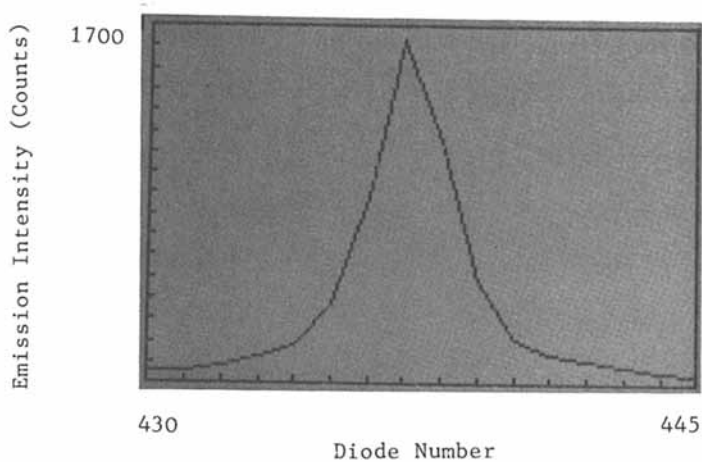


Figure 6. Line profile of Hg line (546 nm) (as in Figure 5) with a signal integration of 1.67 s.

The SPD, because of its excellent spectral response, geometric, electronic, and radiometric stability, low readout lag, and low blooming characteristics, is an ideal detector for applications requiring adequately wide dynamic range with short- and long-term stability, e.g., static and dynamic spectrophotometry. Because the SPD is basically a preamplifier/readout noise limited device, its overall noise (counts) remains very low even at its full signal capacity. For example, with a 14 bit A/D converter (16,384:1) the associated noise (including photon shot noise) for a full ADC range signal is only approximately 4 counts rms. If dark charge is kept low, a $S/N > 4000$ can be achieved with such signals. Indeed, SPD detection systems are able to achieve photometric precision levels better than 10^{-4} AU.

Dynamic Range

SIT & ISIT. Under the definition of dynamic range as the ratio of the largest readable signal to the rms noise of the detection system, there are actually at least four kinds of dynamic range values. We will confine our discussion to the following three types of dynamic range.

Single channel dynamic range is usually equal to the dynamic range of the A/D converter used, since readout noise is arbitrarily set equal to one digital count. A range of 16,384:1 (14 bits) is easily achieved for this range which describes the maximum and minimum signal each channel can measure.

Intraspectral dynamic range is the ratio of the largest and smallest input signals that can be simultaneously measured in a single scan (regardless of the length of signal integration time). This definition is one of the least understood. There are a variety of reasons why this range is substantially less than 16,384:1; for example: (a) Stray light reflected from the intensifier enclosure can obscure low level signals. (b) High dark current and/or background signals upon which the analyte signal is superimposed can reduce this form of dynamic range. Even though both artifacts can be accurately subtracted, the noise associated with them can cause obscuration of the signal. For example: if an analyte signal with an intensity of 9 photoelectrons/scan is superimposed on a line wing of an adjacent line with a signal magnitude of 91 photoelectrons/scan, the S/N for the analyte signal is $9/(91+9)^{1/2} = 0.9$. In the absence of the line wing, the net $S/N = 3$.

Memory dynamic range depends on the size of the available memory. Of course, very wide digital memories can be used to store very large signal values, i.e., the result of on-target and in-memory readout modes. Depending on the noise of the signal and detector, the optimal memory width can be selected, but a minimum range of $10^6:1$ is useful.

ISPD. The ISPD provides a linear dynamic range (1-3%) of at least 16,384:1 (14 bit A/D converter). At illumination levels above 4×10^{-5} foot candle (with a corresponding output brightness of approximately 1 foot lambert), the MCP saturates and thereafter has a non-linear transfer characteristic. However, this level is way above the A/D converter saturation level and has no implications on low light level spectroscopy.

SPD. The dynamic range of SPDs will be discussed in terms of their single channel dynamic range and their intraspectral dynamic range.

Single channel dynamic range is practically limited by the range of affordable A/D converters that can operate at the proper scan rates. With 14 bit A/D converters (16,384:1), linearity is achieved to within at least 2-3% over the entire range. The Variable Integration Time (VIT) technique (2) greatly increases the practical dynamic range. This is done by varying the on-target integration time periods so that high and low intensity signals can be read with comparable S/N ratios. The reciprocity, i.e., the product of signal intensity and signal integration time is linear within a count range exceeding $10^6:1$. The VIT technique allows detection of low light level signals which would otherwise be detectable only by high gain detectors, e.g., PMTs or ISPDs. A good example of this capability is given elsewhere in this book (4).

The intraspectral dynamic range of the SPD is affected by a certain degree of stray light, although substantially less than the ISPD. Furthermore, since detector heads have their own sealed quartz windows, it is possible to use the SPD without its own quartz window and thus reduce the degree of internal reflection. Additionally, internal reflections between the silicon target and the detector quartz window can be reduced by using off-axis optics.

Signal Storage Capability

SIT & ISIT. Storage time of SITs depends only on the dark charge level, which depends on the detector temperature. At room temperature, a storage time of 1-2 seconds is typical. At dry-ice temperature, 20-50 minutes of storage time are possible.

ISPD. Storage time depends on cooling temperature. For long storage periods the MCP must also be cooled to reduce spontaneous photoemission. However, cooling of the photocathode will reduce the red response of the photocathode.

SPD. Signal storage time is small unless the detector is cooled to below -50°C (30-60 minutes).

Lag

SIT & ISIT. Vidicon detectors require some time to adjust to large variations in signal magnitude because of readout discharge lag, i.e., incomplete readout of signal in a single scan. Actually, better than theoretical (based on shot noise) S/N performance is achieved in cw (continuous wave) operation because lag causes signal averaging. However, discharge lag is a distinct disadvantage in single shot measurements. The presence of lag means that at least 5-10 scans are required to read all the charge off the target. This is not a problem when high repetition rate pulses, i.e., a few per second or more, are measured.

ISPD. The SPD readout device is practically discharge lag-free. Any lag of the ISPD will originate from the decay time of the output phosphor (although at very high rate photon counting, the electrical response time of the channels becomes an important factor). As explained with the SIT (under discharge lag), slow phosphor decay time will have little effect on the accuracy of measurements of single pulses or with high repetition rate pulses or cw. It becomes a problem, however, with low repetition rate pulses where each pulse is superimposed on the decay tail of the preceding pulse. Fortunately, the phosphor decay time decreases significantly as the excitation (measured) pulse becomes shorter. Decay time is also affected by the energy level of the pulse and by the granularity of the phosphor. It seems, however, that for short pulses $< 1 \mu\text{s}$, decay time may not become an accuracy limiting factor.

SPD. When high quality devices are used, readout lag of SPDs is very small for light levels below the capacitance saturation of the diodes, i.e., approximately 2×10^8 photons/diode. Above that light level, charge diffuses to the substrate and a few array scans may be necessary to fully read it off the target. It is interesting to note that the vidicon lag is due to incomplete readout of small signals, whereas the reverse is true for SPDs.

Blooming

SIT & ISIT. Blooming will occur when diodes are saturated, i.e., signal will spill over to adjacent diodes. This is partially reduced by the electrical isolation between adjacent diodes. Another phenomenon with similar results is halation or light reflected back to the photocathode from the target (the photocathode is semi-transparent). This is, in essence, a stray light phenomenon that produces an halo around high intensity spectral lines.

ISPD. Blooming problems are very small and similar to those discussed for the SPD (see below), i.e., blooming is limited to charge overspill to adjacent diodes only, once the capacitance level (approximately 8×10^7 electrons) is exceeded. Stray energy radiation problems have been previously discussed.

SPD. With quality devices, blooming seems to be confined to adjacent diodes, i.e., upon saturation of a diode, signal charge will partially spill over to the nearest unsaturated diode. Localized blooming is essential in order to maintain an adequate spatial resolution across the array and to efficiently utilize the VIT readout technique, i.e., the smaller the blooming, the smaller the effect of high level signals on near-by low level signals.

Long Term Stability

SIT & ISIT. Long-term stability is possible, but difficult, to achieve. Instabilities will occur as a result of temperature variations. Examples of parameters affected by environmental conditions and whose variability will degrade detector performance are: target dark charge, coil operation, magnetic interference with coil operation, instabilities in high voltage supply which cause variations in focusing and distortion, variations in cathode voltage which affect readout and lag parameters, etc. In general, the larger the number of set-up parameters, the greater the instability.

ISPD. Good long term stability provided that the MCP has not been previously exposed to high level illumination and that the SPD is accurately thermostated.

SPD. Long term radiometric stability is good. Geometric stability is unaffected by external perturbations, e.g., magnetic field, and is always the same. Electrical stability depends on the design of the preamplifier and signal processing electronics and is usually not a problem. In the past, long in-memory integration periods resulted in output separation into four spectra (for each phase); this has not been observed with the new (SPD) detector head (Princeton Instruments, Inc., Model RY-512). Long term baseline stability depends on cooling and precision thermostating, and can be maintained at or below the level of photon-shot noise.

Distortion

SIT & ISIT. Subject to pin cushion distortion (see above).

ISPD. Electrostatic intensification has a maximum distortion (pin-cushion) of approximately 5%. Proximity intensifiers have

no geometric distortion. Magnification ratios (input/output) can vary from detector to detector in the 0.9 to 1.04 range.

SPD. SPD arrays have no geometric distortion. Variation in resolution, response, dark charge, pattern noise, etc. are random across the array.

Modulation Transfer Function

SIT & ISIT. Pin cushion distortion (see above) results in a variation of the modulation transfer function across the target of the detector with a maximum distortion present in the periphery.

ISPD. Typical MTF values for MCPs are as follows (lp = line pair):

lp/mm	proximity	electrostatic
2.5	86%	90%
7.5	58%	60%
15	20%	25%

The MTF of the SPD is substantially better than that of the MCP intensifiers and therefore contributes little to the overall MTF of the ISPD.

Variable Dimensions

SIT & ISIT. The dimensions of the SIT and ISIT are fixed.

ISPD. A 40 mm MCP can be coupled to a 25 mm SPD (1024 elements) through a 40/25 mm format reducing optical-fiber coupler and thereby result in a proportional increase in the spectral window of the detector.

SPD. Format reducing optical-fiber couplers, e.g., 40 mm to 25 mm, can be used as spectrum demagnifiers. Such devices can increase the spectral coverage of an SPD at the sacrifice of UV response. UV-to-visible chemical converters can be deposited on the input optical-fiber faceplate, but a certain degree of lateral cross-talk could result in a deterioration in resolution. Flexible bundles of coherent (imaging) optical-fibers can be used to bind together (side by side) any number of SPDs in a contiguous manner. This can allow an adaptability of SPDs to any focal plane and any spectral coverage required.

Variable Scan Time

SIT & ISIT. Variation of scan time is possible within a reasonable range, i.e., lowest portion limited by discharge lag, highest portion by dark charge level. Variations between 20-200 μ s are easily achieved.

ISPD. Rather than vary the scan time, it is preferable to vary the on-target integration time. This can be conveniently accomplished over the range from 16 ms to 120 seconds (with cooling to -20° C).

SPD. Scan time can be varied from a few KHz to a few MHz, but variation of scan time through adjustment of exposure time is advantageous.

Conclusions

The primary purpose of this paper has been to provide a convenient reference for researchers who are interested in applying OIDs for low-light level spectroscopy and who need a source of detailed information about these devices to enable them to select the proper detector for a particular application.

This paper has presented an in-depth comparison of four optoelectronic image devices with 25 performance criteria. In using the guidelines presented in this paper for the selection of a particular OID for low-light level applications, one should divide the various criteria discussed into two categories based on the particular application under consideration. The first category should include those criteria which are of paramount importance for the particular application. The other category should include those criteria which are of secondary importance in the particular application. Care should be taken at this stage to avoid mutually exclusive situations. For example, it will be difficult to find a detector which is sensitive to very low-light levels and is simultaneously immune to light shocks. Based on the particular criteria identified in the first category, a particular OID may emerge as being the most satisfactory for the given application. Alternatively, no clear-cut winner may emerge from the comparison which may mean that the selection of a particular OID may not be critical to the given application or that the current state-of-the-art OIDs are unable to meet the requirements of the experiment.

It should be clear from the discussion of the performance criteria of OIDs that no one detector is best suited for all possible spectroscopic applications. Proper selection, therefore, depends on an in-depth understanding of detector characteristics as discussed in this paper. Fortunately, there are already a diversity of OIDs available and more are being developed. This is a rapidly changing area and second-

generation devices with improved performance specifications are being continually developed. Therefore, if current state-of-the-art devices are not satisfactory for a given application, it may not be much longer before improved devices are developed.

Literature Cited

1. Siegmund, Oswald H. W.; Malina, Roger F. in "Image Devices in Spectroscopy," Talmi, Y., Ed.; ACS SYMPOSIUM SERIES No. ACS:Washington, D.C., 1983.
2. Talmi, Y.; Simpson, R. W. Appl. Opt. 1980, 19, 1401.
3. Talmi, Y. Appl. Spectrosc. 1980, 36, 1.
4. Grabau, F.; Talmi, Y. in "Image Devices in Spectroscopy," Talmi, Y., Ed.; ACS SYMPOSIUM SERIES No. 102, ACS:Washington, D.C., 1983.
5. "Model IRY Detector Head Manual," Princeton Instruments, Inc., 1982.
6. Talmi, Y.; Baker, D. C.; Jadamec, J. E.; Saner, W. A. Anal. Chem. 1978, 50, 936A.

RECEIVED July 26, 1983

The Silicon-Intensified Target Vidicon Detector Operation, Characterization, and Application in Atomic Spectroscopy Research

JOHN W. OLESIK¹ and JOHN P. WALTERS²

University of Wisconsin-Madison, Madison, WI 53706

In this paper we briefly discuss the operation of the silicon intensified target (SIT) vidicon, describing what we conclude to be the spectroscopically most important properties of the detector. We provide experimental evaluation of the SIT vidicon characteristics including two-dimensional image fidelity; channel-to-channel and pixel-to-pixel response as a function of position on the detector; and temporal resolution and gating. We illustrate how these unique properties enhance our ability to make spectroscopic measurements while at the same time impose limitations on the use of the SIT vidicon. We describe a variety of experiments which employed an SIT vidicon detection system for atomic spectroscopy with various degrees of spatial and temporal resolution.

The silicon intensified target (SIT) vidicon has a number of unique properties which make it a valuable detector for atomic spectroscopy. The SIT vidicon provides two-dimensional photoelectric detection with high sensitivity and rapid signal readout. Time resolution can be obtained in a time-resolved (real time) mode on the millisecond scale and in a time-gated (equivalent time) mode on the submicrosecond scale.

Coupling an SIT vidicon detector with an on-line computer for detector control, experiment synchronization, data acquisition and data processing results in a powerful and flexible detection system. The flexibility results from the

¹Current address: Department of Chemistry, Indiana University, Bloomington, IN 47405.

²Current address: Department of Chemistry, St. Olaf College, Northfield, MN 55057.

software control of the speed of signal acquisition, spectral resolution, photometric accuracy, exposure time, spatial resolution, and temporal resolution. Complete commercial systems including an SIT vidicon detector, detector controller, high voltage pulser for time gating, and a computer, including software, are available. The Princeton Applied Research Corporation (PARC) OMA II system was used in these studies, mounted in the focal plane of a one meter McPherson model 2051 monochromator.

While the SIT vidicon detection system provides unique and exciting spectroscopic detection capabilities, inherent limitations of vidicon detection prevent it from replacing other detectors such as photographic emulsions, photomultiplier tubes, or linear photodiode arrays. Rather, the SIT vidicon is complementary to the more traditional spectroscopic detectors.

Operation of the SIT Vidicon

Although the operation of vidicon detectors has been described elsewhere (1-4), we briefly summarize it here since the vidicon components and operation affect the characteristics of the SIT vidicon as a spectroscopic detector. Similar to other imaging detectors, the silicon vidicon is made up of three main components. A transducer converts the photon spectral image to its corresponding electrical analog. In the silicon vidicon the silicon target performs this function while in the silicon intensified target vidicon, shown in Figure 1, the scintillator and photocathode act as the transducer. The silicon target acts as a storage device for the electrical analog of the spectral image. The target is built on an n-type silicon wafer which serves as a common cathode. P-type semiconductor anodes are grown on the wafer, approximately eight microns apart. The vidicon signal is acquired by an electron beam, twenty-five microns in diameter, which acts as the reading device.

The operation of a silicon vidicon consists of preparation, exposure, development and reading steps. The target is restored to an equilibrium potential by scanning the electron beam to charge the p-type islands to a negative potential, erasing previously stored images. The n-type substrate is held at ground potential, resulting in a reversed-biased diode condition. This prepares the target for exposure by producing a depletion layer which acts as a storage capacitor. Photoelectrons imaged on the target produce electron-hole pairs. The holes diffuse through the depletion layer into the p-type islands, discharging the capacitors. The development step is performed by scanning the target with the electron beam, the vidicon analog to a photographic developer. The change in current due to recharging of each capacitor is amplified to become the video signal. Since this current is proportional to

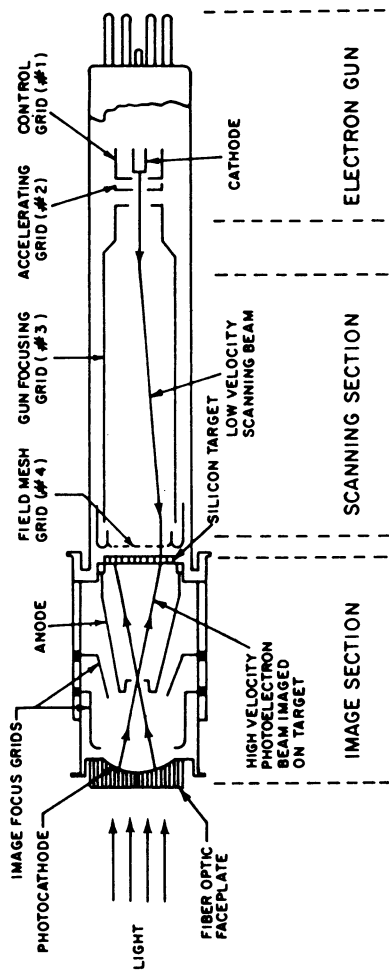


Figure 1. Illustration of the silicon-intensified target (SIT) vidicon. (Reproduced with permission from Ref. 8. Copyright 1978, Princeton Applied Research Corporation.)

the amount of capacitor recharging necessary to reattain the equilibrium potential, and the capacitors are discharged in proportion to the number of photoelectrons, the recharging current is proportional to the incident light intensity. The video signal is digitized and stored in the computer random access memory and/or displayed on a CRT.

The intensifier stage increases the sensitivity of the SIT vidicon over an unintensified silicon vidicon detector. The photoelectrons are accelerated and electrically focused onto the target by an electrostatic field of seven to nine kilovolts. Approximately 1500 electron-hole pairs are produced for each electron which strikes the silicon target. However, because the photocathode has a much lower quantum efficiency than the silicon target, the photosignal gain of the SIT vidicon is only approximately two hundred times that of the unintensified silicon vidicon (3) and substantially less in the ultraviolet region. The sensitivity of the SIT vidicon with a scintillator has been compared (5) to a 1P28 photomultiplier tube integrated signal. The SIT vidicon sensitivity was found to be similar to a 1P28 photomultiplier tube from 400 to 600 nm, somewhat more sensitive from 600 to 800 nm and approximately twenty times less sensitive from 200 to 400 nm. With the new scintillator in the OMA II system, the difference in sensitivity in the ultraviolet region is five to ten times less than the 1P28 PMT. The scintillator is necessary because of the otherwise poor response below 400 nm, due mainly to losses in the fiber optic faceplate. The fiber optic faceplate is necessary because a curved surface is required for electrostatic imaging in the intensifier section (6) of the SIT vidicon tube.

The SIT vidicon detection can be gated by controlling the intensifier stage in a manner similar to a triode tube in the grounded grid configuration (7). A negative voltage pulse (-500 to -1200 volts) is applied to the photocathode to turn the tube on. The on/off gating ratio of the detector is 10^4 to 10^6 .

Control of the SIT vidicon. Regions of the vidicon target to be read out, and therefore the spectral and/or spatial regions to be observed, are controlled by scanning of the electron beam. In the PARC OMA II system the electron beam scanning is under software control. A 500 x 500 array of positions on the vidicon target (pixels, or picture elements) can be randomly addressed and read. Individual regions of the target to be read out, called tracks, are defined by a number of channels (columns of pixels) of a chosen height, y . A frame consists of one readout scan of the selected number of tracks.

The exposure time is determined by the channel time, the time the electron beam takes to read each channel, the number of channels read out, the number of channels grouped together as one resolution element, and the number of scans which are

accumulated. The exposure time can also be controlled by a software-controlled delay before the target is read. However, cooling of the vidicon is required for delay times of more than 100 ms as discussed below.

Vidicon Components Effect on Detection

The most obvious limitation of vidicon detectors is the small detector area. Typically, the SIT vidicon detector area is 12.5 by 12.5 mm. However, the useful detector area may be further limited by distortion which is most severe near the edges of the detector, as will be discussed below. If a polychromator with a dispersion of 0.83 nm/mm is used, a wavelength range of 10 nm can be monitored when the full width of the vidicon is used.

Silicon target. The use of a silicon target for storage of the electrical signal image results in an integrating detector sensitive to energy rather than power. The target is the main source of dark current and limits the on-target storage time to approximately one hundred milliseconds at room temperature (1). The storage time can be increased to up to two hours by cooling the detector (9,10). However, cooling is inconvenient due to the size of the vidicon detector (in comparison to a photodiode array, for example). Some commercially available coolers are constructed so that the focal plane of the polychromator used must be three inches outside of where the cooler and vidicon are attached to the polychromator housing often requiring a specially designed polychromator or additional optics. This is due to the need to insulate the vidicon cooler and prevent frosting of the window between the polychromator and the vidicon. Cooling also results in substantially increased lag, which is discussed below.

Because the target rather than the photocathode is the main dark current source, the dark current signal is independent of the gate width used. The random noise component of the dark current can limit the detectability of light signals. Multiple scans or asynchronous averaging increases detectability and signal-to-noise (11) as shown in Figure 2.

Blooming. Migration of charge on the silicon target and, more importantly, use of electron beam readout results in blooming, or crosstalk, between channels. The crosstalk in the PARC supplied SIT vidicon is specified (8) to be less than 60% between a central channel and each of its two neighbors. Table I shows the measured blooming from a central channel to nearby channels.

Blooming limits the resolution obtainable with vidicon detectors. For example, if an atomic line with a 0.02 nm line width is observed through a polychromator with 0.83 nm/mm

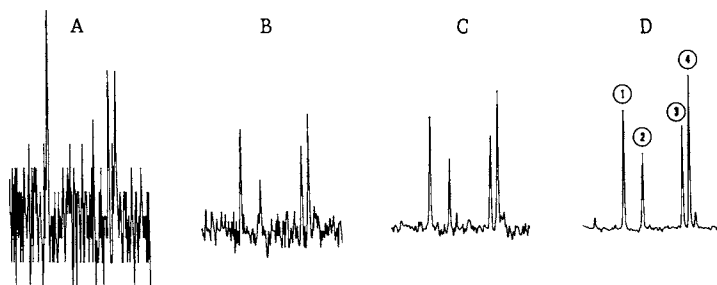


Figure 2. Vidicon detected, copper hollow cathode spectra showing an increase in signal-to-noise ratio as the detection time and number of readout scans is increased.

Key: A, signal from a single readout scan (detection time, 16.6 ms); B, signal from 10 readout scans (detection time, 166 ms); C, signal from 100 readout scans (detection time, 1.66 s); and D, signal from 1000 readout scans (detection time, 16.6 s). The Y axes for all spectra are in arbitrary intensities units. The spectral lines observed are: 1, 329.30 nm; 2, 329.77 nm; 3, 330.80 nm; and 4, 331.13 nm. Detector conditions were: 80 μ s/channel readout; 500 channels read out; 10 prep scans before each spectrum was obtained; and delta Y = 100.

Table I. Blooming in SIT vidicon.*

Channel from center	Intensity	Percentage of center channel intensity
0	19935	100.0%
+ 1	10435	52.3
- 1	11133	55.8
+ 2	2481	12.4
- 2	2360	11.8
+ 3	624	3.1
- 3	622	3.1
+ 4	251	1.3
- 4	399	2.0
+ 5	92	0.4
- 5	346	1.7
+ 6	62	0.0
- 6	185	0.1
+ 7	43	0.0
- 7	99	0.0

* Blooming was measured by using an iron hollow cathode lamp source, a 20 micron entrance slit on a McPherson 1 meter Czerny-Turner polychromator used in first order. The 352.126 nm iron I line was centered on a single channel (X = 230). Five hundred channels, each 80 pixels high (Y = 210 to 290) were monitored in PARC timing mode 1 and scan mode 1 (normal). One hundred readout scans were performed after two preparation scans with a 20 microsecond/channel readout time. (Other channel times of 40, 60, 80, 100, 120 and 140 microseconds were also used with similar blooming resulting.)

dispersion, the measured half-width of the line will be approximately 0.06 nm, due to the 60% crosstalk to neighboring channels. This effect will be much less severe for signals with larger linewidths. Blooming occurs in both dimensions so that if the second dimension of the vidicon detector is used for spatial resolution, it too will be limited by signal blooming. The effects of blooming are most severe when a weak signal of interest is observed near an intense signal or when large changes in intensity occur over short image distances.

Lag due to incomplete signal readout from the target.

When the electron beam scans over the target, the signal is not completely read out in a single pass. This phenomenon, called discharge lag, in a simplistic view, is due to the resistance of the reading electron beam, capacitance of the silicon target, and the capacitive recharge nature of the signal readout. The lag depends on the signal intensity (4,12) because the target capacitance is a function of the charge present on it. The percentage of the signal read out in each pass is a function of the dwell time, or the time the readout beam spends at each pixel, the electron beam current (12), and the relationship between the target and beam voltages. Since the scan rate is controlled by the readout time per channel, the dwell time is a function of the channel time and the number of pixels making up each channel:

$$\text{dwell time} = \text{channel time} / \text{pixels per channel.}$$

The lag was measured for a number of different dwell times. The results are shown in Figure 3.

Lag limits the rate at which the vidicon target can be read out, and therefore, the time resolution attainable in the time-resolved, or real-time, mode. Approximately 30 spectra of 500 channels each can be acquired in a one-second period. Spectra can be obtained more rapidly if the size of the target region scanned, and therefore the wavelength range monitored, are reduced.

With pulsed or transient illumination, lag also results in a nonlinear detector response to incident light intensity. The effects of lag on the linearity of detector response can be reduced by using multiple readout scans, long dwell times, both resulting in longer readout times, or other schemes (13,14, 15).

The vidicon can be cooled in order to reduce the thermally generated dark current, allowing long integration times to monitor weak signals. However, lag is greatly increased when the detector is cooled. As a result, erasure of previous images and target preparation becomes extremely important. The effects of lag can be minimized by using preillumination. In commercial cooled housings, a light emitting diode (LED) is positioned near

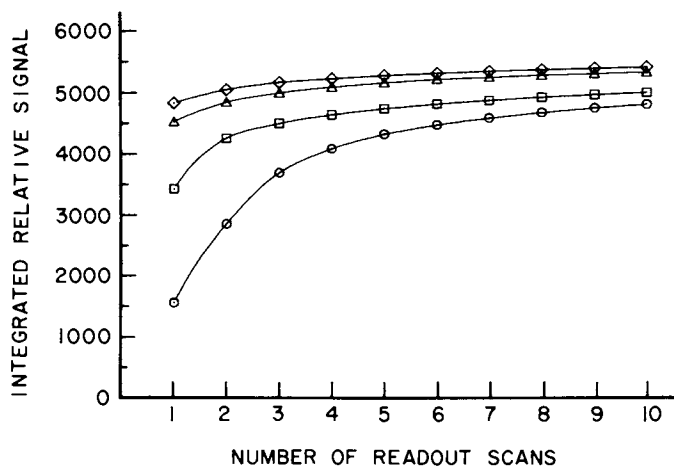


Figure 3. Relative integrated signal showing the effect of lag as a function of dwell time controlled by channel time. Each channel consisted of 500 pixels ($\Delta Y = 500$). Signal is due to a single pulse of a Xe strobe lamp (General Radio, 1539-A Stroboslave). Light was detected in zero order with a $20\text{-}\mu\text{m}$ entrance slit. Dwell time: ○, 40 ns; □, 80 ns; △, 160 ns; and ◇, 240 ns.

the vidicon face. The LED is flashed to completely discharge the silicon diodes in order to totally erase previous images. Readout scans are then used to prepare the target for exposure. Alternatively, the electron beam potential can be shifted between the preparation and reading potential levels to reduce the effects of lag (13,14,15).

Electrostatic image intensifier. The intensifier stage of the SIT vidicon increases sensitivity through electron gain and provides time gating capability. Variable gain is possible by adjustment of the cathode voltage. However, electrostatic focusing of the intensified image introduces losses in resolution and sensitivity near the target edges due to pincushion distortion (16,17) of the image. The distortion also results in a nonlinear wavelength axis when an SIT vidicon is placed at the focal plane of a polychromator. The nonlinearity of 2 to 3% (17) can be calibrated and a fitted equation generated relating the channel number to wavelength. The software for generation of the channel to wavelength function is included in the PARC OMA II system.

Image fidelity when the SIT vidicon is used in the continuous mode was tested by imaging a one-hundred twenty-five micron screen, backlit by a copper hollow cathode lamp, on a 0.5 mm wide entrance slit of the one-meter Czerny-Turner monochromator. The twenty-five centimeter focal length quartz imaging lens was positioned for one to one magnification at 327.4 nm. The resulting image at the focal plane was detected photographically and with the SIT vidicon as shown in Figure 4. Distortion near the center of the vidicon target is less than fifty microns (2 channels). However as larger channel heights are used distortion increases as shown in Figure 5 and Table II. The distortion is due to a change in magnification which causes a skewing of spectral lines toward the outside of the target at large channel heights, as shown in Figure 6.

In the time-gated mode the distortion due to the electron imaging is more severe. Focusing of the photoelectrons in the SIT vidicon is a function of the gate pulse width and voltage. Therefore, for each new time gate-width the gate pulse voltage must be reoptimized. Focusing is also sensitive to the incident light intensity level for short gate widths (7,18). The ratio of photocathode voltage to gate voltage controls the electron image focusing and magnification. As a result, severe pincushion distortion occurs when the gate time is of the same magnitude as the rise and fall times of the gate pulse or when the gate pulse has ringing or a sloping voltage (7). The effect on the observed spectrum will be most severe if the incident light pulse is longer than the gate width. The effect at short gate times can be minimized by modification of the gating circuit (7) or combining an optical gate, such as a Pockels cell, with the electronic gate of the SIT vidicon (18).

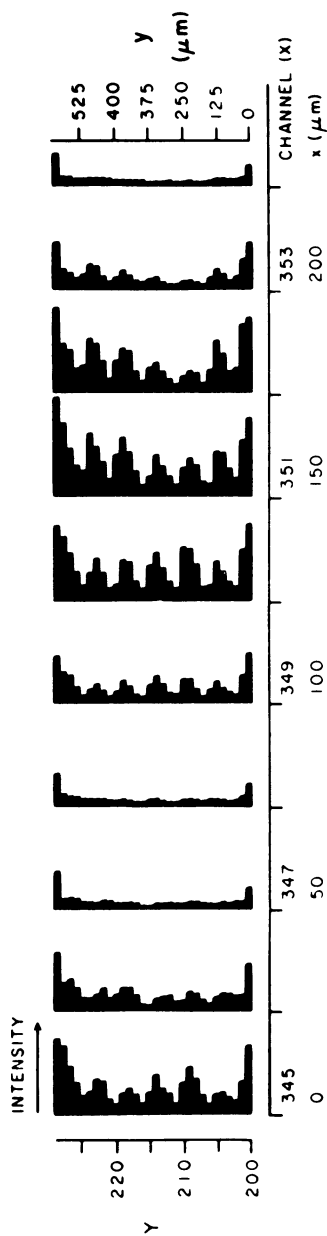


Figure 4. SIT vidicon detected signal from a 250×750 - μm portion of the image of a backlit 125- μm screen imaged with unity magnification at the focal plane. The SIT vidicon signal was obtained with the maximum attainable detector spatial resolution, with each picture element, or with pixel, 25 μm in diameter.

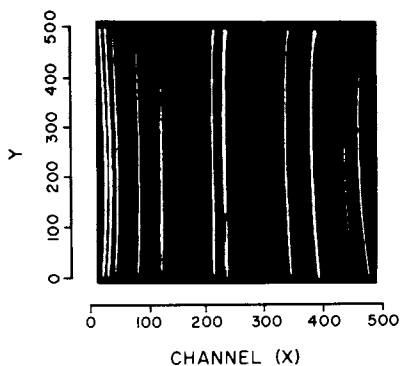


Figure 5. Continuous (nongated) SIT vidicon video signal showing pincushion distortion of the image of emission lines from an iron hollow cathode lamp.

Table II. Distortion of the SIT vidicon detected image in the continuous (nongated) mode.*

Y	X (Channel)						
	29	111	157	265	374	414	468
75-125	-5	-2	-2	-1	+1	+3	+5
125-175	-2	0	0	0	0	0	+1
175-225	0	+1	0	0	0	0	+1
325-375	-4	-1	-2	-1	0	-1	0
375-425	-8	-5	-4	-1	0	0	+1
425-475	-13	-9	-7	-2	+1	+1	+2

* An iron hollow cathode lamp source was used. A one meter monochromator (McPherson 2051) was used with a 20 micron entrance slit. Each spectrum was acquired with a scan height (ΔY) of 50. Below are listed the differences between observed channel of peak intensity and the channel of peak intensity for the centered ($Y = 225-275$) scan.

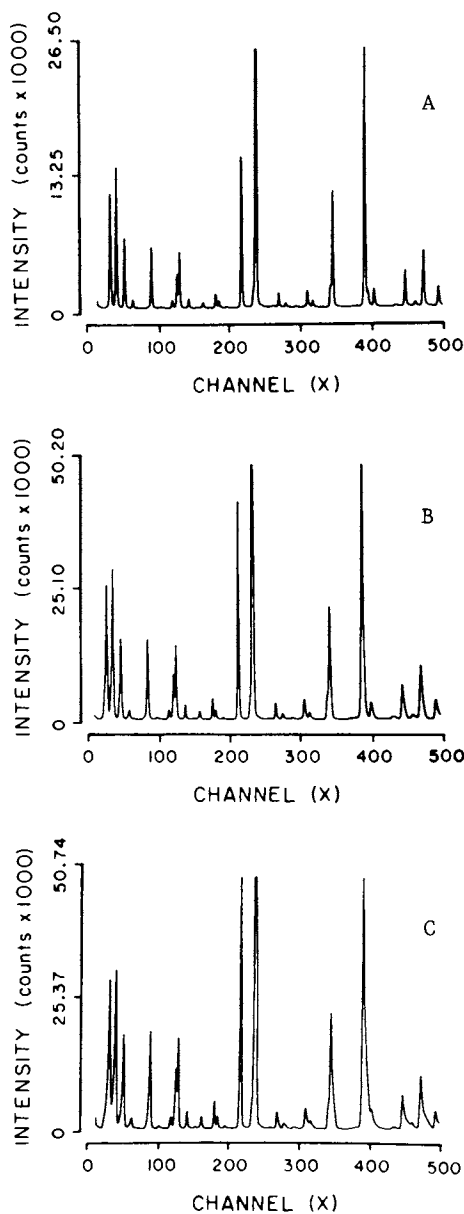


Figure 6. The effect of pincushion distortion on detected spectra. Key: A, spectrum obtained reading out the center 2.4 mm ($\Delta Y = 100$) of the vidicon target; B, spectrum obtained reading out the center 7.2 mm ($\Delta Y = 300$); and C, spectrum obtained reading out the complete 12.5 mm ($\Delta Y = 500$).

While the severe pincushion distortion was expected at short gate times (100 ns or less), and has been reported earlier (18), we also observed severe pincushion distortion at longer gate times. This distortion was observed with a spark discharge light source with a duration of approximately one-hundred microseconds and to a lesser extent with a helium-neon laser source. The distortion was most severe with a one-microsecond gate and less severe at longer and shorter gate widths, as shown in Figure 7. After considerable effort and investigation we have been unable to identify the cause of this distortion or to reduce it.

Using the PARC OMA II system the pulser duty cycle is limited to 0.1% in the 10 nsec to 99.9 microsecond range. The duty cycle is limited to 1.0% in the 1 microsecond to 999 microsecond range. Therefore, when a one-half microsecond gate width is used, the maximum frequency of gates is 200 Hz. When a one-half millisecond gate width is used the detection gate can be on only twice per second.

Channel-to-channel and pixel-to-pixel response. Variation in channel-to-channel and pixel-to-pixel response was measured using an E G & G model 590 calibrated, continuous source lamp system. While changes in response across the target were well within the +/- 10% range specified by PARC within the center 10 mm x 10 mm area (400 channels) of the target, there was a definite dependence of both spectral response and channel-to-channel response precision on spatial position, as seen in Figure 8.

Pixel-to-pixel variation was measured at $x = 150$ and 250 on the SIT target among 10 pixels at each x position. Relative standard deviations in the intensities were found to be 3.3% and 3.5% respectively.

A tradeoff between the sensitivity in the center of the detector and the uniformity across the detector can be made (14) by adjusting the image intensifier focus voltage and the electron gun focus voltage (gun focusing grid G3 and image focusing grids as shown in Figure 1). For the measurements shown in Figure 8 the focusing voltages were adjusted for an optimum combination of sensitivity and uniformity of sensitivity.

Any changes in response from channel-to-channel can be compensated by normalizing each spectrum acquired using a standard spectrum stored in the computer memory. As a result, changes in response of the optical system, such as grating efficiency or detector response can be compensated if known or calibrated.

Examples of Experiments Employing SIT Vidicon Detection

We have used the SIT vidicon detection system in a number of separate experiments. Detection requirements in these

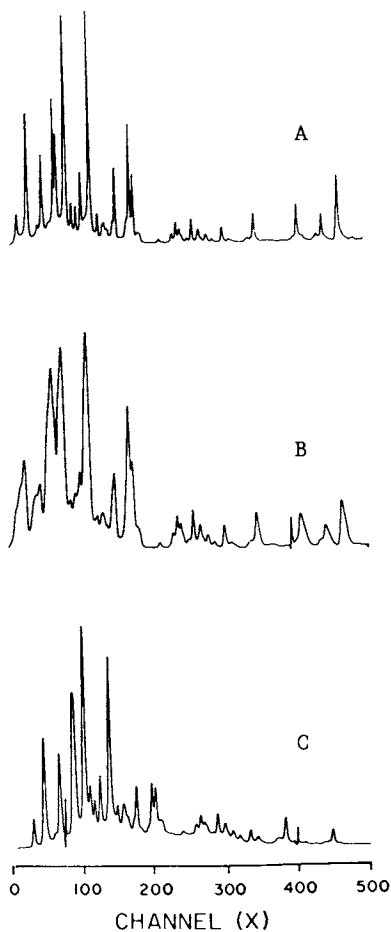


Figure 7. Distortion detected for the gated SIT-vidicon spark-excited spectra at gate times near $1 \mu\text{s}$. Key to detection gate width: A, $6.0 \mu\text{s}$; B, $1.0 \mu\text{s}$; and C, $0.1 \mu\text{s}$.

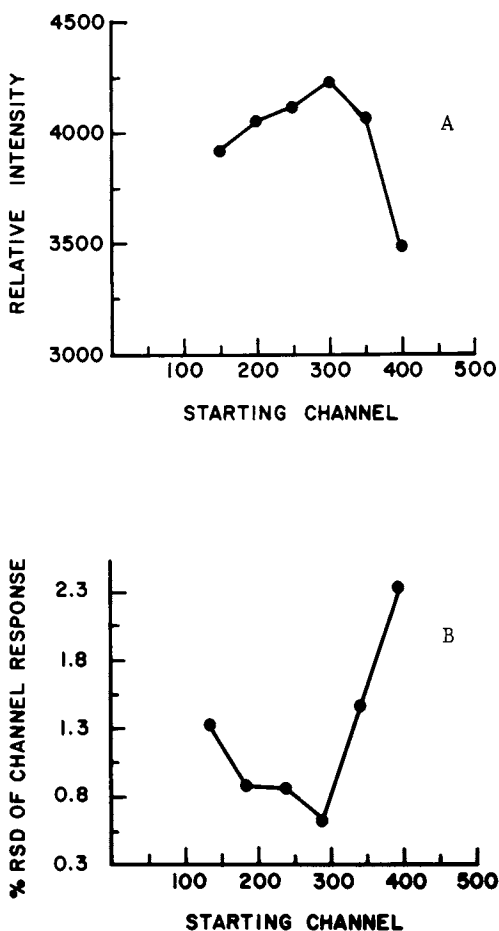


Figure 8. Variation in channel-to-channel response (A) and channel-to-channel response precision (B) with position on the SIT vidicon.

The light source was a calibrated, continuum source lamp (E G & G model 590). The polychromator was used in zero order, and the grating was rotated so that the image of the entrance slit was centered on the channel of interest. A frosted glass diffuser was placed in the optical path to ensure even illumination along the slit height. Each value of average signal (A) was obtained from 10 consecutive channels each of 300 pixels. Each signal was acquired with 100 readout scans at $60 \mu\text{s}/\text{channel}$ while continuously illuminating the entrance slit. Measured precision (B) was obtained from the relative standard deviation of the 10 consecutive channel signals.

experiments ranged from time integrated over twenty seconds and space integrated over two millimeters to time gated to submicrosecond periods and spatially resolved to one-hundred microns. Reasons for choosing the vidicon detector differed for each experiment and showed the flexibility of the vidicon-based detection system.

Time and space integrated spectra. At least three different experiments in our laboratories have used the time and space integrated mode of SIT vidicon detection. The signal-to-background ratio of spark excited emission due to ferrous alloy samples was measured at a variety of spark discharge currents and repetition rates (19,20). For this experiment the dynamic range of 10^4 , the ability to detect closely spaced wavelengths, and the data processing power of the system with on-line computer were most important. Experiments to choose internal standard lines for analysis (21) also used this detection mode. The rapid signal recovery and computer data processing characteristics of the vidicon with on-line computer data acquisition made the vidicon well suited to this experiment. In a third set of experiments, the vidicon detector was used to observe emission from a spark-fed microwave plasma (22). Here the high sensitivity of the SIT vidicon allowed use of short exposure times (less than ten seconds compared to two to five minutes for SA-1 photographic plates or an unintensified diode array). The ability to detect a range of wavelengths simultaneously made the vidicon the detector of choice rather than a single channel photomultiplier tube based detection system. Short exposure times and detection of a number of spectral lines were essential due to the transient nature of the emission signals.

Time-resolved (swept) spectra. The scanning readout of the vidicon target was used to obtain time-resolved spectra. The spark-excited emission due to ferrous alloys shows a characteristic transient behavior (23,24). Using the vidicon, spectra over a 10 nm wavelength range were observed with time resolution of approximately one second, as shown in Figure 9. The time behavior of selected signals can be graphically displayed in histogram form after the spectra are acquired and stored in random access memory (RAM) or on disk. The sampled species emission increases, peaks and fall off with time while the argon plasma emission is constant throughout as shown in Figures 9 and 10.

The time resolution is under software control with programmable delays of three track times to 3000 seconds between acquired spectra. The lower limit is due to the lag phenomenon discussed above. The number of spectra which can be acquired is limited by the computer memory space and the number of channels used. In the OMA II system with optional additional memory,

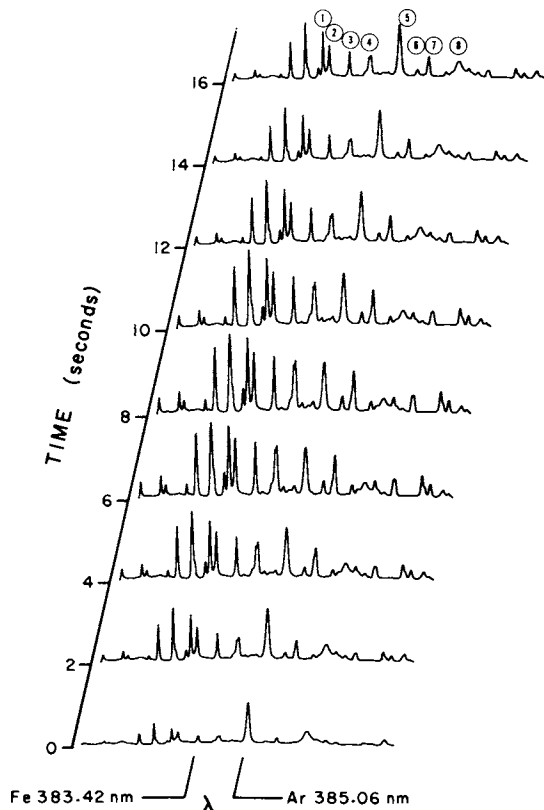


Figure 9. Time-resolved spectra showing the transient emission from a train of stable spark discharges with a mild steel sample. Each spectrum was obtained by adding successive readout signals for a 1-s period. Emission lines observed were: 1, Fe(I) 382.59 nm; 2, Fe(I) 382.78 nm; 3, Fe(I) 383.42 nm; 4, Fe(I) 384.04 and 384.11 nm; 5, Ar(II) 385.06 nm; 6, Fe(I) 385.64 nm; 7, Fe(I) 385.99 nm; and 8, Ar(II) 387.22 nm.

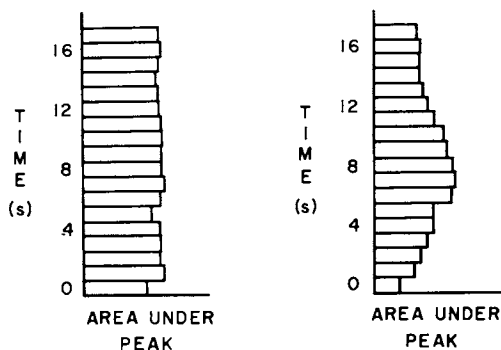


Figure 10. Histogram of Ar(II) 385-nm plasma emission (left) and Fe(I) 383.42-nm sampled species emission (right) as a function of time.

eighteen 500 channel spectra can be stored in RAM in double precision mode or thirty-six in single precision mode. If the number of channels is reduced, decreasing the wavelength range monitored, or channels are grouped together, reducing the spectral resolution, the number of spectra which can be acquired is increased accordingly. If the time between spectra is long enough (3.5 seconds) for transfer of the data from RAM to disk the number of spectra which can be acquired is limited only by the disk storage space (typically one hundred 500 channel spectra on an eight inch diameter disk).

Detection with two-dimensional resolution. The full power of vidicon detection is realized when both dimensions are used in a resolved mode. An example (14) is use of one dimension for wavelength resolution by mounting the vidicon at the focal plane of a polychromator and using the second dimension for time resolution using a streak camera. Subtle effects of vidicon lag and blooming resulted in errors in the measurement of fluorescence lifetimes, if uncorrected (14). Fluorescence measurements have been made (25) using the two-dimensional nature of the vidicon by dispersing excitation light along one direction and fluorescence emission along the second direction, improving the ability to analyze multicomponent mixtures (26,27) by fluorescence spectroscopy.

Light sources such as flames, spark or arc discharges, and inductively coupled plasmas emit radiation which is strongly dependent on the position within the source (28,29,30). Spectral or chemical interferences often show spatial dependence (31). The two-dimensional vidicon can be used to provide both spectral and spatial resolution simultaneously. The optimal spatial region of the light source may vary depending on the signal of interest. The random-access capability of the vidicon could be used to view different regions within the source for different wavelengths without moving the source or optics.

Random-access detection capability. Regions of the vidicon detector target to be read out can be selected under software control. Reading only regions of interest rather than the entire target can reduce the time required between acquisition of spectra, and therefore increase the temporal resolution. Random-access readout can also reduce the amount of RAM storage space necessary, thereby increasing the number of spectra which can be acquired and stored in memory. A single region of interest or a number of regions could be read out.

In one experiment we (34) were interested in the spark-to-spark changes in the emission spectra. The lines of interest were identified while reading the entire 500 channels. Thereafter only the 60-channel region including the lines of interest were read out. The spectra are shown in Figure 11. As

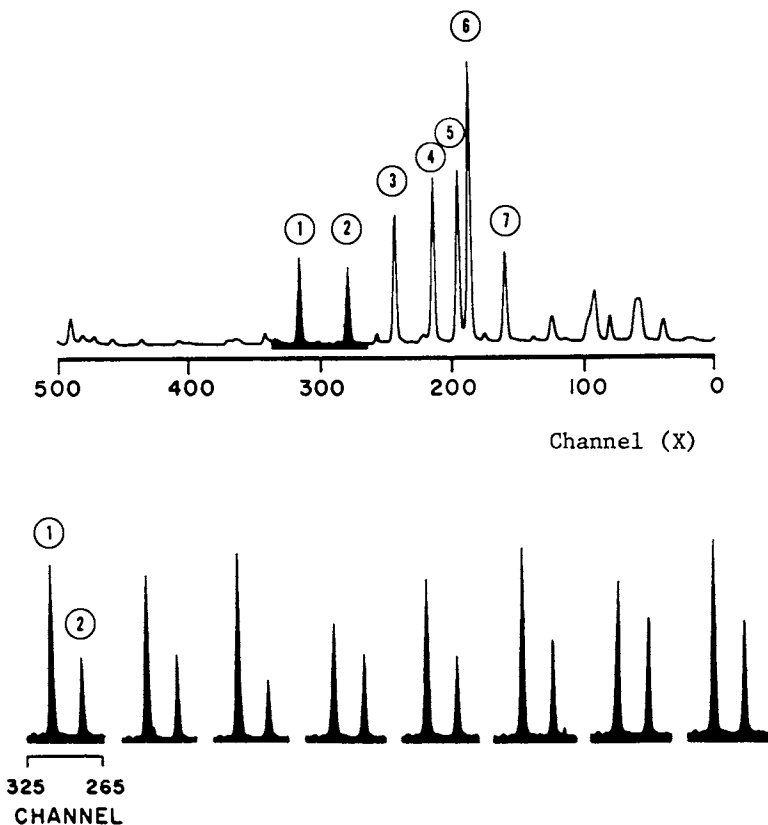


Figure 11. Use of the random access capability of the SIT vidicon to detect single-spark spectra.

Key: top, a complete 500 channel spectrum from 240 spark discharges; and bottom, spectra from consecutive single spark discharges. Emission lines: 1, Fe 292.66 nm; 2, Mn 293.31 nm; 3, Mn 293.93 nm; 4, Fe 294.44 nm; 5, Fe 294.77 nm; 6, Mn 293.31 nm; and 7, Fe 295.38 nm. SIT vidicon parameters (bottom): 20 μ s/channel, 0 prep scans, 5 readout scans, $\Delta Y = 100$, and readout scans triggered by spark fire trigger pulse. Sparks were fired at one break/half cycle (120 Hz).

a result of using a 60-channel region, five readout scans could be performed, detecting the emission from a single spark in a train of sparks, spaced equivalently in time, fired at a repetition rate of 120 Hz. The readout scanning was synchronized to the spark firing by using the external start mode of reading out the vidicon. The spark firing pulse was input into the vidicon detector controller. The five-scan readout began when the spark fire signal was received. Each scan took 1.2 ms, so the readout was complete before the next spark in the train was fired.

Blooming can limit the use of the random access readout mode (12,35). If a strong signal is near, but outside of the region of the target being read out, that signal will continue to grow during the exposure. As the signal increases in size, the effects of blooming from it into the region of interest are increased as well. (This can be seen on the outermost pixels of each channel shown in Figure 4.) One method to reduce this problem is to occasionally readout the entire target during an exposure. However, this will require the longer readout time to scan the entire target. Another way to reduce the problem is to use a scan pattern slightly larger than the region of interest to buffer the region of interest from blooming due to signals outside of that area.

Time-gated spectra. Time gating is important when short-time processes are investigated, such as the spark-excited emission response to changes in the instantaneous discharge current (31,36-40). Time gating is also necessary when a short duration signal is detected in the presence of an intense continuous signal such as scattering of pulsed laser light from a dense plasma (18,41).

Although operation in the time-gated mode introduces complications such as severe distortion at some gate widths and the need to reoptimize the gate pulse voltage for each different gate width, time-gated spectra can be obtained without other time dispersers such as rotating mirrors or optical shutters.

We (40) have used the time-gating ability of the SIT vidicon to study the spark-excited emission response to discharge current and the evolution of spark-excited emission as sampled material crosses the spark gap. Examples of the observed spectra are shown in Figure 12. Spectra obtained in this mode are useful for basic investigations as well as for selecting optimal times for detection. For example, during the first pulsation of the current waveform, the background and argon plasma emission is highest while emission from sampled species is weak. Therefore, the signal-to-background ratio could be improved simply by gating out emission from the early portion of the spark discharge. Also, the neutral iron emission lines are modulated by the discharge current, but out of phase with it (40). Therefore, if a neutral iron line was the signal of

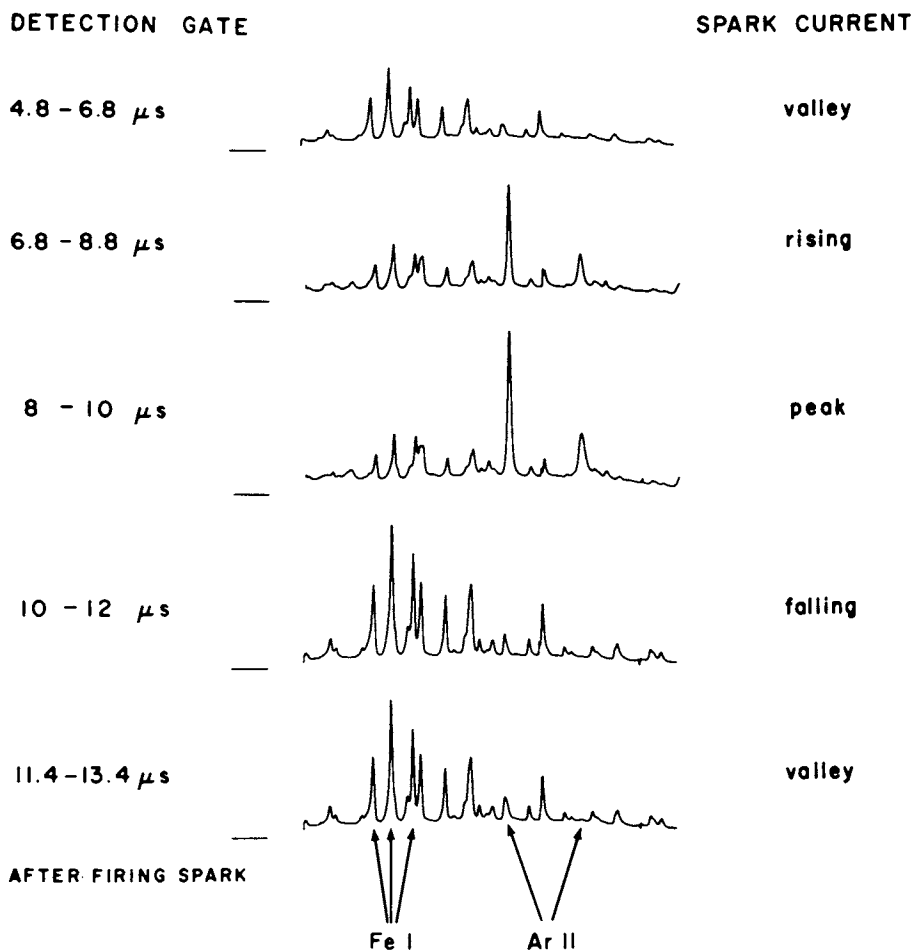


Figure 12. Time-gated spark-excited spectra (in 10-nm region centered at 385 nm) obtained by an SIT vidicon from a mild steel sample at various times during the spark current waveform. Vidicon parameters: 20 μ s/channel, 10 prep scans, 75 readout scans, $\delta Y = 80$, and gated mode with 2- μ s gate time delayed from the spark firing.

interest, it would best be detected during the valleys in the current waveform.

Spatially resolved, time-gated spectra. A number of experiments require spatially resolved, time-gated detection. The ability to obtain two-dimensionally resolved spectral information is especially important in transient systems such as turbulent combustion systems or scattering from irreproducible plasma discharges (41). The two-dimensional nature of the vidicon is especially useful for experiments such as fluorescence detection with spatial resolution (42).

The spark-excited emission observed from sampled species is affected by both the movement of material from the cathode across the spark gap and the discharge current magnitude and direction (31, 36-39). By using the vidicon in a two-dimensional mode with one dimension being wavelength and the second dimension being the axial position within the spark gap, coupled with time-gating, the movement of emitting spark-sampled material can be followed.

While this was possible (and with higher spectral, spatial and temporal resolution) photographically as shown previously (30,36-39), detection with a SIT vidicon allows higher flexibility and more rapid acquisition of spectral data. Examples of detected spectra are shown in Figure 13.

The amount of information generated in this experiment is huge and storage of that information can be a problem. Certainly, the SIT vidicon cannot replace photographic emulsions in terms of the amount of information stored at low cost. For example, using a spectrograph with a linear dispersion of 0.83 nm/mm, the SIT vidicon views a 10 nm wavelength region. To obtain spectra with a spatial resolution of 0.1 mm across the 2 mm spark gap, 20 separate 500 channel spectra must be stored on disk. In order to obtain these spectra at 10 different time gates within the spark discharge over a 60 nm region, 1200 separate spectra would be acquired. With the OMA II system used in these studies, 12 eight-inch disks would be required to store this information. However, all of this information could be stored on a single 4" by 5" photographic plate. Also, due to the blooming and large size of the pixels of the SIT vidicon in comparison with a fine grain photographic emulsion, such as SA-1, the spectral and spatial resolution attainable with the vidicon would not be as high as that attained with the photographic emulsion. However, an external means of obtaining time resolution, such as a rotating mirror, would be required with photographic detection. Also, real time data acquisition and display of the data is not possible photographically.

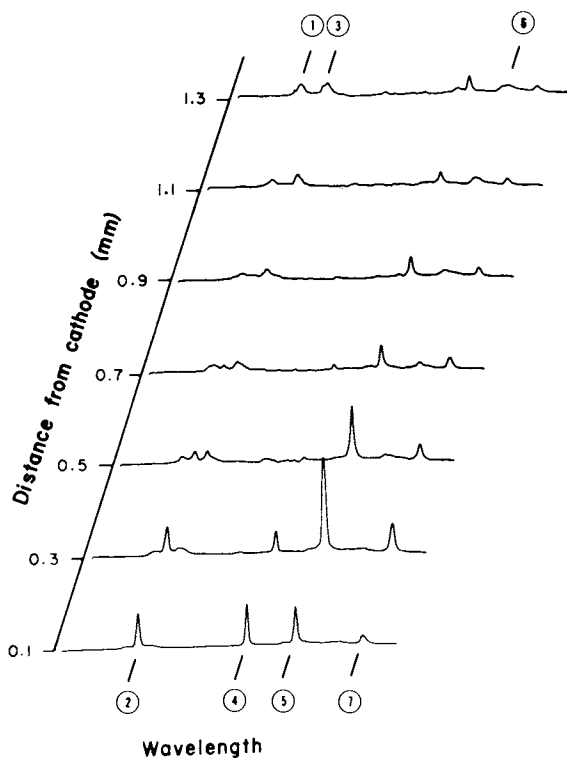


Figure 13. Spatially resolved, spark-excited spectra with a copper sample were obtained by using the two-dimensional detection capabilities of the SIT vidicon. Each spectrum was obtained from an approximately 120- μm -high spatial region along the spark interelectrode axis. The width of the spatial region viewed was approximately 35- μm wide. Emission from 1.0 to 1.3 μs after spark firing was monitored by gating the SIT vidicon intensifier. Vidicon parameters: 20 μs /channel, 5 prep scans, 100 readout scans, and 15 tracks each with a delta $Y=4$. Emission lines detected: 1, Ar(II) 324.37 nm; 2, Cu(I) 324.76 nm; 3, Ar(II); 4, Cu(I) 327.40 nm; 5, Ar(III) 328.59 nm; 6, Ar(II) 329.36 and 329.39 nm; and 7, Ar(III) 330.19 nm.

Conclusions

The SIT vidicon is a unique and useful spectroscopic detector. Among the most important properties of the SIT vidicon are two-dimensional detection, high sensitivity, and rapid signal recovery. The flexibility of the SIT vidicon detection system is a result of the nature of the signal readout and its compatibility with an on-line computer for control, data acquisition, and data processing and is valuable for research and other nonroutine applications. This flexibility allows the detector to be used in a number of modes and with various degrees of temporal and spatial resolution as demonstrated by the applications described in this paper.

However, the SIT vidicon is limited by blooming, lag, distortion, a small detection area, and high cost. As a result, the SIT vidicon will not replace other detectors such as photographic emulsions, photomultiplier tubes, and linear photodiode arrays. Instead, the SIT vidicon is complementary to the other spectroscopic detectors. Also, as with all detectors, spectroscopists using the SIT vidicon must be aware of its detection and imaging characteristics since these affect the detected spectra, sometimes in a subtle manner.

Acknowledgments

The Department of Chemistry, the Graduate School of the University of Wisconsin-Madison, and the National Science Foundation (under grant CHE79-15195) provided financial support for this work.

The assistance of Russell Riley, Robert Schmelzer, Kenneth Spielman, Kenneth Nelson, John Vanwick, Gary Forbess, and Robert Lang in construction of the mechanical apparatus used is acknowledged. Assistance in the design, construction and maintenance of the electronic equipment was provided by Ted Weight, Vincent Fitzgerald, Harland Bright, Bert Rogers, and Larry Cook. The authors also thank G. M. Hieftje and Y. Talmi for useful discussions concerning this manuscript.

Literature Cited

1. Y. Talmi, *American Laboratory* 1978, 10, 79.
2. Y. Talmi, in "Multichannel Image Detectors", ACS SYMPOSIUM SERIES No. 102, American Chemical Society: Washington, D. C., 1979; p. 1.
3. Y. Talmi, *Anal. Chem.* 1975, 47, 699A.
4. J. L. Weber, in Unconventional Spectroscopy, Proceedings of the Society of Photo-optical Instrumentation Engineers, Vol. 82, 1976; p. 60.
5. N. G. Howell and G. H. Morrison, *Anal. Chem.* 1977, 49, 106.

6. J. L. Weber and P. W. Roehrenbeck, *Optical Spectra*, 1979, 13, 58.
7. R. W. Simpson and Y. Talmi, *Rev. Sci. Instrum.* 1977, 48, 1295.
8. Princeton Applied Research Corporation, Model 1215 Multichannel Detector Controller Instruction Manual, 1978.
9. T. B. McCord and M. J. Frankston, *Appl. Opt.* 1975, 14, 1437.
10. J. A. Westphal, J. Kristian, and A. Sandage, *Astrophysics J. Letters* 1975, 197, L95.
11. T. A. Nieman and C. G. Enke, *Anal. Chem.* 1976, 48, 619.
12. E. M. Carlson and C. G. Enke in "Multichannel Image Detectors", ACS SYMPOSIUM SERIES No. 102, American Chemical Society: Washington, D. C., 1979, p. 169.
13. G. W. Liesegang and P. D. Smith, *Appl. Opt.* 1982, 21, 1437.
14. H. Staerk, R. Mitzkus, and H. Meyer, *Appl. Opt.* 1981, 20, 471.
15. G. W. Liesegang and P. D. Smith, *Appl. Opt.* 1981, 20, 2604.
16. Y. Talmi, *Anal. Chem.* 1975, 47, 658A.
17. Y. Talmi, D. C. Baker, J. R. Jadamec, and W. A. Saner, *Anal. Chem.* 1978, 50, 936A.
18. G. F. Albrecht, E. Kaline, and J. Meyer, *Rev. Sci. Instrum.* 1978, 49, 1637.
19. D. N. Washburn, Ph. D. Thesis, University of Wisconsin - Madison, 1981.
20. D. N. Washburn and J. P. Walters, *Appl. Spectrosc.* 1982, 36, 510.
21. D. N. Washburn and J. P. Walters, unpublished research.
22. D. Helmer, Ph. D. Thesis, University of Wisconsin - Madison, 1983.
23. D. Ekimoff, Ph. D. Thesis, University of Wisconsin - Madison, 1981.
24. D. Ekimoff and J. P. Walters, *Anal. Chem.* 1981, 53, 1644.
25. D. W. Johnson, J. B. Callis, and G. D. Christian, *Anal. Chem.* 1977, 49, 747A.
26. D. W. Johnson, J. B. Callis, and G. D. Christian in "Multichannel Image Detectors", ACS SYMPOSIUM SERIES No. 102, American Chemical Society, Washington, D. C., 1979, p. 97.
27. I. M. Warner, G. D. Christian, E. R. Davidson, and J. B. Callis, *Anal. Chem.* 1977, 49, 564.
28. C. S. Rann and A. N. Hambly, *Anal. Chem.* 1965, 37, 879.
29. J. P. Walters and S. A. Goldstein, "How and What to Sample in the Analytical Gap", in Sampling, Standards and Homogeneity, ASTM ST P 540, American Society for Testing and Materials, 1973, p. 45.

30. J. P. Walters and W. S. Eaton, submitted to Anal. Chem. for publication, 1982.
31. J. P. Walters and S. A. Goldstein, submitted to Spectrochimica Acta B, for publication, 1982.
32. G. Horlick and M. Blades, Appl. Spectrosc. 1980, 34, 229.
33. J. E. Roederer, G. J. Bastiaans, M. A. Fernandez, and K. J. Fredden, Appl. Spectrosc. 1982, 36, 383.
34. J. W. Olesik and J. P. Walters, unpublished research.
35. H. L. Felkel and H. L. Pardue, Anal. Chem. 1977, 49, 1112.
36. J. P. Walters and H. V. Malmstadt, Anal. Chem. 1965, 37, 1485.
37. J. P. Walters, Anal. Chem. 1968, 40, 1540.
38. R. D. Sacks and J. P. Walters, Anal. Chem. 1970, 42, 61.
39. S. A. Goldstein, Ph. D. Thesis, University of Wisconsin - Madison, 1973.
40. J. W. Olesik, Ph. D. Thesis, University of Wisconsin - Madison, 1982.
41. N. Bretz, D. Dimock, V. Foote, D. Johnson, D. Long, and E. Tolnas, Appl. Opt. 1978, 17, 192.
42. M. J. Dyer and D. R. Crosley, Optics Letters 1982, 7, 382.

RECEIVED August 4, 1983

Wide Dynamic Range Array Detector for Absorbance and Rotation Spectrometry

PETER J. AIELLO¹ and CHRISTIE G. ENKE²

Department of Chemistry, Michigan State University, East Lansing, MI 48824

Photodiode detectors have a limited dynamic range relative to a photomultiplier tube. Sensitivity (in terms of intensity) can be adjusted by changing the integration time, but the integration time for all diodes in array detector is the same for any given scan, and all portions of a spectrum are acquired within the same limited dynamic range. However, the results of scans taken at varying times can be combined to produce a data set with improved dynamic range. A microprocessor-controlled system for the automatic sequencing of detector integration time and the storage of only the optimum readings is described. An improvement in dynamic range of 215 times that for a single integration time is theoretically possible, but in most systems, stray light and dark current will limit the practical dynamic range attainable.

Introduction and Review

Over the past decade, there has been considerable development in imaging type detectors for the measurement of ultraviolet (UV) and visible light. These new detectors have attracted the interest of a number of analytical spectroscopists. For absorption spectroscopy, analytical chemists have traditionally used such instruments as the photometer, which uses a narrow-band light source (for example the 254 nm emission line from a low pressure Hg lamp or a continuous source with a filter), a sample cell and a photomultiplier tube (PMT) as the detector. While useful for many specific applications, the single-wavelength photometer cannot determine multiple sample components simultaneously or provide a general absorbance characterization of the system. When information at multiple wavelengths is desired,

¹Current address: Merck and Co., Inc., W1-10 Sumneytown Pike, West Point, PA 19486.

²Author to whom correspondence should be directed.

a continuous source (such as a tungsten lamp) and a dispersive element (a prism or grating) is used. The dispersive element is mechanically rotated to vary the wavelength of light passed through a fixed exit slit. This selected monochromatic light beam then passes through the sample cell and is detected by a PMT. Spectrometers of this type maintain the single photometer's characteristics of wide dynamic range of absorbance, good sensitivity and rapid, linear response. In addition, they provide a continuous variation in the wavelength sampled with a relatively high degree of resolution in wavelength selection. Despite the great convenience and analytical power of the scanning spectrophotometer, it has two characteristics which are limiting in a number of areas of application. First, by sampling over only a narrow range of the dispersed light at any given time, it makes inefficient use of the optical information available and thus it prolongs the necessary measurement time. Second, because the wavelength must be physically scanned to provide measurements at multiple wavelengths, this data is acquired at different times. This limits its applicability in situations where the sample's optical properties are changing, particularly if the rate of such changes is an object of the measurement.

An obvious improvement in both these limitations could be achieved with simultaneous multiple wavelength detection. Of course, one would like to have such capability without sacrificing high resolution of wavelength selection, wide dynamic range and good sensitivity at all wavelengths, linear response, good geometric stability, no stray light, rapid response and rapid electronic readout. Unfortunately, no currently available multi-wavelength spectrometer has all these desirable properties.

Several spectrometers have been developed which use multiple detectors arranged in the focal plane of the dispersing element, thus achieving multi-wavelength detection. Multiple detectors are available in a variety of types and spatial geometries. These types of detectors include: the photographic plate, multiple PMT's (direct reader), the image dissector, the silicon vidicon, the charge-coupled device, the charge-injection device, and the photodiode array. The number of photosensitive elements in these detectors can vary from just a few to many thousands and these elements can be arranged linearly or in a two-dimensional array. As the number of elements increases, greater wavelength resolution is possible. When a linear array is placed in the focal plane, each element detects a different wavelength region. This is also true for two-dimensional arrays as the spectrometer entrance slit image is focused on a separate row of detectors for each wavelength region, and the signal from all elements in each row are averaged together. The two-dimensional array, however, has another advantage in that it can be used for two-dimensional applications such as Eschelle grating and streak camera images. Both linear and two-dimensional arrays are available with photosensitive elements of various dimensions. In general, the larger the element, the greater the dynamic range; the smaller the element, the greater the resolution. The ideal element dimensions

would match those of the spectrometer slit; i.e., narrow and tall for the best resolution and dynamic range. A discussion of a few types of multi-channel detectors, including a summary of their advantages and disadvantages follows.

The first multi-wavelength detector used was the photographic plate. It has several advantages: relatively easy channel identification, simple operation, low cost, integration over total exposure time, and availability in a wide variety of physical dimensions. Its disadvantages include limited dynamic range, non-linear response, difficult calibration and a very slow data retrieval procedure. Another type of multichannel detector in use is called the direct reader. This instrument uses multiple PMT's arranged across the focal plane of a polychromator (1). Many desirable characteristics are maintained through the use of the PMT detectors; however, the number of channels for a reasonably sized instrument is severely limited and the PMT's must be arranged at wavelengths appropriate for predetermined specific applications.

An early electronic scanning spectrometer utilized an image dissector as the detector (2). An image dissector is an electron multiplier which is sensitive to a small, electronically selectable region of a relatively large photocathode. The image dissector tube offers advantages such as high resolution, the absence of broadening effects of intense spectral lines and the capability of single photon counting (3). However, even though electronic wavelength scanning can be much faster than mechanical scanning, the image dissector does not provide simultaneous wavelength detection and light impinging on the unsampled area of the photocathode is lost. The single largest application of image dissector tubes is the measurement of low-light levels in astronomy (4).

The silicon vidicon (SV) has been widely used as a spectrometric detector. The development and characterization of vidicon spectrometers has been described in many recent papers (5-11). The light-sensitive surface of a vidicon tube is a two dimensional array of typically 500 by 500 pixels (picture elements). Absorbed photons reduce the charge stored in the pixel. The charge is restored by an electron beam focused on and scanned across the reverse side of the diode surface. The measured charging current at each pixel is proportional to the charge lost which is in turn related to the light intensity integrated over the interval between scans. Advantages of the SV include high scanning speed and large number of pixels. Disadvantages are serious, however. Wide dynamic range is not achievable at maximum resolution because blooming (adjacent pixel cross-talk) causes spectral line broadening. Sensitivity to UV light is low and incomplete readout or lag can be as high as 10% of the charge. For low light level spectroscopy a silicon intensified target tube (SIT) is used. With the SIT, as with the PMT, the sensitivity and spectral response are dependent on the choice of photocathode material. The SIT has been compared to the PMT for the measurement of transient fluorescent signals and has

been proven to provide comparable signal to noise ratios (S/N) (12,13).

Charge-Coupled Devices (CCD) are solid state imaging devices. These contain up to 500 x 500 pixels which provides moderate resolution. Lower resolution CCD's are less expensive than other solid state imaging devices (14,15). High scan speeds are possible, the response is linear, and the dynamic range is about 1000. One significant feature of the frame transfer type of CCD detector is that all elements of the array integrate intensity during exactly the same time frame. The integration period is terminated by simultaneously transferring the integrated intensity signals to an analog shift register from which they are subsequently read out serially. Unfortunately, blooming and lag do occur if saturation is attained. Sensitivity is below that of a typical silicon device, in the UV region of the spectrum.

The charge-injection device (CID), a solid state imaging device in the developmental stage, has several unique features (16). One of these is its capability of nondestructive readout. With this capability, blooming (still a problem if saturation is attained) can be avoided by periodically scanning the array in a nondestructive readout mode. This mode can determine which pixels are near saturation. These pixels can then be selectively sampled in the normal destructive mode so that saturation is avoided while adjacent pixels with low incident light intensity can continue integrating. Another unique capability is that the integrated circuit is fabricated to allow random addressing of pixels. Therefore, faster readout speeds can be achieved if only a subset of the pixel information is required for a particular application.

The characteristics of silicon photodiode (SPD) arrays have been discussed in many recent papers (17-24). Over the last few years, self-scanned linear SPD arrays have been used for a number of analytical spectrochemical measurements (25-33). These arrays (called linear diode arrays or LDA) are currently available with up to 4096 photodiodes. It has been shown that LDA's have superior blooming and lag performance when compared to most other imaging type detectors (19,22). This allows the signal integrating capability of the array to become a very powerful asset. Since blooming does not occur, one can allow several photodiodes to saturate while adjacent photodiodes can integrate low light level signals. E.G.&G. Reticon (34) has made available LDA's specifically designed for spectroscopy. These arrays are self-scanned and provide real-time electronic readout with up to 1024 diodes. Each photodiode is a slit-shaped 25 μm wide by 2.5 mm high. This relatively large active area gives a dynamic range of up to 10,000 and the narrow width allows for excellent wavelength resolution. Although the arrays are much less sensitive than the PMT, useful measurements can be made over a region from 200 to 1000 nm. When improved sensitivity is needed, an electron multiplier type image intensifier can be used. These image intensifiers use an array of electron multipliers in a structure called a microchannel plate (MCP). Each channel in the MCP can provide a gain of up to six orders of magnitude (35).

Complete MCP's can be stacked to provide even higher gains. For response in the vacuum ultra-violet spectral region (50-200 nm) a SSANACON, self-scanned anode array with microchannel plate electron multiplier, has been used (36). This involves photoelectron multiplication through two MCP's, collection of the electrons directly on aluminum anodes and readout with standard diode array circuitry. In cases where analyte concentrations are well above conventional detection limits, multi-element analysis with multi-channel detectors by atomic emission has been demonstrated to be quite feasible (37). Spectral source profiling has also been done with photodiode arrays (27,29,31). In molecular spectrometry, imaging type detectors have been used in spectrophotometry, spectrofluometry and chemiluminescence (23,24,26,33). These detectors are often employed to monitor the output from an HPLC or GC (13,38,39,40).

Automatic Optimization of Integration Time

As indicated in the previous section, one of the most severe limitations of current imaging detectors is their dynamic range. The Reticon "S" series photodiode arrays have been shown to have a dynamic range of about 10,000 (22,34) for a single integration time. The conventional single channel detector, the photomultiplier tube (PMT), exceeds this dynamic range by more than 2 orders of magnitude. In order to extend the dynamic range of SPD detectors, the integration time (time between successive readings) can be varied. When SPD's are arranged in an array, the integration time for each diode is the time between the initiation of sequential scans of the array. Thus the integration time is unavoidably identical for each diode in the array for any given scan. In most analytical spectroscopy applications, however, no single integration time is optimum for every element (wavelength) in the array. Herein is described a solution to this problem which involves acquiring successive spectra at increasing integration times so that data taken at the optimum integration time for each photodiode is available.

The integrating capability of the linear diode array is achieved by charge integration, a technique which enhances the signal and averages the noise. This is very useful as the signal to noise ratio (S/N) under many conditions increases linearly with the integration time, whereas S/N enhancement by averaging replicate measurements increases only with the square root of the number of scans averaged (41,42). Therefore, the maximum resolution and S/N are obtained if each photodiode is allowed to integrate charge until it nears saturation. Figure 1 shows multiple spectra of a quartz halogen lamp taken with a Reticon 512S LDA at integration times of 5, 10, 20, 50, 200 and 500 ms. In each of these spectra, the detector dark current has been subtracted out. Because the dark current is also integrated, the saturation level for this integration of light current appears to decrease with increasing integration time. The total dynamic range is actually decreasing because of the increase in the

integrated dark current. The spectra shown in Figure 1 were obtained with the detector at room temperature. With the detector cooled to liquid nitrogen temperature, the useful maximum integration time is extended to about 24 h (19). It should also be noted that the profiles of these spectra are products of the polychromator transfer coefficient, the lamp spectral output and the detector sensitivity at each wavelength. At the shorter integration times, the photodiodes detecting the wavelengths above 500 nm are nearing saturation. At longer integration times the wavelengths near 300 nm are optimized (half-scale or larger). However, this is achieved at the expense of the information at the longer wavelengths which is now lost due to saturation of those photodiodes. In a normal LDA system, spectra are acquired at various trial integration times and then data are taken at the single integration time which is determined to be the best compromise. This usually results in a severe degradation of the photometric accuracy at these wavelengths for which the signal is weakest.

If different integration times are used for successive scans, the longest integration time scan will provide the best reading for the wavelength where the signal is weakest while the shorter integration time scans will give the best reading for those diodes that were saturated during the longer times. In our system, as shown in Figure 2, the integration time is doubled for each successive scan. The initial integration time, T , should be chosen such that no photodiode has neared saturation. If the integration time is doubled n times (in Figure 2, $n=4$), then the longest integration time is $2^n t$ and the total experimental time, T' , will be

$$T' = 2^{n+1}t - t$$

This means that data are acquired at the optimum integration time for each photodiode in a total time of approximately twice the longest integration time in the sequence. The optimum integration time is between 47.5% and 95% of saturation. The dynamic range improvement, D , will be

$$D = 2^{(n-1)}$$

assuming the dark current is negligible at the longest integration time used.

The number of integration time doublings, n , can be increased until either a time limitation imposed by the experiment is reached, or the integrated dark current exceeds 50% of saturation. The dark current can be reduced by cooling the LDA. The thermoelectric coolers used in our instrument cool the detector to a temperature of about -5 C which provides a maximum useful integration time of about 20 s.

It should be noted that as the integration time is increased, many of the photodiodes may reach saturation while adjacent photodiodes have yet to attain their optimum integration time.

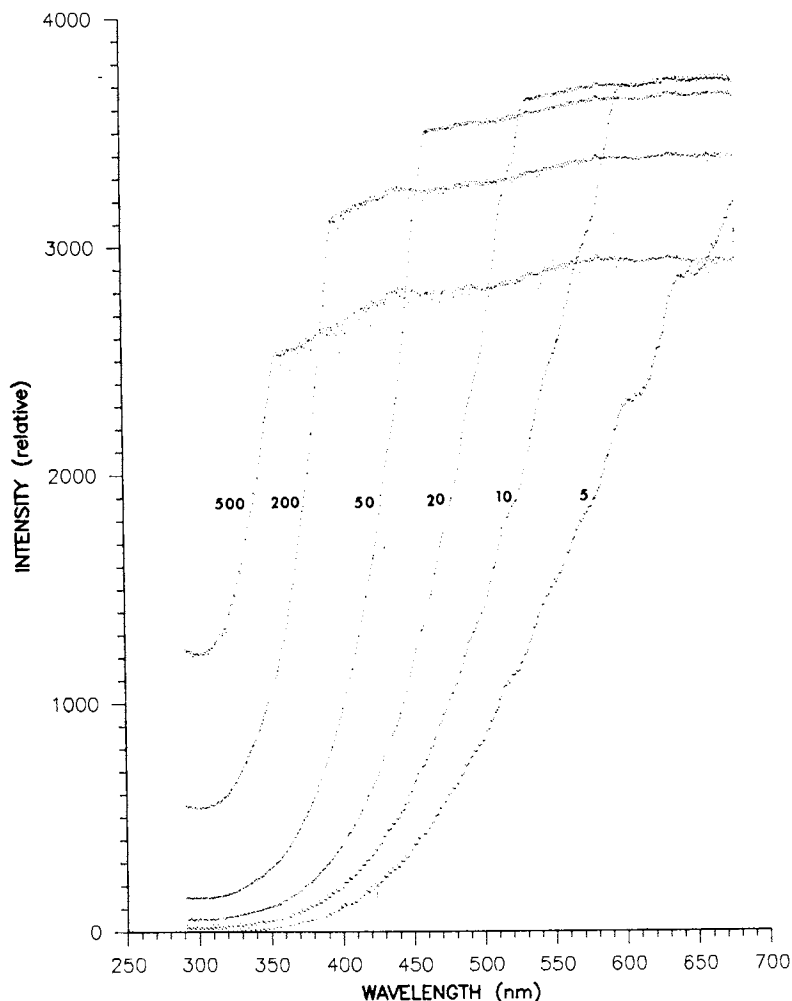


Figure 1. Spectrum of quartz-iodine lamp at various integration times (in milliseconds).

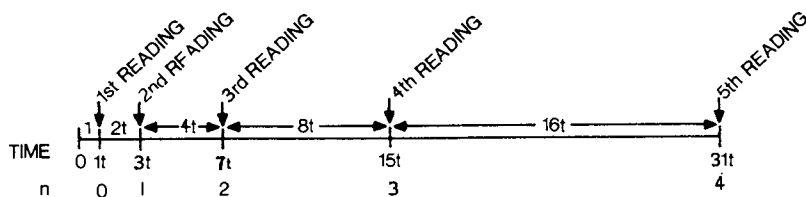


Figure 2. Scanning time sequence for multiple integration time array detector system. Each integration time uses all bits in ADC. Key: t , integration time for minimum sensitivity; and n , number of integration time doublings (number readings - 1). The total time for n doublings is $2(2^n t - t)$. The dynamic range improvement is $2^{(n-1)}$.

This would be a significant problem in other imaging detectors such as CCD's, CID's and vidicons. In the case of these detectors, when saturation is reached, charge will leak from the saturated pixels (picture elements) to adjacent pixels. This "blooming" effect has been shown to be minimal in linear photodiode arrays (21,22). Thus integration times for which many photodiodes are saturated can be used while useful information is still obtained from the non-saturated photodiodes. This information will contain only the integrated light intensity for each photodiode, free of bleed-through from adjacent saturated photodiodes. The procedure by which the integration time is sequenced and only the optimum readings are stored is included in the instrument description below.

Instrument Optics

The optics of the instrument in which the multiple integration time array detector is implemented are described in this section. The goal of the instrument is to provide simultaneous absorbance and optical rotatory dispersion (ORD) measurements in the ultra-violet (UV) and visible spectral regions and to repeat this at very high speeds. An instrument capable of measuring simultaneously more than one physical property of a chemical system has great potential utility. Also such an instrument can assure that the properties measured actually refer to the same material under the same conditions. Figure 3 is a block diagram of the optical setup as configured for measurement of optical rotation and absorbance. The light source used is a 150 W xenon arc lamp. This high intensity is necessary when there is interest in the ultra-violet region of the spectrum because of the relatively low detector sensitivity at shorter wavelengths. The light then passes through a polarizer of the Glan-Thompson prism type. Linearly polarized light then passes through a sample cell which is 1 decimeter in length. If the sample is optically active, the plane of polarization is rotated by an amount that is wavelength dependent. The beam then passes through the analyzer. The analyzing polarizer is rotated under computer control in 0.01 degree increments. The light is then collected and focused by a lens onto the entrance slit of a spectrograph. The entrance slit of the spectrograph is interchangeable which allows the operator to make the best compromise between resolution and signal strength. A reflecting mirror simply folds the light path such that the inlet optics are physically separated from the spectral image produced. The light is then dispersed by a J-Y concave holographic grating. This grating (100 mm focal length, F/2.0) provides a flat-field image on the light sensitive region of the linear diode array detector. The grating has a reciprocal linear dispersion of 32 nm/mm resulting in a 400 nm wide spectral window to be viewed by the detector. The window which is viewed can be changed by physically sliding the detector back and forth in the focal plane. The low F number of the grating helps to maximize the light throughput of the spectrograph. The holographic grating

also serves to reduce stray light as the random error in groove position is virtually nonexistent.

The linear photodiode array (LDA) detector in this spectrometer is the RL512S made by Reticon (34). It has 512 photodiodes each 2.5 mm high and 25 μm wide. The LDA is self-scanned which provides real-time computer compatible serial electronic output for all 512 channels in succession. The detector is responsive over a range of 200–1000 nm. The array can be read out at very high speeds. At a 1 MHz clock frequency (the array can be clocked up to 10 MHz) data from successive channels appear every 4 μs , and the readout time of the complete LDA is only slightly greater than 2.0 ms. It should be noted that this is also the minimum integration time for a 1 MHz clock frequency. The integration time is extended by simply pausing for the desired length of time between readouts. The total integration time is the time from the initiation of the previous readout to the initiation of the current readout. The charge collected at each photodiode is directly proportional to the light intensity integrated over this time.

The Microcomputer and Data Acquisition System

It is apparent that the linear diode array detector can generate data at extremely high rates and that the data acquisition would best be done by computer. Rather than overburden a single minicomputer by interfacing several instruments to it, a single board computer was designed to give each instrument its own control and data acquisition capabilities. A particular single board computer (SBC) designed by Bruce Newcome (43) was used in the LDA spectrometer. The Intel 8085A microprocessor chip used in this microcomputer is powerful enough to fully control all instrument functions as well as to perform the data acquisition process. The system has been mechanically and electronically designed for easy interfacing. A block diagram of the microcomputer system excluding the LDA interface is shown in Figure 4. Ten K-bytes of programmable read-only memory (PROM) on the CPU bus contain the FORTH programming language. There are 22 K-bytes of random access memory (RAM) available for user program space. An interrupt controller is used for Input/Output (I/O) operations as well as data acquisition. Two universal synchronous/asynchronous receiver transmitters (USART) are used, the first for direct terminal I/O, the other for communication to a PDP 11/40 minicomputer. Also interfaced to the CPU bus is a dual floppy disk system. This provides storage space for both data and software. A local graphics monitor is used (256 by 256 pixel resolution) for initial data display. The CPU is also interfaced to a stepper motor which rotates the analyzer in the optical path in 0.01 degree increments.

Figure 5 is a block diagram showing the data acquisition hardware. Since the LDA is self-scanned, the only control the CPU can have on the LDA is to initiate the scan (readout) process. By controlling the timing of the initiation signal, the CPU controls

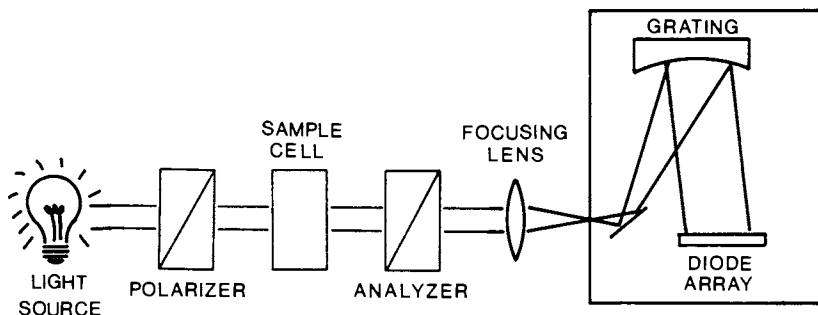


Figure 3. Block diagram of the modular optical system arranged for multiwavelength measurement of optical rotation and absorbance.

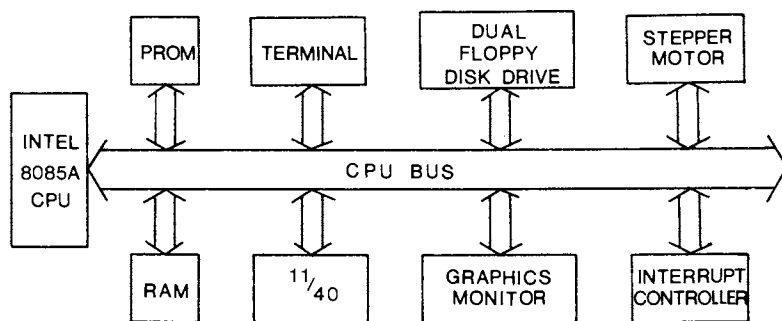


Figure 4. Block diagram of the microcomputer control system.

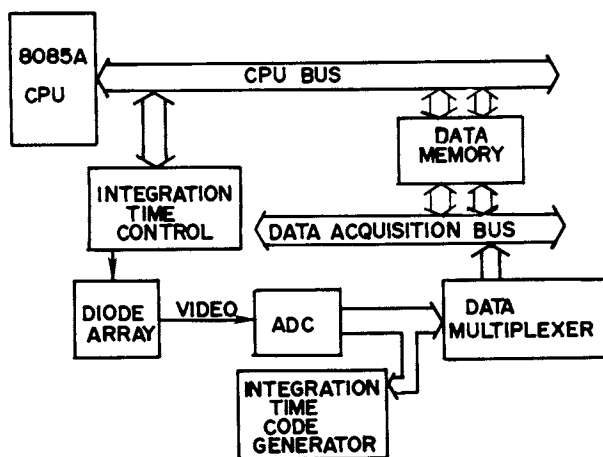


Figure 5. Block diagram of the data acquisition system. Diagram includes the integration time sequencing and data packing hardware.

the integration time of the detector. The data acquisition is done completely in hardware when enabled by the CPU. Normally, when data are acquired at these high speeds, it is done by taking control of the CPU bus while putting the CPU on hold, and storing the data directly in RAM. This is called direct memory access (DMA). However, because the CPU is needed to program the integration time for the scan following the current readout, this straightforward approach could not be used. Instead, data are stored directly in RAM as in DMA, but the memory is not connected to the CPU bus when this is done. During data storage, the RAM is on the "data acquisition" bus. This RAM can be switched between the data acquisition bus and the CPU bus to allow the CPU access to the data after collection.

Each data point is stored in a 16-bit word; 12 bits for the ADC output, and 4 bits for the value of n (integration time doublings) for that conversion. On successive scans each at longer integration times, the converter output and n value overwrite the one taken for that channel on the previous scan, unless the ADC has overranged. ADC overrange occurs if the integrated charge exceeds 95% of the saturation value. Thus, at the end of the longest scan, one 512-word section of memory has the complete spectrum, each point having been recorded at its optimum integration time with the corresponding value of n .

There are actually two sections of RAM which under CPU control are exchanged between the CPU bus and the data acquisition bus. Since the CPU does not need to be inactive during acquisition, it can unload one RAM bank of data while the other is being filled with new data from the data acquisition bus.

Performance

In order to measure the practical dynamic range, the absorbance of a series of neutral density filters was measured. The measurements are all taken at 600 nm. The results are plotted in Figure 6. The initial integration time was 3 ms followed by 13 integration time doublings (14 readings) with the detector at -2 C. The longest integration time of 24.6 s was only slightly longer than the time in which the dark current saturates the array. The response is linear from about 0.0-4.2 absorbance units. For a nominal absorbance of 3.96, an absorbance of 4.03 was measured. This corresponds to a 2% error at an intensity 4 orders of magnitude below the maximum. The dynamic range is thus about 5×10^5 . This could be improved considerably by using a 14-bit ADC to take advantage of the full dynamic range of the LDA (10^4), or by further cooling of the LDA to allow longer integration times.

Figure 7 shows, however, that with the current optics system, stray light causes significant deviations from Beer's Law in measurements of highly absorbing systems. The curve was acquired by measuring the absorbance of KMnO_4 solutions of known concentration using the LDA channel at $\lambda = 545$ nm. The Xe arc lamp was used and an IR cutoff filter was placed in the light path

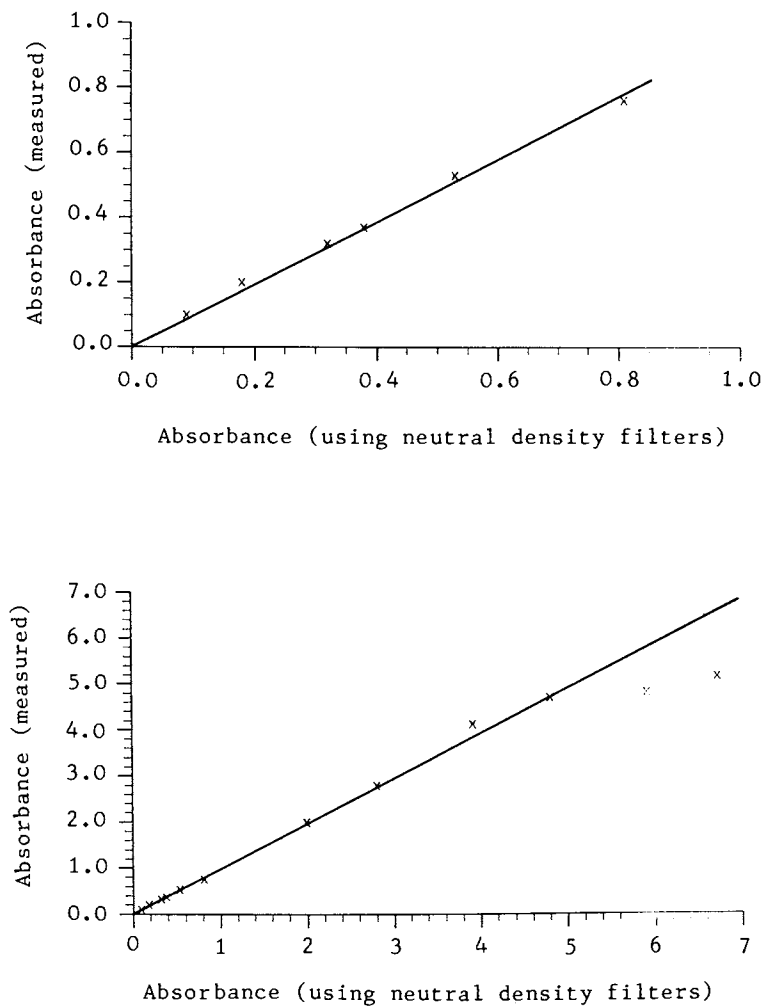


Figure 6. Measured absorbance vs. the nominal absorbance of various combinations of neutral density filters. Bottom curve shows the entire experimental range, and the top curve shows from zero to one in greater detail.

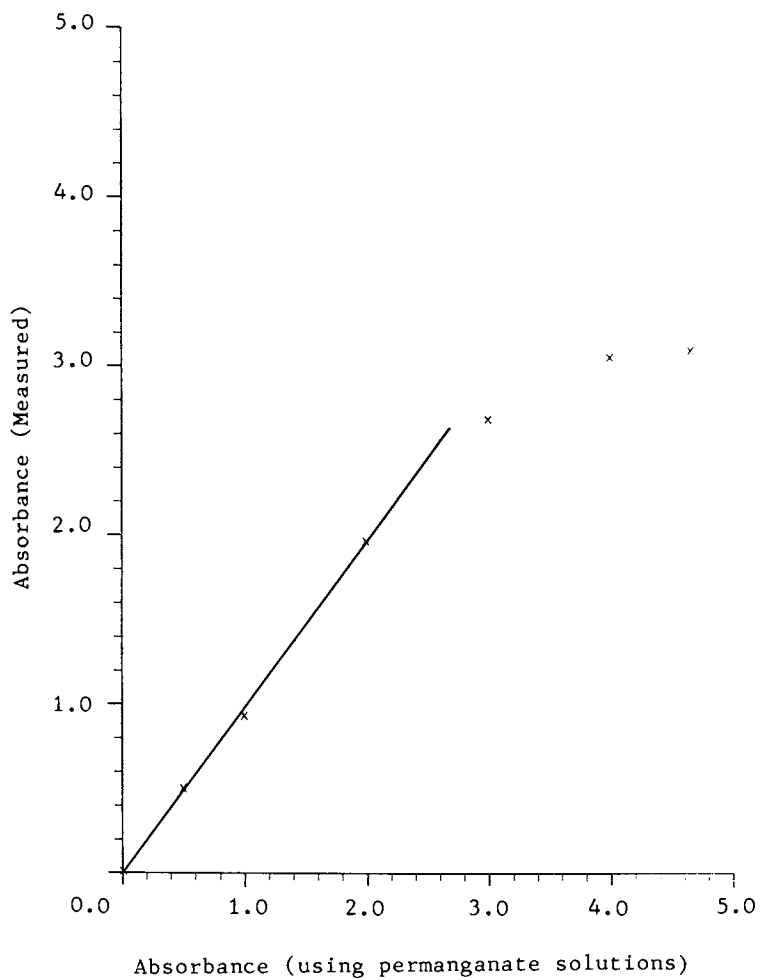


Figure 7. Response vs. known absorbance of $KMnO_4$ solution at 545 nm.

in order to reduce stray light. Using a 12 ms integration time and 10 doublings (11 readings), samples with absorbances of greater than 2 at 545 nm do not result in the decrease in intensity at 545 nm diode expected because stray light of other wavelengths is hitting that photodiode. This problem is common to all array detector absorbance spectrometers where the light intensity varies greatly as a function of wavelength.

Stray light for this instrument was previously determined to be <0.004% (21). However, in an instrument of this type, order overlap and all internal reflections inside the polychromator cannot be eliminated through the use of a narrow bandpass filter as in a normal single wavelength spectrometer. The stray light problem is much worse in our system for short wavelength measurements than for long because both the source intensity and detector sensitivity decrease greatly toward the UV end of the spectrum. If stray light could be eliminated, absorbances up to 4.0 could be measured as demonstrated in Figure 6 where the experiment is not sensitive to stray light interference.

Figure 7 indicates that even with the presence of stray light, the system is quite useable over the critical absorbance range from 0 to 2. However, array detector spectroscopy would be greatly aided by the development of two new devices. One is a filter that would have an absorption spectrum that complements the source spectrum so that the combination would have more uniform spectral intensity. The other is a filter that would pass only the blue part of the spectrum in one region, only the red part in another and only the mid part in between. If such a filter were designed to match the dimensions of an array detector, and the dispersion of the monochromator, each detection element would only be sensitive to its appropriate wavelength. The resulting system would be like a dual monochromator, but would not entail the large losses involved in tandem dispersion systems.

Application to Multiwavelength ORD Spectrometry

The light intensity transmitted through two linear polarizers is a function of the incident light intensity and the \cos^2 of the angle at which the polarizers are set. If the intensity is measured while the analyzer is rotated continuously, the signal detected will vary sinusoidally between 0 (when the polarizers are crossed) and some maximum value with a frequency twice that of the rotation of the analyzer. If the sample shows absorption but not optical activity, the new maximum intensity value observed, I , will be lower than the value of I_{\max} and the absorbance can easily be calculated. If the sample is optically active but does not absorb, the amplitude of the signal will not change ($I = I_{\max}$) but a phase difference will be observed between the sample and the reference signals. The observed rotation is exactly equal to this phase difference. By recording the signal intensity at several analyzer positions, both the intensity and phase information are obtained. If this signal intensity is measured at all wavelengths

simultaneously, complete spectra for both the absorbance and ORD will be measured.

To implement these procedures with this instrument, several spectra are acquired at different angular positions of the analyzer. The data at each wavelength are fit to a \cos^2 function using a non-linear least squares algorithm (43) with only the frequency specified. The resulting peak-to-peak amplitude, phase and amplitude offset parameters are used to calculate the absorbance and ORD spectra. The resulting spectra for a 1.05% albumin solution are shown in Figure 8. The improvement in data collection rate afforded by the array detection make this system useful in following absorption and ORD changes for reaction rate or flow system monitoring applications.

Conclusions

Array detector spectrometry offers many advantages over scanning spectrometers, especially where near simultaneous information at multiple wavelengths is required. With suitable optics and electronics, the resolution and dynamic range of modern array detectors can match that of a medium resolution scanning monochromator and PMT. Sensitivity comparable to the PMT can also be obtained if an intensifier is used. Array detector spectrometers are somewhat more susceptible to stray light interferences than scanning monochromators because the baffling cannot be so exclusive and the use of switched in filters for various wavelength regions is precluded. Because of the many and proven advantages of this new technology, the years ahead should see great strides in both the technology and applications of array detector spectrometry.

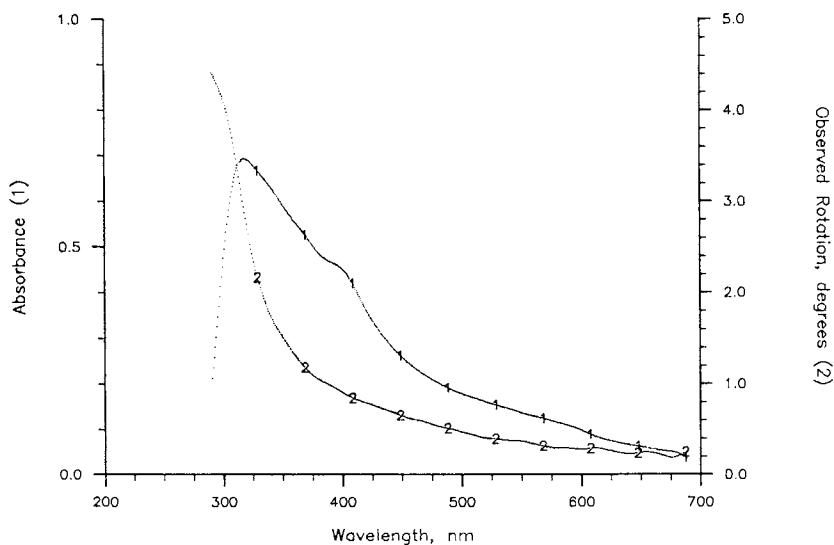


Figure 8. Absorption (1) and rotation (2) spectra for 1.05% albumin solution.

Acknowledgments

This work was supported in part by Abbott Laboratories and the Office of Naval Research. Dr. Fritz S. Allen of the University of New Mexico provided very helpful suggestions concerning the ORD instrumentation.

Literature Cited

1. Willard; Merritt; Dean; Settle. "Instrumental Methods of Analysis"; Sixth Ed., D. Van Nostrand: New York, 1981; p. 165.
2. Harbor, R. A.; Sonnek, G. E. Applied Optics 1966, 5, 1039.
3. Danielsson, A.; Lindblom, P.; Soderman, E. Chimica Scripta 1974, 6, 5.
4. Boyce, P. B. Science 1977, 198, 145.
5. Milano, M. J.; Pardue, H. L.; Cook, T. E.; Santini, R. E.; Margerum, D. W.; Raychera, J. Anal. Chem. 1974, 46, 374.
6. deHaseth, J. A.; Woodward, W. S.; Isenhour, T. L.; Anal. Chem. 1976, 48, 1513.
7. Cook, T. E.; Santini, R. E.; Pardue, H. L. Anal. Chem. 1977, 49, 871.
8. Neiman, T. A.; Enke, C. G. Anal. Chem. 1976, 48, 619.
9. Talmi, Y. Anal. Chem. 1975, 47, 658A.
10. Talmi, Y. Anal. Chem. 1975, 47, 697A.
11. Talmi, Y. Am. Lab. 1978, March, 79.
12. Cooney, R. P.; Vo-Dinh, T.; Walden, G.; Winefordner, J. D. Anal. Chem. 1977, 499, 1048.
13. Cooney, R. P.; Boutilier, G. D.; Winefordner, J. D. Anal. Chem. 1977, 49, 1048.
14. Ratzlaff, K. L.; Paul, S. L. Appl. Spec. 1979, 33, 240.
15. Ratzlaff, K. L. Anal. Chem. 1980, 52, 916.
16. Lewis, H. A.; Denton, M. B. J. Automatic Chem. 1980 August, Preprint.
17. Horlick, G.; Coddling, E. G. Anal. Chem. 1973, 45, 1490.
18. Yates, D. A.; Kuwana, T. Anal. Chem. 1976, 48, 510.
19. Horlick, G. Appl. Spec. 1976, 30, 113.
20. Simpson, R. W. Rev. Sci. Instrum. 1979, 50, 730.
21. Aiello, P. J. M.S. Thesis, Michigan State University, 1980.
22. Talmi, Y.; Simpson, R. W. Appl. Optics 1980, 19, 1401.
23. Marino, D. F.; Ingle, J. D. Jr. Anal. Chem. 1981, 53, 645.
24. Talmi, Y. Appl. Spec. 1982, 36, 1.
25. Chuang, F. S.; Natusch, D. F. S.; O'Keefe, K. R. Anal. Chem. 1981, 53, 645.
26. Milano, M. J.; Kim, K. Anal. Chem. 1977, 49, 555.
27. Franklin, M.; Baber, C.; Koirtyohann, S. R. Spectrochimica Acta 1976, 31, 589.
28. Horlick, G.; Coddling, E. G. Appl. Spec. 1975, 29, 167.
29. Edmunds, T. E.; Horlick, G. Appl. Spec. 1977, 31, 536.
30. Talmi, Y.; Sieper, H. P.; Moenke-Bankenbug, L. Analytica Chimica 1981, 127, 71.
31. Blades, M. W.; Horlick, G. Appl. Spec. 1980, 34, 696.
32. Sandel, B. R.; Broadfoot, A. L. Appl. Optics 1976, 15, 3111.

33. Ryan, M. A.; Miller, R. J.; Ingle, J. D. Jr. Anal. Chem. 1978, 50, 1772.
34. "S-Series Solid State Linear Diode Array", E.G.&G. Reticon Brochure, 1978.
35. Eberhardt, E. H. Appl. Optics 1979, 18, 1418.
36. Broadfoot, A. L.; Sandel, B. R. Appl. Optics 1977, 16, 1533.
37. Felkel, H. L.; Pardue, H. L. Anal. Chem. 1978, 50, 602.
38. McDowell, A. E.; Pardue, H. L. Anal. Chem. 1977, 49, 1171.
39. Dessey, R. E.; Reynolds, W. D.; Nunn, W. G.; Titus, C. A.; Moler, G. F. Clin. Chem. 1976, 22, 1472.
40. Cooney, R. P.; Vo-Dinh, T.; Winefordner, J. D. Anal. Chim. Acta 1977, 89, 9.
41. Carlson, E. M. Ph.D. Thesis, Michigan State University, 1978.
42. McCord, T. B.; Franston, M. J. Appl. Optics 1978, 14, 1437.
43. Newcome, B., unpublished data.
44. Deming, W. E. "Statistical Adjustment of Data"; Wiley: New York, 1943.

RECEIVED August 10, 1983

Inductively Coupled Plasma-Atomic Emission Spectroscopy with Multichannel Array Detection

FREDERICK GRABAU¹

Ames Laboratory, U.S. Department of Energy, Ames, IA 50010

YAIR TALMI

Princeton Instruments, Inc., P.O. Box 2318, Princeton, NJ 08540

Array detectors provide an attractive alternative to the polychrometers commonly used with ICP-AES, because they provide the capability of simultaneous detection of spectral lines and spectral background dispersed on hundreds of virtually independent optical channels. In this paper a critical evaluation of self-scanned photodiode arrays as radiation detectors for ICP-AES is presented. Limited comparisons are also drawn for silicon intensified target vidicons (SIT) and intensified self-scanning photodiode array detectors (ISPD). The figures of merit of primary interest to analytical chemist that are discussed are: noise characteristics and powers of detection, linearity and dynamic range, spectral stripping and interpolative correction for variable underlying background, compromise between resolution and spectral coverage and application to nonideal "real" samples.

In analytical atomic emission spectroscopy, the most popular approach to simultaneous multielement determinations has been based on the use of multiple detectors that monitor discrete wavelengths. The most common form of this approach has involved fixed arrays of narrow slits prearranged along the exit focal plane of a spectrometer, with corresponding arrays of photomultiplier tube (PMT) detectors to monitor the radiation transmitted through these slits. These instruments are ideally suited for the routine, simultaneous multielement determination of the same set of elements, which may number up to 30 or more, in samples of similar total composition. For these purposes, polychromators have provided the wide dynamic range, fast response and excellent signal-to-noise (SNR) performance characteristic of PMT's, specifically when

¹Current address: St. Louis County Water Company, Chesterfield, MO 63017.

operated as energy (integrators) rather than power (current) detectors.

When the analyst is faced with the determination of a broad range of elements in samples of widely varying composition, the limited set of lines observable with a polychromator restricts the scope of application and optimization of these instruments. Optoelectronic image devices (OID)(1-39), particularly self-scanned photodiode arrays (SPD), provide an attractive alternative to the polychromator approach because they too provide the capability of simultaneous detection of dispersed radiation. When these detectors are interfaced with appropriate on-line computer control and data processing facilities, the signals from hundreds of virtually independent, optical (spectral) channels can be integrated and digitized simultaneously. In addition, the contribution of continuum spectral background or undesirable overlapping spectral features present in the "blank" spectrum can be subtracted or "stripped" from the total signal for all channels. If desirable, random or fast-access to the specific spectral features of interest may be employed to conserve computer memory space and time (40). Other capabilities provided by these detectors include: a) Flexibility in choice of mode of signal integration and processing; real-time, in-memory integration or on-target integration; b) monitoring of ultrarapid spectroscopic events; c) compensation for source fluctuations and for sensitivity and spectral response variation; d) high quantum efficiency; and e) linear response. These desirable features of OID's are offset, at least partially, by a few undesirable features that impose ultimate limits on the atomic spectrometric performance of these detectors. A foremost limitation is set by the number of diodes in commercially available diode arrays, and their physical arrangement and spatial resolution. In addition, the low amplification gain of the SPD requires longer signal-integration times, and finally, the dynamic range of the SPD is narrower than that of the PMT.

As shown in the discussion above, there are a multiplicity of desirable and undesirable features of OID's that impact their general application as detectors in analytical atomic emission spectrometry. It is therefore appropriate to compare, in a critical and objective sense, the experimental figures of merit of these devices vis-a-vis the classical polychromator photomultiplier approach. These comparisons should be performed virtually on a continuing basis because of advances in performances, not only of the array detectors themselves but also in the associated spectroscopic excitation sources. An evaluation of the overall performance figures of merit of OID's when they are employed in conjunction with induction-coupled plasma excitation is of particular current interest because of the popularity that this source is attaining for the simultaneous determination of the elements at all concentration levels. In this paper we present such an evaluation for self-scanned, photodiode array detectors

(SPD) and draw comparisons to PMT arrays as used in classical polychromators. To a lesser extent, some comparisons are drawn with silicon intensified target vidicons (SIT) and intensified self-canning photodiode array detectors (ISPD). A similar evaluation of the SPD for spectrophotometry and spectrofluorometry was recently published elsewhere (41).

Apparatus And Procedure

The experimental facilities and operating conditions utilized in this study are summarized in Table I. Both spectrometers were used either as monochromators, in the single wavelength detection mode, or as polychromators in the multichannel detection mode. The conversion of the Jarrell-Ash spectrometer to a polychromator was accomplished by replacing the camera attachment of the spectrometer with an OID array detector. A rotationally adjustable mount allowed the array detector channels to be aligned parallel with the slit image. Spectral line slit images were focused on the detector surface by adjustment of a 45° folding mirror that deflected the exit spectrum onto the camera mount. Selection of either single channel or multichannel detection modes was made by rotation of the 45° mirror to one of two positions, either allowing the exit spectrum to reach the exit slit or deflecting it to the array detector. The slit-height setting for the SPD detector was 2.5 mm, equal to the height of each individual diode.

The 1% HNO₃ reference solutions were prepared from distilled HNO₃ and deionized distilled water. Analyses of the US Geological Survey reference samples were performed after dissolution by sodium hydroxide fusion (42). Reference solutions necessary for the analysis of the glass samples were prepared in a 2% NaCl-HCl matrix to match the total acid and salt content of the glass samples.

Detection limits, defined as the concentration required to provide net analyte signals that were three times greater than the standard deviation of the background scatter, were determined from ten ten-second integrations of the blank and dilute reference solutions for the PMT system. Standard deviation (noise) of the background was calculated from the ten blank integrated signals. The multichannel nature of the SPD and SIT detectors was utilized to determine detection limits with these systems. Pairs of blank spectra were subtracted from each other to obtain net difference spectra. These difference spectra represented the noise and the drift between measurements. The standard deviation of ten adjacent diodes in the region of the analyte wavelength was determined for each of the net difference spectra. The standard deviation of five different spectra were then averaged to produce a representative noise level.

To measure the background irradiance of the ICP in the 180-440 nm region, a precalibrated deuterium arc lamp was used. The

Table I. Instrument Setup and Operating Conditions

Plasma Power Supply:	Plasma Therm, Inc., Model NFS-2500 D with Model AMN-3000 E impedance matching network.
Plasma Torch:	Ames Laboratory construction (43) 20 L/min plasma Ar flow; 1.0 L/min aerosol carrier Ar flow.
Forward Power:	1100W
Ultrasonic Nebulizer:	Ames Laboratory construction (44) 1.4 MHz, water cooled desolvation, 2.6 ml/min sample introduction rate.
Spectrometers:	1) Jarrell-Ash, Model 78-466, 1 meter f/8.7, Czerny-Turner mount with a 1180 g/mm grating blazed at 250 nm, reciprocal linear dispersion of 0.825 nm/mm (0.0206 nm/diode). Entrance slit width 20 μ m, height 2 mm. 2) McPherson, Model 2051, 1 meter, f/8.7, Czerny-Turner mount with a 1800 g/mm holographic grating blazed at 200-700 nm reciprocal linear dispersion of 0.0138 nm/photodiode, entrance slit 20 μ m, height 2 mm.
Lens:	Spherical, 4 cm diameter, 125 mm focal length 30 cm from plasma and entrance slit.
Observation Region:	3 cm segment centered 15 mm above the load coil.
Irradiance Reference:	Optronic Laboratories, Inc., Model UV-40 Ultra-violet Irradiance Standard. Calibrated at 10 nm intervals from 180 nm to 400 nm.

Table I. Continued

Detection System:

Multichannel:

1) EG&G PARC Model 1412 SPD (2.5 mm high perture X 25 um center-to-center, 1024 diode array, Reticon RL/1024S) operated by detector controller EG&G PARC, Model 1218 and data-manipulation by the OMA-2 console Model 1215. SPD was maintained at $-22^{\circ} \pm 0.002^{\circ}\text{C}$. The spectral window with Model 78-466 spectrometer was 21.094 nm.

2) EG&G PARC, Model 1254 silicon intensified vidicon (SIT) detector with ultraviolet to visible converter, operated by detector controller Model 1216 via OMA-2 console Model 1215. Number of channels 500. Spectral window was 10.31 nm.

3) EG&G PARC, Model 1420, microchannel plate (MCP) intensified SPD with 700 channels (ISPD). Temperature: -20°C . Operated by detector controller Model 1412.

Single Channel (Signal Integration):

PMT signal counted 10 times for periods of 10 seconds each using Analog Technology Corporation Model 151, wide range current-to-frequency converter. Sampling times were 100 ms. PMT; EMI Model 978AQ, operated at 700 V.

deuterium lamp was placed at the same optical position normally occupied by the plasma, i.e., 60 cm away from the entrance slit of the polychromator. The PMT response to the calibrated arc lamp was measured over the 180–440 nm region, in wavelength intervals of 10 nm. These measurements were then repeated for the plasma fed with a 1% HNO₃ blank solution. The irradiance of the plasma (I_{p1}), in microwatts/cm²/nm, was then determined according to:

$$I_{p1} = \frac{R_{p1}}{R_D} \times I_D \text{ (at 30 cm)}$$

where R_{p1} and R_D are the PMT response curves (180–440 nm) for the plasma and deuterium lamp, respectively, and I_D represents the calibrated irradiance of the deuterium lamp, at a distance of 30 cm away from the entrance slit. Because all optical parameters remained unchanged for the calibrated lamp and ICP measurements, prior knowledge of the spectral transfer characteristics of the spectrometer (particularly the grating) or the spectral response of the photocathode was not necessary. The measured I_{p1} represented the background irradiance at a distance of 30 cm from the plasma.

Results And Discussion

Linearity And Dynamic Range. There is extensive evidence that emission intensities of many atomic lines excited in an ICP source are linearly related to concentration of the corresponding analytes over a range of at least one million. Trace and major constituents are therefore determinable without changes in the operating condition of the plasma. Ideally, the detection system should have a comparable linear dynamic range performance. As previously discussed (45), there are several definitions of dynamic range that are applicable to the SPD detection system. First, there is the single diode dynamic range for a fixed integration time, defined here as the analyte concentration range that produces a linear signal response. This form of dynamic range can be severely reduced by thermally generated dark charge, because it reduces the effective A/D converter range available for readout of photon generated charges (signal). To reduce the effect of dark charge build up by approximately a factor of 100, the SPD array was cooled to -20°C. The cooling was done thermoelectrically and the temperature was kept constant to within a few millidegrees celsius. Under these conditions a single diode dynamic range of approximately 16,000:1 was routinely achieved (limited only by the 14 bits A/D convertor used).

To enhance the overall dynamic range of the SPD, the variable integration time (VIT) mode of operation can be used (41). In this approach the signals from each spectral window can be

consecutively obtained after integration of 16 ms, 160 ms and 16 seconds. In this manner, theoretical dynamic ranges of 1 to 16,000, 10 to 160,000 and 1,000 to 16,000,000 can be achieved with an overall linear dynamic range of 1.6×10^7 . In reality, the photon noise and the combined detector dark charge and plasma background signal reduce the useful VIT range of the SPD. The overall readout noise associated with a typical 16 second, on target, ICP signal integration was six counts rms (mostly radio frequency interference as discussed below). At the high end, the maximum readable signal is always limited by A/D converter range.

The limit of quantitative determination (LQD) is defined as the concentration required to yield a net intensity ten times greater than the standard deviation of the readout scatter (40). For instance, consider a 16 second signal integration at the Mn 257.6 nm line where the combined dark charge and plasma spectral background signal consumes approximately 20% of the dynamic range of the A/D converter (800 counts dark charge and 2600 counts plasma background). The resultant analytical dynamic range (single diode) would be:

$$\frac{\text{Maximum net signal}}{\text{Net signal at LQD}} = \frac{16,000 - 3400}{10 \times 6} = 210$$

(with proportionally low dark charge levels). Yet, shorter on-detector integration times, usable at higher analyte concentration, would increase this analytical dynamic range. For the same Mn line at 257.6 nm, consecutive integrations of 16 msec, 160 msec and 16 sec would have an accumulated (VIT) analytical linear range of at least 2.1×10^5 .

The excellent dynamic range achieved by the VIT method is represented by the data in Table II and by the graphical presentation in Figure 1. Linearity was retained, within the experimental error of measurements, over a concentration range greater than 10^5 . It should be noted, that the lowest plotted points represent LQD values.

Detector and Spectral Background, Spectral Interferences, and Spectral Stripping. For SPD's it is useful to distinguish between the detector and spectral background underlying most analyte lines. The major component of the detector background arises from thermally generated dark charge. There is in addition a characteristic fixed pattern caused by stray capacitive coupling of transients arising from the clock driving signals and by diode to diode dark charge variation (45). Radio frequency interference from ICP sources may also produce a time variable pattern noise superimposed on the detector background. The spectral background usually results from the cumulative contributions from sources

Table II. Overall dynamic range of the ICP-SPD system, demonstrated in Figure 1.

Beryllium Concentration	Signal Integration Time (Sec)	Number of Consecutive Accumulations ^a	Total Signal-Acquisition Time (Sec)	Average Net Signal (peak area) ^b Counts/ug/16 msec Integration
0.05 ug/L	16	1	16	5.60
1.00 ug/L	8	1	8	5.95
10.00 ug/L	8	1	8	5.61
10.00 ug/L	1.6	1	1.6	5.48
100.00 ug/L	1.6	1	1.6	5.75
100.00 ug/L	0.16	1	0.16	5.80
1.00 mg/L	0.16	1	0.16	5.77
1.00 mg/L	0.16	10	1.6	5.63
10.00 mg/L	0.016	10	0.16	5.48
				5.67 ± 0.16 RSD = 2.75%

^a Accumulations are defined as the number of consecutive SPD readouts (digitized) stored in same memory for SNR enhancement (ensemble averaging).

^b Each measurement was repeated five times to improve precision.

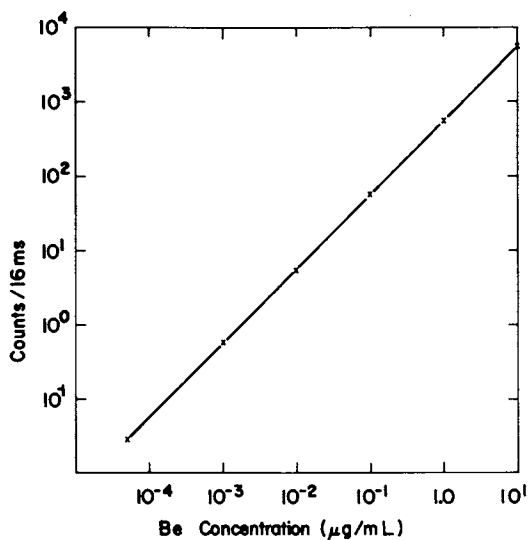


Figure 1. Linear dynamic range of the ICP/SPD demonstrated with Be 313.0 nm.

that cannot be eliminated such as residual far scatter (46), radiative recombination continuum and line broadening effects (47). Usually, the combined detector and spectral background constitute a significant fraction of the total signal measured at the analyte wavelengths. In fact, when analyses are performed at concentrations near the detection limits, the underlying background signal typically constitute more than 95% of the total signal. Thus, subtraction or correction for the total background signal is necessary to assure accuracy of determination. Because the detector background of a particular array is highly reproducible from scan to scan (with the exception of variations due to radio frequency interferences), it can be quantitatively stripped from the total signal to yield a spectrum that is free of detector background. If the spectral background signals from the reference blank and sample solutions are reproducible and their magnitude equal, then the total background signal, i.e., detector plus spectral, can also be stripped. The difference spectrum so obtained often makes it possible to recover useful analyte signals that otherwise may be totally obscured by the background. Figures 2 and 3 illustrate the simplified base line structure and signal recovery achieved through such background spectral stripping procedures.

When optimized ICP parameters are employed, changes in the concentration of concomitants in the sample usually exert a remarkably small interelement or "matrix" effect on the net intensity of analyte lines. If however, the magnitude and structure of the underlying spectral background in the immediate vicinity of the analyte line is significantly altered by the changing concentration of concomitants, this simplified spectral stripping procedure will not provide a satisfactory subtraction of the background signal. Another type of spectral interference that cannot be directly eliminated by these background subtraction methods arises from coincidence or partial spectral overlap of concomitant spectral lines with analyte lines. These interferences can usually be avoided through the judicious selection of analyte lines, but not always. Because both these types of interferences may occur, it is important to determine whether precise corrections can be made for them.

Various approaches have been devised to measure accurately these types of background shifts with simultaneous multielement systems based on polychromators with PMT arrays (48-50). Micro-computer controlled and automated systems of this type are now commercially available. With computer controlled scanning monochromators, background measurements and corrections at selected wavelengths are normally programmed into the analytical determination sequence (40). However, such systems are by definition not multichannel in nature and therefore cannot provide simultaneous multi-element determinations. In contrast, with SPD systems, an entire spectral window is simultaneously measured, digitized and stored in memory (although spectral

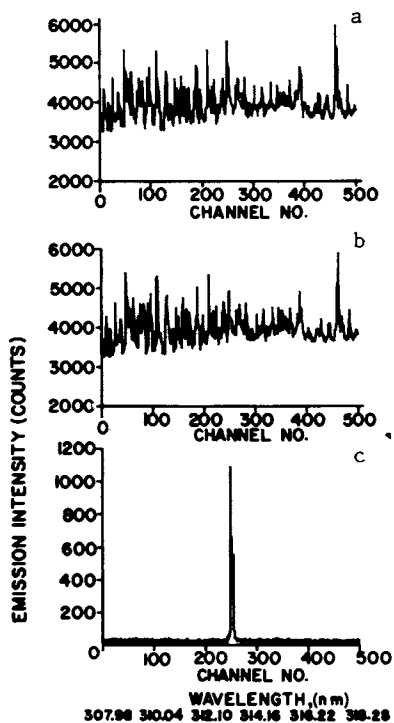


Figure 2. Efficiency of plasma background subtraction. Key: a, emission spectrum of 1 $\mu\text{g/mL}$ Be, 1% HNO_3 ; b, emission spectrum of 1% HNO_3 blank; and c, difference spectrum obtained by subtracting Spectrum b from a. Spectra were obtained after on-target signal integration for 8 s.

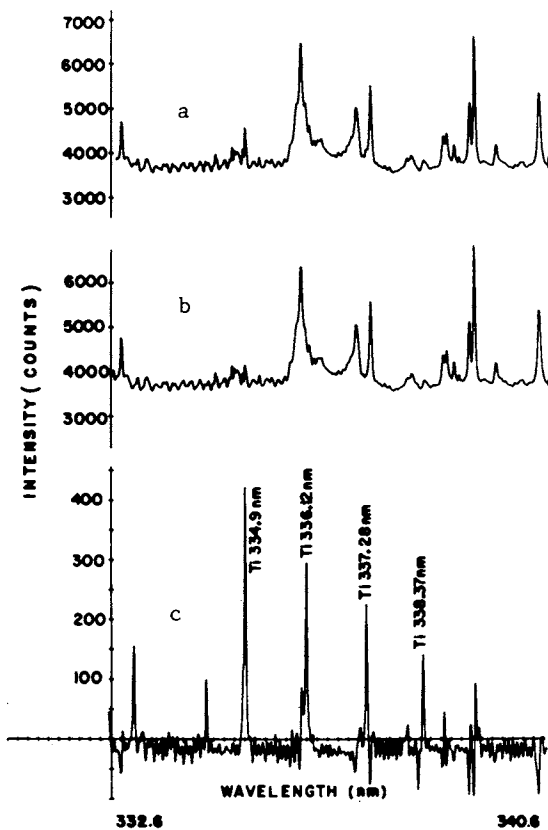


Figure 3. Efficiency of plasma background subtraction. Spectra obtained after on-detector integration for 1.6 s. Key: a, spectrum of 10 µg/mL Ti; b, detector and spectral background; and c, net difference spectrum.

windows may be inadequately narrow for some applications). The analyst may then use a video display for: a) characterizing the nature of the underlying background and determining the most suitable analyte lines; b) determining which analyte lines are least susceptible to shifts in the background magnitude due to changes in the concentrations of the major concomitants; and c) selecting the best wavelengths (diodes) for applying base line background corrections for each analyte line. If appropriate, a computer algorithm may be used to determine background levels from several off analyte line diodes.

The efficiency of background correction techniques may be judged by comparing a series of reference working curves containing increasing concentrations of concomitants. Errors arising from uncorrected background shifts will reduce the slopes of these reference working curves at low analyte concentrations. With PMT polychromators, background correction has been proven effective down to the LQD level, even at high concomitant concentration levels, e.g., 5000 ug/ml Ca, 5000 ug/ml Mg and 500 ug/ml Al (50). For our evaluations, the Tl 190.8 nm and the As 193.7 nm lines were chosen to determine the efficiency of background correction achievable with SPD detectors. Figure 4 shows the spectra at and about the 190.8 nm Tl line measured for 15 ug/ml Tl solutions (1% HNO₃ aqueous) with and without the addition of concomitants. In both cases the blank subtraction (detector plus blank spectral background) was performed. It is apparent that the relatively flat background is amenable to line interpolation corrections, i.e., the choice of wavelength (diode) for background correction, is rather non critical. In the case of the As 193.7 nm line, correction of the background is rendered more difficult because the analyte line is superimposed on the wing of an adjacent Al concomitant line, Figure 5. In this case, at least two correction values measured at wavelengths located on each side of the As line are needed. A straight line interpolation between these two wavelengths is then used to estimate the background level at the analyte wavelength. Analytical calibration curves of Tl and As at four concomitant concentration levels, obtained after blank background subtraction only, are shown in Figures 6 and 7. Clearly, at the highest concomitant concentrations, the LQD analyte level shows an order of magnitude error in concentration due to uncorrected background shifts. When the interpolative background corrections were applied to the same data, the determination errors were drastically reduced, as shown by Figures 8 and 9. In fact, background corrections achieved with SPD, for both types of underlying spectral backgrounds, are comparable to that achieved with the array PMT polychromator (50). The shifts in the analytical curves, visible in Figures 8 and 9 reflect the reduction in the nebulizer efficiency at the high or concomitant concentrations. This matrix effect could be eliminated by utilizing the internal reference line principle to normalize variations in the nebulizer efficiency. For this normalization procedure

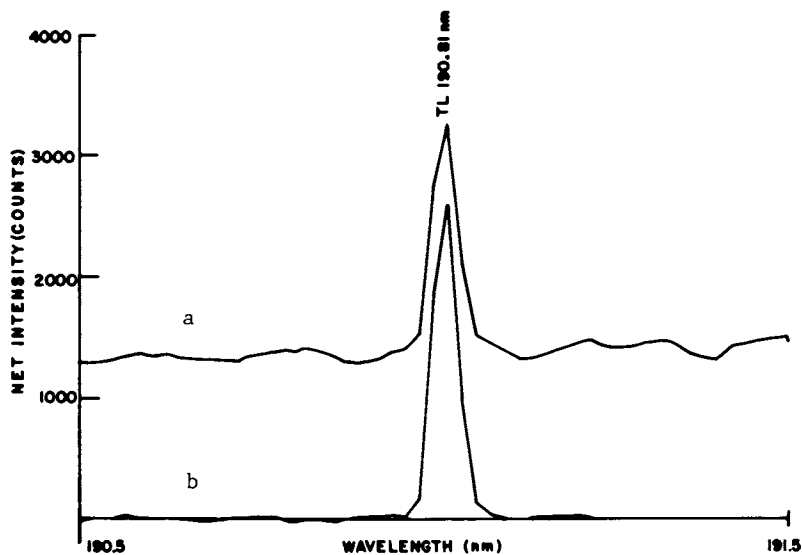


Figure 4. Net spectra after spectral stripping with 1% HNO_3 blank spectrum. Spectra obtained with Spectrometer 2, Table I. Key: a, 15 $\mu\text{g}/\text{mL}$ Tl with 5000 $\mu\text{g}/\text{mL}$ Ca and Mg, and 500 $\mu\text{g}/\text{mL}$ Al; and b, 15 $\mu\text{g}/\text{mL}$ Tl.

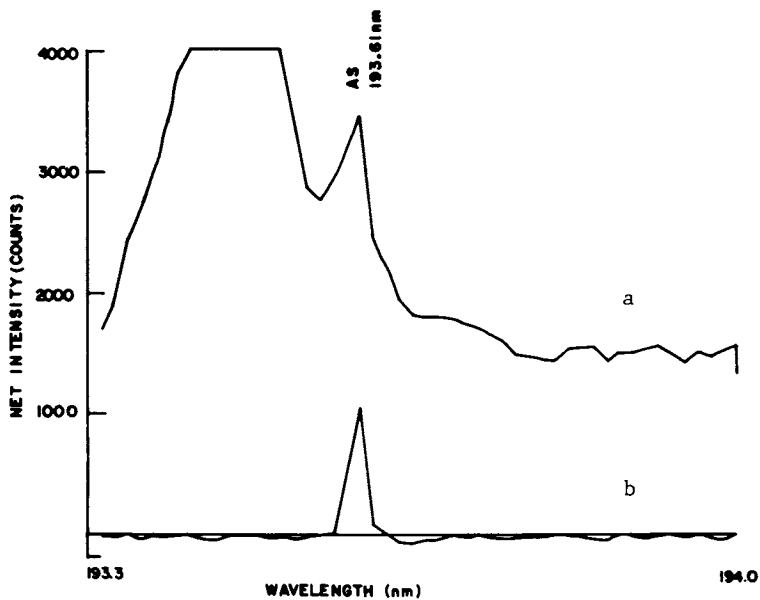


Figure 5. Net spectra after spectral stripping with 1% HNO_3 blank spectrum. Spectra obtained with Spectrometer 2, Table I. Key: a, 2.5 $\mu\text{g}/\text{mL}$ As with 5000 $\mu\text{g}/\text{mL}$ Ca and Mg, and 500 $\mu\text{g}/\text{mL}$ Al; and b, 2.5 $\mu\text{g}/\text{mL}$ As.

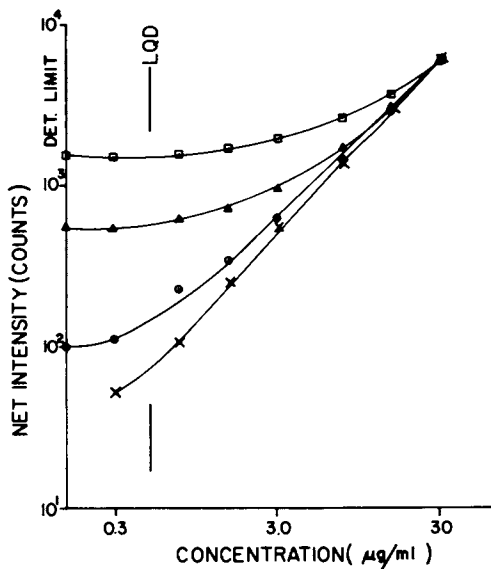


Figure 6. Analytical calibration for Tl 190.8 nm after spectral stripping with 1% HNO_3 blank. Key: \square , high concomitants level = Ca and Mg 5000 $\mu\text{g}/\text{mL}$, Al 500 $\mu\text{g}/\text{mL}$; \triangle , medium concomitants level = Ca and Mg 750 $\mu\text{g}/\text{mL}$, Al 75 $\mu\text{g}/\text{mL}$; \circ , low concomitants level = Ca and Mg 100 $\mu\text{g}/\text{mL}$, Al 10 $\mu\text{g}/\text{mL}$; and \times , no concomitants.

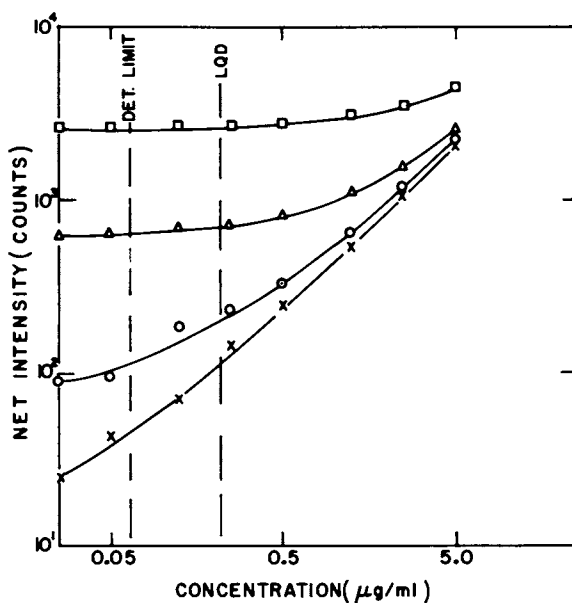


Figure 7. Analytical calibration for As 193.7 nm after spectral stripping with 1% HNO_3 blank. Concomitant concentrations are the same as in Figure 6.

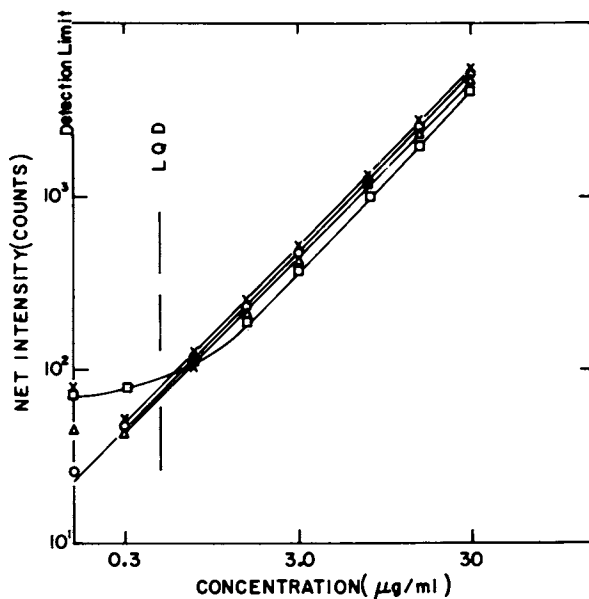


Figure 8. Analytical calibration for Tl 190.8 nm after spectral stripping with 1% HNO_3 blank and interpolative background correction. Concomitant concentrations are the same as in Figure 6.

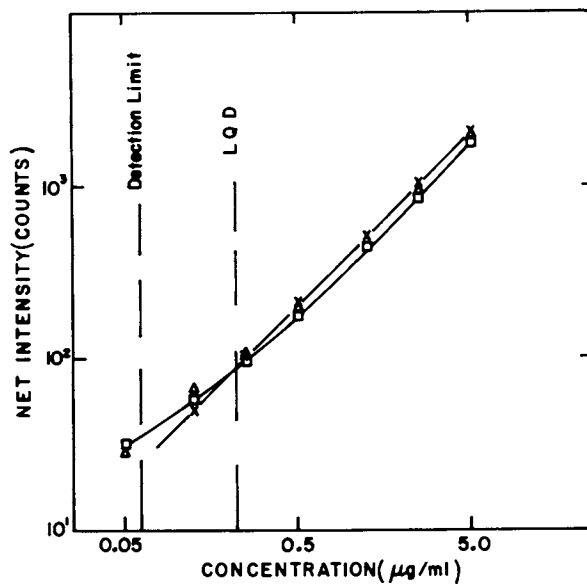


Figure 9. Analytical calibration for As 193.7 nm after spectral stripping with 1% HNO_3 blank and interpolative background correction. Concomitant concentrations are the same as in Figure 6.

to be successful, the internal reference line should fall in the same SPD spectral window.

Although the baseline, interpolative background-correction method is very effective its limitation must be understood. Whereas spectral interferences caused by uniform baseline shifts and by broad smoothly sloping line wings (for spatial frequency features at the SPD focal plane) can be fairly accurately corrected, those caused by spectral overlapping with concomitant lines cannot be corrected by this simple baseline, interpolative procedure. Moreover, regardless of whether a PMT or an SPD detector is used, accuracy of this interpolative background correction method depends on the stray radiant energy (SRE) characteristics of the spectrometer used. This effect is demonstrated by a comparison between Figures 4 and 5 and Figures 10 and 11. The spectra shown in Figures 4 and 5 were obtained with spectrometer 2 (Table I) equipped with a low SRE holographic grating. Those shown in Figures 10 and 11 were obtained with spectrometer 1 (Table I) equipped with a mechanically ruled (and rather old) grating that produced highly structured and irregular background shifts. These structures, often overlap analyte spectral lines. The effect of this overlap was significant even at concentration levels well above the limit of quantitative determination. As shown in Figure 12, similarly structured backgrounds were observed for the SPD and the PMT, thus ruling out SPD diode-to-diode response variations as the cause for this phenomenon. Highly structured SRE backgrounds have also been observed with other spectrometers utilizing ruled gratings (46). Although most state of the art ruled gratings do not produce structured SRE features, a large number of gratings still in service may be unsuitable for accurate background shift correction.

When it is impossible to select analyte lines that are completely free from spectral overlap by concomitant spectral lines, array detectors may be used to reduce the adverse effect of such spectral interferences. To accomplish this task, the spectrum of the known concomitant is first measured and stored. One or more concomitant lines that are known to be located in an interference free zone within the measured spectral window are then used as internal reference lines. The relative intensities of these lines in the sample spectrum are then used to establish a correction factor by which the stored concomitant spectrum is multiplied and subtracted from the sample spectrum. This correction procedure can be performed for each known concomitant present in the sample. A prior knowledge of the concentration of each concomitant is not required.

A simplified version of this spectral stripping technique was demonstrated with the SPD for the V doublet (309.27, 309.31 nm), which is unresolved from the Al doublet (309.27, 209.28 nm). The spectra of pure Al, pure V (as shown in Figure 13), and various mixture solutions of the two were first measured and stored.

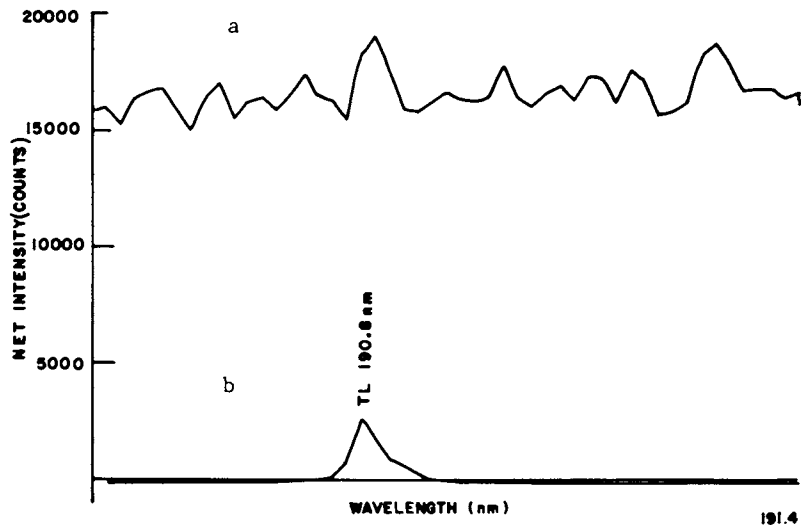


Figure 10. Net spectra as in Figure 4, but obtained with Spectrometer 1, Table I.

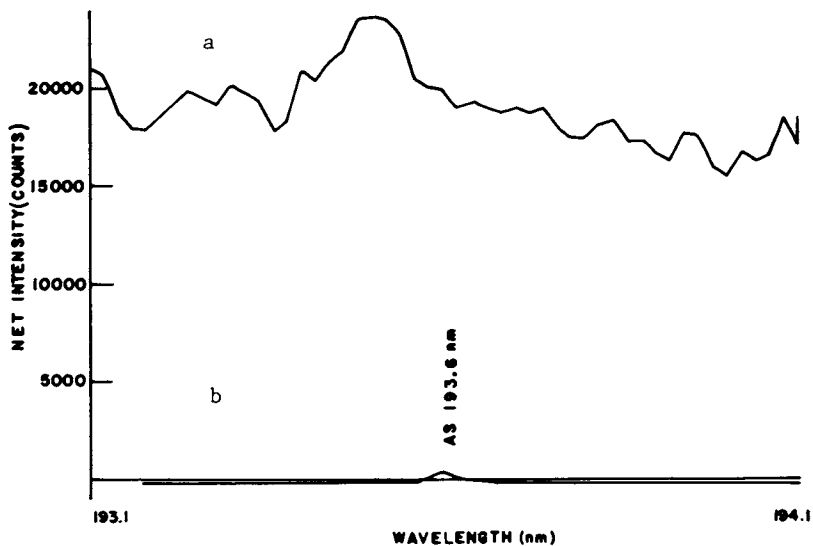


Figure 11. Net spectra as in Figure 5, but obtained with Spectrometer 1, Table I.

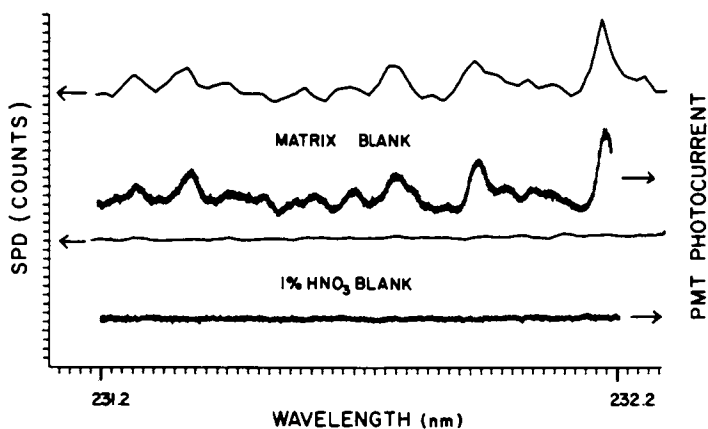


Figure 12. Spectra of 1% HNO₃ blank and high concomitant blank obtained with the SPD and PMT detection systems by using Spectrometer 1, Table I.

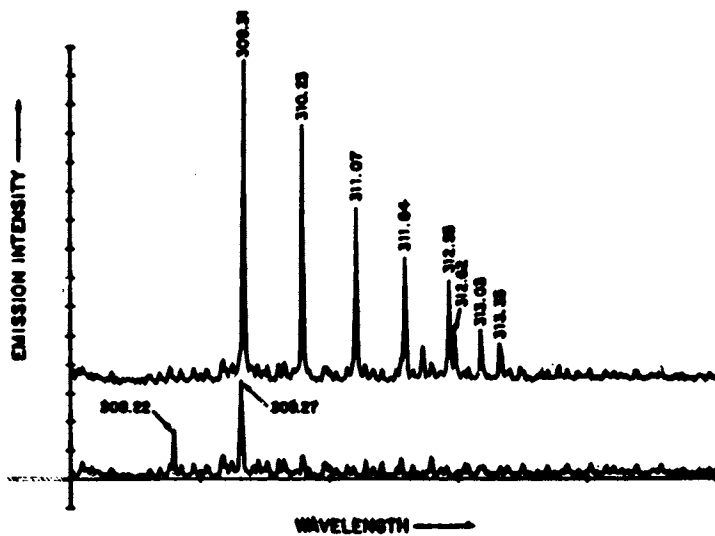


Figure 13. Spectra of 1% HNO₃ aqueous solutions of pure V (top) and Al (bottom) at a concentration of 400 µg/mL. Signal integration time = 100 ms.

The Al 309.3 / Al 308.2 intensity ratio was measured on the spectrum of pure Al, and intensity of the Al 308.22 nm reference line was measured in each of the Al, V mixture spectra and multiplied by this correction ratio to calculate the intensity contribution of Al to the 309.3 nm unresolved Al, V doublet. The accuracy of determining the actual intensity of V at the 309.3 nm line, in this fashion, Table III, decreased as the Al/V concentration ratio increased. This is expected because the combined signal of the resolved V, Al doublet was maintained at a relatively constant level and therefore, also its associated noise i.e., mostly due to photon noise and superimposed RF interference. At the same time, the fraction of the V signal (within the combined signal) was reduced, resulting in a corresponding reduced precision and accuracy. When analyzing "real" samples with complex matrices, the accuracy of spectral stripping becomes very dependent on the selection of appropriate concomitant reference lines. Generally, under such circumstances, the accuracy of spectral stripping can be significantly improved by resorting to matrix-form, least-squares deconvolution techniques (51) that rely on a much wider statistical data base, i.e., the entire digitized spectrum (1024 points).

Finally, it is important to clarify a few common misconceptions regarding these spectral stripping techniques. First, errors may be caused by unstable geometric registration, i.e., wavelength-to-diode calibration, resulting from thermal expansion or contraction of the polychromator system. Second, the statistical nature of these techniques sets a limit on their accuracy, e.g., it deteriorates as the subtracted interfering lines become more intense and the sought analyte lines less intense.

Detection Limits, Noise Characteristics and S/N Consideration.

The detection limits measured with the unintensified SPD detection system operated in the on-target integration readout mode are compared to those obtained with the ISPD (intensified SPD) and the SIT (both high gain multichannel detectors) and the PMT, a high gain single channel detector, Table IV. It is important to realize that the SIT used in this study was uncooled. It is possible to cool a SIT to dry-ice temperatures and thus effectively achieve long signal integration times (52). However, cooling a SIT is mechanically difficult, and requires elaborate scanning and target preparation techniques, to overcome the high discharge lag characteristics of vidicon devices. It is, generally, rather difficult to maintain a good linearity (signal reciprocity) with cooled SIT's. Ultrasonic sample nebulization was used throughout this study. These comparative detection limit values, however, must be cautiously evaluated since the absolute performance of all four detectors can vary by a factor of 2 - 4. This is particularly true for the SIT, for which spatial and spectral variations in photocathode response, signal amplification, efficiency of the

Table III. Peak Area Counts

Soln. No.	Al:V Conc. Ratio	Measured ^a Al 308.22nm	Calculated Al 309.2nm	Measured 310.2 V	Expected ^b V 309.2nm	Measured 309.2nm(Al+V)	Calculated V 309.2 nm	% Error
Soln. No. 1	1:1	2497	5362	13538	19007	24316	18954	-0.3%
			(2497 X 2.147)		(13538 X 1.404)		(24316 - 5362)	
Soln. No. 2	10:1	11790	25318	6731	9450	34871	9553	+1.08%
Soln. No. 3	100:1	11330	24330	686	963	25142	812	-15.7%
Ratio $\frac{V_{309.2}}{V_{310.2}} = 1.404$ measured from pure V spectrum								

^a Different signal integration times were used for each solution mixture. ^b Vanadium conc was 10ng/ml.

TABLE IV. Detection Limits.

Element	Spectral line, nm	Detection Limit, ng/ml							
		16.4 sec	32.8 sec	82 sec	164 sec	10 sec	15 sec	16 sec	
As	193.7	70	35	14	7	2	40	3	
Se	196.0	150	75	30	15	3	65	3	
Cr	205.5	2	1	0.4	0.2	0.15	3.2	0.2	
Zn	213.8	0.3	0.15	0.06	0.03	0.026	0.22	0.04	
Co	228.6	0.5	0.25	0.1	-----*	0.16	-----	0.2	
Cd	228.8	0.2	0.1	0.04	-----*	0.05	-----	0.1	
Ni	231.6	0.7	0.35	0.15	-----*	0.15	1.1	0.4	
Ba	233.5	0.2	0.1	0.04	-----*	0.05	0.5	0.1	
Be	234.8	0.02	0.01	0.004	-----*	0.008	-----	0.01	
Mn	257.6	0.04	0.02	-----*	-----*	0.014	0.07	0.02	
Pb	283.3	6	3	-----*	-----*	4	14	5	
V	311.0	0.12	-----*	-----*	-----*	-----*	0.3	0.2	
Be	313.0	0.004	-----*	-----*	-----*	0.13	0.02	0.004	
Cu	324.7	0.07	-----*	-----*	-----*	0.003	0.4	0.1	
Sr	338.0	0.6	-----*	-----*	-----*	0.15	2	0.5	
Al	396.1	0.25	-----*	-----*	-----*	1	-----	0.9	
Mn	403.0	0.5	-----*	-----*	-----*	0.8	1.6	1.3	

* Maximum wavelength for this on-detector integration time.

Detection limits determined as described in Apparatus and Procedure section.

UV-to-visible converter, and amplifier noise may affect both the response and the signal-to-noise characteristics of the detector.

At first glance the excellent detection limits obtained with the unintensified SPD, compared with those obtained with the high gain detectors may seem puzzling. An examination of the S/N characteristics of both the SPD and the plasma source can provide some insight into this pleasing performance.

Detector readout noise is the predominant source of noise for the combined ICP/SPD system. Radio frequency (RF) interference from the ICP appears as a superimposed periodic beat pattern, as shown in Figure 14. With appropriate grounding and shielding at the plasma enclosure, this noise can be reduced to approximately 5 counts rms or less. As noted earlier integration of signal may be performed either in-memory or on-target (45). With in-memory integration, the SPD is read at the normal scan rate and the signals from consecutive readouts are accumulated in the computer memory, i.e., ensemble averaging. With on-target integration, the signal is accumulated (temporarily stored) in the diodes and read only at the end of the integration period. With readout noise limited systems, the on-target integration mode has definite advantage, because read noise is introduced only once during the final (and only) array readout, resulting in a S/N improvement that is nearly proportional to the time of integration. With photon shot-noise limited systems, either readout mode will provide a S/N that is proportional to the square root of the total amplitude of the integrated signal. As noted earlier when the line intensities surpass the A/D converter limit, e.g., 16,384 counts, a combination of in-memory and on-target integrations offers the optimal readout mode and greatly extends the dynamic range of the system.

Cooling the array to -20°C reduces the dark charge signal by approximately a factor of 100, thus enabling proportionally longer on-target signal integration periods. Typical average dark charge signal levels, at this temperature, vary from array to array within the 30-180 counts/second range. Thus, if, for example, the maximum A/D converter range allotted for dark charge readout is set at 12,000 counts/diode (allowing analyte signals of up to 4384 counts) the maximum corresponding integration times are in the 400 to 67 seconds range.

The following examples will demonstrate the merit of on-target signal integration. Consider an SPD detection system with an average quantum efficiency of 0.5; a readout noise, N_R , of 1200 electrons/diode/scan (one scan is 16.667 ms) or one count rms (if the preamplifier gain is set at 1 count = 1200 electrons); a dark charge signal, D , of 100 counts/diode/second; a plasma background signal, P , of 50 counts/diode/second (2000 photons/diode/scan); an RF noise, N_{RF} , of 5 counts rms/diode/scan; and an analyte signal, S , of 0.5 count/diode/second (20 photons/diode/scan).

- a) S/N after 1 second of on-target signal integration:
Total signal ($S+P+D$) is 150.5 counts/diode/second. The

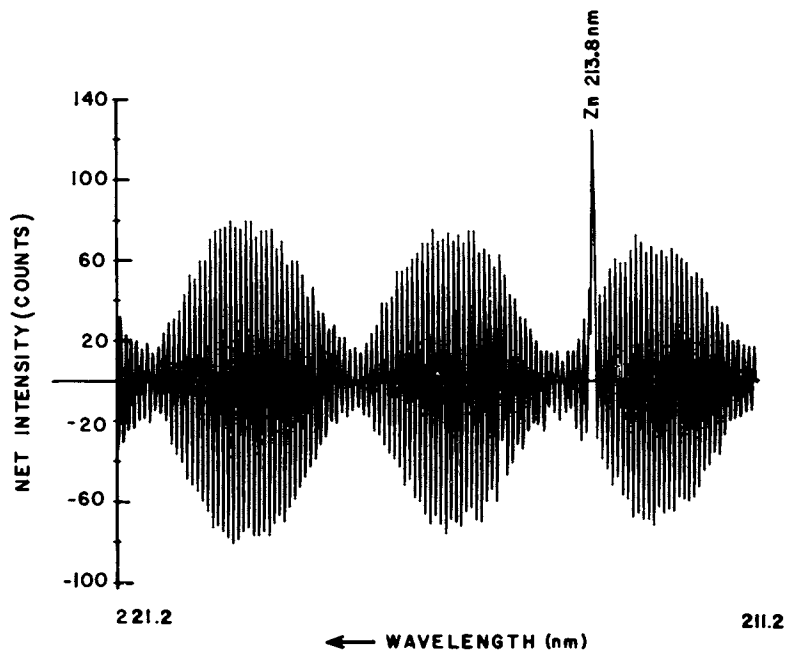


Figure 14. The effect of radio frequency interference (periodic pattern noise) on the S/N performance of the SPD when inadequate RF shielding was used. The emission signal of Zn 213.8 nm at $2.0 \mu\text{g/mL}$ happened to be located at the node in this particular case. Signal integration time was 16 s. Spectral background subtraction was performed.

corresponding signal shot noise, N_S , is $(150.5 \times 1200)^{1/2}/1200 = 0.35$ counts rms. In this case the total system noise,

$$N_T = N_{RF} = 5 \text{ counts rms and } S/N = \frac{0.5}{5} = 0.1.$$

b) S/N after 100 seconds of on-target signal integration: Total signal integrated on-target is 15050 counts/diode. Corresponding signal shot noise, N_S , is $(15050 \times 1200)^{1/2}/1200 = 3.5$ counts rms.

$$N_T = [(N_R)^2 + (N_{RF})^2 + (N_S)^2]^{1/2} = 6.2 \text{ counts rms and } S/N = 8.1$$

Thus, a 100 fold increase in signal integration time improves S/N by a factor of 81. If radio frequency interference could be further reduced, an almost linear improvement in S/N can be achieved. For comparison, if a 100 second (6000 scans) in-memory signal integration was used instead, a S/N = 0.65 will be obtained since $N_R = (6000 \times 1)^{1/2} = 77.5$ counts rms. It should be noted that for analyte signals greater than 1200 counts/diode/scan, both modes of integration will result in an equal S/N performance. In contrast, in the absence of source flicker noise limitations, high gain detectors such as PMTs are photon shot-noise limited and therefore show a S/N improvement that is only proportional to the square root of the integration time. Generally, whereas the SPD achieves similar S/N performance whenever long signal integration time is affordable, it is significantly inferior to the PMT when low level light signals of short duration are measured. On the other hand, at sufficiently high radiant flux levels (whether background or analyte) the measured signal for the PMT detector was found to be flicker noise limited, as shown by Figure 15. Under such conditions S/N will scarcely improve with increased integration time.

Table IV clearly shows that the detection limit performance of the SPD, relative to that of the PMT declines as shorter wavelength analyte lines are selected. This decline cannot be simply explained on the basis of reduced optical transfer efficiency of the polychromator since the same polychromator was used with all four detectors. Neither can a reduced spectral response be the cause for the poorer performance at the low UV spectral range since the quantum efficiency of the SPD in this region is very high, being approximately 40-50%. The relative loss of detectability is related to a corresponding reduction in both plasma background and analyte irradiance at shorter wavelengths. As shown in Figure 16, the background irradiance declines rapidly at the short wavelengths. The few scattered data points above the irradiance curve are attributed to line and band emission superimposed on the continuum background of the plasma.

This decline in plasma background level affects the relative S/N performance of the PMT and SPD detection systems in the following manner:

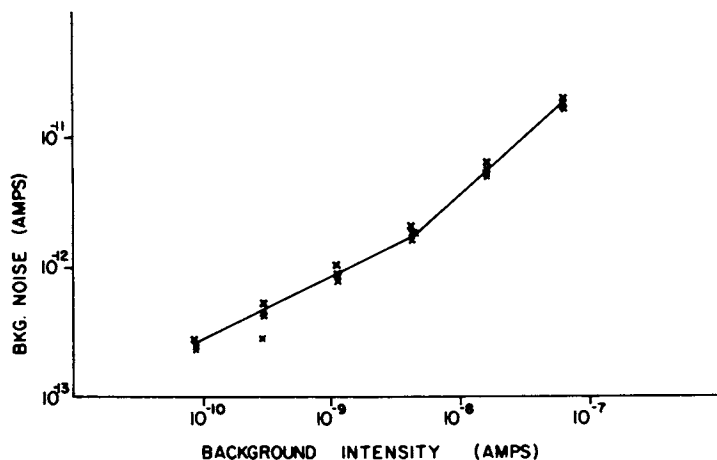


Figure 15. Relationship between the plasma background emission intensity and its associated noise measured with a photomultiplier detection system.

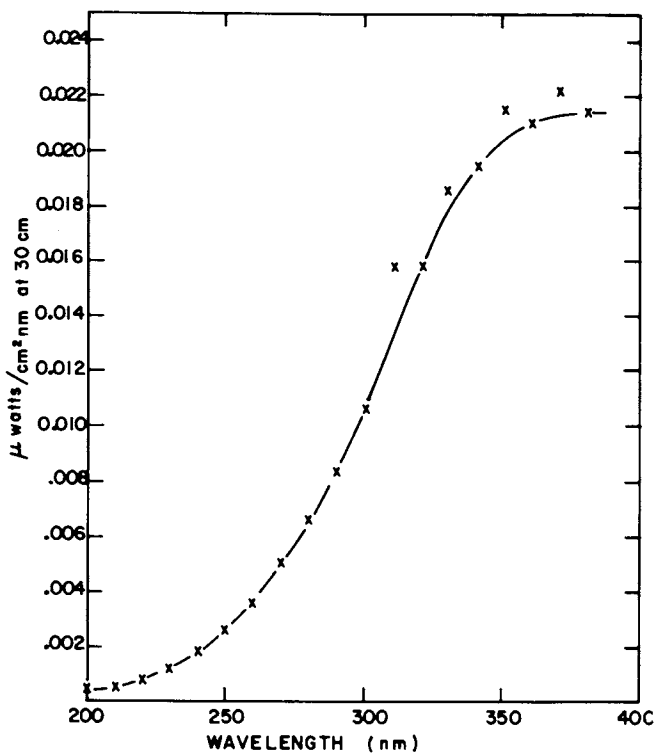


Figure 16. Plasma irradiance in the 200–380-nm spectral range at a distance of 30 cm from the ICP. A 1% HNO_3 aqueous solution was aspirated.

- I. ICP/PMT: When detection limit levels are approached the dominant noise feature is either the shot noise or the flicker noise of the plasma background (Figure 15). Because the background level drops at lower wavelengths, so does the absolute level of the associated noise. Simultaneously, there is a corresponding reduction in the analyte line irradiance (signal), at lower wavelengths, as shown in Figure 17. This decline is partially a result of a corresponding reduction in the grating transfer efficiency and photocathode quantum efficiency near the VUV spectral region. Thus, because signal and noise decrease simultaneously, with wavelength, the net result is a detection limit (S/N) performance that is relatively wavelength independent.
- II. ICP/SPD: The noise of the ICP/SPD detection system is practically independent of the plasma background level, i.e., it is radiofrequency interference noise, or more generally readout noise, limited. Therefore, because the net analyte signals drop with wavelengths, Figure 17, so do also the S/N values, and the detection limit values are raised. As previously discussed, a nearly linear improvement in detection limit can be achieved with an increase in integration time (See Table IV).

The high gain of the ISPD resulted in a S/N performance that is basically plasma background noise limited over the entire wavelength region examined, as evidenced by the very similar detection limits obtained with the ISPD and the PMT in Table IV. As expected, an increase in the integration period with the ISPD resulted in a square root improvement in detection limits.

The SIT is also a high gain detector, but its readout noise is typically higher, its UV response is poorer and its cooling is difficult and inefficient. Indeed, the detection limits obtained with the SIT were significantly inferior to those obtained with either the PMT or the ISPD, especially in the UV region.

Whereas the plasma background signal (except at high levels) is predominantly shot noise limited, the net analyte signal is dominated by flicker noise (except at the detection limit region) as demonstrated by the signal to noise relationship data in Tables V and VI. Source flicker noise dependence of the net analyte intensity is a multiparameter phenomenon which may stem from 120 Hz power beats of the plasma, variations in gas flow rates or variations in the rate of nebulization.

The multichannel nature of the SPD could be used to reduce the effect of flicker noise by utilizing the classic internal reference technique. The intensities of a few carefully selected lines are simultaneously integrated with the analyte lines and used as introduction-evaporization-atomization-excitation indicators. This approach can significantly reduce flicker noise and thus improve the S/N performance of the system as shown in Table VII. As expected, at low concentration levels, where the system becomes RFI noise limited, this method offers a very limited S/N improvement.

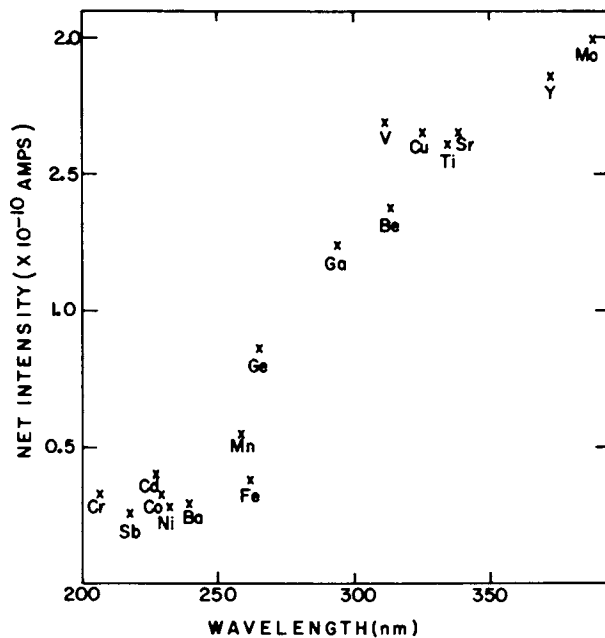


Figure 17. Relationship between the net signal intensity of analyte lines at the detection limit with a PMT and the line wavelength.

Table V. Signal-to-noise relationship demonstrated with Be 313.04 nm line

Concentration, ug/l	Integration Time (sec)	Peak Area ^a (Counts)	Peak Height ^b (Counts)	SNR	
				Peak Area	Peak Height
1	1.666	5192 ⁺⁷⁴	2810 ⁺³⁴	70.2	82.7
1	0.166	514 ⁺¹²	279 ^{+3.4}	43.0	82.1
10	0.166	5180 ⁺⁸⁰	2830 ⁺⁴²	64.8	67.4
10	0.0166	500 ⁺¹⁵	290 ⁺⁸	33.3	36.3

a. Seven central diodes in each peak were summed.

b. The net peak-height value, for each line, was obtained by subtracting the background value, measured with a diode positioned eight diodes (200 um) away.

Table VI. Signal-to-noise relationship demonstrated with Zn 213.8 nm line

Concentration, ug/l	Integration Time, S	Peak Height, Counts	Peak Area, Counts	SNR	
				Peak Height	Peak Area
10,000	0.83	15120 ⁺²⁹⁷	39728 ⁺⁶⁹⁰	50.9	57.6
1,000	1.66	3002 ⁺⁷²	7860 ⁺¹⁶²	41.7	48.5
100	8.30	1520 ⁺²⁶	3910 ⁺⁸⁴	58.5	46.6
10	8.30	160 ^{+9^a}	390 ^{+30^a}	17.7	13
10	16.60	322 ^{+6.3}	782 ⁺²⁴	51.1	32.6

a. RFI noise was high compared to signal level, resulting in reduced S/N ratio.

Table VII. Improvement in S/N (precision) through the use of spectral line internal standards

Concentration ^a ug/ml	Y 321.7 nm	Ti 323.4 nm	Ratio $\frac{Y}{Ti}$
	% RSD	% RSD	% RSD
0.01	3.1%	2.9%	2.7%
0.03	1.9%	1.8%	1.9%
0.1	1.6%	0.7%	0.5%
0.3	0.6%	0.5%	0.2%
1.0	1.0%	0.9%	0.2%
3.0	0.8%	0.7%	0.1%

a. 1% HNO₃ aqueous solutions with matrix concentration levels (400 Mg/ml) of Na, Ca and Mg were used

Wavelength Calibration And Spectral Resolution. The wavelength calibration accuracy of the SPD depends, in principle, only on the corresponding accuracy of the spectrometer's reciprocal linear dispersion. In this study, the wavelength-to-diode calibration was proven adequately linear to determine wavelength to within ± 0.02 nm over the entire 20 nm spectral window (1024 diodes) of the array, from any pair of known spectral lines.

The accuracy of this wavelength calibration is not affected by nonlinear, mechanical, tolerance-dependent processes, such as backlash of scanning monochromator. When mechanical scanning is utilized to sequentially display different spectral windows across the SPD, a single reference line from either the plasma background emission, e.g., Argon line, an analyte or a matrix line, or even from an external light source, e.g., Hg lamp, is sufficient to accurately calibrate each of these spectral windows. Each spectrum is individually stored during the course of the analysis and recalled later, at the user's convenience.

Although line identification and peak finding in stored spectra are simplified by recognition of marker concomitant lines, peak height values, are highly dependent upon the relative superimposition of line profiles on individual diodes. Peak height will be nearly halved when a line profile is equally divided between two adjacent diodes rather than centered on a single one. It is therefore essential that the user determines the effect of this "array discreteness" on the accuracy of determination and accordingly set the reciprocal linear dispersion of the spectrometer. Thermal insulation and/or control of the spectrometer SPD system should also be considered, because thermal expansion may reduce the accuracy of the diode-to-wavelength calibration.

The spectral resolution of a detector is defined here as equal to its spatial resolution (in μm) times the reciprocal linear dispersion of the spectrometer (in $\text{nm}/\mu\text{m}$). It was measured to be 1.5 - 2.5 and 2-4 times poorer for the SPD and SIT, respectively, compared to that of a PMT. All measurements were performed with the same spectrometer, utilizing 20 μm slit widths. Because, the proximity focused, microchannel plate (MCP) intensifier broadens the line images, the spectral resolution of the ISPD was found to be significantly worse than that of the SPD. Peak widths measured at half maximum intensity were four diodes wide even when only a single diode width was illuminated.

With the SPD, the minimum useful slit width is set by the 25 μm center-to-center spacing of the individual diodes. However, the very architecture of the diode array promotes a certain degree of signal cross-talk between adjacent diodes since any charge generated between them could be read out by either one. Also, in each measured spectral window only a few lines will be perfectly centered on a single diode; others will fall on portions of two adjacent diodes. As a result, the actual spatial resolution of the SPD is approximately 38 to 50 μm , whereas the PMT-spectrometer

(20 μm slit width) does achieve a spatial resolution close to 20 μm . Therefore, if the SPD is to achieve a spectral resolution comparable to that of the PMT the linear dispersion of the grating must be increased by a factor of 2-2.5, thus limiting the spectral window projected on the one inch (1024 diodes) array to 8-10 nm. Digital centroid finding techniques, so useful for resolution enhancement in photon-counting image detectors cannot be used with SPDs.

Application Studies. Although several papers have been published on the potential applications of ICP image detector systems, these studies have rarely involved samples of complex composition. To evaluate the advantages and limitations of the SPD detector when interfaced to general purpose spectrometers, we selected the determination of trace concentrations in glass and the analysis of microliter volumes of solutions as typical examples.

Determination of Trace Concentrations in Glass. The U.S. Geological Survey glass reference samples Nos. GSC-488, GSD-1439 and GSE-382 were dissolved in a manner described by Floyd et. al. (42). The constituents of the glass samples (SiO_2 , 62%; Al_2O_3 , 14%; Fe_2O_3 , 5%; FeO , 1.5%; MgO , 4.0%; CaO , 5.0%; Na_2O , 4.0%; K_2O , 3.6%)

The dissolved glass sample solutions contained approximately 2% NaCl . Such high salinity solutions are notorious for their adverse effects on nebulization and transport processes and have therefore required the use of reference solutions of similar salinity. Tables VIII to X summarize some of the analytical results obtained from two of the spectral windows studied. One of the spectra obtained is shown in Figure 18. Spectrometer 2, Table 1, was used to obtain both the SPD results and the PMT results (42) so that differences in linear dispersion and grating quality would not be a factor in the comparison. To achieve optimal S/N performance for all sought analytes, without saturating the A/D converter, data was aquired at a few different integration times (VIT). Both peak height and peak area were measured for each analyte line, since differences in concentration values obtained for each, serves as a further indication of spectral interference problems. The entire analysis time, including four reference samples three glass samples and two reference blanks, each measured five times at two different integration times, was approximately one hour. This included cleanout times between samples to avoid memory effects and storage of the digitized spectra on floppy disk.

Because the data manipulation and interpretation schemes were rather simplistic in their approach, not fully realizing the potential advantages of the "parallel" nature of the SPD these results cannot be considered optimal. However, these results are adequately characteristic of the overall performance of the SPD detection system and are therefore indicative of both its deficiencies and advantages over single channel photomultiplier detectors and could therefore, suggest some future modifications

Table VIII. Comparison of results for glass reference sample, GSC-488, with spectrometer 2, Table I.

<u>Element</u>	<u>Wave- Length</u>	<u>Concentration ug/gm</u>			<u>PMT</u> (40)	<u>Wave- Length</u>
		<u>SPD</u> Peak Height	<u>SPD</u> Peak Area	<u>USGS</u> Reference Value		
Y	321.6 nm	5.0	4.4	8	7	371.0 nm
Ti	323.4	11.9	14.0	11	8	334.9
Ti	323.6	15	11.4	11		
Cu	324.7	14.1	----	9	6	324.7
Cu	327.3	12.5	14.1	9		
Cd	326.1	15.8	12.6	3	2.6	214.4
Be	332.1	----	----	3.5	3.2	313.0
Be	265.0	----	----	3.5		
Mn	257.6	219	183	200	215	257.6
Mn	260.5	169	182	200		
Cr	266.6	4.1	----	7		
Cr	267.7	12.2	9.4	7	11	267.7

Table IX. Comparison of results for glass reference sample, GSD-1439, with spectrometer 2, Table I.

<u>Element</u>	<u>Wave- Length</u>	<u>Concentration ug/gm</u>			<u>PMT</u> (40)	<u>Wave- Length</u>
		<u>SPD</u> Peak Height	<u>SPD</u> Peak Area	<u>USGS</u> Reference Value		
Y	321.6 nm	51.3	47.3	48	47	371.0 nm
Ti	323.4	51.7	53.4	44	50	334.9
Ti	323.6	50.4	48.5	44		
Cu	324.7	51.6	44.7	45	40	324.7
Cu	327.3	48.6	52.0	45		
Cd	326.1	52.9	48.2	30	28	214.4
Be	332.1	----	----	44	40	313.0
Be	265.0	----	45.7	44		
Mn	257.6	254	205	210	212	257.6
Mn	260.5	189	204	210		
Cr	266.6	49.5	45.9	47		
Cr	267.7	66.8	61.0	47	44	267.7

Table X. Comparison of results for glass reference sample, GSE-382, with spectrometer 2, Table I.

<u>Element</u>	<u>Wave- Length</u>	<u>Concentration ug/gm</u>			<u>PMT</u> (40)	<u>Wave- Length</u>
		<u>SPD</u> Peak Height	<u>SPD</u> Peak Area	<u>USGS</u> Reference Value		
Y	321.6 nm	482	495	490	501	371.0 nm
Ti	323.4	524	498	490	499	334.9
Ti	323.6	510	506	490		
Cu	324.7	513	509	500	502	324.7
Cu	327.3	516	539	500		
Cd	326.1	484	502	420	425	214.4
Be	332.1	506	---	500	512	313.0
Be	265.0	478	474	500		
Mn	257.6	596	589	600	596	257.6
Mn	260.5	591	589	600		
Cr	266.6	460	458	490		
Cr	267.7	496	503	490	480	267.7

necessary to render SPD's analytically practical. Net peak height values were determined by subtracting background values obtained from a nearby diode located in a spectral interference free zone, not necessarily in the immediate vicinity of the analyte peak. With peak areas, on the other hand, background values were obtained by the rather simplistic method of interpolation between the visually selected wing diodes. Both peak area and peak height measurements were subject to spectral interferences to varying degrees without a consistent accuracy advantage by either technique. As expected, the accuracy of measurements was also dependent on the number of diodes grouped in each peak area, Table XI, a rather subjective parameter, particularly at low analyte concentrations.

Tables VIII, IX and X demonstrate that the accuracy of the SPD is generally similar to the accuracy of the PMT. In the case of some spectral lines the SPD results were less accurate than the PMT results. This is caused by the lower resolving power of the SPD causing it to be more subject to specific spectral interference. The adverse effects of spectral line interferences resulted in relatively large concentration errors for the low analyte concentration sample. The effect of these spectral interferences is twofold. First, there is the analyte signal intensity error caused by coincident spectral line interferences from unresolved matrix lines. Second, there is the background interpolation

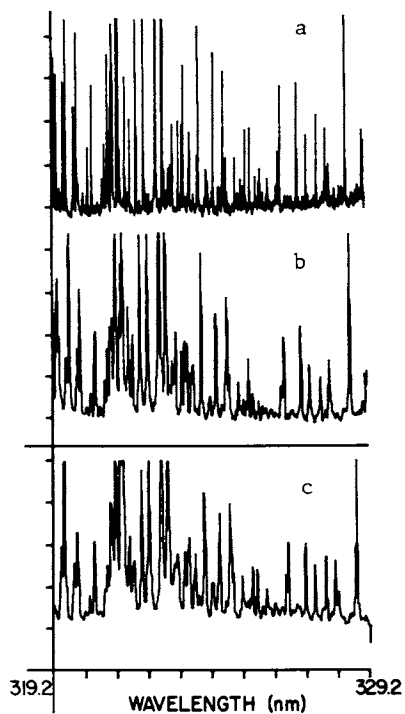


Figure 18. Emission spectra, in the 319.2–329.3-nm spectral region, obtained from a GSC-484 glass reference sample. Key: a, PMT (20- μm slit width, scan rate, 0.125 nm/s); b, SPD (16 s of signal on-target integration); and c, SIT (16 s of signal in-memory integration).

Table XI. An example of the effect of line peak width, i.e., the number of diodes summed for peak area calculation, on the measurement accuracy.

Element, ^a (Wavelength, nm)	Percent Error 5-diode Summation	Percent Error 3-diode Summation
Cu (324.7)	1.6	-0.4
Cu (327.3)	7.0	-5.0
Ti (323.5)	9.5	5.0
Ti (323.7)	11.5	6.0
Y (324.2)	4.0	2.0

a. These measurements are for the USGS No. GSE-382 reference sample obtained with spectrometer 1, Table I.

error caused by partially unresolved spectral interferences affecting the intensity value of the wing diodes and therefore also the value of the subtractable background. The significantly improved accuracies obtained for the higher concentration glass sample, GSE-382, were not merely a result of improvement in S/N, but were rather mostly due to the diminishing effect of matrix spectral interferences. Results of poorer accuracy were obtained with the SPD when a lower dispersion spectrometer 1, Table I, was used for the analysis of the glass samples. The lower dispersion increased the incidence of spectral line overlap.

Trace Elements in Microliter Samples. The transformation of microliter volumes of sample into an aerosol followed by injection of the latter into flame and plasma vaporization-excitation cells has been employed for atomic emission, absorption and fluorescence determination of trace constituents in discrete volumes of solution. Before the advent of array detectors, these approaches have been limited to one-element-at-a-time determinations. Busch, et.al. (6) have utilized SIT vidicons for simultaneous determination of K, Na and Ca in 100 uL serum samples by flame atomic emission. Biologic fluids contain high matrix levels which diminish the accuracy of ICP-AES determinations unless correction for background shifts is performed. Unfortunately, often only small volumes of such samples are available, thus precluding wavelength scanning necessary for background correction with conventional slew scanning PMT spectrometers.

We have used ICP-AES with a SIT detector for the simultaneous multielement determination of trace elements in 100 uL volumes of dilute whole blood, blood serum and urine samples. The analyte solutions were ultrasonically nebulized at a rate of 1.2 ml/min. to achieve high nebulization efficiency without

excessively broadening the emission pulse duration. Alternate sample and reference solution segments delivered to the ultrasonic nebulizer were isolated from each other by air bubbles(53). A 100 uL disposable pipet was inserted into the end of the uptake tube of the ultrasonic nebulization system. Each discrete sample segment was isolated by air bubbles and was introduced into the pipet by switching on the peristaltic pump. The peristaltic pump and the data acquisition program were simultaneously initiated. The program waits for a prespecified period of time to allow a desolvated sample segment to reach the plasma before beginning to integrate the emission pulse. Correct wait and integrate times were derived from emission vs. time plots obtained with a PMT detector, as exemplified in Figure 19. Wait times were selected to ensure that integration begins just prior to the emergence of the emission pulse. Most emission pulses were integrated for 15 seconds. Blood serum and urine samples were introduced as solutions with 1% HCl. Whole blood samples were diluted to 10% to improve the nebulization performance.

Sample memory was greatly reduced through quick flushing of the sample delivery system and the transducer tip by a following 1% HCl reference blank segment. Lowering the sample duty cycle in this fashion reduced accumulation of sample droplets on the nebulizer surfaces, thereby reducing cleanout time. A 15 second background signal integration performed 50 seconds after a sample pulse emergence showed a very small sample memory effect, i.e., less than 0.02% of the original sample signal remained. Whole blood solutions if continuously ultrasonically nebulized and desolvated deposited a carbon residue on the injector tip of the plasma torch. This residue accumulated rapidly and clogged the tip after a few minutes of whole blood solution nebulization. Again this problem was practically eliminated by nebulizing larger blank segments following each whole blood sample.

Detection limits for ultrasonically nebulized 100 uL samples are compared, in Table XII, to the best detection limits reported in the literature for ICP-AES with ultrasonic nebulization, and to detection limits for graphite furnace atomic absorption. Relative detection limits for SIT detection of 100 microliter samples are a factor of 4 to 5 worse than SIT detection limits obtained with a continuous ultrasonic nebulization, Table IV. Not much better detection limits are expected with the SPD since integration times are limited to 16 seconds. (See Table IV). The brief emission pulse would not permit longer integration times to improve the detection limits. These relative detection limits are 2-3 orders of magnitude worse than those reported for graphite furnace AA. Worse yet biologic fluids are less efficiently nebulized than dilute acidic solutions and therefore produce poorer detection limits. Indeed, unlike graphite furnace AA, dilution of whole blood is definitely necessary for successful nebulization. Thus, detection limits are raised by a factor of 2.2 times in 50% urine, by 3.5 times in 50% serum, and by 14

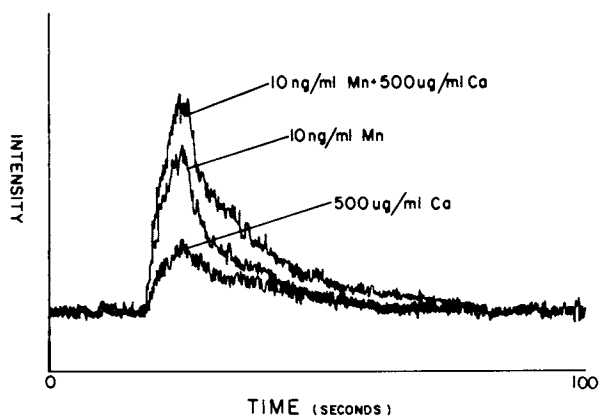


Figure 19. Emission pulse from $100 \mu\text{L}$, $1.0 \mu\text{g/mL Mn}$; $10 \text{ ng/mL Mn} + 500 \mu\text{g/mL Ca}$; and $500 \mu\text{g/mL Ca}$, observed with a PMT at 257.6 nm .

times in 10% blood compared to values reported for dilute acid solutions. The normal concentration of many trace elements in biological fluids is below the limit of quantitative determination of pulsed (100 uL) ICP-AES. Nevertheless, clinically significant elements such as Na, K, Mg, Ca, P, Fe, Cu and Zn can still be determined by this technique. Significantly improved detection limits, although at the expense of reduced spectral resolution, could be expected with the ISPD detector.

Table XII. Detection limits obtained with an SIT from 100 uL samples compared to continuous nebulization and compared to AAS detection limits.

Element	Wave- Length nm	Detection Limits ng/ml			AAS graphite furnace
		ICP-AES			
		continuous sonic nebulization	ultra- SIT	pulsed nebulization	
Al	308.2	0.2	-----	4	0.02
As	193.7	2	40	200	0.2
Be	313.0	0.003	0.02	0.08	0.03
Cd	226.5	0.07	-----	1.2	0.001
Co	228.6	0.2	-----	1.0	0.4
Cr	205.5	0.08	3	3	0.003
Cu	324.7	0.06	0.4	1	0.01
Fe	261.1	0.09	-----	4	0.05
Mn	257.6	0.01	0.07	0.3	0.002
Mo	386.3	0.3	-----	25	0.05
Ni	351.5	0.2	-----	6	0.04
Pb	283.3	1	14	70	0.02
Se	196.0	1	65	350	0.1
V	311.0	0.06	0.3	2	0.02
Zn	213.8	0.1	0.2	1	0.001

Figure 19 is also an example of the background shift errors encountered with ICP-AES. The three emission (100 uL) pulses were measured with a PMT at 257.6 nm. Without the benefit of background correction the calcium concomitant caused an error of 52% in the determination of the Mn in the Ca interfered solution. With the SIT, where an entire spectral window was simultaneously recorded for the Mn + Ca solutions, background subtraction was possible and resulted in a mere 3% error in the Mn measurement. This error is within the 1-3% sampling precision obtained with 100 uL samples.

Copper and zinc were determined in 100 uL samples of whole blood, horse blood serum and human urine to demonstrate the applicability of this technique to real samples. Sample preparation was kept to a minimum. Straightforward dilution was the

only preparatory step. It was, however, found advantageous to incorporate an internal reference, Y, in the diluted solution in order to monitor the nebulization efficiency of each sample. Ultrasonic nebulization of dilute blood solutions was greatly improved by increasing the power input to the ultrasonic transducer from 100 watts to 150 watts. The nebulization efficiency was monitored by observing the net analyte intensities. The increase in power improved the nebulization efficiency of 1% HNO₃ solution by 25% that of 50% blood serum, by 50% and that of 10% whole blood by 500%. Determination of copper and zinc in whole blood samples made from a reference curve and by the method of standard additions are shown in Table XIII. The zinc 213.8 nm line was superimposed as a shoulder on the intense P 213.6 nm line and baseline interpolation was necessary to compensate for P spectral interference. Similarly all useful Cu lines were spectrally overlapped by iron lines. The corrections for the iron interferences were performed through line ratio comparisons with other non-interfered iron lines, simultaneously measured. Without these correction procedures, concentration errors for Cu and Zn would have exceeded 100%.

It seems, therefore, that pulsed ICP-AES (100 uL) could be successfully employed in the determination of clinically significant elements such as Na, K, Mg, Ca, P, Fe, Cu and Zn in whole blood, blood serum, urine and spinal fluids. The array detectors have a definite advantage in compensating for background and specific spectral interferences.

With the detectors used in this study, all of the clinically significant elements could not have been observed simultaneously in a single spectral window. With the SPD detector Mg, P, Fe, Cu and Zn are determinable in a single simultaneous spectral window, 202-225 nm. The remaining three may be determined in a 40 nm window as shown by Busch (K 808.8 nm; Na 818.3 nm, second order; Ca 845.4 nm, second order), since a lower spectral resolution is required in this region.

Conclusion

This study suggests that determinations with accuracy similar to PMT systems can be achieved with SPD detectors if polychromators with higher dispersion and high quality gratings are used. However, for such systems to be practical, the spectral window (reduced by the increased dispersion) must also be increased. A new 4096 element diode array is now available from Reticon (Model RL-4096/20 with a 15 um centers and a 508 um diode height). The aspect ratio, however, is only 34:1 compared to the 100:1 ratio of the RL-10245 detector. Consequently, photon collection is also less efficient, theoretically resulting in worse detection limits. This loss in photon collection can be greatly alleviated by 'concentrating' the spectral signal with a cylindrical lens, directly attached to the array (54).

The simultaneous spectral window of this new 4096 element detector, with a PMT-like spectral resolution will be extended to at least 32 nm. Because analyte spectral lines are randomly distributed across the entire UV-visible spectrum, the increase in the probability of their inclusion in each expanded spectral window is more than just four fold. Most probably, for the majority of analytical applications only 3-5 such expanded spectral windows will suffice to include all analyte lines sought.

A different solution to this spectral window vs. spectral resolution dilemma maintains the 1024 diode array but resorts to the use of a multiple entrance slit SPD/plychromator scheme (8) that should be able to produce a rapid succession of consecutively interchanging and selectively chosen spectral windows. With this technique a randomly accessed spectral window may be observed without the requirement of a high tolerance mechanical scanning device.

Finally, the effects of spectral interferences could be at least partially alleviated by more effectively exploiting the multichannel nature of the SPD. Spectral interferences could be easily recognized via line intensity ratios and alternative, non-interfered analyte lines could be chosen or spectral stripping procedures may be used, as previously discussed.

Acknowledgments

We would like to thank Dr. Velmer Fassel, in whose laboratory this work was performed, for his hospitality and highly appreciated assistance in reviewing this manuscript.

Literature Cited

1. Aldous, K.M.; Mitchell, D.G.; Jackson, K.W. Anal. Chem. 1975, 47, 1035.
2. Betty, K.R.; Horlick, G. Appl. Spectrosc. 1978, 32, 31.
3. Boumans, P.W.J.M.; Brouwer, G. Spectrochimica Acta 1972, 27B, 247.
4. Boumans, P.W.J.M.; Rumphorst, R.E.; Williamson, L.; DeBoer, F.J. Spectrochim Acta 1973, 28B, 277.
5. Busch, K.W.; Howell, N.G.; Morrison, G.H. Anal. Chem. 1974, 46, 575.
6. Busch, K.W.; Howell, N.G.; Morrison, G.H. Anal. Chem. 1974, 46, 1231.
7. Busch, K.W.; Howell, N.G.; Morrison, G.H. Anal. Chem. 1974, 46, 2047.
8. Busch, K.W.; Malloy, B.; Talmi, Y. Anal. Chem. 1979, 51, 670.
9. Chester, T.L.; Haraguchi, H.; Knapp, D.O.; Messman, J.D.; Winefordner, J.D. Applied Spectroscopy 1976, 30, 410.
10. Chuang, F.S.; Natusch, D.F.S.; O'Keefe, K.R. Anal. Chem. 1978, 50, 525.
11. Coddling, E.G.; Horlick, G. Applied Spectroscopy 1973, 27, 366.

12. Codding, E.G.; Horlick, G. Spectrosc. Letters 1974, 7, 33.
13. Cook, T.; Milano, M.; Pardue, H.L. Clinical Chem. 1974, 20, 1422.
14. Cook, T.E.; Santini, R.E.; Pardue, H.L. Anal. Chem. 1977, 49, 871.
15. Cooney, R.P.; Boutilier, G.D.; Winefordner, J.D. Anal. Chem. 1977, 49, 1048.
16. Felkel, Jr., H.L.; Pardue, H.L. Anal. Chem. 1977, 49, 1112.
17. Felkel, Jr., H.L.; Pardue, H.L. Anal. Chem. 1978, 50, 603.
18. Franklin, M.; Barber, C.; Koirtjohann, S.R. Spectrochimica Acta 1976, 31B, 589.
19. Friche, F.L.; Rose, O.; Caruso, J.A. Anal. Chem. 1975, 47, 2018.
20. Furuta, N.; McLeod, C.W.; Haraguchi, H.; Fuwa, F. Bulletin of the Chemical Society of Japan 1979, 52, 2913.
21. Furuta, N.; McLeod, C.W.; Haraguchi, H.; Fuwa, F. Applied Spectroscopy 1980, 34, 211.
22. Ganjei, J.D.; Howell, N.G.; Rogh, J.R.; Morrison, G.H. Anal. Chem. 1976, 48, 505.
23. Gustausson, A.; Ingman, F. Spectrochimica Acta 1978, 34B, 31.
24. Horlick, G. Applied Spectroscopy 1976, 30, 113.
25. Horlick, G.; Codding, E.G. Anal. Chem. 1973, 45, 1490.
26. Horlick, G.; Codding, E.G. Anal. Chem. 1974, 46, 133.
27. Horlick, G.; Codding, E.G.; Leung, S.T. Applied Spectroscopy 1975, 29, 48.
28. Horlick, G.; Codding, E.G. Applied Spectroscopy 1975, 29, 167.
29. Howell, N.G.; Ganjei, J.D.; Morrison, G.H. Anal. Chem. 1976, 48, 319.
30. Howell, N.G.; Morrison, G.H. Anal. Chem. 1977, 49, 106.
31. Jackson, K.W.; Aldous, K.M.; Mitchel, D.G. Spectrosc. Letters 1973, 6, 315.
32. Jackson, K.W.; Aldous, K.M.; Mitchell, D.G. Applied Spectroscopy 1974, 28, 569.
33. Knapp, D.O.; Omenetto, N.; Hart, L.P.; Plankey, F.W.; Winefordner, J.D. Analytica Chimica Acta 1974, 69, 455.
34. Milano, M.J.; Pardue, H.L.; Cook, T.E.; Santini, R.E.; Margerum, D.W.; Raycheba, J.M.T. Anal. Chem. 1974, 46, 374.
35. Mitchell, D.G.; Jackson, K.W.; Aldous, K.M. Anal. Chem. 1973, 45, 1215A.
36. Talmi, Y., Ed.; "Multichannel Image Detectors", ACS MONOGRAPH SERIES No. 102, ACS: Washington, D.C, 1979.
37. VanDerPiepen, H.; Claase, C; DeVilliers, D.B. Spectrochimica Acta 1976, 31B, 389.
38. Wood, D.L.; Dargis, A.B.; Nash, D.L. Applied Spectroscopy 1975, 29, 310.
39. Hughes, S.K.; Brown, R.M.; Fry, R.C. Applied Spectroscopy 1981, 35, 396.
40. Butler, C.C.; Kniseley, R.N.; Fassel, V.A.; Anal. Chem. 1975, 47, 825.
41. Talmi, Y. Applied Spectroscopy 1982, 36, 1.
42. Floyd, M.A.; Fassel, V.A.; Katzenberger, J.M.; D'Silva, A.P. Anal. Chem. 1980, 52, 431-438.
43. Fassel, V.A.; Kniseley, R.N. Anal. Chem. 1974, 46, 1110A-1155A.

44. Olson, K.W.; Haas, W.J.; Fassel, V.A. Anal. Chem 1977, 49, 632.
45. Talmi, Y.; Simpson, R.W. Applied Optics 1980, 19, 1401.
46. Larson, G.F.; Fassel, V.A.; Winge, R.K.; Kniseley, R.N. Applied Spectroscopy 1976, 30, 384.
47. Larson, G.F.; Fassel, V.A. accepted for publication in Applied Spectroscopy.
48. Skogerboe, R.K.; Lamothe, P.J.; Bastiaans, G.J.; Freeland, S.J.; Coleman, G.N. Applied Spectroscopy 1976, 30, 495.
49. Koirtiyohann, S.R.; Glass, E.D.; Yates, D.A.; Hinterberger, E.J.; Liche, F.E. Anal. Chem. 1977, 49, 1121.
50. Haas, W.J.; Winge, R.K.; Fassel, V.A.; Kniseley, R.N. Proc. 29th Pittsburgh Conference on Analytical Chemistry and Applied Spectroscopy 1978.
51. Stermberg, J.C.; Stillo, H.S.; Schwendeman, R.H. Anal. Chem. 1960, 32, 84.
52. Talmi, Y.; Baker, D.C.; Jadamec, J.R.; Saner, W.A. Anal. Chem. 1978, 50, 937A.
53. Kniseley, R.N.; Fassel, V.A.; Butler, C.C. Clinical Chemistry 1973, 19, 801.
54. Talmi, Y. unpublished data 1978.

RECEIVED September 23, 1983

Multielement Emission Spectrometry Using a Charge-Injection Device Detector

G. R. SIMS and M. B. DENTON

Department of Chemistry, University of Arizona, Tucson, AZ 85721

A Charge Injection Device (CID) camera system has been designed and constructed for use as a detector for atomic emission spectrometry. Operational procedures to reduce noise, increase dynamic range, and reduce pixel cross talk are discussed. Preliminary detection limits which often meet or exceed comparable photomultiplier tube detector capabilities are presented.

Inductively coupled plasma (ICP) and direct current plasma (DCP) atomic emission spectrometry have become widely accepted techniques for simultaneous multielemental analysis. These techniques are highly sensitive and have a very wide dynamic range. A wealth of information is contained in the emission signal, including several atomic and ionic emission lines for each element in the sample. In even the simplest sample, there are thousands of observable spectral lines. To make full use of this enormous spectral information the analyst requires an instrument capable of observing a very wide spectral range simultaneously, preferably from 190 nm to 800 nm with a resolution of approximately 0.01 nm.

State-of-the-art emission spectrometers presently use a bank of photomultiplier tubes for detectors. One photomultiplier tube must be used for each spectral line monitored. The number of photomultiplier tubes used in the spectrometer is restricted by physical restraints and cost. Modern instruments commonly employ 10 to 20 photomultiplier tubes (although more can be used with many instruments). Thus, only a very small fragment of the spectrum is simultaneously examined. A further complication arises if the severity of the background continuum or spectral interferences needs to be evaluated. Either a photomultiplier tube and slit assembly must be dedicated to measuring background or some type of refractor plate mechanism employed to locally scan the region surrounding the analytical line.

0097-6156/83/0236-0117\$06.00/0
© 1983 American Chemical Society

A much more desirable detector system is an electronic analog to photographic film, i.e. a television camera. However, any such camera needs to be very specialized to meet the unique demands of emission spectrometry. Traditional television cameras (orthocons, plumbacons, vidicons, etc.) have been investigated with respect to their potential as spectroscopic detectors but they suffer from one or more of a variety of problems which render them impractical for general use (1,2,3).

In recent years, a new class of television camera detector based on integrated circuit technology has become available. These include the charge injection device (CID) (4,5), the charge coupled device (CCD), and the photodiode array. Of these new detectors, the CID has many features which qualify it as a unique detector for emission spectrometry. These include:

1. a fair to excellent quantum yield over the spectral range of interest;
2. good sensitivity and a high signal-to-noise ratio;
3. random or pseudo-random pixel addressing;
4. selective destructive readout mode;
5. non-destructive readout mode;
6. a very low level of pixel cross talk;
7. a reasonable dynamic range with the ability to increase the effective upper dynamic range bound by mixing readout modes; and
8. the ability to integrate for extremely long periods of time when adequately cooled.

Recently, a camera system which uses a CID device designed specifically as a detector for emission spectrometry has been constructed and undergone preliminary evaluation. The device used in this study is the General Electric Co. CID-11 (Figure 1) which has 244 rows and 248 columns resulting in 60,512 pixels. The horizontal and vertical shift registers allow rapid "slew scan" access to any pixel on the device (pseudo-random addressing). Charge in pixels may be read out in a destructive or non-destructive mode. (See "Operational Consideration and Characteristics when Employing Charge Injection and Charge Coupled Devices in Practical Chemical Analysis" in this symposia proceedings for detailed information on charge injection device readout modes).

The camera system is comprised of a high speed microprocessor based controller, a remote camera head, and a host computer (Figure 2). The remote camera head houses the CID sensor, clock drivers, all analog circuits, and analog to digital converters. The analog circuits consist of a charge amplifier followed by a correlated double sample integrator. The video signal is digitized to 12 bits at a rate of 1 μ Sec/bit.

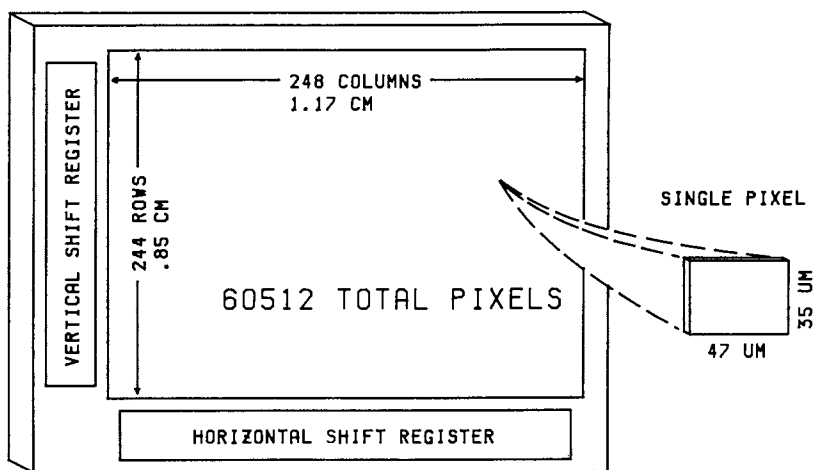


Figure 1. Dimensions and layout of the CID-11 sensor.

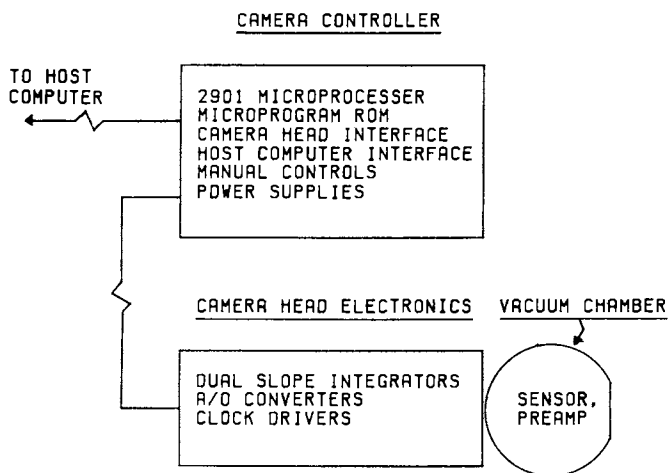


Figure 2. The CID camera system electronics.

The CID sensor and charge amplifier are operated in a vacuum where they are cooled via a copper cold finger to 77°K with liquid nitrogen. The cooling practically eliminates all thermally generated charge making integration times of many hours possible.

The camera controller is based on a high speed 2901 bit slice microprocessor with microcode and programs residing in read only memory. Readout rate is 30,000 pixels per second for adjacent pixels with 90 microseconds maximum addressing latency for pseudo-random addressing. The host microcomputer provides the controller with an X and Y coordinate and the number of pixels to be read on each axis (ΔX and ΔY). This establishes the position and number of pixels to be read. The host computer then informs the controller of the type of readout to be performed (non-destructive, destructive, or massive injection). The controller generates all timing to address the pixels, perform the readout, digitize the information, and transmit the digitized data to the host computer.

The host computer is a Digital Equipment Corp. PDP 11/23 microcomputer which controls the experiment dynamically by transmitting a string of commands to the camera controller, receiving digital data from the controller, then making decisions based on that data on how to proceed with the experiment.

Two monitors are used to visually examine the spectrum in real time as it is collected and a graphics terminal is used to examine the spectrum once it has been subjected to image processing. A digital plotter provides hard copies of processed spectra.

The spectrometer used is a modified Spectrametrics Spectraspan III echelle grating spectrometer with a quartz prism cross disperser. An echelle spectrometer was chosen because of its two dimensional format display. This format allows efficient simultaneous examination of a much wider spectral range than with a linear dispersion spectrometer when a two dimensional television camera type detector is used.

The standard 0.75 M Spectraspan III has an approximately 6 cm x 7.5 cm display. Since the CID used is only 1.1 x 0.85 cm, only a very small portion of this display could be observed at any one time. However, this problem has been recently reduced by substituting a 15 cm focal length, f/1.4 Schmidt corrected Cassegrain telescope (Nye Optical, Spring Valley, CA) for the camera mirror (Figure 3). This reduces the display dimensions five fold. The focal plane remains flat and a minimum resolution of 0.1 nm is achieved. With this optical system the entire 200 to 800 nm region cannot be viewed simultaneously. Further image reduction is possible, but resolution will be compromised

since the number of pixels on the CID sensor is the limiting factor in resolution.

The standard Spectrametrics Spectrajet III D.C. plasma and nebulizer assembly was used as the spectral source. No alterations in the source or nebulizer were made and it was operated according to the manufacturer's recommendations.

The quantum yield of the CID-11 has been measured (6,7) in the visible and near I.R. The maximum quantum yield is $\approx 27\%$ at 580 nm, it falls to $\approx 20\%$ at 800 nm and to $\approx 5\%$ at 1000 nm. At 400 nm the quantum yield is $\approx 3\%$. With this particular device no measurements have been made at shorter wavelengths, however, studies by Lewis and Denton (8) indicate that a similar CID does respond to 190 nm.

At low light levels the major source of noise in the CID system is a combination of Johnson noise and shot noise from the first stage of the charge amplifier. The system noise and gain of our CID camera were evaluated using the mean-variance method (10). The system noise for a single readout is 800 electrons (rms) and the gain is set for 1350 electrons per A/D count.

Since the CID is a surface channel MOS device, there exists a region in the silicon, silicon oxide interface where charge becomes trapped and immobile. These charge traps must be filled with a "bias charge" (or "fat zero") before response to light is linear (7). Based on the amplifier gain and CID linearity measurements we estimate the bias charge necessary for this CID system is 715,000 electrons. The full well capacity is approximately 3,200,000 electrons leaving a usable range of 2,500,000 electrons. These figures deviate modestly from those reported earlier (7) and probably reflect different methods of measuring system gain.

Figure 4 is a plot demonstrating detector response linearity. The non-linear "foot" of the curve is due to charge filling the surface state traps and the non-linear tail is due to charge leaking out of the pixels (blooming). In normal operation, after the CID is injected to clear all charge from the pixels (charge is injected from the pixels into the silicon substrate) a light emitting diode is flashed to introduce sufficient bias charge to avoid operating in the non-linear foot of the curve. Within the linear response region the deviation from linearity is no greater than 0.05% as measured from the second derivative of a linearity plot (10).

The CID-11 is a multiplexed device having two separate video outputs. The multiplexer switching signal couples into the video outputs in such a way as to introduce a fixed pattern signal (also referred to as "fixed pattern noise") which is easily corrected (9). Fixed pattern signal subtraction is accomplished as follows:

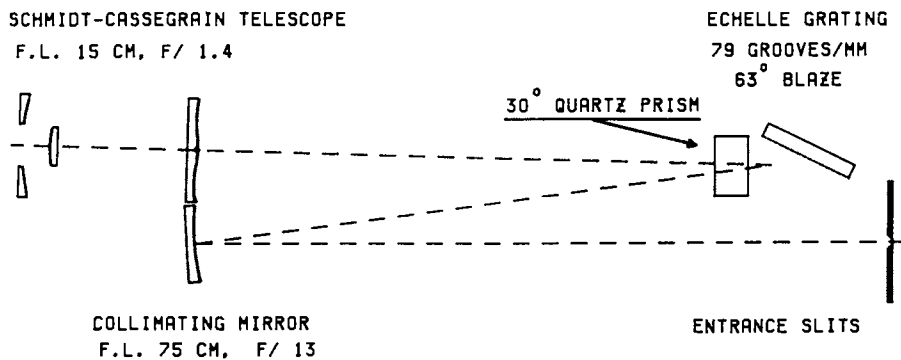


Figure 3. Optical diagram of the modified echelle spectrometer.

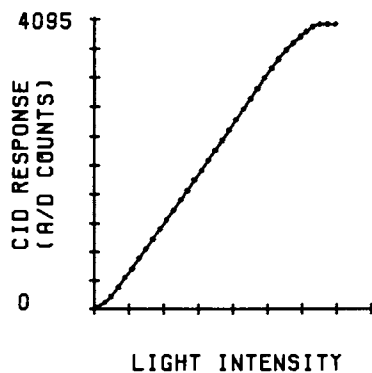


Figure 4. Plot of response linearity for the CID-11 camera system.

1. all pixels are cleared of charge by injection;
2. the array is flashed with a small amount of light to bring it into the linear response region (bias flash);
3. the array is read out non-destructively and the data (fixed pattern signal plus bias flash) is stored in computer memory;
4. a shutter is opened to make an exposure;
5. the shutter is closed and the array is read out. The data (spectrum plus fixed pattern response plus bias flash) is stored in computer memory;
6. the computer subtracts fixed pattern signal and bias flash leaving only the corrected spectrum.

Since a bias flash is made, measured, and subtracted for every exposure, the flash does not need to be especially uniform or reproducible. Figure 5A is a plot of a spectrum (sodium D lines) before the fixed pattern signal and bias flash are subtracted. Figure 5B shows the same spectrum after subtraction. There is no evidence of fixed pattern signal remaining after the subtraction.

When the bias flash is made, not every pixel will receive the same number of photons. The variation arises from:

1. non-uniformity of the bias flash across the array and
 2. photon shot noise associated with the bias flash.
- These variations are measured twice, in a non-destructive manner, once during the initial fixed pattern signal/bias flash readout and once during the final readout. When these two measurements are subtracted, these variations cancel, thus photon shot noise associated with the bias flash does not appear in the corrected spectrum. Of course, readout noise and spectrum shot noise are still present.

One of the benefits of the unique non-destructive readout capabilities of the CID is the ability to reduce the effect of preamplifier noise. If multiple readouts are made and averaged, the effective readout noise will diminish with the square root of the number of re-reads. By making and averaging 25 re-reads, we can reduce the effective readout noise $25^{1/2}$ or five fold. Figure 6A is a plot of a spectrum (three argon lines in the near I.R.) taken with only one readout. Figure 6B shows the same spectrum except that the signal was read non-destructively sixteen times and the readouts were averaged. It must be emphasized that this is multiple re-reads of the same charge, not multiple exposures or longer integration. The spectrometer shutter remains closed throughout the sixteen re-reads.

Photon shot noise from the spectrum being measured quickly becomes the predominant source of noise when effective readout noise is lowered through averaging non-

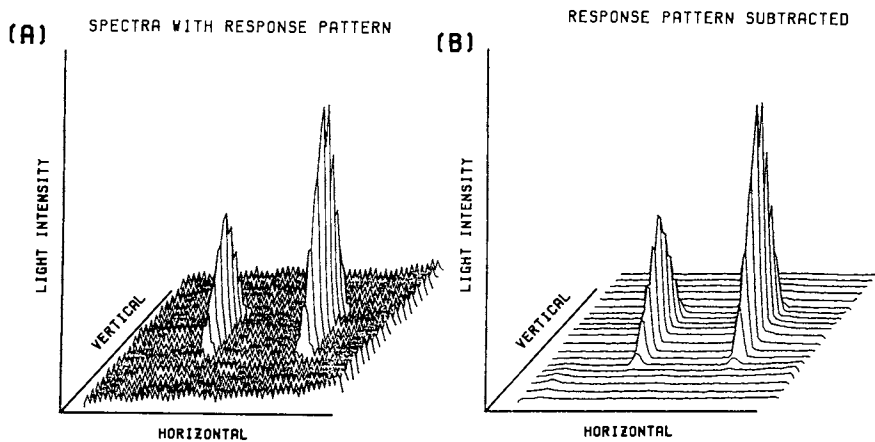


Figure 5. Plot of a spectrum with fixed pattern signal (left) and the fixed pattern signal subtracted from the spectrum (right).

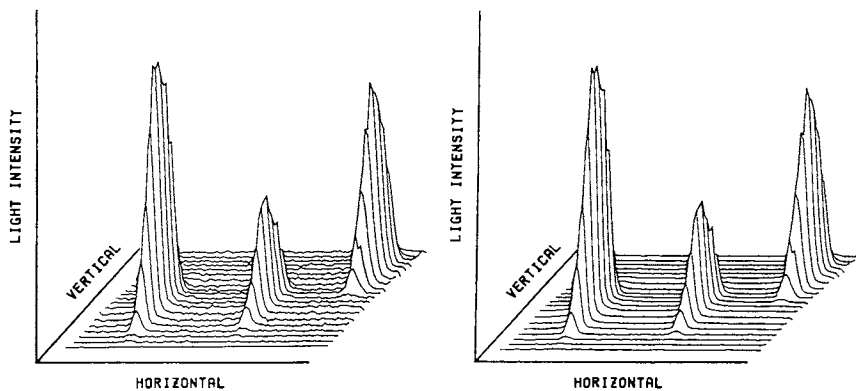


Figure 6. Plot of readout noise on a spectrum taken with one readout (left), and the effective readout noise reduced by averaging multiple nondestructive rereads (right).

destructive readouts. Since the effective readout noise can be reduced to 160 electrons, shot noise arising from exposure to the spectrum becomes equivalent to effective readout noise when the spectrum reaches $160^2 = 25600$ electrons or 19 A/D counts.

Figures 7A, 7B, 7C, and 7D demonstrate the magnitude of blooming and how it can be eliminated through "selective knockdown." Selective knockdown is a term used when a destructive readout is performed on a selected group of pixels. In this mode of operation, no data is actually collected as the purpose of the readout is simply to remove charge from the pixels before saturation and/or blooming can occur. Figure 7A is a plot of a spectrum (same argon lines as discussed before) at half saturation. No crosstalk between pixels is evident. Figure 7B shows the same spectral lines, but now the most intense line has just passed saturation. Notice the blooming along the vertical axis; this is the direction of the column electrodes on the CID (4,5). Figure 7C shows the same spectral lines after approximately two-fold overexposure. The two intense lines are well past saturation and blooming is apparent. Blooming is not observed to increase past this point with additional exposure. Figure 7D shows a spectrum which was also two-fold overexposed, except here the two intense lines were prevented from blooming by performing several selective knockdowns on pixels associated with the strong spectral lines each time they approach saturation. At the same time, the weak line in the middle was allowed to integrate.

Mixing destructive and nondestructive readouts is a very useful tool for increasing the dynamic range of the CID camera system. However, dynamic range can be extended to virtually any desired level by using short integration times for intense spectral lines and long integration times (several minutes is not uncommon) for extremely weak spectral lines.

While waiting for weak lines to integrate, intense lines must be prevented from blooming with the selective knockdown procedure.

The unique capability of mixing destructive and non-destructive readout modes is the key to using different integration times for different spectral lines. The host computer can inquire if a particular line has integrated long enough to give a good signal-to-noise ratio, and if it has, multiple non-destructive readouts are made on the pixels associated with that spectral line. Otherwise, the integration is continued. Once a spectral line has been read out and its integration time is recorded, the line is added to a list of lines which should periodically undergo selective knockdown.

The D.C. plasma emits continuum and line radiation

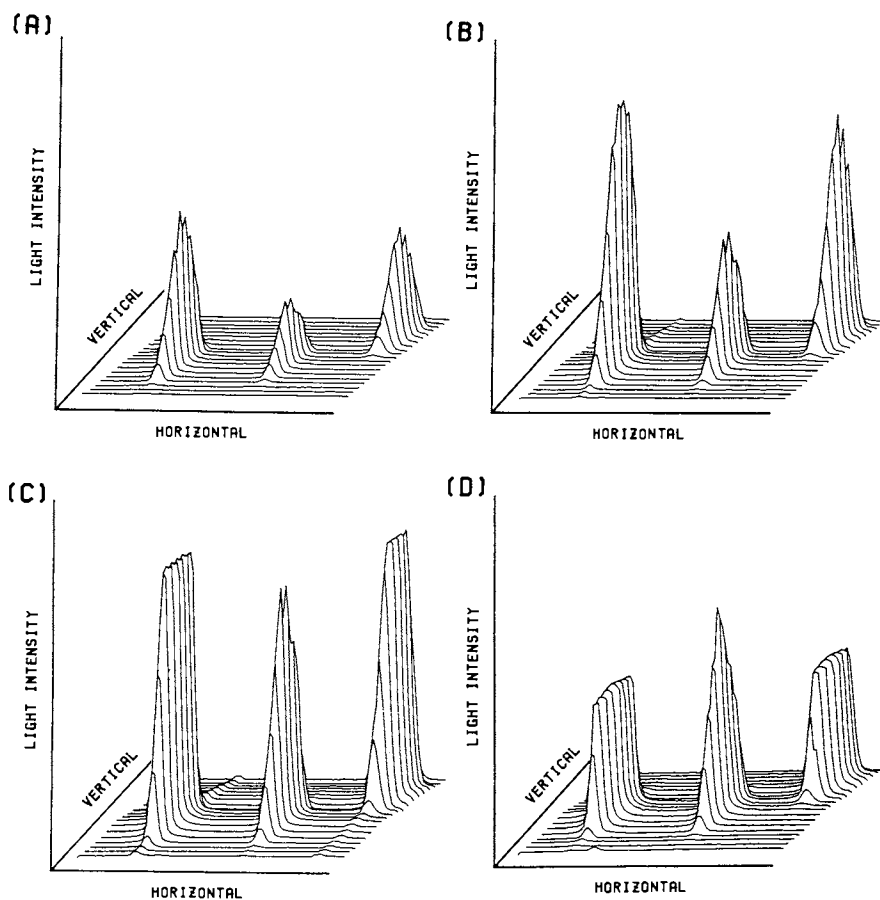


Figure 7. Plot of a spectrum with pixels at half-charge saturation (A), blooming from pixels at full-charge saturation (B), blooming from pixels at $2\times$ full-charge saturation (C), and blooming eliminated through the use of selective knockdown (D).

which can severely interfere with an analysis, but a spectrum can be easily corrected with background subtraction. The spectrum in Figure 8A was taken by nebulizing an iron solution and integrating for approximately 1 minute. The prominent line is an iron line near 400 nm. Most of the remaining information is background from the plasma alone. Background was measured simply by nebulizing a blank solution of deionized water and integrating for the same length of time as the spectrum in Figure 8A. The background is plotted in Figure 8B. The spectrum was subtracted from the background and the result is plotted in Figure 8C. Notice that once the background is subtracted, several spectral lines from the analytical solution became apparent.

Figure 9 is a typical working curve obtained with the CID system. The concentration range is from 0.1 to 100 ppm Mn. To set optimal signal-to-noise ratios for all concentrations, the integration times were dynamically varied. Integration times ranged from ≈ 15 seconds for the 100 ppm solution to ≈ 100 seconds for the 0.1 ppm solution. Table 1 is a list of detection limits determined thus far along with detection limits obtained by Spectrametrics (11), with their standard photomultiplier tube based system. The detection limits were obtained under similar conditions, i.e., the same nebulizer, identical slit sizes, nebulizer and plasma gas flow rates, etc. The optical systems of the spectrometers were the same since these detection limits were performed before the optical system of our spectrometer was altered. The only significant difference is that the photomultiplier tube based detection limits were achieved by averaging nine integrations of ten seconds each. The CID system detection limits were achieved with a single integration of 300 seconds. In both sets of detection limits, a signal equal to three times the standard deviation of the background noise was used as the criteria for detection limit. Under these conditions, detection limits with the CID system are much better than the PMT based system in the near I.R. and longer wavelength visible regions of the spectrum. Detection limits become comparable in the blue region, and then become worse in the ultraviolet. For the worst case measured, the CID had a detection limit 13 fold poorer than the PMT system (Zn at 202 nm). Because of the recent reduction in the spectrometer focal plane size we can now examine emission lines from several elements simultaneously. Figure 10 is a spectrum taken after the focal plane reduction, demonstrating the enormous amount of spectral information within a small wavelength interval. Because of limitations in computer memory, only a 248 x 40 (9920 pixel) portion of the spectrum is plotted.

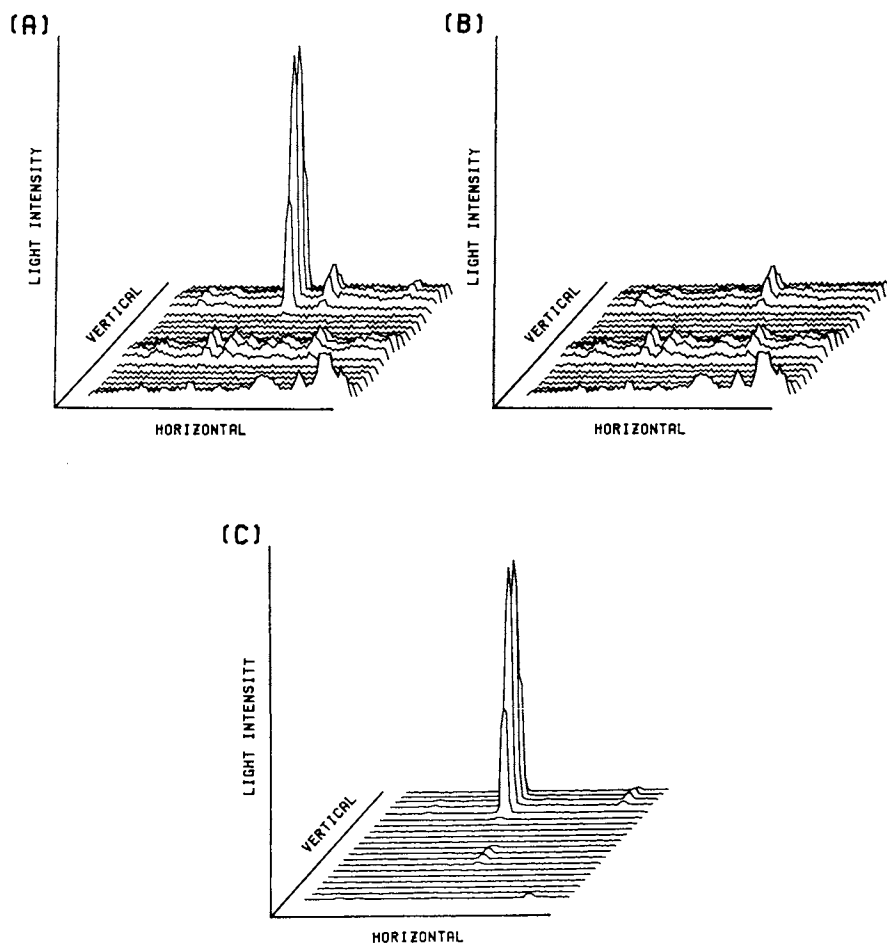


Figure 8. Plot of a spectrum showing analytical lines with background from the plasma (A), plot of the background from the plasma (B), and background subtracted from the analytical signal (C).

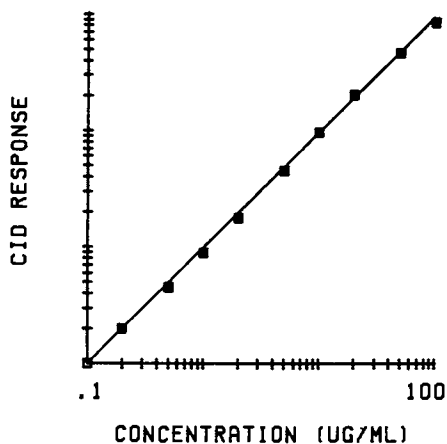


Figure 9. Working curve of manganese taken with the CID camera system.

TABLE I. Detection Limits

<u>Element</u>	<u>Wavelength (nM)</u>	<u>CID Preliminary Detection Limit (ppm)</u>	<u>Spectraspan III Literature Detection Limit (ppm)</u>
K	766.49	<<0.0001	0.02
Cr	520.45	0.025	0.100
Ca	445.48	0.010	0.09
Mg	279.55	0.005	0.0002
Mn	257.61	0.010	0.003
Zn	202.55	0.075	0.006
Cs	852.12	1.0	--
Cs	455.35	--	10.

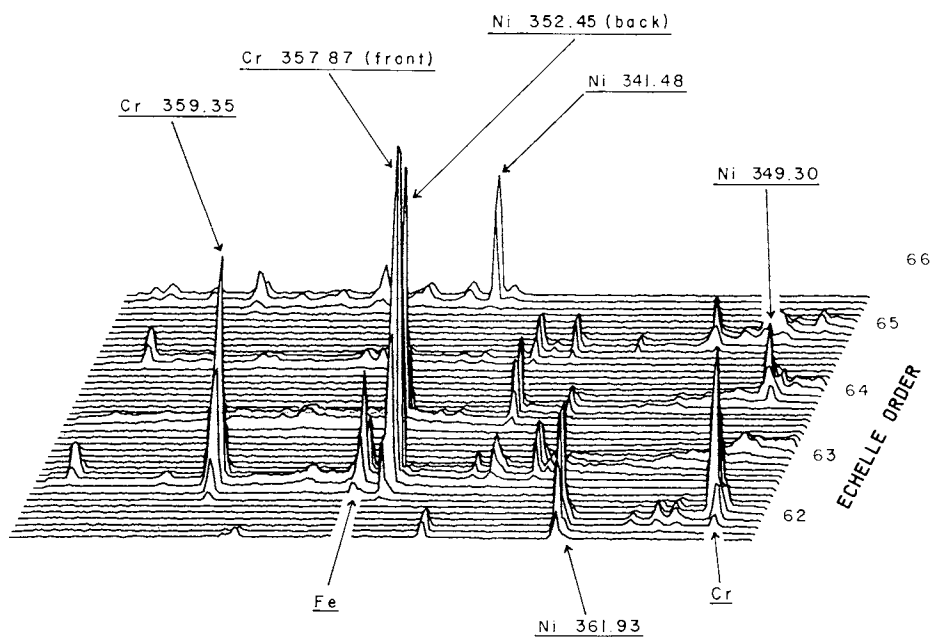


Figure 10. Pixel readout (248×40) covering parts of five echelle orders.

Conclusions

These initial investigations of the charge injection device have indicated that the device promises to be a successful detector for simultaneous multielement analysis in atomic emission spectrometry. The unique non-destructive readout, coupled with selective knockdown and pseudo-random addressing give the CID system capabilities unparalleled in any other detector available today. The device has been shown to have at least an adequate sensitivity, can be operated in a manner which reduces pixel cross talk, and the dynamic range of the system can be extended to virtually any desired level.

The ability to simultaneously examine a wide spectral range opens an entire new realm of possibilities for the analyst. For instance, if self-absorption becomes a problem for an atomic emission line, the possibility now exists to dynamically switch to an ionic emission line. Another possibility is that if a spectral interference becomes a problem at the most sensitive line for a given element, the decision can be made to switch to a less sensitive line, which may have less interference.

Productive research in the area of CID camera detectors is expected to continue for some time since new and better CID detectors, (98,774 pixels and ~300,000 pixels) are now or will soon be available. The capability to examine simultaneously from the near I.R. to the vacuum ultraviolet with adequate resolution will soon be realized.

Acknowledgments

This work was partially supported by the Office of Naval Research.

Literature Cited

1. Talmi, Y. Anal. Chem. 1975, 47, 7, 268A.
2. Talmi, Y. Anal. Chem. 1975, 45, 7, 658A.
3. Busch, K.W.; Malloy, B. ACS Symposia Series 1979, 102, 27.
4. Michon, G.J.; Burke, H.K. IEEE Digest of Technical Papers 1973, p. 138.
5. Michon, G.J.; Burke, H.K. IEEE International Solid State Circuits Conference 1974, p. 26.
6. Aikens, R.S.; Lynds, C.R.; Nelson, R.E. SPIE Proceedings, 1976, 78, 65.
7. Aikens, R. AURA Engineering Technical Report No. 66 1980.
8. Lewis, H.; Denton, M.B. Journal of Automatic Chemistry 1981, 3, 9.

9. Michon, G.J.; Burke, H.K.; Vogelsong, T.L.; Wang, K. SPIE Proceedings, 1979, 302, 67.
10. Mortara, L.; Fowler, A. SPIE Proceedings 1981, 290, 28.
11. Handbook of Spectral Line Characteristics for the DC Plasma/Echelle Systems, Spectrametrics Inc. 1982.

RECEIVED April 26, 1983

Charge-Injection and Charge-Coupled Devices in Practical Chemical Analysis

Operation Characteristics and Considerations

M. B. DENTON, H. A. LEWIS, and G. R. SIMS

Department of Chemistry, University of Arizona, Tucson, AZ 85721

The increasing demand on multispecie chemical analysis and use of highly sophisticated computer controlled instrumentation has made significant changes in the modern laboratory. Optical spectroscopy ranging from Raman through Atomic is under considerable pressure to replace the "tried and true" photomultiplier tube (PMT) with multichannel devices. Two classes of solid state devices, the Charge Coupled Device (CCD) and the Charge Injection Device (CID), hold great promise for meeting this need. Operating modes of these devices are reviewed. Characteristics pertinent to analytical spectroscopy are presented.

A basic limitation existing today in a number of areas of optical spectroscopy is the lack of a viable, compact, rugged, easily operated, sensitive device capable of simultaneously monitoring any or all portions of a reasonably wide spectral region with sufficient resolution. First photographic emulsions and more recently photomultiplier tubes have been widely employed for spectroscopic detection. The former, while being an integrating media with an extremely large number of resolution elements suffers from many significant problems not the least of which involve the logistics of calibration and data readout. Photomultiplier tubes (PMTs) provide many desirable features including sensitivity, wide dynamic range, reasonable spectral response in the vacuum ultraviolet to visible region, and ease of calibration and readout. Unfortunately, the conventional photomultiplier tube is a single channel device. This characteristic has resulted in two general classes of wavelength dispersion optical systems. The scanning or slew scanning approach sequentially observes a discrete window in the spectral region of interest. While

0097-6156/83/0236-0133\$06.50/0
© 1983 American Chemical Society

highly successful for many applications this approach does not provide simultaneous observation of a large wavelength region. The second method involves the use of a number of individual slits and PMTs carefully aligned to provide simultaneous readout of a number of discrete wavelengths. This method has become widely employed in the area of atomic emission spectroscopy. This polychromator or "direct reader" approach proved to be first popular for spark emission and recently has undergone a flurry of activity with the increasing popularity of inductively coupled, microwave, and direct current plasmas. This configuration is often bulky, provides the ability to simultaneously monitor only a very limited number of wavelengths, is expensive, and is not readily flexible regarding changing the wavelengths observed. A tremendous need exists today for some type of electronic camera capable of meeting the stringent characteristics dictated by various different spectroscopic techniques.

Television-type cameras have been adapted for use as multichannel detectors in spectroscopic systems (1-3). These devices possess a large number of picture elements (pixels) to cover a wide wavelength range rapidly and yet are compact in size. Wavelength selection can be made electronically instead of through the manual adjustment of slit-photomultiplier tube assemblies. Some of the camera devices that have been applied are silicon vidicon tubes (4-8), silicon intensified target (SIT) tubes (9-12), image dissector (ID) tubes (8,13-15), photodiode arrays (16-19), and charge-coupled device (CCD) arrays (20,21). The silicon vidicon, SIT, and ID all employ an electron beam to carry the video signal. Uncertainties in the control of this beam can hamper precise pixel selection in these devices. In addition the silicon vidicon and the SIT suffer from cross-talk between pixels at high illumination levels (blooming) as well as incomplete removal of the charge signal on the target during readout (lag). In an effort to avoid these problems along with mechanical limitations resulting from the delicate nature of vacuum tubes, solid-state cameras have been developed.

The photodiode array, CCD, and the charge-injection device (CID) (22-26) are solid state sensors which are constructed by employing integrated circuit fabrication technology. The photon generated charge is collected and stored in either reverse-biased photodiodes (the photodiode array) or in metal-oxide-semiconductor (MOS) capacitors (the CCD and the CID). This results in minimal lag and digitally precise pixel addressing. In general the overall package is smaller, easier to cool, and less expensive than the vacuum tube cameras.

The charge coupled device has received wide spread

application in the field of astronomy providing both spatial resolution and sensitivity (27). Such devices are fabricated by RCA, Fairchild Semiconductor, General Electric Company of Britain, Hamamatsu, Thompson-CSF of France, and Texas Instruments. This manuscript will discuss primarily the RCA devices with brief references to other products. A CCD can be thought of as a large number of photodetecting analog shift registers. The RCA devices used for the data presented in this paper are 512 pixels wide and 320 pixels high as shown in Figure 1. (CCD's have been made as large as the Texas Instruments 800 x 800 device or 640,000 pixels).

Photons striking a given pixel are stored during an exposure and subsequently clocked horizontally to a "catchment" high speed shift register and then down to the readout preamplifier (see Figure 2), resulting in a serial raster scan row by row of the charge stored in the array. (Note the authors have chosen to orient the devices with the long axis horizontal for spectroscopic applications in contrast to the vertical orientation common with astronomers due to the spectral display of the optical system employed.)

This mode of readout necessitates that the source be blocked during readout to prevent smearing of the image. Fabrication of a device with half of the array blocked (Figure 3) allows high speed parallel horizontal shifting of the charge from the photoactive region into the storage region followed by raster scan readout of the storage region. This mode of readout, "frame transfer", can be used for frame by frame (TV) readout since it can usually be assumed that the parallel horizontal shift can be accomplished so fast that smearing will be negligible. However, this approach reduces the number of usable pixels by one half.

The most easily understood charge transfer mode involves use of three phase clocking. Initially the array's capacitor plates are reverse biased to create potential wells under one or two of the three capacitor plates comprising a pixel (Figure 4 A or B). Transfer is accomplished by sequentially dropping a new potential well (Figure B, D, or F) followed by bringing up the previous well C, E or G. The charge originally under ϕ_1 in A has advanced one full pixel by step G.

The upper dynamic range is limited by the amount of charge that can be quantitatively stored in a single pixel well. Over-illumination of a pixel causes the charge to spill over into surrounding pixel wells, a phenomenon known as "blooming".

A novel method for increasing the sensitivity and, coincidentally the dynamic range, has been employed by astronomers (though generally not widely publicized). Every

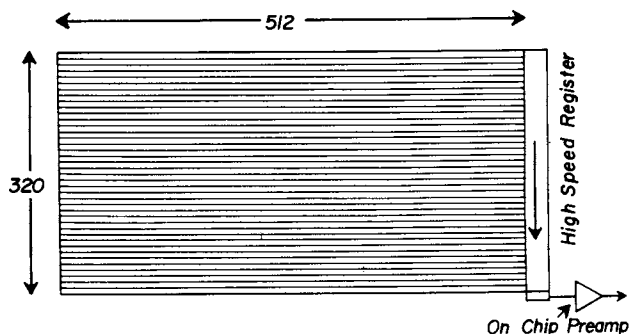


Figure 1. The pixel layout for the RCA charge-coupled device (CCD) used in these studies provides a 512×320 array or 163,840 sensor elements (pixels).

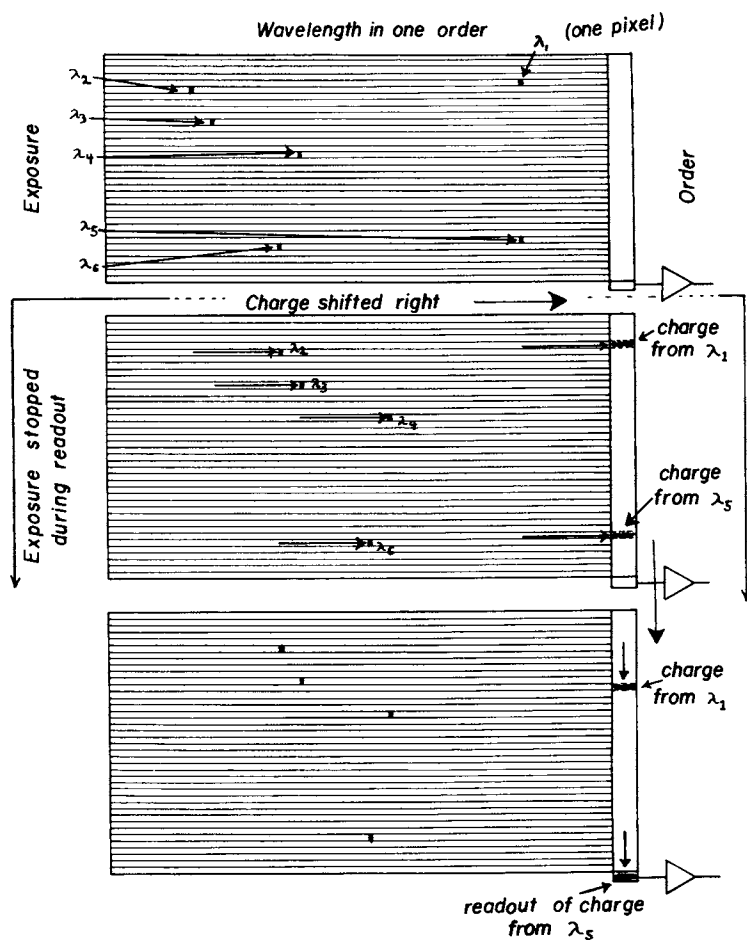


Figure 2. Spectroscopic information is initially imaged on the CCD. A readout is performed by shifting information horizontally to the high-speed shift register and is made serial by shifting vertically into the video preamplifier.

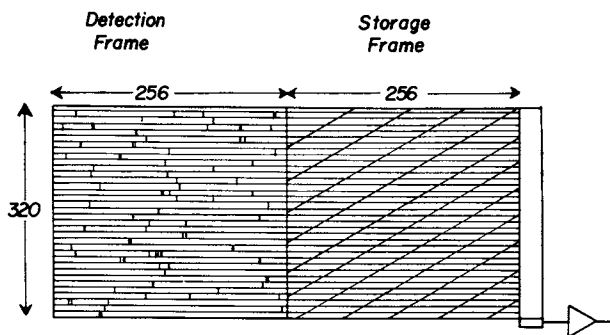
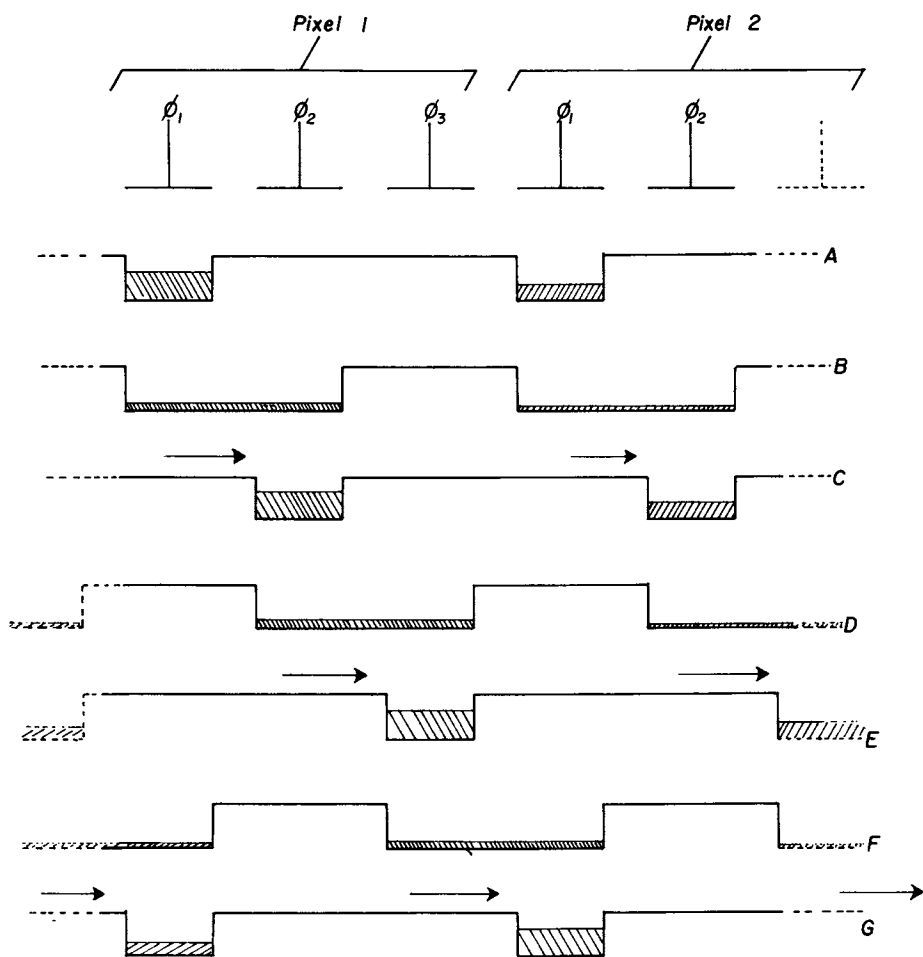


Figure 3. For continuous frame-by-frame readout, one-half of the device is reserved to store video information. Spectral information is gathered in the detection frame and is transferred to the storage frame so rapidly that blurring is minimized.



CCD 3 Phase Readout

Figure 4. Charge is collected first at the ϕ_1 (A) or ϕ_1 and ϕ_2 (B) electrodes and is subsequently shifted by dropping a new potential well and then bringing up the previous well. Note that by Step G the charge has advanced one pixel.

readout in a CCD is accompanied by a certain amount of noise regardless of the amount of charge read. Any process which increases the charge due to signal will therefore improve signal-to-noise. The astronomer's trick is to combine the charge acquired in a number of pixels to generate a single charge grouping on the chip, a so called "super pixel". This larger combined charge is shifted to the on chip readout amplifier and measured in a single readout. Since each readout has a superimposed noise level of approximately 50 electrons due to preamplifier shot noise and Johnson noise (28) in a single readout, the larger signal in a given readout improves signal-to-noise at very low light levels. If spectral information is properly configured on the device, this procedure results in the signal from a larger area being read with the noise from only one readout at a cost of decreased image resolution. Since the RCA 53612 device has 163,840 pixels, the trade off of lost resolution is often not regarded as serious. It is important to note that the charge is combined on-chip.

From an analytical spectroscopic viewpoint this type of operation has several desirable features. The slit image from a spectrometer is usually rectangular. Creation of a "super pixel" shaped like the slit image can greatly increase the system performance. Additionally the dynamic range is operationally increased since the total charge that can be stored in a super pixel is equal to the combined well capacities (i.e., a super pixel made from an array of 1×4 pixels can hold 4 fold more charge than that of a single pixel but is limited to four fold or 10^6 electrons by the linearity of the on-chip preamplifier). Currently, studies are underway to evaluate the use of such devices in chemical analysis. Figures 5 and 6 show analytical working curves for potassium and sodium obtained with D.C. plasma emission. Even when using the "super pixel" technique the upper end of the working curve starts to tail off and blooming is beginning to be observed.

The good signal to noise, however, indicates that the real forte of these current generation CCD devices lies in spectroscopic applications where maximum sensitivity is needed and high dynamic range is not as important. These devices should be most useful in areas such as trace level molecular fluorescence and Raman spectroscopy.

The second major problem limiting CCD's is that of spectral response. Most devices currently manufactured are front side illuminated (see Figure 7). In this geometry photons must penetrate through the pixel electrodes and then generate charge in the pixel well. Spectral response can be severely limited since more energetic photons (shorter wavelengths) are rapidly absorbed and never make their way to the photoactive region. Front side devices often have

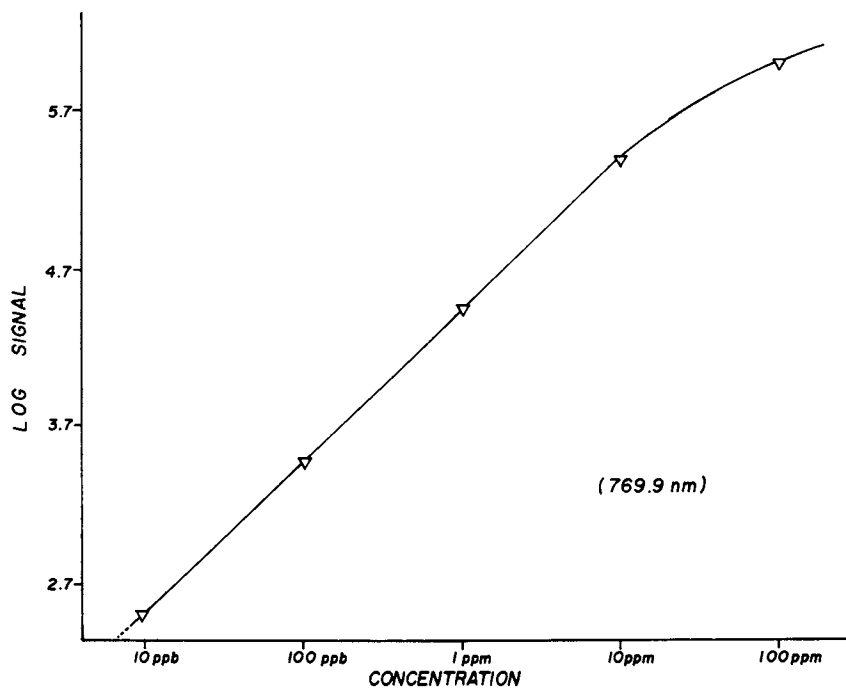


Figure 5. Analytical working curve for potassium. The curve was obtained using a RCA 53612 CCD with a direct current plasma source.

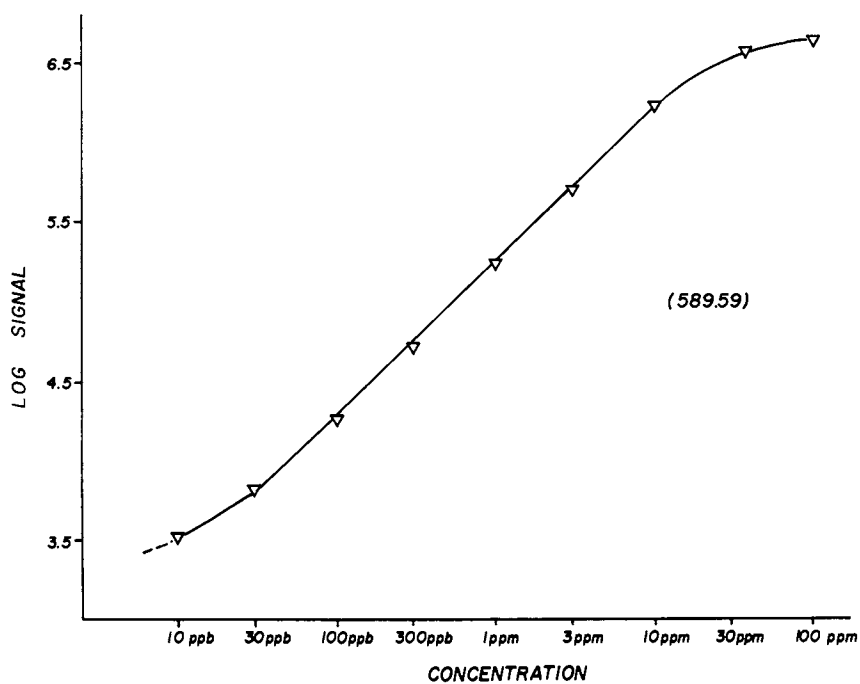


Figure 6. Analytical working curve for sodium. The curve was obtained using a RCA 53612 CCD with a direct current plasma source. The nonlinear tail on the low end of the working curve is due to sodium in the laboratory water.

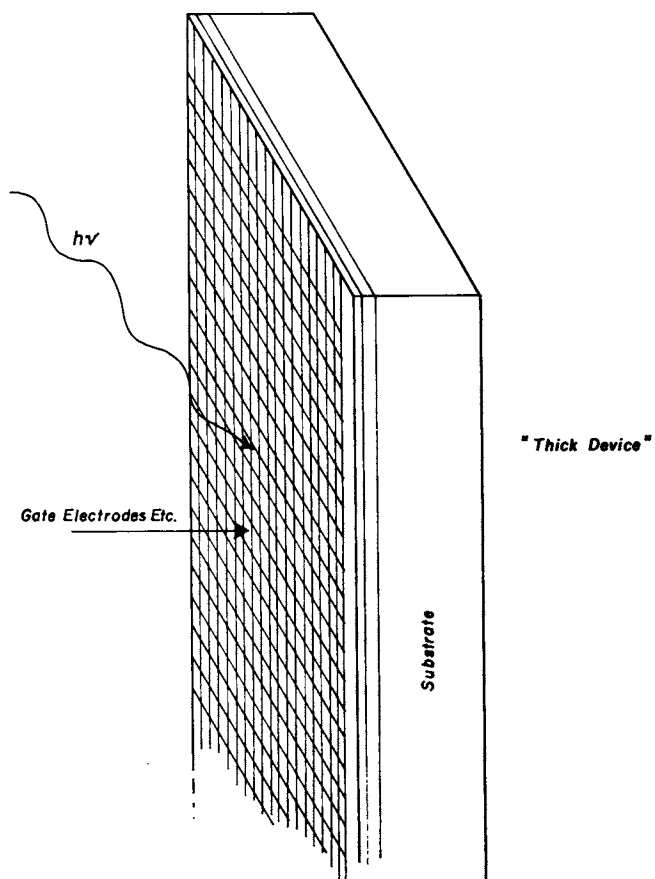


Figure 7. Front-illuminated or thick devices require photons to penetrate a substantial array of electrodes, which results in a poor response below 450 nm.

poor response in the visible blue and do not operate at all in the UV. One solution to this problem offered by RCA is the so called "thinned" or "backside illuminated" device shown in Figure 8. In this configuration the silicon is thinned to 8 to 12 microns and laminated to a 500 micron thick glass substrate. Photons enter the device through the glass from the side opposite the electrodes. From an astronomer's viewpoint this achieves two major goals. The visible blue spectral region is now available and the glass plate acts as a light impedance matchèr (reduces reflection losses) between air and silicon increasing quantum efficiency from approximately 50% to over 80%. The glass chosen must have the same thermal expansion properties as the silicon or the 12 micron silicon wafer would be destroyed. Unfortunately, the soda lime glass chosen cuts off sharply in the UV.

RCA has recently provided us with a custom device in which the glass substrate has been etched away from the photo active region (see Figure 9) (i.e., bare 10 micron silicon is exposed. Even though the device appears to be rather fragile, no problems have been experienced. Spectral response data for all three types of devices are shown in Figure 10. Another solid state array detector with a number of extremely interesting characteristics is the charge-injection device. The CID sensor currently produced by General Electric consists of a two-dimensional array of discrete pixels, each of which is composed of a pair of silicon-type MOS capacitors. Figure 11 depicts a small portion of the row/column structure. Light striking the bulk silicon generates charge carriers which are stored underneath the capacitor with the greatest negative potential during the frame (integration) time (Figure 12). This can best be understood by plotting potential well curves with stored charge underneath the capacitor plates (See Figure 12B). During the readout of of each pixel this charge is transferred from one of the capacitors to the other, or to the substrate.

Several of the important readout concepts are illustrated in Figures 13 and 14. Initially, each pixel site consisting of a row and column MOS capacitor can be thought of as having some initial bias potential V_R (row) and V_C (column) and an empty "well" (see Figure 13). If both of these potentials are 15 volts negative and photons irradiate the surface, charge starts to collect in the well (see Figure 13B). If the row which crosses the particular pixel element about to be read out is clamped to zero volts, the charge stored under each of the MOS capacitors within that row are transferred to each of the adjacent column electrodes (see Figure 13C). If a single column is now clamped to zero, the charge stored under each of the capaci-

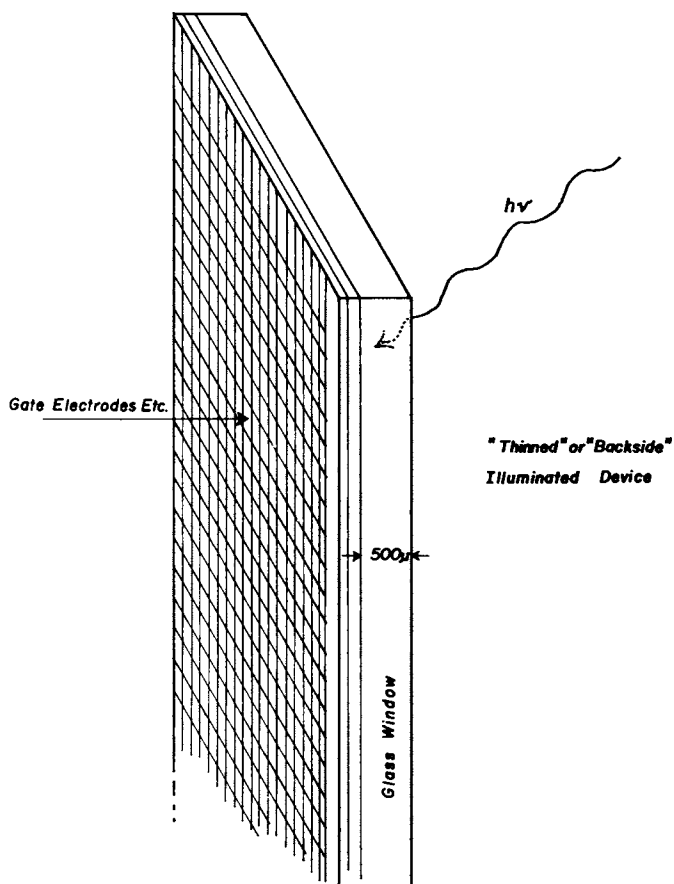


Figure 8. In special RCA-thinned devices the silicon is etched to 10- μm thick and a 500- μm glass window is placed on the back side.

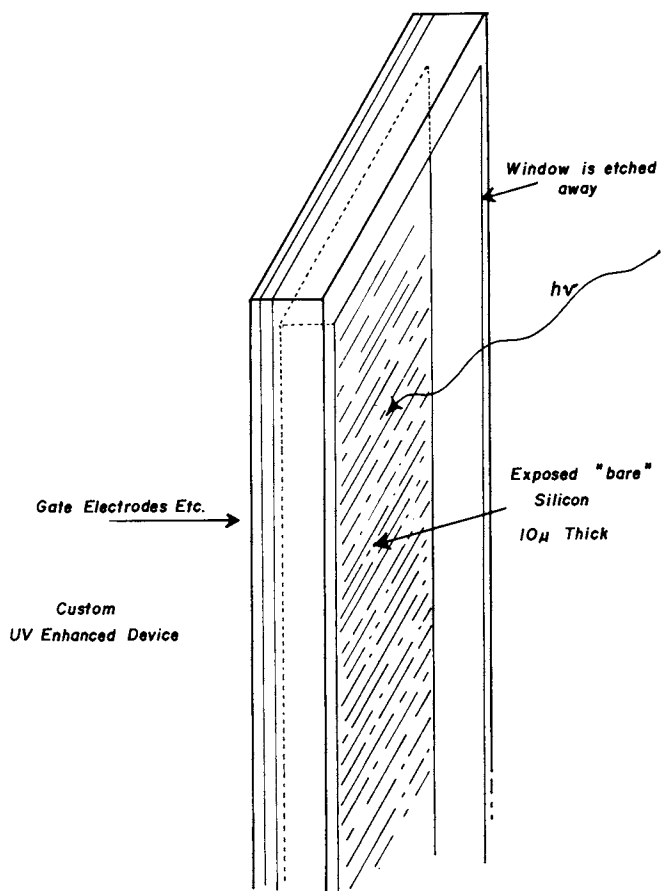


Figure 9. The RCA custom UV-enhanced charge-coupled device studied has had the 500- μ m glass substrate removed to leave 10 μ m of exposed photoactive silicon.

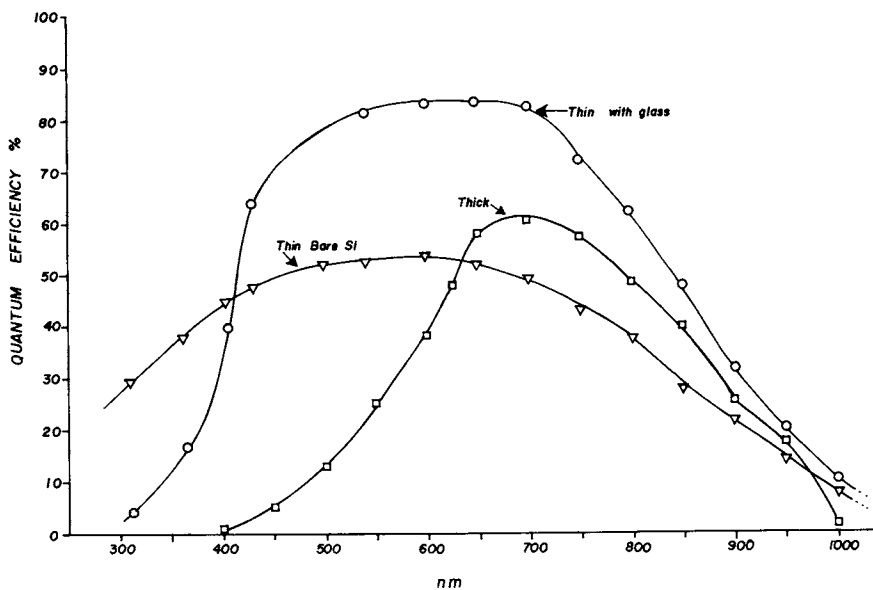


Figure 10. Spectral response curves for three CCD detectors. Key: \circ , thin with glass; Δ , thin bare Si; and \square , thick. Note the quantum efficiency axis is linear.

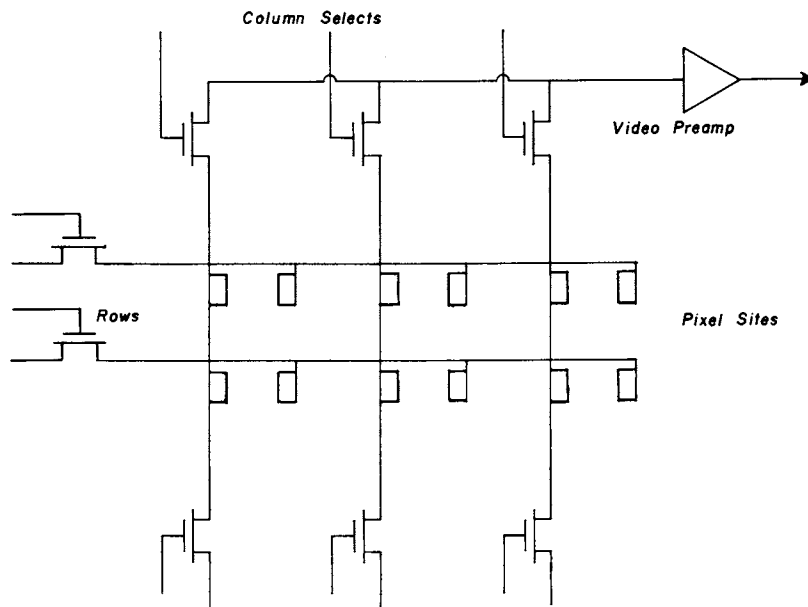


Figure 11. Diagram of a small portion of a charge-injection device array showing row and column FLT selection and video preamplifier. Individual pixel (resolution) elements are comprised of a pair of metal oxide insulated capacitor plates; one plate on a row and one plate on a column. (Reproduced with permission from Ref. 26. Copyright 1981, J. Auto. Chem.)

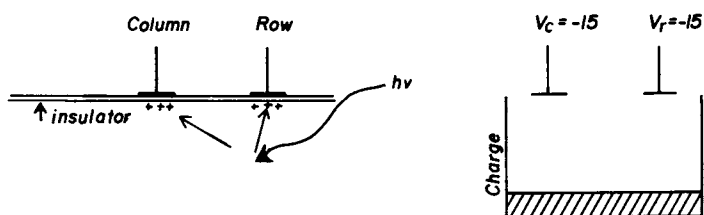


Figure 12. Photons striking the bulk silicon generate positive charge carriers which are stored beneath the negatively biased capacitor plates (left). The quantity of charge stored beneath the plates is often depicted in a well diagram (right). (Reproduced with permission from Ref. 26. Copyright 1981, J. Auto. Chem.)

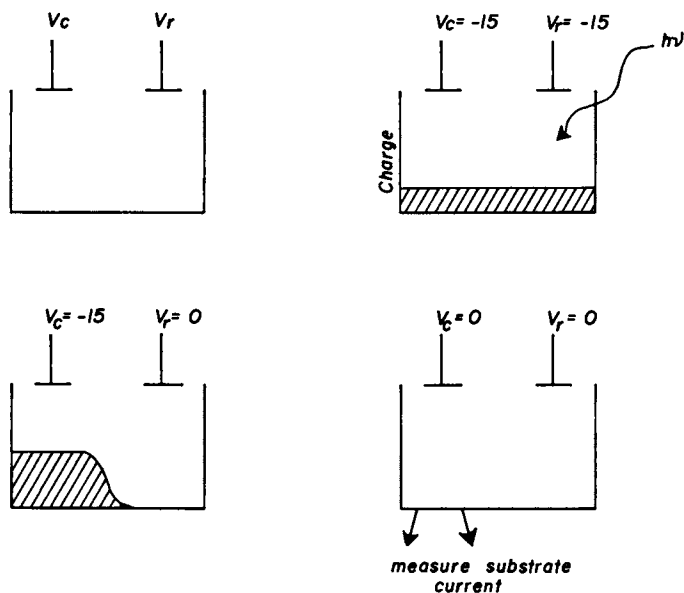


Figure 13. The injection mode readout for CCDs. Only the charge that is stored at the pixel site where both the column and row are clamped to zero is injected into the substrate. (Reproduced with permission from Ref. 26. Copyright 1981, J. Auto. Chem.)

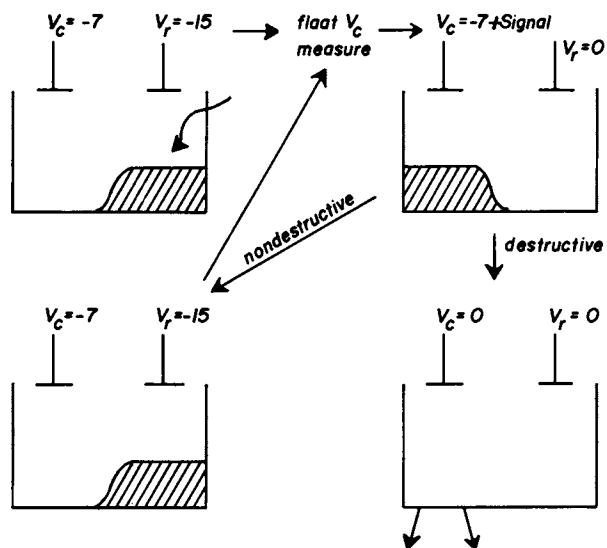


Figure 14. The measuring sequence for combined nondestructive/destructive readout. In nondestructive mode the sequence is cycled as many times as desired to improve signal-to-noise. (Reproduced with permission from Ref. 26. Copyright 1981, J. Auto. Chem.)

tors in the column, except for the pixel site which is in the process of being selected, merely moves back to their row capacitor (which is still negative). However, for the one pixel site under selection, both the column and row capacitors are at zero potential, resulting in injection of the stored charge into the substrate (see Figure 13D). The resultant current can be measured to provide the video signal. One should note that only the pixel at the intersection of the selected row and column has both capacitor plates at zero potential. All the other pixel sites have one of the two capacitors still biased negative under which charge is stored.

While this original prototype mode of CID operation functions, it does not realize one of the most unique capabilities of the CID. To achieve a nondestructive readout capability, a column potential is reduced (see Figure 16A) resulting in accumulation of charge under the row capacitor. For readout, the column containing the desired pixel is allowed to float and its potential is measured (i.e., the column when floated will initially remain at approximately -7 volts). Next, the row containing the pixel is clamped to zero volts and the charge in the selected pixel moves over to its column capacitor (see Figure 14B), changing the "apparent" potential (or charge) on the entire column (i.e., the column will now be at some potential less negative than -7 volts dependent on the amount of charge transferred from the row capacitor plate). This change in "apparent" column potential is dependent on the entire column capacitance and the charge accumulated in the selected pixel. If the row is returned to a more negative potential, the charge moves back under the row capacitor plate (Figure 14C) and the process can be repeated in a nondestructive readout mode, (i.e., V_c is allowed to float, measured, and the processes repeated, etc.). Destructive readout is accomplished by clamping the column to zero potential while the row is still zero (Figure 14D), causing the charge to be injected, as in Figure 13D.

With nondestructive readout, blooming, which can still be a problem in the solid-state cameras, can be effectively eliminated by periodically scanning the array in a nondestructive readout mode to determine which pixels are near saturation. These pixels can be subsequently read out in the destructive mode, sufficiently often to prevent the leakage of charge into adjacent pixels. At the same time, pixels under low illumination can be allowed to integrate charge to maximize the signal-to-noise ratio of weak lines. By averaging many repeated, nondestructive readouts of the signal stored in a pixel, the readout noise, which is predominantly due to white noise generated in the first stage of the preamplifier, can be reduced by the square root of the number of complete readouts (24).

CID devices such as the General Electric RA-128 can also be fabricated to provide random addressing of the array. With this capability only the desired pixels need be interrogated instead of sequentially scanning through the whole array as is required in most other solid-state devices. Therefore, faster readout speeds are possible for rapid analysis.

On the basis of these characteristics, the CID shows definite potential as a multichannel detector for elemental analysis, provided it is able to detect light in the ultraviolet region where many elements have their strongest emission lines. Early studies of the spectral response of CID's did not extend below 400 nm (23) or else indicate that the response quickly falls off in the UV (22). For a number of reasons the UV response of the CID has not been measured accurately. The detector arrays are normally manufactured with glass windows. In addition, the spectral response measurements were made using glass lenses (25). Since glass absorbs light below approximately 350 nm the value of previous studies is negated. In recent studies (26) the spectral response for five CID sensors was measured from 190 to 800 nm using front surface mirrors and quartz optics to eliminate the absorption of glass. Five CID-40B sensors were used to determine the extent of the variation in sensitivity between sensors.

The results as shown in Figure 15 indicate an approximately eight to ten percent quantum efficiency in the ultraviolet rising to the forty to fifty percent efficiency in the visible. Therefore, the CID is capable of a very respectable level of performance.

Optical Systems for Use with Array Detectors

Careful design and matching of optical dispersion systems are necessary to effectively employ the capabilities of CID and CCD arrays. Since these devices are two dimensional (x-y) and reasonably small [CID-11B providing 60,512 pixels is 0.9 x 1.1 cm and the RCA 53645 CCD providing 163,840 pixels is 1.41 x 1.73 cm] appropriate spectral image formatting is essential. Parameters which must be considered include total field imaging quality, spectral coverage, dispersion, light throughput, and stray light. (Note: In certain areas of spectrochemical analysis such as inductively coupled plasma atomic emission spectrometry (ICP-AES) stray light from very intense emission lines associated with major sample constituents can cause significant interference problems with weak emission lines from trace sample components.) Additionally, the optimum system should be reasonably compact and rugged for field use.

One promising approach toward achieving the desired x-y

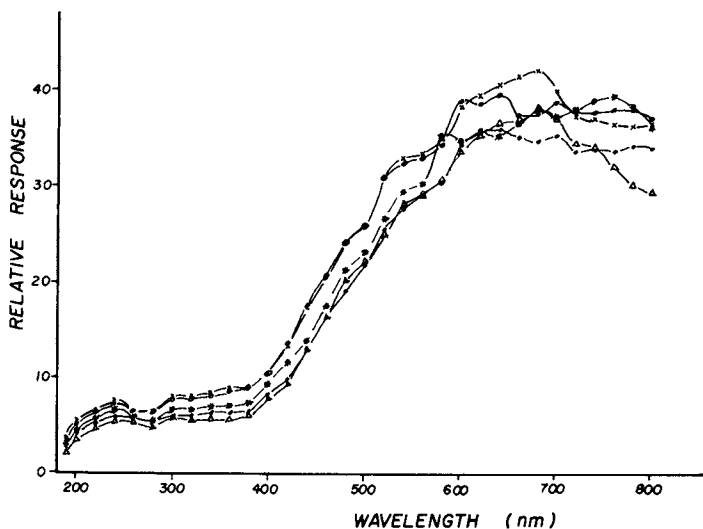


Figure 15. Spectral response data for five CID-40B devices. Key to chip: x, 4242-1; o, 4242-7; Δ , 4242-3; \bullet , 4242-5; and *, 4245-1.

forming is through the use of a properly configured echelle cross-dispersion spectrometer. Essentially this involves using an echelle grating (a special deeply grooved and coarsely ruled grating operated in high orders to achieve high dispersion) and some type of a cross disperser to prevent overlap of the various orders (generally a prism or first order grating) followed by some form of image reduction. Several configurations of both approaches have been evaluated by others (7,29-34) and within our laboratory.

Figure 16 shows the use of a prism to provide "order sorting vertical dispersion." This approach has been employed in a variety of commercial systems. Another approach used in a number of astronomical applications uses a conventional first order grating to provide order sorting (see Figure 17).

This geometry should reduce stray light associated with reflections from the prism faces but introduces the possibility of second order interferences from the order sorting grating. While the optimal optical configuration will no doubt be resolved in the battle field of the market place, the use of two dimensional array detectors in future commercial instruments is near at hand.

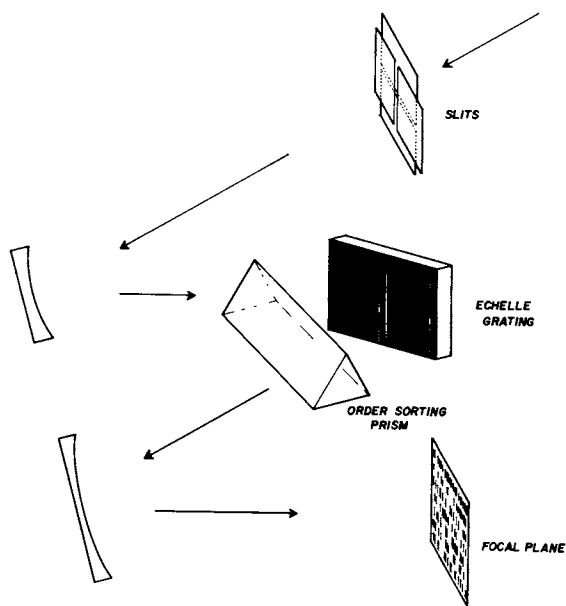


Figure 16. A prism or a grating usually is used to start orders in an echelle spectrometer.

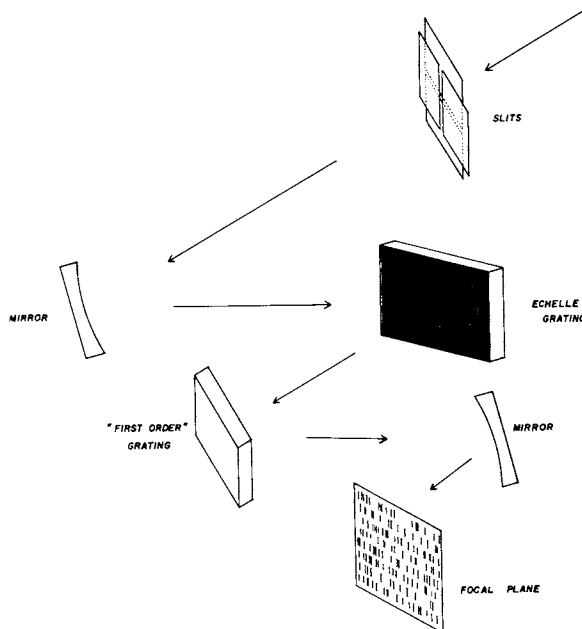


Figure 17. A crossed grating echelle configuration is being evaluated currently for improved stray light rejection in a smaller size package.

Acknowledgments

This research was partially supported by the Office of Naval Research and Dow Chemical Corporation.

Literature Cited

1. Talmi, Y., Anal. Chem. 1975, 47, 658A.
2. Talmi, Y., Anal. Chem. 1975, 47, 699A.
3. Talmi, Y., "Multichannel Image Detectors," ACS Symposium Series Vol. 102, Washington, D.C., 1979.
4. Mitchell, D.G.; Jackson, K.W.; Aldous, K.M., Anal. Chem. 1973, 45, 1915A.
5. Knapp, D.O.; Omenetto, N.; Hart, L.P.; Plankey, F.W.; Winefordner, J.D., Anal. Chim. Acta 1974, 69, 455.
6. Howell, N.G.; Morrison, G.H., Anal. Chem. 1977, 49, 106.
7. Felkel, Jr., H.L.; Pardue, H.L. Anal. Chem. 1977, 49, 1112.
8. Felkel, Jr., H.L.; Pardue, H.L. Anal. Chem. 1978, 50, 602.
9. Aldous, K.M.; Mitchell, D.G.; Jackson, K.W. Anal. Chem. 1975, 45, 1034.
10. Chester, T.L.; Haraguchi, H.; Knapp, D.O.; Messman, J.D.; Winefordner, J.D. Appl. Spectrosc. 1976, 30, 410.
11. Busch, K.W.; Malloy, B. Anal. Chem. 1979, 51, 670.
12. Furuta, N.; McLeod, C.W.; Haraguchi, H.; Fuwa, K.; Appl. Spectrosc. 1980, 34, 211.
13. Golightly, D.W.; Kniseley, R.N.; Fassel, V.A., Spectrochim. Acta B 1970, 25, 451.
14. Danielsson, A.; Lindblom, P. Appl. Spectrosc. 1976, 30, 151.
15. Felkel, Jr., H.L.; Pardue, H.L. Clin. Chem. 1978, 24, 602.
16. Horlick, G.; Coddling, E.G.; Appl. Spectrosc. 1975, 29, 167.
17. Horlick, G. Appl. Spectrosc. 1976, 30, 113.
18. Yates, D.A.; Kuwana, T. Anal. Chem. 1976, 48, 510.
19. Chuang, F.S.; Natusch, D.F.S.; O'Keefe, K.R. Anal. Chem. 1978, 50, 525.
20. Ratzlaff, K.L.; Paul, S.L. Appl. Spectrosc. 1979, 33, 240.
21. Ratzlaff, K.L. Anal. Chem. 1980, 52, 916.
22. Michon, G.J.; Burke, H.K.; Brown, D.M. Proc. of a Symposium on "Charge Coupled Device Technology for Scientific Imaging Applications," 1975, pp. 106-115.
23. Burke, H.K.; Michon, G.J. IEEE Transactions of Electron Devices, ED-23 1976, p. 189.

24. Aikens, R.S.; Lynds, C.R.; Nelson, R.E. Proc. of the Society of Photo-Optical Instrumental Engineers, Vol. 78, "Low Light Level Devices," 1976, pp. 65-71.
25. Coates, P.; General Electric Company, Syracuse, New York, personal communication, 1977.
26. Lewis, H.A.; Denton, M.B. J. Auto. Chem. 1981, 3, 9.
27. Kristian, J.; Blouke, M. Sci. American Oct. 1982, 247, 67.
28. Aikens, R.S. "Operations Manual for 81s CCD Camera Systems," Photometrics Ltd., Tucson, Arizona, 1981.
29. Liller, W. Appl. Opt. 1970, 9, 2332.
30. Harrison, G.R. J. Opt. Amer. 1949, 39, 522.
31. Keliher, P.N.; Wohlers, C.C. Anal. Chem. 1976, 48, 333A.
32. York, P.G.; Jenkins, E.B.; Zucchini, P.; Lowrance, J.L. SPIE Proc., June 10-11, 1981 "Solid State Imagers for Astronomy."
33. Boland, B.C.; Jones, B.B.; Engstrom, S.F.T. Solar Physics 1971, 17, 333.
34. Elliott, W.G. Amer. Lab. 1970, 2, 67.

RECEIVED April 26, 1983

Luminescence Measurements with an Intensified Diode Array

JAMES D. INGLE, JR. and MARY ANDRIEU RYAN¹

Department of Chemistry, Oregon State University, Corvallis, OR 97331

In the past, molecular luminescence spectrometry was always conducted with single channel systems involving a photomultiplier tube (PMT) as the detector. The availability of multichannel detectors with internal gain has provided a new powerful tool for luminescence measurements, and several types of applications have been reported (1-15). This paper is concerned with the application of an intensified diode array (IDA) for dynamic molecular fluorescence and chemiluminescence measurements. In this paper the types of measurements and analytical systems for which multichannel detectors are used in our laboratory are introduced. Next the specific IDA system used is presented along with important hardware and software considerations. Third, the characteristics of the IDA detector are reviewed to give some perspective about its influence on the quality of measurements. Finally, some typical applications to chemical systems are presented to illustrate the advantages of multichannel detection.

¹Current address: Tektronix, Inc., Beaverton, OR 97977.

0097-6156/83/0236-0155\$06.00/0
© 1983 American Chemical Society

Types of Chemical Systems Studied

In fluorescence kinetics-based (FL KB) measurements, the analyte is reacted with a selective reagent to form a fluorescent product. Under suitable conditions the initial rate, measured as a change in the FL signal over a selected time period, is proportional to the analyte concentration. Low detection limits (ng/mL and sub ng/mL) are provided by the technique for inorganic and organic analytes. Excellent selectivity arises due to the use of fluorescence monitoring (a small fraction of molecules fluoresce, excitation and emission wavelengths can be optimized), the use of a specific optimized chemical reactions, and finally the use of a kinetic measurement (discrimination against steady state background fluorescence and scattering signals and species which react at significantly different rates). Instrumentally, KB FL measurements are usually made with a scanning emission monochromator which is set to monitor a specific wavelength band during the course of a reaction.

In chemiluminescence (CL) measurements the analyte is mixed with suitable reagents to cause a reaction to occur in which an intermediate or product in an excited electronic state is formed. The flash of light produced is quantitated as a peak height or area. Metal analytes are usually determined by their enhancement of a blank CL reaction. In some cases the analyte can be the CL precursor. The technique is suitable for trace determination of a wide variety of species with often good selectivity. Typically no wavelength selection device is employed and radiation at all wavelengths is directed to a PMT since all the CL arises from the reaction of interest.

For both types of measurements described above, the luminescence signal is dynamic or changes with time. Because the reactions studied for KB FL measurements have half-lives of 2-30 min, significant intensity changes can occur over even a few seconds. The flash of light observed in many CL reactions typically has a duration of several seconds or less. Clearly in both situations an undistorted spectrum cannot be acquired with a conventional scanning monochromator.

Instrumentation

A multiple wavelength spectrometer is constructed by placing a multichannel detector in the focal plane of a spectrograph so that each detector element intercepts a different small wavelength range. The multichannel detector used for this work is a Tracor Northern TN-1710-21 IDA. It consists of a Reticon 512 element diode array (DA) with 0.45 mm high diodes separated by 50 μ m spacings. The DA is cooled with a Peltier thermoelectric cooler. The DA is mounted at the output of a microchannel plate intensifier (MCP) which has a photocathode with an extend-

ed red response to provide sensitivity in the red part of the spectrum. The MCP is an electrostatically-focused image inverting intensifier with a nominal luminous gain of 35,000. A scintillator in front of the photocathode determines the response in the UV. The commercial IDA is provided with pre-amplifier and timing electronics. We chose to build our own data acquisition and control system, although such a system can also be purchased from Tracor Northern.

The use of the IDA for luminescence spectral measurements is illustrated in Figure 1. Fluorescence or chemiluminescence from a sample cell is focused on the slit of an $f/3$ spectrograph. The spectrograph disperses the radiation in its focal plane where the spectrum is incident on the photocathode of the IDA. Some of the photons impinging on the photocathode cause ejection of photoelectrons from the photocathode. Each photoelectron passes into a channel of the MCP and emerges at the other end as a charge packet of $10^3 - 10^4$ electrons. The charge packet strikes the phosphor to produce a photon packet for every initial photoelectron. The photon packet is impinging on a particular diode element and causes many electron-hole pairs to be created. After a suitable viewing or integration time, the signals from the individual diodes are read out in a sequential manner. The diode signals are related to the amount of charge required to destroy the electron-hole pairs created by impinging light or thermal effects. The charge pulse is converted to a proportional voltage pulse of about 2 μ s duration and a maximum peak height of 10 V. The maximum value is determined by the saturation level of the diodes (which is limited by the maximum number of electron-hole pairs that can be generated). Fiber optic faceplates between the photocathode and input of MCP and between the phosphor and the DA ensure that good spatial integrity is obtained. Thus a photon of a particular wavelength which strikes a particular part of the photocathode will eventually result in a signal at a particular diode. The reciprocal linear dispersion of the spectrograph used is about 25 nm/mm yielding 1.3 nm/diode over the wavelength range 200 - 840 nm.

Hardware. To employ the IDA, the user must supply a clock signal, a begin scan signal, and data acquisition hardware. The hardware to accomplish this has been based on a PDP 11/20 minicomputer or a KIM microcomputer plus additional external hardware (13-15). The clock signal determines the rate at which the diodes are interrogated during readout and was 33 kHz with the minicomputer and 125 kHz with the microcomputer. This means the time to read out all 512 diodes and hence the minimum integration time varies from 15 ms to 3.7 ms, respectively. For the microcomputer, direct memory access (DMA) circuitry was used to increase the data acquisition rate.

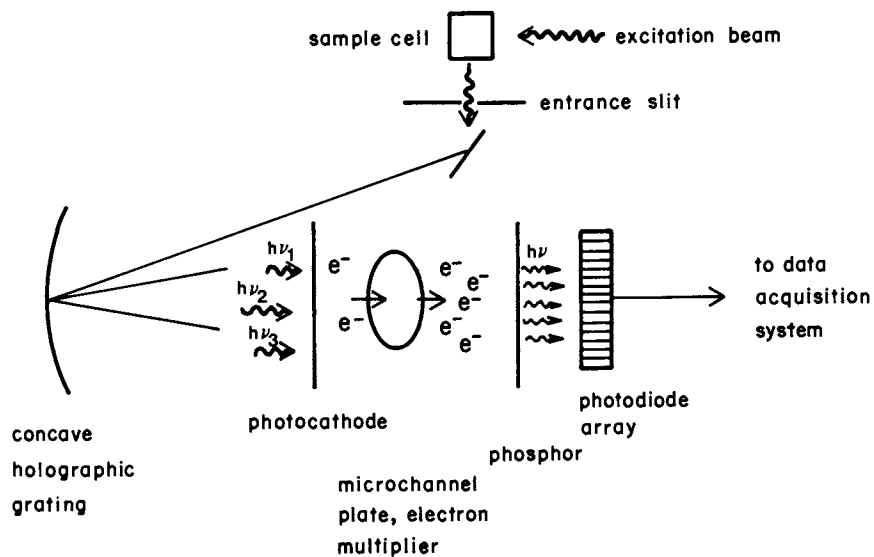


Figure 1. Instrumental configuration for fluorescence measurements with an intensified diode array.

The begin scan signal is used to start the DA diode interrogation and to control the integration time of a spectrum. The array is cleared with one begin scan signal, the photon signal is integrated, and then another begin scan signal is used for signal readout. The time between begin scan signals determines the integration time.

The diode array signals are output on a video line. This was connected to a fast sample-and-hold and then a fast (2 μ s) 12 bit ADC. This allows the peak signal voltage from each diode to be sampled and converted to a 12 bit digital representation to be stored in computer memory. Sequential memory locations are used for the signal from each diode with the saturation signal corresponding to 10^{12} or 4096.

Software. The software was tailored to fit our particular application. Some of the important options are described below:

1. Successive 512 point spectra are stored in successive blocks of memory where the integration time (t), time between spectra, and a number of spectra are user chosen.
2. Under user control, s number of successive scans can be summed in the same memory locations for signal averaging.
3. To save memory space, the data from the first n diodes can be ignored (not stored).
4. To save memory space and time, the last m diodes can be clocked at a faster clock rate and the data ignored.
5. After spectra are acquired, they can be displayed on a graphics terminal. Overlapping of different spectra and scale expansion allow easy comparison of spectra.
6. The signal from one diode or the sum of signals from n diodes can be displayed.
7. The sum or difference of any two spectra or of signals from one or more diodes can be calculated or displayed. The difference option can be used to calculate a rate or subtract a blank.
8. The mean and standard deviation of the signals from any group of diodes for a series of equivalent runs can be calculated and displayed.
9. A wavelength calibration program allows readout of signal information in terms of nanometers rather than diode numbers.

Performance Characteristics

Dark Signal Characteristics. The dark signal characteristics are measured with no light impinging the IDA and are important because the dark signal limits the maximum integration time and can limit the S/N at low light levels. Without cooling, the DA reaches saturation in about 10 s, while it takes about 50 s with cooling to about -10°C . Normally the heat from the high temperature side of the Peltier cooler is dissipated by ambient air movement. Considerable dark signal drift is observed throughout

a day as the air temperature changes. We found it essential to use a cooling collar based on circulation of tap water to dissipate the heat. This lowered the dark signal by over a factor of two, but more significantly it lowered the drift in the dark signal. Better thermostating control of the Peltier cooler would reduce the drift problem also.

It was determined that after a large dark signal had accumulated, several scans were required to reach a constant dark signal level for successive scans. This problem was alleviated by continually scanning (providing begin scan pulses) every 20 ms between spectra to keep the dark signal accumulation at a small value.

Intensifier Characteristics. The intensifier gain can be varied between about 200 and 10^4 . Intensification is essential for luminescence measurements to produce photon signals above the dark and readout noise of the DA. The S/N under signal carried noise situations (signal shot or flicker noise) is independent of the intensifier gain. The intensifier degrades the resolution of the DA by about a factor of 2 to 3.5 diode elements. At the lowest intensifier gain setting the dark signal characteristics are equivalent to those obtained with the intensifier bias voltage off. At full intensifier gain, the dark signal is increased about 10% and the dark signal noise is doubled. This is suspected to be due to thermal electrons generated at the photocathode that receive the same intensifier gain as photoelectrons.

When light is removed from the photocathode of the intensifier, a decaying light signal is observed due to residual phosphorescence from the phosphor used in the intensifier. It appears to be composed of two components with half-lives of tens of milliseconds and a few seconds. This behavior did not significantly affect our luminescence measurements. Because integration times were typically 1 s or greater, the shorter-lived component response time is insignificant. In other experiments (not involving luminescence) with pulsed light sources, the phosphor lifetime did distort signals modulated at frequencies greater than 10 Hz. The longer-lived decay component effect was insignificant in our time sequence experiments because the relative change in signal between sequential spectra was a fraction of full scale.

Signal and S/N Relationships. As a first approximation the following characteristics are expected to apply:

$$n_T = n_O + n_D + n_L \quad (1)$$

$$\sigma_T = (\sigma_R^2 + \sigma_D^2 + \sigma_L^2)^{1/2} \quad (2)$$

$$n_D, n_L \propto c, t, s \quad (3)$$

$$\sigma_D, \sigma_L \propto c^{1/2}, t^{1/2}, s^{1/2} \quad (4)$$

where

n_0 = offset signal (fixed pattern "noise")

n_D = dark signal

n_L = light signal

n_T = total signal

σ_R = readout noise

σ_D = dark current noise

σ_L = light signal noise

σ_T = total noise

c = number of channels added together

t = integration time

s = number of scans added together

Equations 1 and 2 just indicate that the total signal or noise in counts is due to the sum of three independent effects: the offset or readout process, the dark signal, and the light signal. Relationship 3 indicates that if we add the signals from two channels together, integrate twice as long, or sum the signals from two scans, the dark and light signals should double. For relationship 4, it is assumed that signal levels are low enough that fundamental shot noise is limiting, which is proportional to the square root of the signal and hence the square root of factors directly proportional to the signal.

The above relationships were tested by varying c , t , and s over a large range (14). First dark signal measurements were made and then measurements were made with the IDA photocathode illuminated with uniform white light. The contributions of dark and readout signal and noise were subtracted from the total signal to obtain the contribution from only the light signal.

Most of the above relationships are shown to be true and S/N's of 500 were obtained in some cases. The dependence of signals and noise on the number of channels added together is approximate due to diode to diode variations in dark signal and diode responsivity. The dark signal was not proportional to t above about 25% of DA saturation; a negative deviation was observed. The same affect was observed for the light signal if the dark signal component reaches 25% saturation in the integration time. Hence it is critical that the dark signal subtracted from the total signal to obtain the net light is measured with

the same integration time. In this case, the net light signal is proportional to the incident light intensity.

The light signal noise (σ_L) was found not to be proportional to the square root of the number of channels unless the diodes chosen were separated by 9 diodes. The noise σ_L increased faster than $c^{1/2}$ for small separations because the signals from adjacent and near diodes are not independent. This is believed to be due to the resolution degradation caused by the intensifier. Photons striking a 50 μm spot on the intensifier photocathode cause an eventual burst of photons over several hundred micrometers. Thus the signals from several diodes can track together the signal caused by photons arriving at one spot on the photocathode.

Detection Limit Considerations. For low light level measurements, the S/N is limited by readout or dark noise. The readout noise (σ_R) is about 3.5 counts. Above 1 s integration times and with full intensifier gain, the dark signal noise becomes limiting. The noise generated by the data acquisition circuitry is insignificant compared to the readout noise on the video line generated by the IDA and its electronics. Since in our system, 1 readout count is equivalent to about 5000 e's or about 1-2 photoelectrons at full intensifier gain (~ 6000), the readout noise is about 1.7×10^4 electrons. Thus our system can detect the presence of 4-8 photoelectrons in one diode channel, and hence is near the photon counting limit.

Applications of the IDA

Several chemical systems were studied with the spectrofluorometer with IDA detection to learn about the potential advantages provided by multichannel detection. A detection limit of 0.2 ng/mL was obtained for measurements of the steady state fluorescence of quinine sulfate (12). Here an 8 s integration time was employed and the signals from the 6 diodes (7.5 nm range) centered at the wavelength of peak emission were averaged. The low detection obtained indicates that the IDA is a powerful quantitative tool for trace fluorescence measurements. The detection with the IDA is only about ten times higher than obtained with the same spectrofluorometer with monochromator wavelength selection and PMT detection (the slit width was about 4 larger than used with the IDA).

Although only information from 6 of the 512 diodes was used for quantitative information in this case, the complete emission spectrum was obtained in a matter of seconds. This is about two orders of magnitude less than the time necessary to scan a spectrum with a conventional spectrofluorometer. The ability to acquire spectra rapidly provides a considerable time savings, particularly in situations where it is necessary to survey the fluorescence characteristics of a number of compounds. The

wavelengths of emission maxima and relative fluorescence intensities at a number of different excitation wavelengths can be established in a relatively short time.

For measurement of steady-state fluorescence, the rapid acquisition of spectra is a convenience but not essential. However, the rapid acquisition of spectral information is essential for measurement of transient species or where the luminescence signal continually changes with time. This will be demonstrated first for kinetic-based luminescence measurements and then chemiluminescence measurements.

Fluorescence Kinetic-Based Measurements. Our studies of the reaction rate determination of thiamine (vitamin B1) will be used to demonstrate the unique capabilities of rapid acquisition of spectra in kinetic measurements. The kinetic method is based on the oxidation of thiamine by Hg^{2+} in basic solutions to highly fluorescent thiochrome (16). The initial rate, taken as the change in fluorescence signal at 444 nm that occurs in a fixed time after mixing the sample and reagents, is directly proportional to the thiamine concentration.

Figure 2 shows emission spectra of a solution containing thiamine and riboflavin (vitamin B2) taken with the IDA at various times. Curve A is the spectrum of the original vitamin sample solution acidified to pH 2 with Hg^{2+} added. Under computer control this initial spectrum is acquired in 2 s and then pH 12.2 buffer is injected into the sample cell to raise the reaction mixture pH to initiate the thiochrome reaction. Curves B, C, and D are the emission spectra obtained at 16, 40, and 60 s after initiation of the reaction with a 2 s integration time. These spectra are now used to illustrate a number of important points.

1. The growth of the thiochrome peak centered at 444 nm is obvious.
2. The difference in the sum of the signals from the 10 diodes (533-545 nm) centered at the wavelength of peak emission of thiochrome is automatically calculated from the stored spectra to give a number proportional to the rate. The detection limit for thiamine is 6×10^{-8} M and illustrates the detectivity of the IDA. This is only a factor of 2 greater than the detection limit obtained with an equivalent system based on PMT detection.
3. The first order and second order (not shown) Rayleigh scattering peaks of the 365 nm excitation light are obvious. The detectivity of the IDA is also illustrated by the distinct water Raman band at 417 nm.
4. The initial fluorescence peak centered at 550 nm is due to the intrinsic fluorescence of riboflavin. Its intensity is decreased when the pH is increased. This illustrates the use of the IDA as a diagnostic tool since potential spectral interferences in a real sample can be readily identified

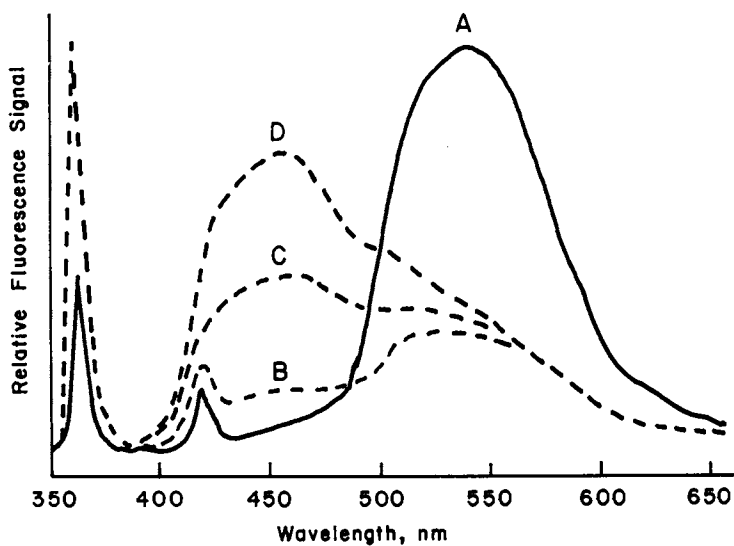


Figure 2. Fluorescence emission spectra taken during the course of the thiochrome reaction. The sample contained thiamine and riboflavin. (Reproduced with permission from Ref. 13. Copyright 1981, Pergamon Press.)

simultaneously as the primary analytical information is obtained. In this case there is a small spectral overlap of the tail of the riboflavin peak with the maximum of thiochrome fluorescence.

5. The computer was programmed to not only calculate the rate of the thiochrome reaction but to subtract a previously stored blank spectrum from spectrum A to obtain a signal proportional to the riboflavin concentration. A detection limit of 7×10^{-10} M was obtained for riboflavin. Thus the multiple wavelength capability of the IDA was used for simultaneous determination of vitamins in one vitamin pill sample to provide a significant time savings over using two analytical procedures on two separate samples.

The diagnostic capabilities of IDA detection were further revealed when applying the thiochrome rate method to other matrices such as urine and cereal (13). Fluorescence spectra of samples can be rapidly obtained at different pH's or excitation wavelengths. Shifts in the maxima of emission spectra under these different conditions reveal the presence of additional fluorescent species. Spectra of potential interferents can be compared to the spectrum of the sample to confirm the presence of certain species.

In the case of urine samples, a fluorescent compound was formed at a rate comparable to the thiochrome reaction when the pH was increased. The appearance of this fluorescence peak was readily observed when the difference in spectra taken at different times was calculated and displayed. This information could not be obtained with a conventional scanning spectrofluorometer.

Clearly by obtaining the complete fluorescence spectrum of sample, unique or unexpected interferences or problems can be identified which might affect the quality of the measurement. Differences in the magnitude of the Rayleigh scatter peak or the general background baseline are often indicative of scattering components in the sample. This can explain a decrease in measurement precision due to an increase in background noise.

Chemiluminescence Measurements. For chemiluminescence measurements, the IDA is used as a fundamental and diagnostic tool rather than a quantitative analysis tool. This is because the light levels in CL are very low, and normally no wavelength selection is employed. Even with a monochromator and a PMT detector, detection limits are seriously degraded.

For most chemiluminescence reactions, a multichannel spectrometer is essential to obtain spectra information because with discrete sampling (injection of the final reagent to initiate the reaction), the CL reaction lasts only at most a few seconds. Some chemiluminescence reactions proceed for minutes or even hours, but still there are usually significant intensity changes over a minute such that a distorted spectrum would be

obtained with a scanning monochromator. We have used the IDA to obtain spectra during six different CL reactions (12,15). Knowledge of the CL spectrum, and hence wavelength of peak emission provides the following advantages.

1. For later quantitative analysis with a PMT, the PMT photocathode response can be chosen for maximum detectability.
2. The CL spectrum can be compared to the absorption spectra of reactants, products, and suspected interfering species to determine if spectral absorption interferences or if self-absorption is significant.
3. The CL spectrum can be compared to fluorescence spectra of intermediates or products to identify the excited species responsible for CL, and hence provide mechanistic information. The spectrum shown in Figure 3 is for the reaction of OCl^- with H_2O_2 . The two peaks at 636 and 703 nm clearly indicate that singlet O_2 is the species responsible for CL.
4. The CL spectrum of the blank reaction can be compared to the CL spectrum obtained with the analyte to establish if the analyte is an activator that increases the rate of the blank CL reaction or induces a new CL reaction to occur.

For CL spectra we found it critical to obtain a "dark" spectrum immediately before automated initiation of the reaction by injection of the final reagent and acquisition of the CL spectrum. Subtraction of the dark spectrum from the CL spectrum compensates for dark signal drift. Also, signal averaging of many spectra (one from each reaction run) is often essential to achieve a reasonable S/N.

Conclusions

Our studies have demonstrated that a molecular luminescence spectrometer with IDA multichannel detector is a powerful quantitative, fundamental, and diagnostic tool. For molecular fluorescence it allows survey spectra to be obtained quickly. The simultaneous wavelength coverage is essential for obtaining fluorescence spectra during kinetic reactions. For steady state or kinetic measurements, complete fluorescence spectral information can be critical in identifying spectral overlap problems in real samples which can go unnoticed in conventional measurements where only one narrow wavelength range is monitored. For CL measurements, the spectral information is useful for diagnosis of spectral absorption problems, as well as for providing mechanistic information.

A molecular absorption spectrophotometer based on diode array detection has been available for many years. Although some commercial molecular fluorescence spectrometers have provision for attaching a multichannel detector, it is

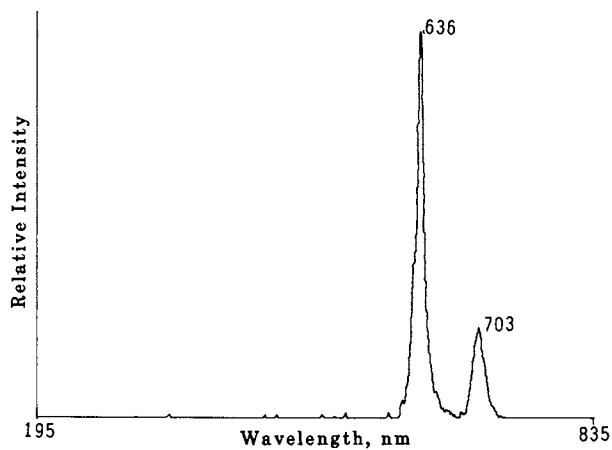


Figure 3. Chemiluminescence spectrum of $H_2O_2-OCl^-$ singlet oxygen reaction. (Reproduced from Ref. 15. Copyright 1981, American Chemical Society.)

surprising that none have been designed totally around an intensified diode array. This should occur in the future.

It is natural to compare the performance of an optimized spectrofluorometer with PMT detection and photon counting signal processing to a spectrofluorometer with IDA detection for routine quantitative measurements. Here the sum of the signals from a few diodes defines a spectral bandpass equivalent to that defined by a monochromator with PMT detection. With our system, some loss of detectability occurs in certain situations.

Detectability is sometimes limited by the readout noise, the dark signal noise, or the size of the individual diode array detector elements. For short integration times (< 1 s), readout noise can be limiting for very weak signals. Others (17) have demonstrated that with proper design of the electrical readout circuitry, the readout noise can be reduced a factor of 10 compared to our system, and single photoelectron detection can be achieved. This would be particularly critical for CL measurements. Often for FL measurements a short integration time is used because diode saturation would occur with longer integration times. Thus the present magnitude of the readout noise is often not limiting because photon carried noise is dominant.

For longer integration times used with weaker signals (or if the readout noise was reduced), dark signal noise can be limiting. In our system, the dark signal corresponds to about 80 photoelectrons/s or about a factor of 10 greater than achieved with a good cooled PMT system. This means the relative dark signal noise is greater with the IDA than a PMT. Reduction of the dark signal rate, especially the component from the intensifier photocathode, would help. Cooling the intensifier photocathode is possible but would be inconvenient. This again would be most critical for CL measurements. We have observed many situations where a CL signal was easily observed with a PMT but was not detectable with the IDA. For many situations with fluorescence measurements, the background fluorescence or scattering signal count rate is greater than the dark signal count rate such that dark signal noise is not limiting.

The readout and dark signal noise problems are aggravated by the small size of the diode detector element compared to a PMT photocathode. In some instances the PMT photocathode views about 100 times more photons/s than a diode detector element (factoring out the intensifier gain). This is the price paid for multiple wavelength coverage. This disadvantage can, of course, be reduced by using a larger spectrograph entrance slit width and summing the signals from n diodes. In the later case, the readout or dark signal noise increases by \sqrt{n} .

As previously mentioned, the S/N near the detection limit is often limited for complex real samples by background signal noise, and above the detection limit, where the analyte fluorescence signal is greater than the background signal, by analytical signal noise. If shot noise is limiting, the smaller detec-

tor element size can still cause a S/N disadvantage since the S/N is proportional to the number of photons viewed per unit time.

The S-series Reticon DA has diodes about 5 times taller (2.5 mm) than the DA we used, and thus should help this problem. Looking to the future, it would be useful to have diode arrays with detector elements 5-10 mm high and with only 100 diodes per inch (250 μm spacing). This would increase the number of photons impinging on a diode array element to be more nearly comparable to that impinging on a PMT. The larger diode width would reduce resolution for the same wavelength coverage but in molecular luminescence high resolution is not often required and typically we sum the signals from 5-10 diodes for quantitative measurements. Hopefully this new diode array could be constructed without a significant increase in the dark signal accumulation rate and with a larger saturation level.

Finally, it should be noted that with our present system and certain samples, background or analyte photon signal fluxes are large enough that measurements are flicker noise limited (noise proportional to the signal). In this case, the IDA already provides detection limits equivalent to that obtained with PMT detection.

Acknowledgments

Acknowledgment is made to the NSF (Grant No. CHE-76-16711 and CHE-79-21293) for partial support of this research, and one of us (M. A. R.) gratefully acknowledges an NSF graduate fellowship and an American Chemical Society, Division of Analytical Chemistry Summer Fellowship sponsored by General Motors Research Laboratory.

Literature Cited

1. Johnson, D. W.; Callis, J. B.; Christian, G. D. Anal. Chem. 1977, 49, 747A.
2. Kohen, E.; Kohen, C.; Salmon, J. M. Mikrochim. Acta. 1976, II, 195.
3. Fillard, J. P.; deMurcia, M.; Gasiot, J.; Chor, S. J. J. Phys. E. 1975, 8, 993.
4. Jadamec, J. R.; Saner, W. A.; Talmi, Y. Anal. Chem. 1977, 49, 1316.
5. Conney, R. P.; Vo-Dinh, T.; Winefordner, J. D. Anal. Chim. Acta. 1977, 89, 94.
6. Conney, R. P.; Vo-Dinh, T.; Walden, G.; Winefordner, J. D. Anal. Chem. 1977, 49, 939.
7. Steinhart, H.; Sandmann, J. Anal. Chem. 1977, 49, 950.
8. Johnson, D. W.; Callis, J. B.; Christian, G. D., "Higher Order Strategies for Fluorescence Analysis Using an Image Detector", Talmi, Y. Ed.; ACS Symposium Series No. 102, ACS: Washington, DC, 1979; p. 97.

9. Jadamec, J. R.; Sanner, W. A.; Sager, R. W., "Versatility of an Optical Multichannel Analyzer as an HPLC Detector", Talmi, Y. Ed.; ACS Symposium Series No. 102, ACS: Washington, DC, 1979; p. 115.
10. Hirschberg, J. G.; Wouters, A. W.; Kohen, E.; Kohen, C; Thorell, B.; Eisenberg, B.; Salmon, J. M.; Ploem, J. S., "A High Resolution Grating Microspectrofluorometer with Topographic Option for Studies in Living Cells", Talmi, Y. Ed.; ACS Symposium Series No. 102, ACS: Washington, DC, 1979; p. 263.
11. Talmi, Y.; Baker, D. C.; Jadamec, J. R.; Sanner, W. A. Anal. Chem. 1978, 50, 936A.
12. Ryan, M. A.; Miller, R. J.; Ingle, J. D., Jr. Anal. Chem. 1978, 50, 1772.
13. Ryan, M. A.; Ingle, J. D., Jr. Talanta 1981, 28, 225.
14. Ryan, M. A.; Ingle, J. D., Jr. Anal. Chem., submitted.
15. Marino, D. F.; Ingle, J. D., Jr. Anal. Chem. 1981, 53, 645.
16. Ryan, M. A.; Ingle, J. D., Jr. Anal. Chem. 1980, 52, 2177.
17. Simpson, R. W. Rev. Sci. Instrum. 1979, 50, 730.

RECEIVED May 23, 1983

Time-Resolved Resonance Raman Spectroscopy of Radiation-Chemical Processes

G. N. R. TRIPATHI

Radiation Laboratory, University of Notre Dame, Notre Dame, IN 46556

A tunable pulsed laser Raman spectrometer for time resolved Raman studies of radiation-chemical processes is described. This apparatus utilizes the state of art optical multichannel detection and analysis techniques for data acquisition and electron pulse radiolysis for initiating the reactions. By using this technique the resonance Raman spectra of intermediates with absorption spectra in the 248-900 nm region, and mean lifetimes > 30 ns can be examined. This apparatus can be used to time resolve the vibrational spectral overlap between transients absorbing in the same region, and to follow their decay kinetics by monitoring the well resolved Raman peaks. For kinetic measurements at millisecond time scale, the Raman technique is preferable over optical absorption method where low frequency noise is quite bothersome. A time resolved Raman study of the pulse radiolytic oxidation of aqueous tetrafluorohydroquinone and p-methoxyphenol is briefly discussed.

Time resolved electronic absorption and emission spectroscopy has been extensively used for solution phase kinetic studies of fast chemical processes initiated by ionizing radiation. A wealth of information on rate parameters and reaction mechanisms on a variety of chemical reactions has been obtained by this technique. As valuable as these techniques are, they have limitations. In particular, the electronic spectra in solution are often broad and featureless and offer little structural information. As a consequence, the identification of a reaction intermediate is based on chemical intuition and not on its spectral characteristics. Moreover, when more than one transient is present in the system with overlapping electronic absorption, the kinetic monitoring of the individual concentration becomes difficult. Vibra-

0097-6156/83/0236-0171\$06.00/0
© 1983 American Chemical Society

tional spectra, on the other hand, provide "finger-print" information on molecular structure. However, they have been difficult to generate on reactive species in solutions due to low concentrations generally available for observation and due to their transient existence.

With advent of tunable lasers resonance Raman spectroscopy has developed as a powerful tool for obtaining the solution phase vibrational spectra of molecular species in low concentration. Ordinary Raman scattering has very poor sensitivity and also lacks selectivity. The Raman band-intensities of individual components in a mixture largely depend on their relative concentrations. Resonance Raman occurs when excitation is made in the electronic absorption of a molecule. Then the scattering cross-section is enhanced by several orders of magnitude (2,3). By taking advantage of this resonance enhancement, the Raman spectrum of a low concentration solute can be obtained with reduced interference from the solvent Raman lines. Resonance Raman spectra of radicals as low as 10^{-7} M in concentration are reported (3). By comparing the spectra recorded in resonance and off resonance regions, the resonant scatterer and solvent Raman bands can be easily distinguished. If several species are present in the system, the Raman spectra of each one can be excited selectively by tuning the excitation wavelength into their electronic absorption bands. The resonance Raman spectra exhibit selective resonance enhancement of only those fundamental vibrations which couple with the electronic transition in resonance, and therefore, are simple and easier to interpret. Furthermore, the identification of the resonance enhanced modes can lead to a definite assignment of the resonant electronic transition.

For time resolved studies in solutions the Raman spectra must be generated by short laser pulses, and advantage of the resonance effect must be taken to selectively enhance the Raman intensity of the transient. Recent developments in the time resolved resonance Raman spectroscopy (TRRS) are mostly based on the short pulse laser excitation and optical multichannel detection. Bridoux and Delhaye (4) were the first to introduce this technique in Raman spectroscopy. The first transient Raman spectrum (p-terphenyl anion) was observed at Riso National Laboratory, Denmark, in 1976 by generating radicals by a single electron pulse obtained from a Febetron accelerator (repetition rate, 0.01 Hz) (5). The early developments (1976-1978) in TRRS, with applications in photochemistry and photobiology, are discussed by M.A. El-Sayed (6). In the last four years (1978-1982) improvements in the multi-channel photon detector and low jitter short pulse laser technology have greatly expanded the scope of studies by TRRS. Recently, this technique has been extended to a wide range of applications involving chemical and biochemical reactions, physical relaxation phenomena, surface and micellar reactions, combustion diagnostics, analytical microanalysis and electro-chemistry (7).

Electron pulse radiolysis is a well established method for initiating fast chemical reactions in controlled conditions, and for producing a high concentration of transient species in a short time, facilitating their observation by TRRS technique. However, very few laboratories have demonstrated capability to carry out such experiments (5,8). A single pulse Raman experiment such as used at Riso, Denmark, requires a high laser pulse energy for scattering. This can induce unwanted photochemical and nonlinear effects. An important advantage in optical multichannel detection lies in its capability to integrate the data from a large number of pulses in a reasonable time to improve signal/noise ratio. However, in single pulse experiments this advantage is lost. By using an electron accelerator which can be operated at a high repetition rate, the Raman spectra generated by a large number of low energy laser pulses can be integrated and averaged in a short time. We have applied this approach in developing a time resolved resonance Raman apparatus which will be described here (11).

In the time resolved Raman measurements on radiation-chemical systems, optical multichannel detection offers some distinct advantages over the photon counting techniques. The intense Cerenkov pulse associated with the electron pulse is intense enough to saturate a photomultiplier tube (PMT). In an optical multichannel detector, the Cerenkov pulse can be effectively gated off by turning the detector on within a few nanoseconds after the electron pulse is over. Apart from this, such spectra are free from the variation in electron or laser pulse intensity unlike the spectra obtained by single channel devices.

Description of the Apparatus

Fig. 1 shows a schematic of the time resolved resonance Raman apparatus for radiation chemical studies. The essential components of the experimental set up are (a) a pulsed electron radiation source for inducing the reactions, (b) a tunable pulsed laser to probe the Raman scattering, (c) a Spex double monochromator for analyzing the scattered light, and (d) a gated detector for recording the spectra.

The electron accelerator employed has been an AS 2000 Van de Graaff accelerator manufactured by High Energy Corporation, Burlington, Mass. The electronic control circuit has been modified considerably, and at present, this accelerator is capable of delivering 30 ns to 5 μ s electron pulses of 2 - 2.5 MeV energy and \sim 1.2 A current at a repetition rate of 60Hz or less. The accelerator can also be operated in the continuous beam mode. The focussed beam has a diameter of 0.3 cm at the output window.

A nitrogen or excimer pumped dye laser has been used as the excitation source. To avoid unwanted photochemical effects, the laser pulse energy used for scattering has been less than 0.5 mJ. The Van de Graaff accelerator and laser are triggered externally

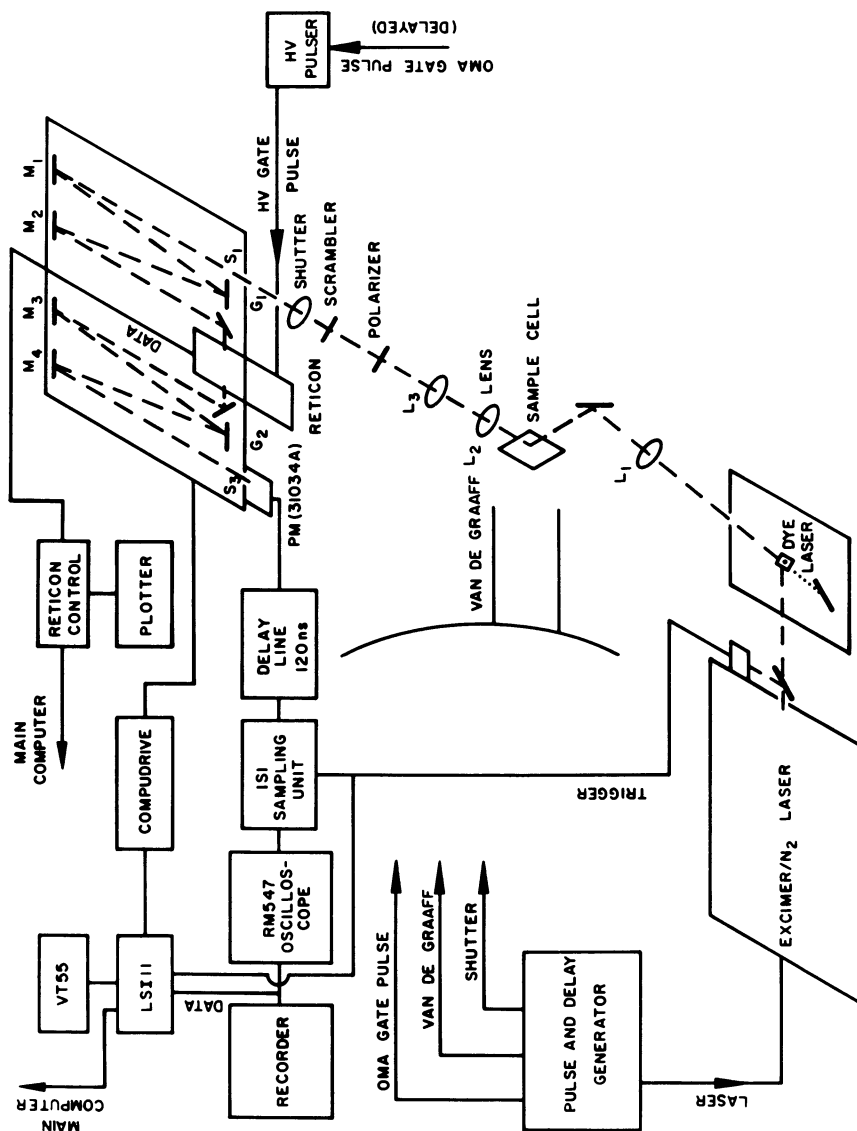


Figure 1. Schematic of the time-resolved resonance Raman apparatus for radiation-chemical studies.

by TTL pulses derived from a common pulse generator for synchronized operation. The electron irradiation is done from the side of the Raman cell, and the laser excitation from the bottom. The laser beam is passed through the irradiated region within 1 mm of the exit window of the Raman cell. The scattered light is collected normal to the plane of the electron and laser beam by a lens of short focal length, and focussed on the spectrometer slit by another lens of f/n comparable to that of the spectrometer ($f/7.8$). A polarization scrambler is inserted in the optical path before the slit to compensate for the polarization effects of the spectrometer gratings. For polarization studies of the Raman bands a polarizer is introduced in the optical path before the scrambler. A Spex 1402 spectrometer (0.85 m, Czerny Turner) with holographic gratings (1800 groves/mm) has been used as the dispersive element. The Raman scattering is detected by an optical multi-channel analyser (OMA), EG & G-PARC model 1215 utilizing a microchannel plate intensified diode array detector model 1420. With the detector placed in the focal plane of the first stage of the spectrometer, approx. 450 cm^{-1} of the spectrum can be recorded on the 700 intensified channels, and averaged in the memory or directly on target. The detector is operated in gated mode at gate pulse width in the range of 5–20 ns and its operation is synchronized with the Raman signal. By gating the detector the Raman spectra produced a few nanoseconds after the termination of electron pulse can be obtained. The time resolution is achieved by delaying the laser pulse electronically with respect to the electron pulse.

A PMT detector mounted at the exit slit of the second stage of the Spex spectrometer is used primarily for alignment purposes. The PMT signal is sampled by a LSI Tektronix sampling oscilloscope gated at the peak of the laser pulse. The output of the sampling unit is digitized and processed by an LSI 11/2 microcomputer interfaced to a PDP 11/55 computer to store the data files. The LSI 11/2 can be used to rotate the gratings with precision, scan a spectrum, control the experiments and carry out the signal averaging task. PMT detection in pulse radiolysis experiments has been used only for long-lived species (10). By use of an appropriately synchronized fast electromechanical shutter, it is possible to block the Cerenkov pulse, while allowing the Raman signal to reach the spectrometer. However, even with this arrangement, it is difficult to employ PMT detection for studies at times shorter than milliseconds.

The Raman cell used in these studies has to be small in volume to insure its uniform irradiation. A cylindrical Suprasil quartz cell, 0.1 – 0.2 ml in volume with optically flat bottom window, with an inlet on the side near the bottom and an outlet at the top, has been found quite suitable. To avoid product accumulation and bubble formation due to localized heating, the solution is flowed continuously and also precooled with iced water before entering the Raman cell. For deoxygenation, the

solution is bubbled with a mixture of two gases instead of one ($N_2O + N_2$ or $Ar + N_2$) to avoid saturation. This is necessary to prevent bubble formation.

This apparatus is suitable for transient Raman studies of radiation-chemical intermediates with absorption spectra ($\epsilon > 10^4 M^{-1} cm^{-1}$) lying in the region 248-900 nm, and mean lifetimes > 30 ns.

Application

Using this technique, we have examined the resonance Raman spectra of a number of phenoxyl (eg. Fig. 2) and semiquinone radicals produced in the electron pulse radiolysis of corresponding phenols and hydroquinones (9-15). These radicals absorb in the 350-500 nm region and exhibit only moderate resonance enhancement (extinction coefficient, $\sim 3-7 \times 10^3 M^{-1} cm^{-1}$). However, we have obtained excellent Raman spectra and also were able to follow the decay kinetics. We cite here two examples which demonstrate the quality of the results obtained, and also the advantages of this technique over the optical absorption method.

Electronic absorption spectrum of tetrafluoro-p-benzosemiquinone (TFPBSQ) anion (13) is difficult to distinguish from its protonated counterpart (p-benzosemiquinone; PBSQ) (9). We present in Fig. 3 the resonance Raman spectra of TFPBSQ and PBSQ radicals using optical multichannel detection. The semiquinone radicals were produced by 1 μs electron pulse radiolysis of a 2mM hydroquinone aqueous solution (N_2O saturated, pH ~ 11) and were measured 10 μs after the electron pulse. These spectra were obtained by averaging over approx. 2200 individual spectra, accumulated at a rate of 7.5 spectra per second. The S/N ratio for the most intense peak is better than 100. The primary oxidizing species in this case has been the OH radical. Secondary oxidation of hydroquinone by Br_2 , produced in N_2O saturated, 0.1 M KBr solutions, yield identical Raman spectra. The Raman spectra of the two radicals show characteristic manifestation of their structural differences in contrast to the similarity in their electronic absorption spectra. The prominent peaks at 1620 cm^{-1} (CC stretch) and 1435 cm^{-1} (CO stretch) in PBSQ are shifted to 1677 cm^{-1} and 1556 cm^{-1} respectively in TFPBSQ. The TFPBSQ spectrum shows no Raman band in the frequency region 500-1500 cm^{-1} , although one at 1161 cm^{-1} (assigned to CH bend) is observed in the PBSQ spectrum.

TFPBSQ radical is observed to decay at ms times in time resolved Raman and optical absorption experiments (13). However, in this time domain, the low frequency noise is quite bothersome in kinetic measurements by the latter method. The Raman measurements are free from such disturbances. Fig. 4 depicts the decay of the Raman signal (1677 cm^{-1} band) of TFPBSQ (initial concentration, approx. 50 μM) measured at different time delays of the probe laser pulse (437 nm) after the electron beam. While the

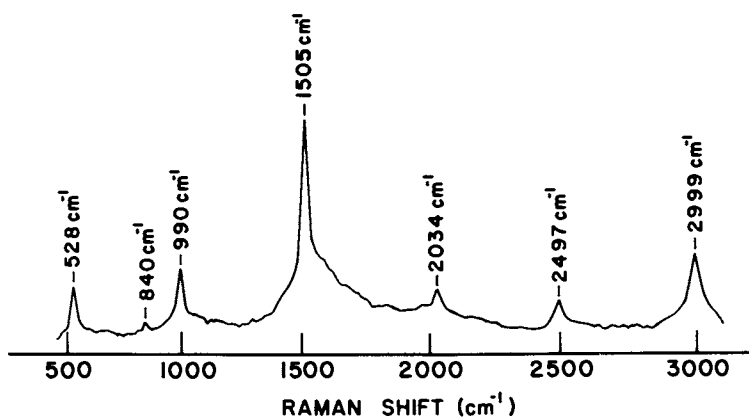


Figure 2. Resonance Raman spectrum of phenoxyl radical excited at 399 nm (excimer-pumped dye laser), 0.5 μ s after the electron pulse. Radical concentration is approximately 10^{-4} M. The S/N ratio for the 1505- cm^{-1} band is better than 50/1.

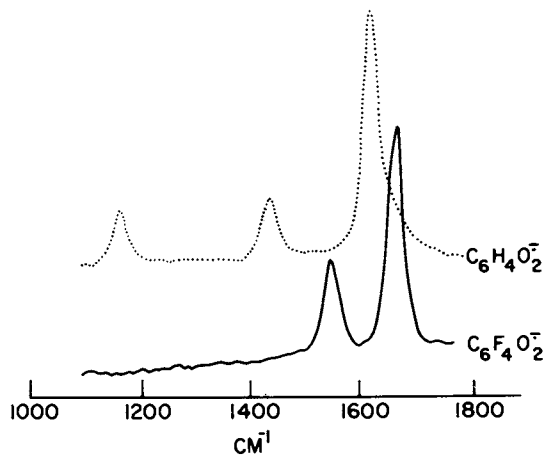


Figure 3. Resonance Raman spectrum (1000–1800 cm^{-1}) of tetrafluoro-*p*-benzoquinone radical anion ($\lambda_e = 437.8$) observed 10 μ s after its creation by 1 μ s electron pulse radiolysis of a basic solution of tetrafluorohydroquinone (2×10^{-3} M; pH \sim 11) in water. The dotted line shows the Raman spectrum of *p*-benzoquinone anion obtained under similar conditions.

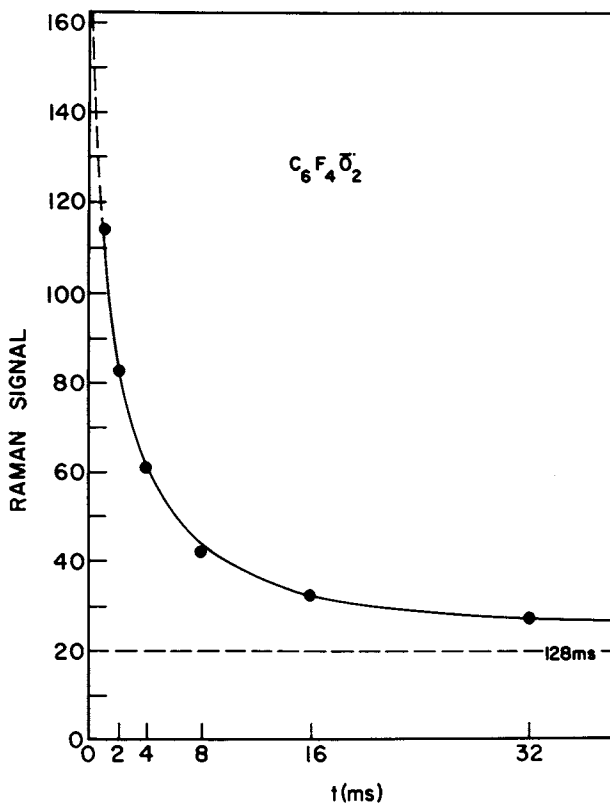
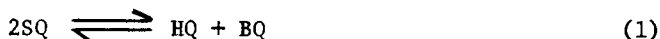


Figure 4. Decay of the Raman signal of tetrafluoro-*p*-benzoquinone anion (1677-cm^{-1} band) as a function of time (Δt) between the irradiation pulse and the probe laser.

initial decay is quite rapid, the kinetics are obviously complicated since the residual signal magnitude at 128 ms delay (20%) is appreciably greater than 2-3% magnitude expected if the limiting decay rate represents a second order process. This radical, very probably, decays by disproportionation.



which explains the persistence of its signal at 128 ms. The rate constant for disproportionation was estimated at approx. $10^7 \text{ M}^{-1} \text{ s}^{-1}$. From a study of the effect of hydroquinone (HQ) concentration on semiquinone (SQ) decay, the equilibrium constant for this reaction (eq. 1) is estimated at approx. 100.

The electron radiolytic oxidation of para substituted phenols in basic aqueous solutions produces a phenoxy radical along with p-benzosemiquinone anion depending on the site of the OH attack. The absorption spectra of these two radicals overlap (400-460 nm). The time resolved resonance Raman technique can be used to obtain the spectra of both the radicals and also for estimating the relative yields of the two reactions. In Fig. 5 the Raman spectra ($1400-1700 \text{ cm}^{-1}$) obtained at different time intervals after the pulse radiolysis of a 2 mM aqueous solution of p-methoxyphenol (N_2O saturated; $\text{pH} \sim 11$) are depicted. The Raman excitation wavelength was 437.8 nm. The Raman spectra obtained between 100 μs and 10,000 μs do not show any observable variation in intensity or peak positions and are identified with p-benzosemiquinone anion. The spectrum shown in Fig. 5d has approximately one fifth the intensity of a spectrum obtained under identical conditions in the pulse radiolysis of a 2mM hydroquinone solution. Therefore, approx. 20% of the OH radicals, produced by the reaction of electron pulse with N_2O saturated water, are estimated to attack at the OCH_3 site. The Raman spectra obtained between 100 ns - 10 μs clearly show the presence of another species with a decay time at the microsecond range along with the long lived species (PBSQ). After subtracting digitally the PBSQ contribution (Fig. 5d) from the 100 ns data (Fig. 5a) the Raman spectrum of the short lived species, identified as p-methoxy-phenoxy radical, is obtained (Fig. 5e). Since the PBSQ radical is relatively less reactive, its Raman bands can be used as an internal standard marker for following the kinetic behavior of p-methoxyphenoxy radical. From the observed spectral intensities the Raman scattering cross-section of PBSQ vibrations is estimated to be approx. 2-5 times higher than that of p-methoxy-phenoxy vibrations, at 437.8 nm.

In summary, we have combined state of the art optical multi-channel analysis techniques with the well established method of electron pulse radiolysis to construct a pulsed laser Raman spectrometer for time resolved studies of transient intermediates in solution. This apparatus can be applied to time resolve the vibrational spectral overlap between transients decaying at differ-

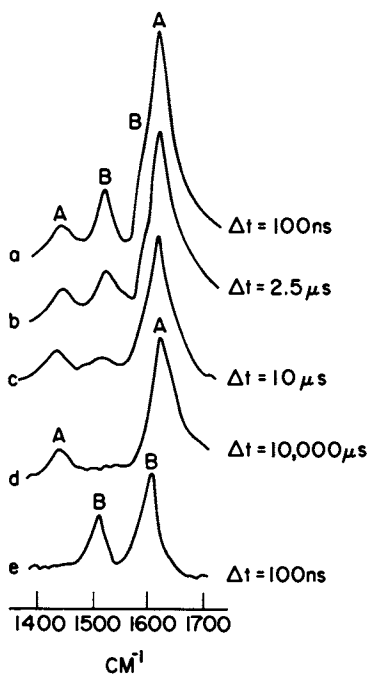


Figure 5. Resonance Raman spectra ($1400\text{--}1700\text{ cm}^{-1}$) of transient intermediates produced in the pulse radiolysis of a 2 mM aqueous solution of *p*-methoxyphenol (N_2O saturated; $pH \sim 11$). Key: a-d, the spectra obtained at different times (Δt) after the electron pulse; d, the spectrum of *p*-benzosemiquinone anion (marked A); and e, the spectrum of *p*-methoxyphenoxy radical (marked B) obtained after subtracting d from a. This figure illustrates the use of time-resolved resonance Raman spectroscopy to time-resolve the spectral overlap between transients decaying at different time scales.

ent time scales, identify them on the basis of their characteristic Raman bands, and to elucidate their structure as manifested in their vibrational spectra. Their reaction dynamics can be followed by monitoring the temporal changes of the well resolved Raman peaks. The resonance Raman band intensities contain useful information for assigning the "poorly resolved" electronic spectra of intermediates in solution. For example, for the 400-450 nm electronic absorption in p-benzoquinone anions conflicting assignments have been proposed (${}^2B_{3g} \rightarrow {}^2B_{1u}$ and ${}^2B_{3g} \rightarrow {}^2A_u$) by the quantum chemists. However, on the basis of the resonance Raman studies of this radical, we have clearly shown the electronic transition to be ${}^2B_{3g} \rightarrow {}^2B_{1u}$ (9,10). The time resolved resonance Raman spectroscopy, is no doubt, a powerful new technique for investigating the radiation induced processes in chemical, biological and physical systems.

Acknowledgment

I wish to thank Professor Robert H. Schuler, Director of the Notre Dame Radiation Laboratory, for his advice and encouragement in the development of this technique. The TRRS applications cited in this paper are results of our collaborative work.

Literature Cited

1. The research described herein was supported by the Office of Basic Energy Sciences of the Department of Energy. This is Document No. NDRL-2433 from the Notre Dame Radiation Laboratory.
2. Champion, P.M.; Albrecht, A.C. Ann. Rev. Phys. Chem. 1982, 33, 353. Tang, J; Albrecht, A.C. "In Raman Spectroscopy"; Szymanski, H., Ed.; Plenum: New York, 1970, Vol.II, p.33.
3. Tripathi, G.N.R. Chem. Phys. Lett. 1981, 81, 375.
4. Bridoux, M.; Delhaye, M. in "Advances in Infrared and Raman Spectroscopy"; Clark, R.; Hester, R.E., Eds.; Hyden, Vol.II, p. 140.
5. Pagsberg, P; Wilbrandt, R.; Hansen, K.B.; Weisberg, K.V. Chem. Phys. Lett. 1976, 39, 538. Hansen, K.B.; Wilbrandt, R.; Pagsberg, P. Rev. Sci. Instrum. 1979, 50, 50.
6. El-Sayed, M.A. in "Multichannel Image Detectors"; Talmi, Y., Ed.; ACS SYMPOSIUM SERIES No. 102, ACS: Washington, D.C. 1979; p. 215.
7. Proceeding of the "International Conference on Time Resolved Vibrational Spectroscopy", Lake Placid, New York, Aug. 16-21, 1982; G. Atkinson, (Department of Chemistry, Syracuse University), Ed.. The references on most of the time resolved vibrational spectroscopic applications between 1976-82 can be obtained from the papers presented in this conference.

8. Dallinger, R.F.; Farquharson, S.; Woodruff, W.H.; Rogers, M.A.J. J. Am. Chem. Soc. 1981, 103, 7033; Lee, P.C.; Schmidt, K.; Gordon, S.; Meisel, D. Chem. Phys. Lett. 1981, 80, 242.
9. Tripathi, G.N.R. J. Chem. Phys. 1981, 74, 6044.
10. Tripathi, G.N.R.; Schuler, R.H. J. Chem. Phys. 1982, 76, 2139.
11. Tripathi, G.N.R.; Schuler, R.H. J. Chem. Phys. 1982, 76, 4289.
12. Tripathi, G.N.R.; Schuler, R.H. Chem. Phys. Lett. 1982, 88, 253.
13. Tripathi, G.N.R.; Schuler, R.H. J. Phys. Chem. (in press).
14. Tripathi, G.N.R.; Schuler, R.H. Chem. Phys. Lett. (in press).
15. Schuler, R.H.; Tripathi, G.N.R.; Prabenda, M.; Chipman, D.M. J. Phys. Chem. (in press).

RECEIVED June 7, 1983

Picosecond Emission Spectroscopy with Intensified Photodiode Arrays

P. F. BARBARA and A. J. G. STRANDJORD

Department of Chemistry, University of Minnesota, Minneapolis, MN 55455

A spectrometer for recording time and wavelength resolved fluorescence data is described in detail. The instrument employs non-linear optical techniques and photodiode array detection to yield emission spectra at variable delay times after molecular excitation. Examples are given of the utilization of the apparatus in the study of the excited state relaxation of aromatic molecules. Experiments to evaluate the accuracy of the technique are also presented.

Following photo excitation a solution sample returns to thermal equilibrium by a variety of photochemical and photo-physical processes. The faster processes, e.g. vibrational relaxation and solvent relaxation, have only recently begun to be studied by direct kinetic methods (1-5). Picosecond emission spectroscopy has been especially useful in elucidating these ultrafast processes (1,3,5). As electronically excited molecules relax, their fluorescence spectrum shows time dependence that reflects the relaxation processes.

Many features of the emission spectrum can show time dependence, including the spectral shape (1,3,6-9), the peak intensity, the linear polarization (10) and, in principle, the circular polarization (11). In extreme cases, the emission spectrum can actually have two separate fluorescence bands from two different isomers of the electronically excited molecules (12-15). For molecules with this behavior, it is possible to determine the kinetics of excited state isomerization by transient emission spectroscopy.

If one ignores polarization effects, the ideal experimental data for the transient emission spectrum of a molecule would be a high resolution three dimensional plot of emission-intensity versus emission-wavelength and delay time after molecular excitation. Most published transient emission data, however, are of the form integrated emission intensity over all emission-wavelengths versus delay time. These data, obviously, have less useful information than the multidimensional approach.

0097-6156/83/0236-0183\$06.00/0
© 1983 American Chemical Society

In the present paper we describe an apparatus for recording transient emission spectra that yields data which approach the ideal multidimensional case. We emphasize in the discussion the advantages of multichannel detection for transient emission data. We also briefly compare our approach to alternative methods for recording time and wavelength resolved fluorescence data on the picosecond time scale.

Several experimental methods can be found in the literature for recording picosecond time and emission-wavelength resolved fluorescence data. They can be classified according to how many data points, $I(t_i, \lambda_j)$, are acquired for each pulse of the excitation laser, where $I(t_i, \lambda_j)$ is a single point on the multidimensional representation of time and wavelength resolved emission data. The most common technique is to record, for each laser pulse, the full kinetics at a single narrow emission wavelength region with a streak-camera/two dimensional optical multichannel analyzer. This approach yields excellent kinetic data, i.e. $I(t, \lambda = \text{constant})$, but is not well suited for recording emission spectra at fixed delay time, i.e. $I(t = \text{constant}, \lambda)$.

A few reports have appeared on combining the streak camera temporal dispersion with polychromators and three dimensional optical multichannel detection. This approach yields three dimensional fluorescence data for each laser pulse. With the present technological limitations of three dimensional detectors and streak cameras, however, data of this type suffer from low wavelength resolution. As detector and streak camera technology improve, this technique may become the method of choice for time and wavelength resolved emission spectra.

An excellent alternative to the streak camera approach is fluorescence time resolution by the "up-conversion" method, which we describe in detail below. In the simplest form of this technique, non-linear optical methods are employed to essentially construct a picosecond "shutter" or "gate". In most applications a single emission datum is acquired for each laser pulse, i.e. $I(t = \text{constant}, \lambda = \text{constant})$. By repeating the experiment at different delay times, kinetic traces can be acquired that are of comparable quality to those obtained by streak camera methods (16-17). Alternatively, if delay time is held constant but λ is scanned, high quality emission spectra can be obtained (3).

In this paper we describe a novel apparatus that combines the "upconversion" method with multichannel optical detection. This instrument records, for each laser pulse, a high-resolution emission spectrum at a chosen delay time, i.e. $I(t = \text{constant}, \lambda)$.

The paper is organized in the following way. First, a brief introduction to fluorescence upconversion and other non-linear processes is given. This is followed by a description of an apparatus for making up converted fluorescence measurements, and experimental examples for this instrument. The following text describes the advantages of optical multichannel detections for

these types of measurements, and compares multichannel detection to single channel measurements. Finally, some further measurements on the performance of the apparatus are presented.

Apparatus

Background. The discussion begins with a brief review of how non-linear optical crystals are practically utilized in laser spectrometer systems. The most common use of these materials is the production of laser radiation at different frequencies than that of the laser fundamental, W . For example, second harmonic generation is often utilized to create radiation at $2W$ from the fundamental light W . Another technique often used is sum frequency mixing in non-linear optical materials. For example, light of frequency $3W$ can be generated efficiently by mixing W light with $2W$ light. The $2W$ light is prepared independently by second harmonic generation. In general, sum frequency mixing can be employed to produce radiation at a sum-frequency, W_s , of two light beams of arbitrary frequency W_a and W_b , i.e. $W_s = W_a + W_b$. In practice, the efficiency of the mixing process depends on many parameters which we describe below.

Over 15 years ago Duquay and Hansen (18) suggested an alternative use of sum-frequency generation, namely picosecond optical sampling. This technique has become a popular method for measuring the duration of ultra-short light pulses. It also has been used recently in time resolved molecular fluorescence experiments, the subject of this paper. In this application, sum frequency mixing is usually called upconversion. The fluorescence radiation of W_f is mixed (upconverted) in a nonlinear crystal with a picosecond duration "gate" pulse (W_g) to produce upconverted light at $W_f + W_g$. The intensity of the upconverted light is linearly related to the intensity of the fluorescence that arrives at the crystal at the same time as the gate pulse. The incorporation of conversion in a practically useful fluorescence spectrometer is described in the next section.

Overview. The experimental apparatus we describe (Fig. 1) is a time and wavelength resolved fluorescence spectrometer which was constructed in our laboratory in 1981. Two types of picosecond experimental data can be acquired with the apparatus: 1) time-resolved fluorescence traces at narrow (15 nm) emission wavelength regions (method A) and 2) wavelength-resolved "gated" fluorescence spectra of fixed delay times after molecular excitation (method B). In principle, both techniques can yield the same information by repeating method A at several emission wavelengths or by repeating method B at different delay times. In practice, however, method A is better suited for determining quantitative kinetic data, while method B is more appropriate for studying subtle time-dependent fluorescence spectral shape and band position variations.

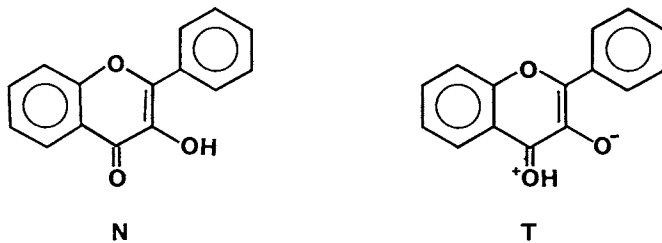
The apparatus employs a passively mode locked Nd/YAG laser oscillator, a Pockel cell pulse extractor, and Nd/YAG laser amplifier to produce ~ 10 mJoule, 30 psec laser pulses at 1064 nm. Non-linear crystals convert $\sim 30\%$ of this light to 355 nm, which is used for excitation of the sample. The optical path length of the 355 nm light is varied by a computer-controlled time delay stage.

The sample fluorescence is time resolved by the upconversion method. The fluorescence is upconverted in a Type II KDP crystal by a portion of the 1064 nm light which travels a fixed path that is portrayed in Figure 1. The "upconverted" light intensity ($\lambda_{uc}^{-1} = \lambda_{fl}^{-1} + (1064 \text{ nm})^{-1}$) from the KDP upconverting crystal is measured as a function of delay stage length to extract the fluorescence time dependence. This approach, yields accurate kinetic traces with excellent sensitivity (1,3,16,17).

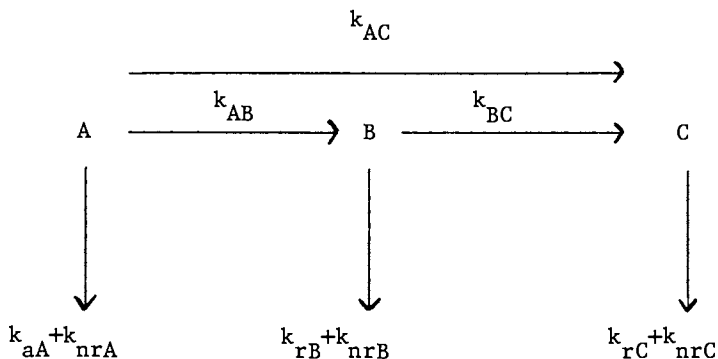
Experimental Examples

Method A. For Method A we determine the upconverted light pulse intensity with a photomultiplier tube (pmt) which is interfaced by integrator/hold and analog/digital electronics to our Cromemco computer. Data collection is automated to enhance accuracy and the signal/noise ratio by i) signal averaging over several laser pulses, ii) correcting the data for laser energy fluctuation, and iii) rejecting data from poorly mode-locked pulses. The repetition rate of the laser is 10 pulses per second. The digitally recorded signal is the ratio of upconverted light intensity to total time integrated fluorescence intensity as a function of delay stage length. This ratio is especially insensitive to laser intensity fluctuations and other sources of noise and error (16).

Method A is particularly useful for studying the dynamics of dual fluorescent systems, including excimer formation and excited state isomerization. For example, we have studied the dynamics of the excited state isomerization of 3-hydroxyflavone (3HF). The stable ground-state form of 3HF is the "normal" (N) isomer. Optical excitation of N yields N*, which rapidly rearranges to give a different electronically excited isomer, namely the "tautomer" form (T*). The fluorescence maxima for the N* and T* forms are 413 nm and 543 nm, respectively.



In a recent paper (12) we showed that the species responsible for the green (543 nm) fluorescence of 3HF was formed kinetically from blue (413 nm) emitting species by two kinetic components. We rationalized this complex behavior by a model (Scheme 1) in which there are two pathways for excited state isomerization, i.e., a slow and a fast component.



Scheme 1

Here A is the initially state which is the source of the fast component of the blue emission; B is a "relaxed" form of A which fluoresces to give the slower blue component; C is the sole source of green emission. k_{nrA} and k_{nrB} are the non-radiative decay rates for A and B, and k_{rA} and k_{rB} are the radiative rates for these species. C represents the T* tautomer and A and B are two different forms of N*, see Strandjord, et al. (12), for further details. k_{AC} and k_{BC} are the "fast" and "slow" rate constants for ESIPT, respectively.

Figure 2 portrays time integrated fluorescence spectra of 3HF that reveal the dual fluorescence bands of this molecule (12-15). Spectra are presented for methanol solvent and D₁-Methanol solvent for which the 3HF alcoholic proton is exchanged with a deuteron. Kinetic traces recorded by method A for 3HF are shown in Figure 3. Each trace was acquired in ~ 500 sec. of instrument time, i.e., 5000 laser pulses.

The "blue" emission decays with a "short" and "long" first-order time constant, τ_A and τ_B , respectively. The green emission, in turn, is formed with these same time constants. In many environments, however, τ_A is much less than our instrument time resolution (~ 30 psec), see below. In these cases, the blue emission appears to exhibit a single decay time, τ_B . Accordingly, the green emission formation kinetics shows an "immediate" component and a "delayed" component associated with τ_A and τ_B ,

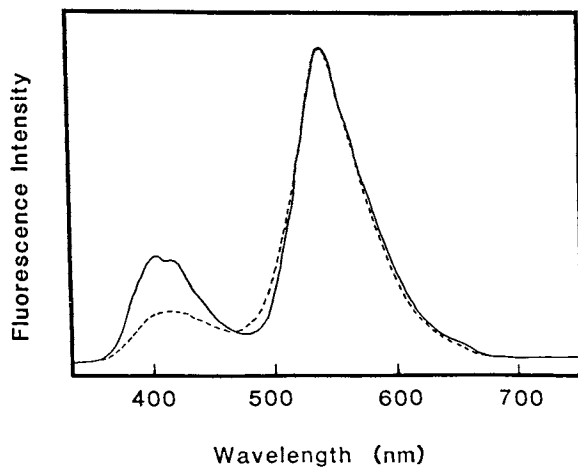


Figure 2. Time-integrated fluorescence spectra (297 K) of 10^{-5} M solutions of 3 HF in methanol (—) and MeOD (---). The spectra are plotted on the same relative intensity scale.

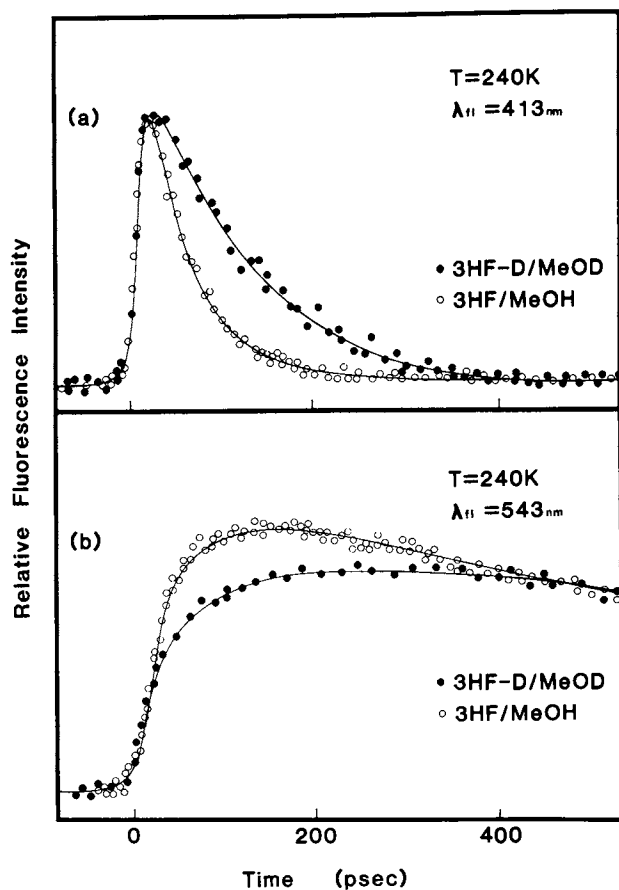


Figure 3. Time-resolved fluorescence traces of 3 HF in MeOH and MeOD acquired by Method A (see text). The 413-nm emission was indirectly monitored by upconversion at 297 nm, and the 543-nm emission was monitored by upconversion at 360 nm. The points in the figure are experimental data, and the solid lines are computer fits to this data. (The fitting algorithm has been described elsewhere (1).)

respectively, see Figure 3. Either the blue or green emission can, therefore, be used to determine τ_B (12).

We have been able to study the experimentally determined time constants, e.g. τ_B , for 3HF fluorescence as a function of solvent, temperature and isotopic substitution of the solute and solvent. These data, when combined with other spectroscopic measurements have been employed in the investigation of the isomerization mechanism of 3HF.

Method B. Very few molecules exhibit dramatic fluorescence dynamics of the type observed for 3HF. In most cases the observed effects are more subtle, involving a slight time-dependent variation in the fluorescence band profile. Effects of this type can be due to vibrational relaxation, solvent relaxation and torsional relaxation.

We employ method B to study effects of this type. In this mode, our apparatus yields relative high-resolution fluorescence spectra at different time windows after excitation of the sample by the 355 nm pulse. The spectra are acquired by the upconversion method. The upconverted fluorescence spectrum is recorded simultaneously at all monitored wavelengths by an optical multichannel analyzer. It is constructed from a polychromator (HR320 Instruments SA) and an intensified silicon photodiode array detector (Princeton Applied Research Model 1412). The detector is interfaced to our Cromemco computer.

We have used this approach to investigate the excited state relaxation dynamics of 2-(2'-hydroxyphenyl)benzothiazole, HBR (1). The fluorescence properties of this molecule are well described by a kinetic scheme outlined in Figure 4.

Barbara, Brus and Rentzepis recently reported that the rapidly formed (< 4 psec) keto (2) fluorescence spectrum of HBT exhibited a band-shape evolution for ~ 10 psec after excitation of (1) (8). These authors, who monitored the fluorescence kinetics at different 10 nm wide regions, observed that the high energy edge (475 nm) of the keto fluorescence suffered a rapid bathochromic shift for ~ 10 psec. Our time-resolved kinetic traces also exhibit evidence for a short-lived broadened blue edge (1). We have observed that the 460 ± 10 nm emission exhibits a < 10 psec risetime and two lifetimes, one 20 ± 10 psec and the other > 2000 psec. The 490 nm kinetics, in contrast, exhibits a single > 2000 psec lifetime, but two risetimes. One of these is < 10 psec, our instrument resolution with deconvolution, and the other is 30 ± 10 psec. The dual risetime kinetics at 480 nm are clearly distinguishable from the response of our apparatus to emission with a single < 5 psec risetime. We assume that the < 10 psec formation component represents k^{-1} in Figure 4, see reference (1).

In an attempt to further characterize this interesting phenomenon, we have investigated the fluorescence of HBT in argon by method B (1). We observe that the early (~ 50 psec)

fluorescence spectrum of HBT is indeed detectably different from spectra recorded from 100 psec - 2000 psec, see Figures 5 and 6. The 50 psec spectrum as compared to the 250 psec spectrum, on the same relative emission intensity scale, actually shows more intensity at 465 nm but less at 485 nm. This is supported by the experiments described in the previous section. The fluorescence band-shape shows much less evolution during the period 100 - 2000 psec. Figure 5 shows spectra in the region of the onset of 2* emission. Detectable variations between the ~ 50 psec and > 100 psec spectrum are also present in the > 490 nm region, but we have not investigated this wavelength region in detail. The wavelength scales for the upconverted spectra in Figures 5 and 6 were calculated from the formula

$$\lambda_{uc}^{-1} = \lambda_{fl}^{-1} + 1064^{-1} \text{ nm}$$

the λ_{uc} values are the experimentally observed wavelengths, see above.

It is interesting to note that the "gated" spectra are highly reproducible. This is demonstrated in the lower panel of Figure 5 where traces from two separate determinations of the 115 psec spectrum are plotted on the same intensity scale.

The spectra in Figure 5 have not been corrected for the wavelength dependent sensitivity of our apparatus in the "gated" mode. We discuss this subject in detail below. This correction, which should be identical for all time values, is, however, small as judged by a comparison of the non-time-resolved emission spectrum (Figure 6a) to the late time-gated spectrum which should be responsible for more than 99% of the non-time-resolved fluorescence (Figure 6b).

The time evolution of the fluorescence spectrum of HBT shown in Figure 5 is entirely consistent with the previous proposal that 2* is initially created with excess vibrational energy that dissipates on the 10-30 psec time scale (8). The broadened and shifted high-energy edge of 2* band as compared to the relaxed (> 250 psec) spectrum, seems to be analogous to other examples of fluorescence band-shape time dependence due to vibrational relaxation in the excited-electronic state (2,6). We have concluded, therefore, that 2* is created from the 1* \rightarrow 2* process with an initial vibrational excess.

Photodiode Array Versus Photomultiplier Detection. The advantages of photodiode array detection, PDA, as compared to photomultiplier tube, pmt, detection for emission spectroscopy are well known (19). These advantages are especially important for the specific examples we discuss here, namely, upconverting emission spectroscopy. This is dramatically demonstrated in Figure 7 where we compare single channel pmt versus multichannel PDA detection of a small portion of the upconverted fluorescence spectrum of coumarin 520 in ethanol solvent at room temperature.

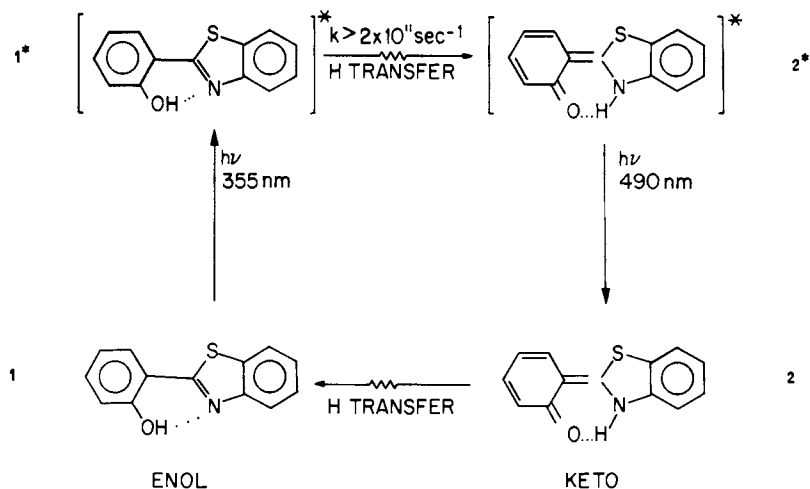


Figure 4. A representation of the phototautomerization mechanism of 2-(2-hydroxyphenyl)benzothiazole (HBT) in nonpolar solvents.

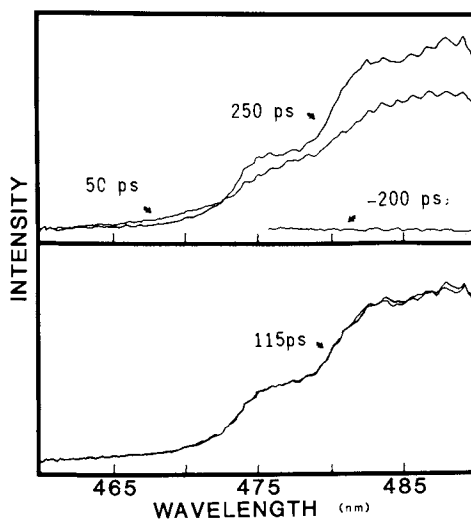


Figure 5. Time-resolved fluorescence spectra of HBT in an argon matrix at 12 K acquired by Method B. The time labels on the spectra represent different delay times with respect to excitation by the 355-nm, 30-ps laser pulse. The wavelength scale, λ_{fl} , has been calculated from the formula

$$\lambda_{fl}^{-1} = \lambda_m^{-1} + (1064 \text{ nm})^{-1}$$

where λ_m is the actual observation wavelength of the upconverted fluorescence. (Reproduced from Ref. 1. Copyright 1983, American Chemical Society.)

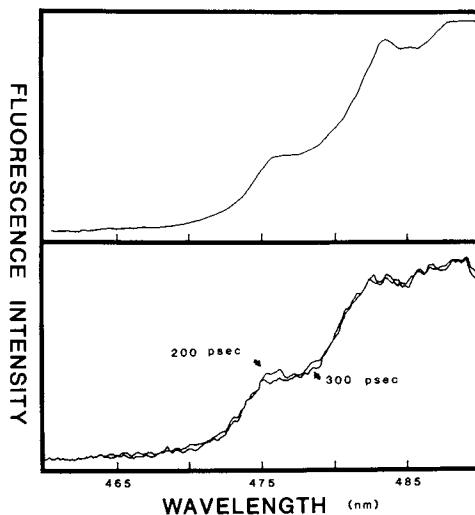


Figure 6. A time-integrated fluorescence spectrum of HBT (top) under the sample conditions described in Figure 5. The bottom panel portrays a spectrum of the type described in Figure 5. (Reproduced from Ref. 1. Copyright 1983, American Chemical Society.)

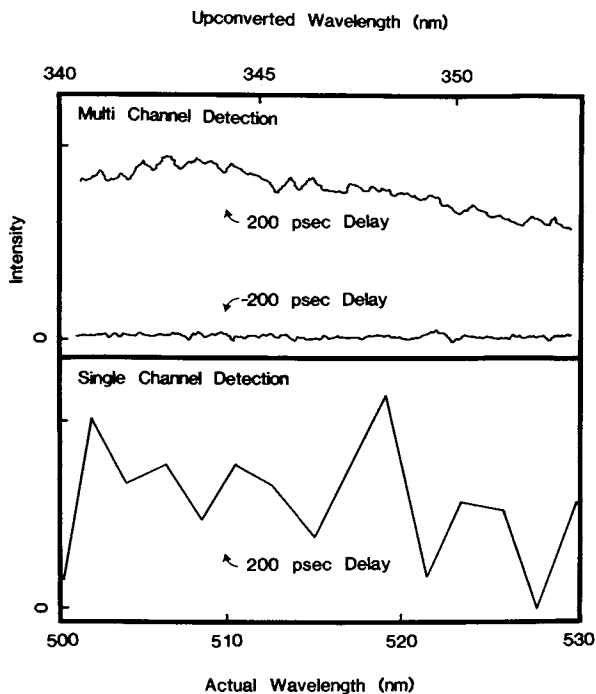


Figure 7. A comparison of photodiode array multichannel detection to photomultiplier tube single channel detection for the upconverted emission spectrum of coumarin 520.

The fluorescence spectrum of this molecule is broad and structureless in the wavelength region of Figure 7. With PDA optical multichannel detection we observe, as expected, no signal at negative delay time with respect to the arrival time of the 355 nm pulse at the sample, and at 200 psec after the pulse arrives, the broad structureless spectrum of coumarin 520 is observed. The experimental parameters were as follows: 1.0 mm entrance slits on the Instruments SA HR 320 spectrometer, total accumulation time 60 sec., a laser repetition rate of 10 pulses-per-second, and certain PDA settings which are described below.

Single channel pmt detection of the same spectrum with the same HR 320 spectrometer exhibits at least on order of magnitude lower signal to noise ratio. For the pmt measurements, entrance and exit slits of 1.0 mm were employed and the HR 320 wavelength was scanned digitally. The total accumulation time was the same for the PDA and pmt determinations.

Why does multichannel PDA detection exhibit such improved signal to noise over single channel pmt detection? A major factor is clearly that the signal averaging intergration time of each of 170 resolution elements in the PDA case is the full acquisition time, i.e., 60 seconds, while the acquisition time for the PMT experiments is a small fraction, 1/20, of the total acquisition time due to the necessity of scanning for single channel detection.

A second very important factor is associated with pulse-to-pulse fluctuations of the laser intensity, which in our system can be as great as ~30%. The PDA experiment for time resolved upconverted spectra is especially insensitive to intensity fluctuations of the laser intensity because the spectrum is acquired simultaneously and the fluctuations of the different channels are correlated. In contrast, for single channel detection these fluctuations are uncorrelated and contribute noise to the spectrum. As mentioned above, we have attempted in the single channel case to correct for these fluctuations by ratio-metry using the time integrated fluorescence intensity as a measure of the laser fluctuation. But our experience is that the correlation of upconverted light intensity with the integrated fluorescence intensity is not perfectly linear, as expected from ideal considerations, and actually exhibits large fluctuations about the expected linear relationship. The nonideality may be due to pulse-to-pulse fluctuations of the spatial characteristics of the laser which could vary the efficiency of upconversion.

A third and final factor that, in principle, can be an advantage of PDA detection is associated with signal averaging. For the PDA measurements the signal averaging for Figure 7 was accomplished primarily by analog intergration of the signal on the photodiode array. In detail, a 20 second delay was incorporated between three read cycles of the PDA, and the signal was digitized only three times, i.e. each read cycle. For the pmt

measurements, in contrast, the signal is digitized for each laser pulse and digitization and readout noise can contribute significantly to the data. In principle, an analog integration scheme might also be incorporated with the pmt detector. In practice, commercially available long time (>1 sec) integrators for pmt detectors are subject to electrical drift which contributes to the overall noise characteristics of the system. Perhaps the important conclusion here is that commercially available PDA detectors like PAR 1420 have superbly constructed signal processing electronics that allow for near ideal analog signal averaging, but comparable equipment for pmt detectors are not, to our knowledge, available.

Instrument Performance

Wavelength Sensitivity. The overall wavelength sensitivity of emission spectrometers plays a central role in determining the accuracy of the recorded data and the range of emission wavelengths that can effectively be studied by a particular apparatus. The upconversion method adds a source of wavelength dependent sensitivity that is both useful and problematic.

On the positive side, upconversion allows efficient detection of red wavelengths (> 650 nm) where direct detection spectrometers are insensitive. For example, for our spectrometer 700 nm fluorescence is upconverted to 422 nm. This latter wavelength is in a region where our pmt and array detectors are quite sensitive.

A disadvantage of the upconversion approach, however, is that the efficiency of non-linear mixing can be a strong function of the wavelengths of each of the beams and their orientation relative to the direction of the optical axis of the non-linear crystal. This phenomenon is a result of the phase-matching requirement for sum frequency generation. A detailed discussion of phase matching in fluorescence upconversion can be found elsewhere (16).

Practically speaking, we have found that it is possible to upconvert an ~ 75 nm wide region of visible fluorescence with a less than 80% drop in efficiency toward the edges of the region. This is accomplished by simultaneously satisfying the phase match requirement at several wavelengths by focussing the fluorescence light in the Type II KDP crystal. The crystal is tilted to maximize the conversion efficiency at the center of the desired region. This approach yields ~ 75 nm wide spectra throughout the visible, near ultraviolet and near infrared region, depending on the crystal angle and the spectrometer settings.

Accurate fluorescence spectra can be produced from the raw upconverted data by suitable data processing on our Cromemco computer. Typically, we correct for the channel dependent gain of the photodiode array and the wavelength dependent efficiency of the upconversion process which we determine independently.

The wavelength axes of the spectra are also calibrated by the fluorescence processing software.

Linearity. A common source of error for picosecond time-resolved emission spectrometers is a non-linear response of the detector to emission intensity. Streak camera temporal dispersors, for example, exhibit a limited dynamic range, which, in unfavorable cases, can lead to severe experimental artifacts (20-21).

The apparatus we describe in this paper has two potential sources of errors due to non-linearity, namely, the upconversion process and the actual detector, i.e. photodiode array or pmt.

The upconversion process can, in principle, be non-linear at high fluorescence light intensity. We have examined the linearity of upconversion for our apparatus by studying the upconverted light intensity versus fluorescence intensity at fixed delay time. The observed dependence in Figure 8 demonstrates that the upconversion process is operating in the linear range for the experimental conditions we typically invoke. The fluorescence intensity in Figure 9 was varied by calibrated neutral density filters. The linearity of the pmt and associated electronics was verified independently.

We have also studied the digital signal intensity versus light intensity behavior of the photodiode array detector used in method B. Non-linear effects have been observed for Vidicon multichannel analyzers when employed in measuring the intensity of picosecond duration light. Photodiode arrays, in contrast, have rarely been employed in picosecond spectrometer, and, we are not aware of a previous study of the linearity of these devices for the detection of high intensity picosecond duration light.

The digital signal intensity from the photodiode array that was described above versus intensity of ~ 50 psec duration light is shown in Figure 9. A linear behavior is, in fact, observed.

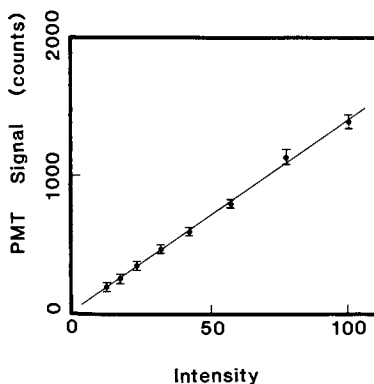


Figure 8. A plot of measured upconverted signal intensity (PMT voltage) vs. fluorescence intensity at fixed delay time. The data were acquired using Method A, and the fluorescence intensity was varied with neutral density filters. PMT voltage was monitored by integrator and hold electronics followed by an analog to digital converter.

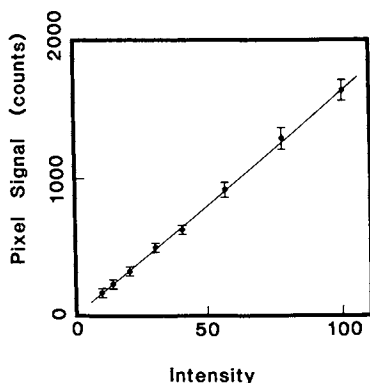


Figure 9. An evaluation of the response of the photodiode arrays signal as a function of light intensity of ~ 50 ps duration. The light intensity was varied with a neutral density filter. The light was created by exciting a solution of tetraphenyl ethylene in hexane with ~ 30 -ps, 355-nm light pulses. This molecule is known to have a fluorescence lifetime of 6 ± 3 ps in these environments.

Acknowledgement

Acknowledgement is made for partial support of this research to the following agencies: 1) the Donors of the Petroleum Research Fund (administered by the American Chemical Society), 2) the Research Corporation and 3) the Graduate School of the University of Minnesota.

Literature Cited

1. Ding, K., Courtney, S.H., Strandjord, A.J.G., Flom, S., Friedrich, D., and Barbara, P.F., *J. Phys. Chem.*, 1983, 87(7), 1184.
2. Barbara, P.F., Rentzepis, P.M., and Brus, L.E., *J. Chem. Phys.*, 1980, 72, 6802.
3. Choi, K., Boczar, B.P., and Topp, M.R., *Chem. Phys.*, 1981, 57, 415.
4. Doany, F.E., Greene, B.I., Liang, Y., Negus, D.K., and Hochstrasser, R.M., in "Picosecond Phenomena", Springer, 1980.
5. Okamura, T., Sumitani, M., Yoshihara, K., *Chem. Phys. Lett.*, 1983, 94(3), 339.
6. Barbara, P.F., Rand, S.D., and P.M. Rentzepis, *J. Amer. Chem. Soc.*, 1981, 103, 2156.
7. Barbara, P.F., Rentzepis, P.M., and Brus, L.E., *J. Amer. Chem. Soc.*, 1980, 102, 2786.
8. Barbara, P.F., Brus, L.E., and Rentzepis, P.M., *J. Amer. Chem. Soc.*, 1980, 102, 5631.

9. Barbara, P.F., Brus, L.E., and Rentzepis, P.M., Chem. Phys. Lett., 1980, 69, 447.
10. Waldeck, D.H., Lotshaw, W.T., McDonald, D.B., and Fleming, G.R., Chem. Phys. Lett., 1982, 88(3), 297.
11. Turner, D.H., Tinoco, I., and Maestre, M., J. Amer. Chem. Soc., 1974, 96(13), 4340.
12. Strandjord, A.J.G., Courtney, S.H., Friedrich, D.M., and Barbara, P.F., J. Phys. Chem., 1983, 87(7), 1125-1133.
13. Itoh, M., Tokumura, K., Tanimoto, Y., Okada, Y., Takeuchi, H., Obi, K., and Tanaka, I., J. Amer. Chem. Soc., 1982, 104, 4146.
14. Sengupta, P.K., and Kasha, M., Chem. Phys. Lett., 1979, 68(2,3), 382.
15. Woolfe, G.J., and Thistlewaite, P.J., J. Amer. Chem. Soc., 1981, 103, 6916.
16. Hallidy, L. A., and Topp, M.R., Chem. Phys. Lett., 1977, 46, 8.
17. Beddard, G.S., Doust, T., Meech, S.R., and Phillips, D., J. Photochem., 1981, 17, 427.
18. Duguay, M.A., and Hansen, J.W., Appl. Phys. Lett., 1968, 13, 178.
19. Talmi, Y., Image Devices in Spectroscopy, this journal.
20. Lieber, A., in "Picosecond Phenomena", Springer Series in Chemical Physics, eds. Shank, C.V., Ippen, E.P., and Shapiro, S.L., (Springer, Berlin, 1976) p. 178.
21. Yu, W., in "Picosecond Phenomena", Springer Series in Chemical Physics", eds. Shank, C.V., Ippen, E.P., and Shapiro, S.L., (Springer, Berlin, 1978) p. 347.

RECEIVED August 12, 1983

Picosecond Spectroscopy and Applications to Chemical and Biological Systems

E. F. HILINSKI, S. V. MILTON, and P. M. RENTZEPIS

Bell Laboratories, Murray Hill, NJ 07974

The mechanisms of a number of photochemical reactions and photophysical processes have been elucidated by means of picosecond emission, absorption, and Raman spectroscopy. Picosecond spectroscopy enables one to observe ultrafast events in great detail as a reaction evolves. Most picosecond laser systems currently rely on optical multichannel detectors (OMCDs) as a means by which spectra of transient species and states are recorded and their formation and decay kinetics measured. In this paper, we describe some early optical detection methods used to obtain picosecond spectroscopic data. Also we present examples of the application of picosecond absorption and emission spectroscopy to such mechanistic problems as the photodissociation of haloaromatic compounds, the visual transduction process, and intermolecular photoinitiated electron transfer.

Picosecond spectroscopy provides a means of studying ultrafast events which occur in physical, chemical, and biological processes. Several types of laser systems are currently available which possess time resolution ranging from less than one picosecond to several picoseconds. These systems can be used to observe transient states and species involved in a reaction and to measure their formation and decay kinetics by means of picosecond absorption, emission and Raman spectroscopy. Technological advances in lasers and optical detection systems have permitted an increasing number of photochemical reactions to be studied in greater detail than was previously possible. Several recent reviews (1-4) have been written which describe these picosecond laser systems and several applications of them

0097-6156/83/0236-0201\$06.00/0
© 1983 American Chemical Society

to important biological and chemical problems. Here we will briefly present several of the earlier as well as more recent optical techniques which have been used to study the transient species and states generated by picosecond laser excitation. We shall also discuss some experiments performed utilizing picosecond spectroscopy which provide examples of the types of problems which can be studied and the detailed information which can be obtained.

Methods of Optical Detection

When the generation of picosecond laser pulses first became possible in the laboratory, methods of electronic detection which currently are in such widespread use for measurements performed on the picosecond time scale, e.g. streak cameras and two-dimensional photodiode arrays, were not readily available to the experimenter. Techniques had to be developed not only to measure accurately the kinetics of photoinitiated events which occur on this ultrashort time scale, but more importantly to monitor the width and shape of the laser pulse to ensure reliable and reproducible generation of these pulses.

Initially a two photon fluorescence (TPF) technique (5,6) was utilized to monitor both chemical kinetics and laser pulses. The TPF apparatus ordinarily consists of a few optical components which direct the laser pulses into an optical cell containing a suitable fluorescent chemical.(7) The laser pulse is then allowed to traverse the cell and reflect back upon itself (Figure 1a). Another arrangement is a triangular configuration of mirrors in which a beam splitter divides the laser pulse into two equal pulses which are then redirected by two mirrors to intersect within the sample cell (Figure 1b). A photograph is made of the resulting fluorescence. The photograph is then analyzed with a densitometer in order to determine the fluorescence intensity versus position. The final densitometer trace is analyzed to extract temporal information about the light pulses.

Another early method used to monitor the laser pulse was the three photon fluorescence (3PF) technique.(8,9) The advantage of 3PF over TPF is two-fold: the contrast ratio is 10:1 for 3PF as opposed to 3:1 for TPF; and in addition to temporal information about the pulses available by TPF, 3PF also provides pulse shape information.(10-13) This additional information is obtained because the third-order correlation function which relates the 3PF intensity to the pulse intensity includes dependence upon the phase of the pulse frequency components.(11) Again, the resulting fluorescence is photographed, and a densitometer trace is made to determine fluorescence intensities. Azulene is an example of a molecule which has been studied quite extensively.(14-20) Typical data are shown in Figure 2.

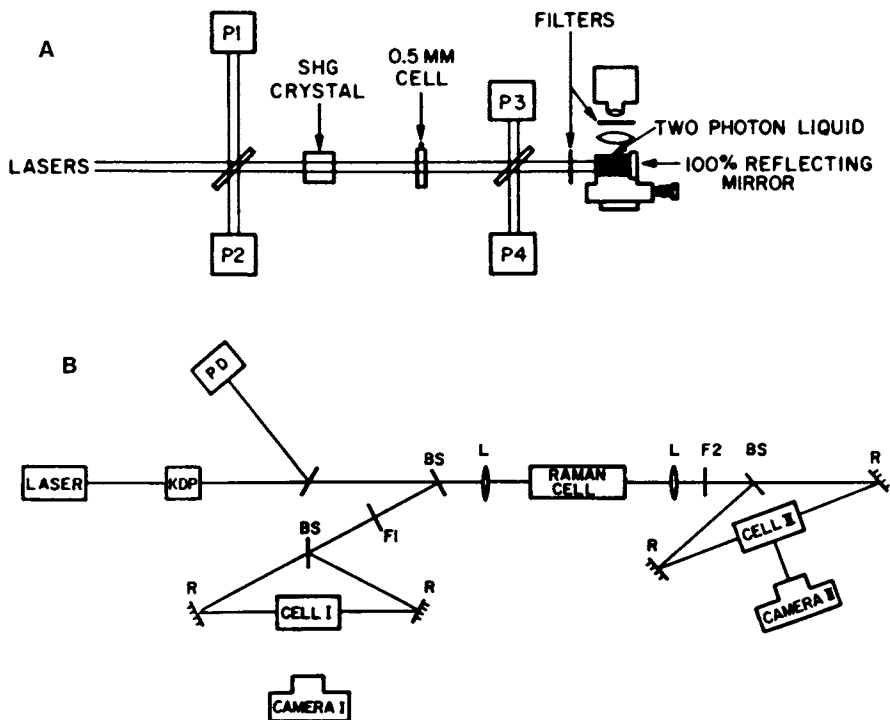


Figure 1. (A) Apparatus used for time-resolved picosecond absorption spectroscopy which utilizes the TPF technique. A set of photodiodes and oscilloscopes (P1, P2, P3, and P4) are used to measure the intensity of the laser pulse before and after each pass through the cell. (Reproduced with permission from Ref. 15. Copyright 1969, North-Holland Publishing Company.)

(B) An alternative TPF experimental arrangement consisting of two TPF triangles, one contains the sample being studied and the other contains a standard chemical used for TPF. Key: BS, beam splitter; F, optical filter; R, reflector; L, lens; PD, photodiode; potassium dihydrogenphosphate (KDP) second-harmonic generating crystal. (Reproduced with permission from Ref. 20. Copyright 1978, Weizmann Science Press of Israel.)

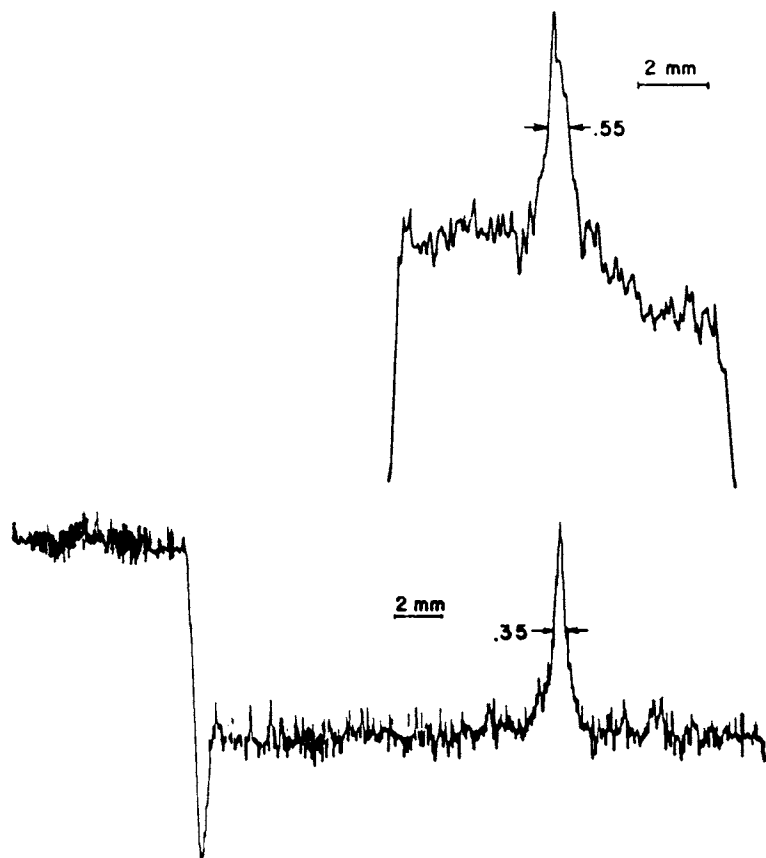


Figure 2. Typical experimental data for consecutive TPF of azulene in solution excited at 530 nm. The upper microdensitometer trace corresponds to the azulene pattern; the lower trace is the TPF pattern of a BBOT dye solution obtained simultaneously with the azulene data. (Reproduced with permission from Ref. 20. Copyright 1978, Weizmann Science Press of Israel.)

Although the use of TPF and 3PF methods proved to be highly successful in some chemical systems, they were not applicable to most. Other experimental techniques had to be developed. The optical multichannel detector (OMCD) played an important role in the development of new techniques. Recording data in a point-by-point fashion, i.e. using a probe light of a single frequency and at a particular delay time after excitation with one laser shot, makes data gathering intrinsically more difficult to correlate with conditions of the excitation process. With the advent of multichannel photodiode arrays, one can now monitor an entire sequence of events occurring after excitation by each laser pulse. Coupled with a polychromator, echelon, or streak camera, the amount of information available per shot is orders of magnitude greater than with a single photomultiplier tube (PMT) or photodiode (PD) arrangement. Listed in Table I are some advantages and disadvantages of both OMCDs and PMT/PDs. Although we still do use PMTs and PDs for some special applications in our experiments, we believe that the advantages of the OMCD far surpass its disadvantages.

Concurrent with the development of suitable photodiode arrays, techniques were being developed for generating dispersion in both the time and wavelength domains. In 1970 it was observed (21) that focusing intense picosecond pulses into some solids and liquids produced superbroadened continua with bandwidths of $>10^4 \text{cm}^{-1}$. It was also shown (22) that these "white light" pulses had durations on the order of the picosecond pulses which produced them. These continuum pulses have proven to be very useful for time-resolved spectroscopy.

Time dispersion can be achieved by use of an echelon (23), a stepped optical delay which provides discrete temporal dispersion by subjecting the cross section of the interrogating pulse to a series of different optical pathlengths. An echelon can be built in a number of different ways; one of which is with a set of optically contacted glass or quartz plates which impresses the time lag along the cross section of the beam depending upon the thickness of glass that the light has to traverse. The advantages of this method are substantial when coupled to an OMCD. Using this technique, one can measure the kinetics of a chemical event with picosecond time resolution. When an OMCD is used in conjunction with a polychromator, the changes in light absorption as a function of time and wavelength which are exhibited by the molecule under investigation can be monitored.

Acridine has been studied by means of the echelon technique.(24,25) The changes in absorption (ΔA) were measured with a double beam picosecond spectrometer similar to the one shown in Figure 3. The difference absorption spectrum at one selected delay time after excitation was calculated according to

Table I. Advantages and Disadvantages of OMCDs and PMT/PDs

<u>OMCD</u>		<u>PMT or PD</u>	
Advantages	Disadvantages	Advantages	Disadvantages
<p>Simultaneous measurements over extended range</p> <p>Automatically takes care of shot-to-shot fluctuations in energy; therefore fewer shots are needed for averaged data. Also the data are much more readily interpreted.</p> <p>Typically S-20 response, ~300-800 nm range, which is more than adequate for most of the work.</p>	<p>Lower light sensitivity (can be enhanced with the use of multi-channel intensifier plates. With the intensifier plate in front of the detector near photon-counting capability may be achieved.)</p> <p>Somewhat more difficult than PMTs or PDs to use due to increased complexity and extra necessary hardware</p> <p>High initial cost</p>	<p>Near photon-counting capability</p> <p>Very easy to use and align</p> <p>Comparatively lower cost</p> <p>A PMT or PD with particular spectral response can be chosen depending on usage requirements.</p>	<p>Capable of only one measurement at a time</p> <p>Large quantities of accumulated data are needed in order to obtain comparable information of an OMCD. Also data are not as readily interpreted.</p>

$$\Delta A(\lambda) = -\log_{10} \left\{ \frac{S^{\text{ex}(\lambda)}}{R^{\text{ex}(\lambda)}} \right\} / \left\{ \frac{S^{\text{noex}(\lambda)}}{R^{\text{noex}(\lambda)}} \right\} \quad (1)$$

where ΔA is the change in absorbance, $S^{\text{ex}(\lambda)}$ and $R^{\text{ex}(\lambda)}$ are the intensities as a function of wavelength of the sample probe and the reference probe, respectively, when the sample is subjected to excitation by the laser pulse. $S^{\text{noex}(\lambda)}$ and $R^{\text{noex}(\lambda)}$ are the probe light intensities when the sample is not subjected to excitation by the laser pulse.

A single picosecond pulse at 1060 nm was extracted from a mode-locked train of an Nd^{3+} :glass laser. After subsequent amplifications of the ~ 6 -ps FWHM laser pulse, peak powers of ~ 50 gigawatts are easily generated. Part of the fundamental light is then converted into the second harmonic (530 nm) by means of a KDP crystal. The second harmonic and fundamental are then frequency mixed with another KDP (Type II) crystal to produce the third harmonic (355 nm). The remaining 1060-nm and 530-nm pulses are used to produce the picosecond "white light" continuum pulse in CCl_4 . The continuum is then dispersed in time through an echelon and focused onto the sample. One of the first segments of light out of the echelon is always timed for arrival at the sample cell at a known time relative to excitation. This timing is achieved either by the bleaching of a dye such as DODCI, which under high power displays a recovery time of a few picoseconds, or by means of a Kerr effect optical shutter, for example a CS_2 cell.

The 355-nm pulse is used to excite the sample, and the continuum segments (probe pulses) are used to monitor the resulting ΔA . The probe pulses, after passing through the sample are then focused into a monochromator which has mounted to its output a two dimensional silicon intensified target photodiode array connected to a computer. With the monochromator set at 430 nm, Sundstrom et. al. (24) directly measured the population growth rate of the lowest triplet state of acridine, which when calculated from the data illustrated in Figure 4 is $3 \times 10^{10} \text{ sec}^{-1}$.

Another example of the use of optical multichannel detection is the picosecond spectroscopic study of acridine, s-tetrazine, and rhodamine B by Barbara et. al. (26). In this type of study, a sample containing the compound of interest is placed in the path of an ~ 6 -ps FWHM laser pulse. The laser pulse is focused onto the sample cell, and the emitted light is collected and directed, by an assembly of lenses, into a streak camera which is capable of time-resolving the emission. Processing and analysis of the streak camera data are accomplished by means of an assembly consisting of a two-dimensional photodiode array

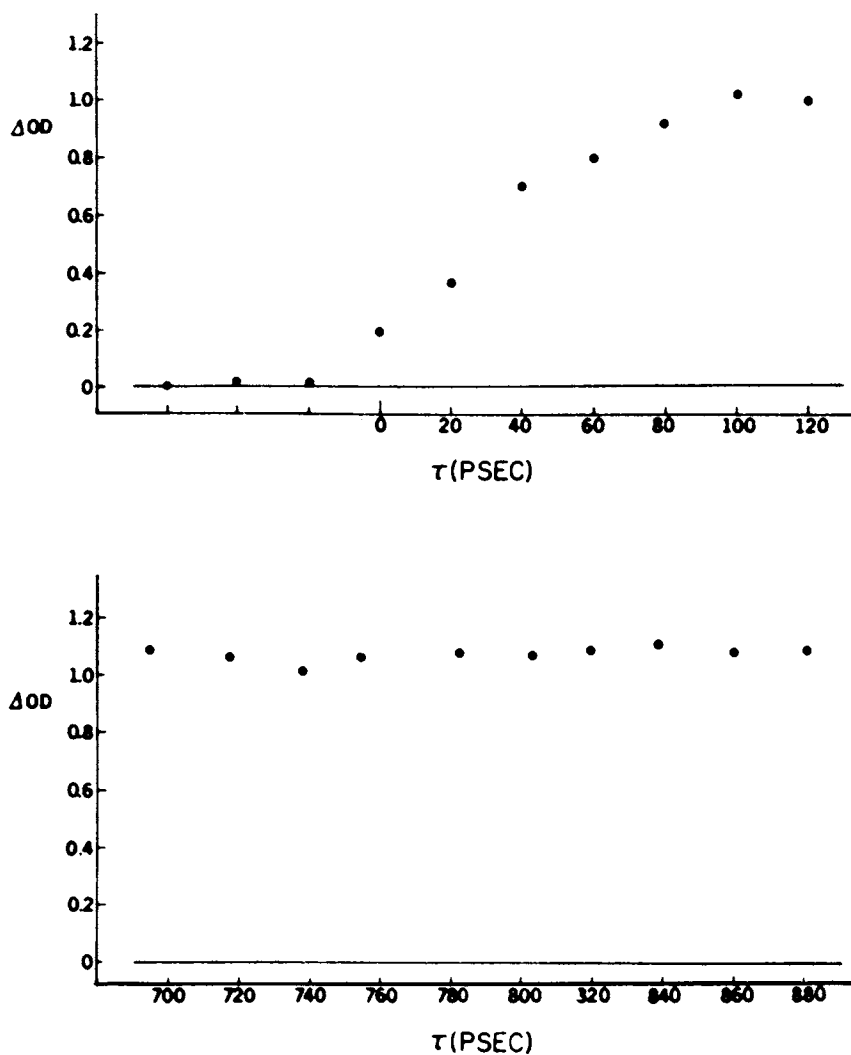


Figure 4. Absorption changes in acridine monitored at 430 nm from 0 to 800 ps after excitation at 355 nm. The polarizations of exciting and probing light pulses were parallel to each other. (Reproduced with permission from Ref. 24. Copyright 1977, American Institute of Physics.)

(vidicon or reticon), optical multi-channel analyzer (OMA), and a computer.

We shall use the picosecond laser system described by Barbara et. al. (26) as an example of an apparatus which can be used for emission studies and include a discussion of the problems and limitations that must be considered and corrected in order to obtain meaningful, reliable data. They used a passively mode-locked Nd^{3+} :glass oscillator to generate a train of 1060-nm, 6-ps FWHM pulses. Single pulses were extracted electro-optically from the pulse train which emerges from the laser cavity and amplified to ~ 100 mJ by means of three Nd^{3+} :YAG amplifiers. Samples of acridine were excited with the third harmonic (355 nm) of the laser fundamental wavelength. The second harmonic (532 nm) was used for excitation of s-tetrazine and rhodamine B. The excitation light pulse was focused to a 2-mm spot on the sample. A small fraction of the 532-nm laser pulse was directed into the streak camera and was used as a timing marker which preceded the excitation pulse.

Figure 5 illustrates a typical streak image of the time dependent fluorescence which results by excitation of rhodamine B at 530 nm with a 0.1 mJ laser pulse. The prepulse is observed at 50 ps before the appearance of the time-dependent fluorescence signal. Distortions of the streak image are the result of a number of contributing causes which include vignetting in the optics relaying the emitted light from the sample to the streak camera slit, channel-dependent sensitivity within the OMA, non-linearity in the time base of the streak camera, and changes in gain along the surface of the photocathode of the streak camera. Calibrations of the time base can be made optically by use of etalons which split an incoming laser pulse and delay the split pulses spatially, and therefore temporally, by known amounts of time. These temporally split pulses are then detected by means of the streak camera/vidicon/OMA/computer system. Variations in signal intensity along the time axis can be corrected by measurement of intensity vs. time for a long-lived emission at selected streak speeds. This measurement provides a gain profile for the streak camera. The gain profile of the streak camera and the time-base correction can be applied as corrections to raw streak data at the time of data processing. Figure 5 illustrates the change in appearance of data obtained for the time-resolved fluorescence of rhodamine B after corrections are made which compensate for optical detection errors. The apparent fluorescence decay which is quite obvious in Figure 5 is the result of distortion caused by the method of signal detection. Once corrected a practically constant fluorescence intensity is observed in the 120-350 ps range of time after excitation. This should be the case since rhodamine B exhibits a fluorescence lifetime in the range of nanoseconds.

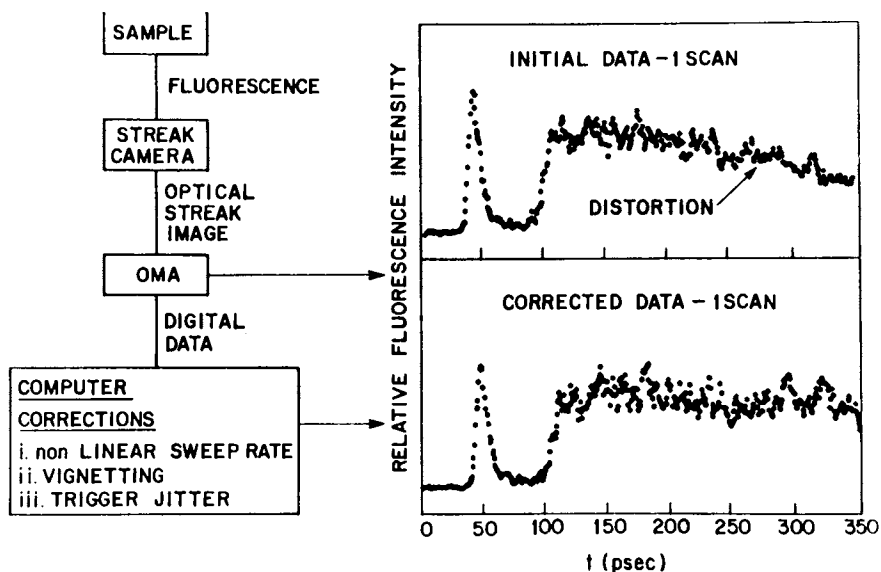


Figure 5. The data processing system with actual time-resolved fluorescence measured for a 5×10^{-4} M rhodamine B in ethanol (1-mm pathlength) excited by a 0.1-mJ, 530-nm laser pulse. The data obtained initially from the OMA are corrected by computer. In these data, the average time between points (individual OMA channels) is 0.8 ps. (Reproduced with permission from Ref. 26. Copyright 1980, North-Holland Publishing Company.)

Typically, in measurements of time-resolved luminescence in the time regime of tens of picoseconds, data obtained from 10 to 20 laser shots are averaged to improve the signal-to-noise ratio and to minimize the effects of shot-to-shot variations in the laser pulse energy and shape. Once the reliability of the data has been ensured by application of the corrections described above and made necessary by detector-induced distortions, the time-resolved fluorescence data is analyzed in terms of a kinetic model which assumes that the emitting state is formed with a risetime, τ_R , and a decay time, τ_F . Deconvolution of the excitation pulse from the observed molecular fluorescence is performed numerically. The shape of the excitation pulse to be removed from the streak camera data is assumed to be the same as the prepulse shape, and therefore the prepulse is generally used for the deconvolution procedure. Figure 6 illustrates the quality of the fit of the time-dependent fluorescence data which can be achieved.

In their study of the fluorescence of acridine in hexane induced by a 0.1 mJ, 355-nm laser pulse, Barbara et. al. (26) demonstrated the sensitivity of this technique for the measurement of τ_R and τ_F . The best fit of the data, in this case, is a risetime, τ_R , which is pulse-width limited and a decay lifetime, τ_F , of 38 ps. These data which are illustrated in Figure 6 indicate that risetimes as short as 3 ps can be accurately determined, and decay lifetimes can be fitted with an accuracy of $\sim 10\%$.

Applications of Picosecond Spectroscopy

Photodissociation of Haloaromatic Compounds. Picosecond emission spectroscopy was recently employed (27,28) to study the photodissociation of haloaromatics and the subsequent fluorescence of the formed radicals. An earlier paper by Huppert et. al. (29) describes the predissociative pathways of the haloaromatics following excitation at 266 and 355 nm. What makes the more recent work different is that, after the initial excitation by a 266-nm 25-ps FWHM pulse, a second 355-nm 25-ps pulse irradiates the same area of the sample. With this two-color fluorescence technique they were able to observe clearly the reaction dynamics of the radicals which were formed by the initial light pulse.

The compounds which were investigated by means of the two-color fluorescence technique were 1-(bromomethyl)naphthalene, 1-(chloromethyl)naphthalene, 2-(bromomethyl)naphthalene, and 2-(chloromethyl)naphthalene. Fluorescence which resulted when a particular (halomethyl)naphthalene in hexane was excited at 266 nm alone or at 266 and 355 nm was monitored in either of two ways. Emission intensity vs. time for a particular range of wavelengths was measured by means of an Imacon streak camera and

Princeton Applied Research (PAR) 1205A OMA detection system. Emission intensity vs. wavelength was measured without time resolution by means of a polychromator and PAR 1205A detection system.

When excited at 266 nm, all four compounds exhibited a broad blue fluorescence centered at ~ 400 nm with lifetimes ranging from 100 to 3500 ps. Excitation with a second 355-nm laser pulse which was delayed relative to the first 266-nm pulse produced a fluorescence centered at ~ 600 nm with a lifetime of ~ 10 ns. Since the emission spectra (Figure 7) obtained by excitation of 1-(chloromethyl)naphthalene and 1-(bromomethyl)-naphthalene are superimposable in the region from 550 to 750 nm, this red fluorescence was attributed to the 1-naphthylmethyl radical. In a similar manner, the red fluorescence resulting from two-color excitation of 2-(chloromethyl)naphthalene and 2-(bromomethyl)naphthalene was attributed to the 2-naphthylmethyl radical. This two-color fluorescence technique used in conjunction with OMCDs has proven to be a powerful tool in the study of photodissociation of haloaromatic compounds.

The Visual Transduction Process. Picosecond absorption spectroscopy which utilizes OMCDs also has provided important mechanistic information that previously was not available by means of other techniques. Detailed pathways of a number of reactions which are important from a physical, chemical, and/or biological viewpoint have been elucidated by means of this technique. A recent picosecond spectroscopic study by Spalink et. al. (30) has demonstrated that an experimental criterion, which has been used to support the hypothesis that *cis-trans* isomerization (31) is the primary event in the visual transduction process, is not true. This criterion is based on the commonly occurring statement that both the naturally occurring 11-*cis*-rhodopsin and the synthetic 9-*cis*-rhodopsin lead to the same primary photochemical product, bathorhodopsin. Of course, the existence of a common intermediate generated from either 11-*cis*- or 9-*cis*-rhodopsin would support the commonly proposed mechanism of *cis-trans* isomerization as the primary event in the visual transduction process. However, the data obtained by Spalink et. al. (30) indicate that a common intermediate is not generated from both rhodopsins.

Using a mode-locked Nd³⁺:YAG laser system to generate picosecond sample excitation pulses and picosecond probing continuum pulses in their double beam spectrometer, Spalink et. al. (30) were able to measure difference absorption spectra of irradiated samples of 11-*cis*-rhodopsin and 9-*cis*-rhodopsin at selected times after excitation by means of a PAR OMA-2 optical multichannel detection system. The difference absorption spectral data were obtained over the entire spectral range from 410 nm to 650 nm at one time with an OMCD as opposed to the

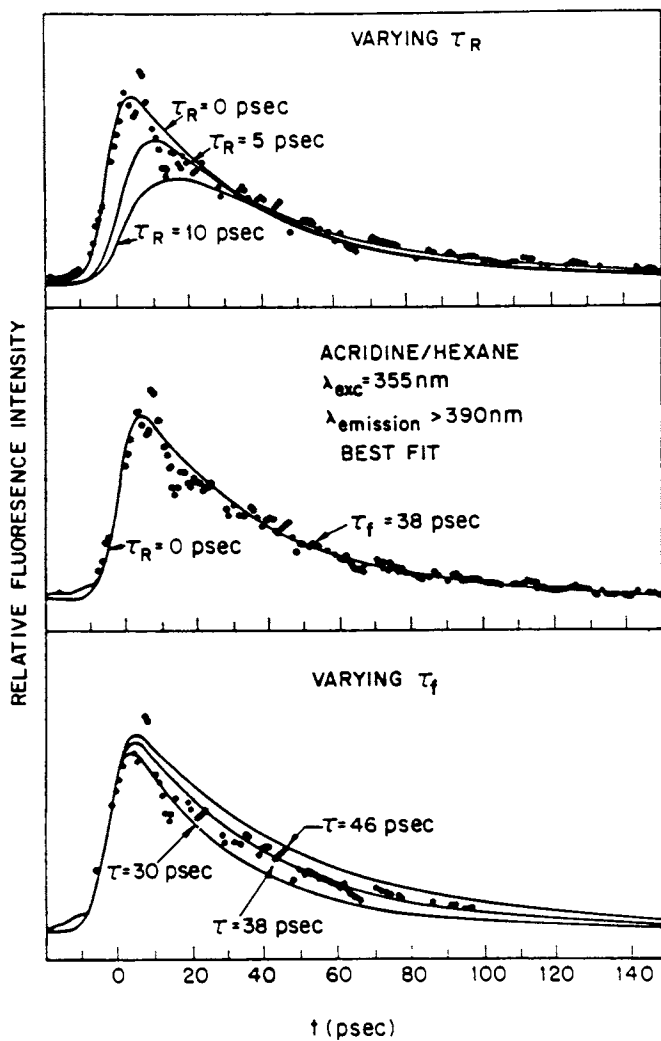


Figure 6. Time-resolved fluorescence of a 1.1×10^{-3} M acridine in hexane excited by a 0.1-mJ, 355-nm laser pulse. The experimental points, which are averaged from nine laser shots, are displayed with the computer-generated curves that were calculated to fit fluorescence risetimes, τ_R , and fluorescence decay times, τ_f , to the experimental data. (Reproduced with permission from Ref. 26. Copyright 1980, North-Holland Publishing Company.)

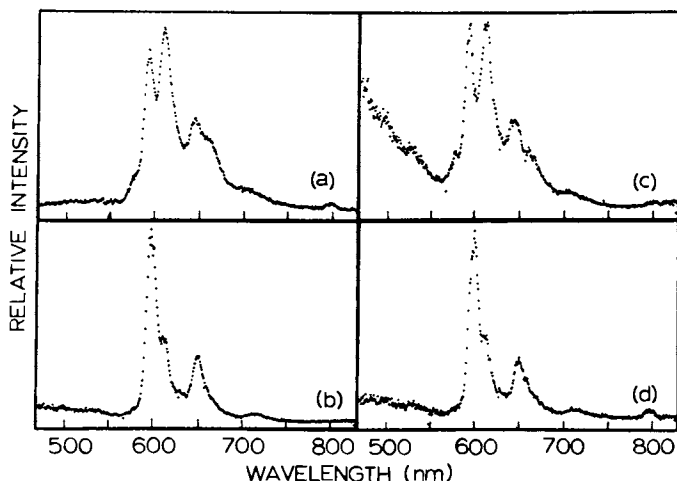


Figure 7. Two-color fluorescence spectra of the 1-naphthylmethyl and 2-naphthylmethyl radicals. Spectra were produced by excitation of the sample with a 25-ps, 266-nm laser pulse followed by a 25-ps, 355-nm pulse delayed by ~ 60 ps. Key to (halomethyl)naphthalenes: a, 1-(chloromethyl)naphthalene; b, 2-(chloromethyl)naphthalene; c, 1-(bromomethyl)naphthalene; and d, 2-(bromomethyl)naphthalene. Note: the fluorescence in the blue region of Spectrum c is due to impurities that contaminated the sample of 1-(bromomethyl)naphthalene (28).

older, tedious wavelength-by-wavelength method. The difference absorption spectrum at one selected delay time after excitation was calculated according to equation 1 and is the average of data obtained from at least 55 excitations by laser pulses.

Figure 8 illustrates the difference spectra obtained 85 ps after excitation of samples of 9-*cis*-rhodopsin and 11-*cis*-rhodopsin at room temperature with 25-ps, 532-nm laser pulses. The time of 85 ps after excitation was selected to ensure that only the batho-intermediate was observed.⁽³⁰⁾ Inspection of both spectra reveals two important differences that had previously gone undetected. First, the spectral bands of positive ΔA and of negative ΔA and the isosbestic point which result from excitation of 9-*cis*-rhodopsin are shifted bathochromically by ~ 10 nm relative to the corresponding positions in the difference spectrum measured 85 ps after excitation of 11-*cis*-rhodopsin. This 10-nm shift to longer wavelengths is similar to the shift observed for the ground-state absorption maximum of 9-*cis*-rhodopsin relative to 11-*cis*-rhodopsin (Figure 8). The second difference is that, although both 11-*cis*-rhodopsin and 9-*cis*-rhodopsin exhibit the same amount of decreased absorption corresponding to ground-state depopulation, the ratio of their absorption maxima is not 1:1, as should be expected for the generation of a common intermediate from both precursors, but 1.5:1.

Computer subtraction of the two negative static absorption spectra from the two difference absorption spectra obtained via

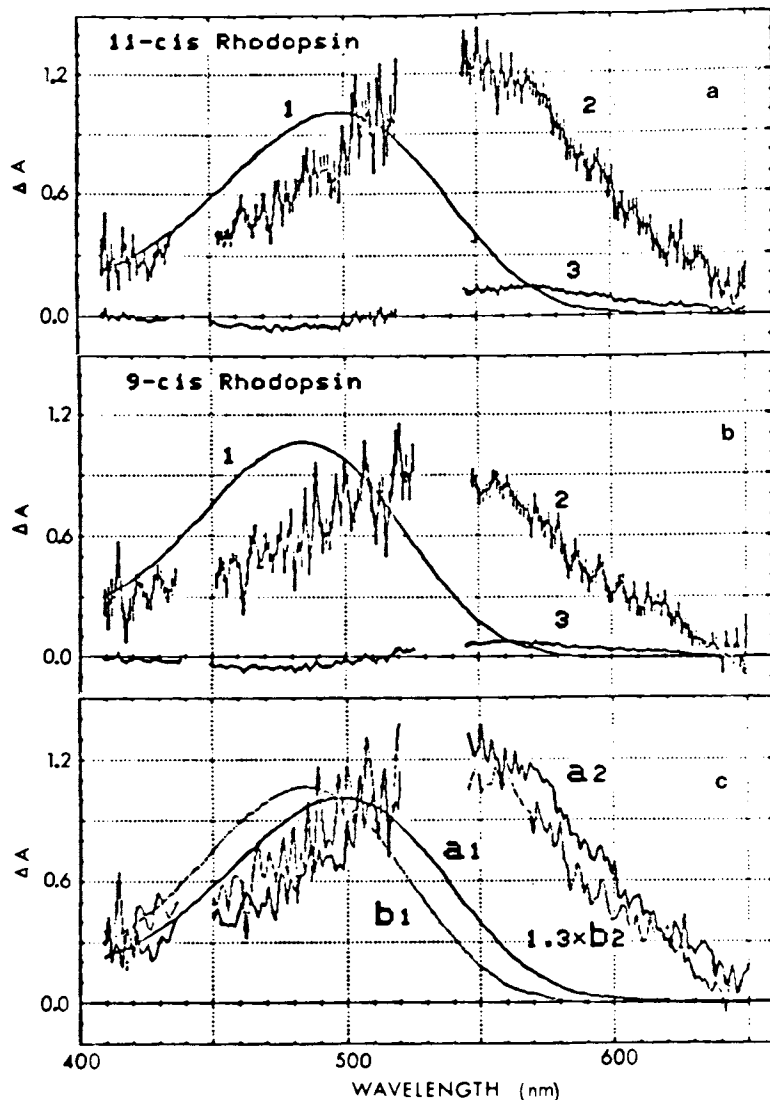


Figure 8. (a) (1) 11-cis-Rhodopsin absorption spectrum; (2) calculated spectrum of bathorhodopsin from excitation of 11-cis-rhodopsin [resolved from difference spectrum (curve 3) by assuming a 15% bleach]; and (3) difference absorption spectrum obtained by 532-nm excitation of a sample of 11-cis-rhodopsin.

(b) (1) 9-cis-Rhodopsin spectrum; (2) calculated spectrum of bathorhodopsin from excitation of 9-cis-rhodopsin [resolved from difference spectrum (curve 3) by assuming a 13% bleach]; and (3) difference absorption spectrum obtained by 532-nm excitation of a sample of 9-cis-rhodopsin.

(c) Comparison of the two calculated bathorhodopsin spectra (a_2 and b_2). Both spectra are scaled to the same maximum absorption to illustrate the relative spectral shift. The 11-cis- and 9-cis-rhodopsin spectra are a_1 and b_1 , respectively. The region from 525 to 545 nm is eliminated from the spectra as a result of a Raman notch filter used to remove scattered 532-nm laser light. (Reproduced with permission from Ref. 30.)

an OMCD yields the absorption spectra of the bathorhodopsins formed 85 ps after excitation of 11-*cis*-rhodopsin and 9-*cis*-rhodopsin (Figure 8c). Appropriate scaling of the two absorption bands clearly reveals that they are not superimposable. The differences between the absorption spectra obtained by excitation of 9-*cis*-rhodopsin and 11-*cis*-rhodopsin were found to persist to a time of at least 8 ns after excitation of the sample. These data clearly demonstrate that excitation of 9-*cis*-rhodopsin and 11-*cis*-rhodopsin by 532-nm light does not lead to the formation of a common intermediate. Although these picosecond absorption data do not provide direct structural information, such as that given by Raman or infra-red spectroscopy, they are convincing evidence that one should not accept the *cis*-trans isomerization mechanism on the basis of the formation of a common batho-intermediate from both 11-*cis*-rhodopsin and 9-*cis*-rhodopsin. Additional picosecond spectroscopic data strongly suggest that the primary event in the visual transduction process involves a slight skeletal deformation coupled with a proton translocation (32,33).

Intermolecular Photo-Induced Electron Transfer. Picosecond absorption spectroscopy has also been applied recently to studies of intermolecular electron transfer on the picosecond time scale.(34) As in the previously described study of rhodopsin, the photo-induced intermolecular electron transfer between chloranil (CHL) and the arenes, naphthalene (NAP), 9,10-dihydrophenanthrene (DHP), and indene (IN) was studied by means of picosecond absorption spectroscopy which utilizes an OMCD. Difference absorption spectra of samples of CHL and one of these particular arenes in acetonitrile were measured at selected delay times after excitation at 355-nm with 25-ps FWHM laser pulses. These picosecond spectroscopic studies revealed information about the mechanism of intermolecular electron transfer and subsequent radical ion formation that was not possible in previous spectroscopic studies performed on the nanosecond (35-37) and microsecond (38,39) time scales.

The difference absorption spectra taken at selected delay times after excitation permit one to monitor the evolution of the electron transfer reaction (Figure 9). The study of the CHL/DHP system will be used as an example. At 25 ps after excitation at 355 nm, a broad absorption band near 485 nm is observed and has been assigned to the $S_n \leftarrow S_1$ transition of CHL. The $T_n \leftarrow T_1$ absorption band of CHL at ~ 510 nm along with the first traces of the $D_n \leftarrow D_0$ absorption band of $DHP^{\cdot-}$ at 625 nm are apparent at 75 ps after excitation. The reaction proceeds through several intermediate steps until at ~ 2 ns the absorption bands of $CHL^{\cdot-}$ and $DHP^{\cdot-}$ are the only bands which can be observed.

The early stages of the photo-induced electron transfer between the donor arenes and the acceptor molecule, CHL, are composed of dynamic events which could not be resolved in the

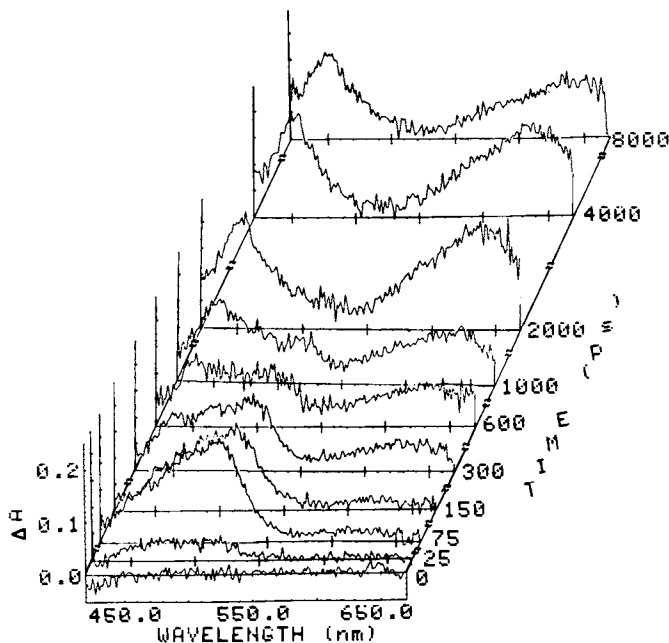


Figure 9. Difference absorption spectra obtained at different times after 355-nm excitation of 0.027 M chloranil, and 0.080 M 9,10-dihydrophenanthrene in acetonitrile.

studies performed on the slower time scales. In the systems of CHL/DHP (see Figure 9) and CHL/NAP, the absorption bands of the cation radicals from the time of 75–100 ps after excitation, when they are first observed, to times of ~ 1 ns after excitation exhibit changes in position of absorption maximum in the case of DHP⁺ and changes in intensities of vibrational bands in the case of NAP⁺. These changes, revealed by picosecond laser excitation and interrogation coupled with optical multichannel detection, were interpreted in terms of changes in the relative position of the initially formed ion pairs by means of a diffusion process until an equilibrium position is established between cation, anion, and solvent molecules. In recent picosecond spectroscopic studies, Simons and Peters have also observed shifts of the absorption maximum of benzophenone radical anion generated by photoreduction of benzophenone by amines. (40,41)

Summary

In the preceding discussion, we have presented several optical detection methods that can be used when one employs picosecond emission or absorption spectroscopy as a means of

identifying transient states and species involved in photochemical reactions and measuring their formation and decay kinetics. We limited our discussion to only a few methods of optical detection, but we believe that these examples demonstrate the advantages of optical multichannel detectors. The examples of applications of picosecond spectroscopy enable us to appreciate the capabilities of OMCDs, namely kinetic data and optical absorption and emission spectra can be obtained and interpreted more readily with OMCDs than by other point-by-point methods. The versatility of OMCDs and, of course, advances in laser technology have been responsible for the increasing numbers of applications of picosecond spectroscopy to problems in areas of physics, chemistry, and biology.

Literature Cited

1. Hilinski, E. F.; Rentzepis, P. M. Acc. Chem. Res. 1983, in press.
2. Hilinski, E. F.; Rentzepis, P. M. Nature, in press.
3. Rentzepis, P. M. Science 1982, 218, 1183.
4. Rentzepis, P. M. Science 1978, 202, 174.
5. Giordmaine, J. A.; Rentzepis, P. M.; Shapiro, S. L.; Wecht, K. W. Appl. Phys. Letters 1967, 11, 216.
6. Rentzepis, P. M.; Duguay, M. A. Appl. Phys. Letters 1967, 11, 218.
7. A typical solution used for TPF and 3PF is BBOT (2,5-bis-[5-t-butylbenzoxazolyl(2 ')] - thiophene) in ethylene dichloride.
8. Rentzepis, P. M.; Mitschele, C. J. Appl. Phys. Letters 1970, 17, 122.
9. Rentzepis, P. M. Bull. Am. Phys. Soc. 1970, 15, 282.
10. Weber, H. P. Phys. Letters 1968, 27A, 321.
11. Weber, H. P.; Dondliker, R. Phys. Letters 1968, 28A, 77.
12. Klauder, J. R.; Duguay, M. A.; Giordmaine, J. A.; Shapiro, S. L. Appl. Phys. Letters 1968, 13, 174.
13. Drexhage, K. H. Appl. Phys. Letters 1969, 14, 318.
14. Rentzepis, P. M. Chem. Phys. Letters 1968, 2, 177.
15. Rentzepis, P. M. Chem. Phys. Letters 1969, 3, 717.
16. Rentzepis, P. M. Science 1970, 169, 239.
17. Huppert, D.; Jortner, J.; Rentzepis, P. M. Chem. Phys. Letters 1972, 13, 225.
18. Huppert, D.; Jortner, J.; Rentzepis, P. M. J. Chem. Phys. 1972, 56, 4826.
19. Wirth, P.; Schneider, S.; Dorr, F. Chem. Phys. Letters 1977, 46, 20.
20. Huppert, D.; Jortner, J.; Rentzepis, P. M. Isr. J. Chem. 1977, 16, 277.
21. Alfano, R. R.; Shapiro, S. L. Phys. Rev. Letters 1970, 24, 584.

22. Busch, G. E.; Jones, R. P.; Rentzepis, P. M. Chem. Phys. Letters 1973, 18, 178.
23. Topp, M. R.; Rentzepis, P. M.; Jones, R. P. J. Appl. Phys. 1971, 42, 3451.
24. Sundstrom, V.; Rentzepis, P. M.; Lim, E. C. J. Chem. Phys. 1977, 66, 4287.
25. Noe, L. J.; Degenkolb, E. O.; Rentzepis, P. M. J. Chem. Phys. 1978, 68, 4435.
26. Barbara, P. F.; Brus, L. E.; Rentzepis, P. M. Chem. Phys. Lett. 1980, 69, 447.
27. Kelley, D. F.; Milton, S. V.; Rentzepis, P. M., submitted for publication.
28. Huppert, D.; Milton, S. V.; Rentzepis, P. M., in preparation.
29. Huppert, D.; Rand, S. D.; Reynolds, A. H.; Rentzepis, P. M. J. Chem. Phys. 1982, 77(3), 1214.
30. Spalink, J.D.; Reynolds, A. H.; Rentzepis, P. M.; Applebury, M. L.; Sperling, W. Proc. Natl. Acad. Sci. USA, in press.
31. Ottolenghi, M. Adv. in Photochemistry 1980, 12, 97.
32. Busch, G. E.; Applebury, M. L.; Lamola, A. A.; Rentzepis, P. M. Proc. Natl. Acad. Sci. USA 1972, 69, 2802.
33. Peters, K.; Applebury, M. L.; Rentzepis, P. M. Proc. Natl. Acad. Sci. USA 1977, 74, 3119.
34. Hilinski, E. F.; Milton, S. V.; Rentzepis, P. M., submitted for publication.
35. Gshwind, R.; Haselbach, E. Helv. Chimica Acta 1979, 97, 941.
36. Delcourt, M. O.; Rossi, M. J., personal communication.
37. Ottolenghi, M. Acc. Chem. Res. 1973, 6, 153.
38. Rehn, D.; Weller, A. Ber. Bunsenges. Physik. Chem. 1969, 73, 834.
39. Rehn, D.; Weller, A. Isr. J. Chem. 1970, 8, 259 and references cited therein.
40. Simons, J. D.; Peters, K. S. J. Am. Chem. Soc. 1982, 104, 6542.
41. Simons, J. D.; Peters, K. S. J. Am. Chem. Soc. 1981, 103, 6403.

RECEIVED August 4, 1983

Data Acquisition System for a Jitter-Free Signal Averaging Streak Camera

W. KNOX and L. FORSLEY

Laboratory for Laser Energetics, University of Rochester, Rochester, NY 14623

A streak camera which has ± 2 ps shot-to-shot jitter has been developed. With this degree of precision, a simple method of signal averaging of picosecond fluorescence events may be employed: direct summation. This results in a substantial increase in the signal-to-noise ratio of time-resolved fluorescence measurements over single-shot records.

In this article we discuss the implementation of an optical multichannel analyzer on a jitter-free streak camera which allows signal averaging without operator intervention at a repetition rate of 1 Hz and provides for acquisition routines which are specifically suited to this application. Several experimental examples are discussed which illustrate the features of the system.

Streak Camera

The streak camera (1, 2) is a versatile method of fluorescence detection with picosecond resolution (3, 4). The photocathode responds over a wide spectral range (190 nm to \sim 850 nm for S-20), it responds equally to any polarization of light and is non-selective in terms of solid angle of incident light. These features combine to make the streak camera an attractive system for general use in picosecond photophysics.

One difficulty with the conventional streak camera is the lack of absolute synchronization between the sweep circuit and the transient

0097-6156/83/0236-0221\$06.00/0
© 1983 American Chemical Society

under study. This leads to uncertainty in the time axis due to jitter in the recorded transient. For fast sweeps which are necessary for picosecond time resolution, the jitter in the best conventional electronic sweep generators (30-100 psec) may be a substantial fraction of the entire recorded trace width, making simple averaging methods impossible.

This problem has been dealt with by using an intense time marker (5,6) and sliding successive shots to superimpose their marker pulses before averaging. This technique requires an operator to monitor the acquisition process and manually select data for averaging. Corrections for field distortion and intensity response must be applied to each shot before shifting and averaging. Therefore, it is not practical to average several hundred shots routinely with this technique. A synchronously driven streak camera uses amplified RF from a synchronously driven dye laser to provide sweep voltage for the camera (7), but this method is not applicable to single-shot systems.

Limited signal-to-noise ratio in single shot fluorescence recordings has been a primary difficulty with streak cameras. In picosecond fluorometry experiments the signal level available on a single-shot basis may be particularly restricted by one or more of the following parameters: excitation energy, fluorescence lifetime, $f/\#$ of collection optics, quantum efficiency of fluorescence and concentration of fluorescent species. In these cases it is desirable to average many shots (30-1000) to obtain acceptable signal-to-noise ratio, thus a simple and efficient method of averaging single-shot streaks is necessary.

Jitter-Free Streak Camera

A picosecond high-power semiconductor switch has been used to generate a high-voltage electrical ramp pulse for the streak camera which is synchronized to within 2 psec to the transient under study (8). Using a linear photoconductive process in semi-insulating GaAs:Cr, sweep speeds in the range of 6 psec/mm to 50 psec/mm have been obtained with no timing drift (9). The system has been described in several articles (4, 8-11), but the principle of operation will be briefly reviewed.

The typical requirement for deflection is a ramp pulse of 2-5 kv with 1-10 nsec risetime. Electronic sweep drivers such as avalanche transistor stacks, spark gaps, krytrons, and microwave triodes have been used in commercial streak cameras with jitter of as low as ± 30 psec but typically 100 psec. All sweep electronics exhibit an internal trigger delay of 10-100 nsec which depends upon parameters such as voltage, age of device, ambient temperature, etc. Variability in one or all any of these parameters leads to a timing drift of a few nsec as an inherent slowly varying instability on top of the shot-to-shot jitter which cannot be controlled. Conventional electronics are not capable of providing a high-voltage ramp pulse which is precisely synchronized with a picosecond event, that is with jitter of < 1 psec. The jitter inherent in these devices originates in the statistical nature of the avalanche multiplication process which is used in the generation of the ramp pulse.

In order to obtain jitter-free deflection, the ramp voltage is generated by optically implanting carriers in a bulk semiconductor which is biased at a high voltage (1–5 kV). Since the linear photoconductive process has no intrinsic instability such as in avalanche switching the voltage waveform is synchronized to within ~ 1 ps to the incident optical pulse. Residual timing fluctuation depends only upon laser pulse stability.

The GaAs:Cr photoconductive switch is operated at room temperature and DC bias which results in simple and reliable operation. Since the photoconductive process has no intrinsic delay, there is no drift of time origin over long periods, and the internal delay does not depend on the sweep speed as in the case of a conventional driver.

Signal averaging can be performed in a simple manner with a low jitter streak camera since the signals do not have to be selected or individually corrected before summation. Using an active-passive mode-locked Nd³⁺:YAG laser generating 30 psec pulses at a repetition rate of 1 Hz, 300 shots can be accumulated in 5 minutes without operator intervention. The signal-to-noise ratio increases as the square-root of the number of shots averaged, so this results in almost 20 times the single-shot signal-to-noise ratio.

This technique can be directly employed at higher repetition rates, and recently operation at up to 500 Hz has been demonstrated. It should be noted that this deflection scheme is applicable to any streak camera. The switch requires ~ 100 μ J of incident optical energy.

Data Acquisition

When signals are averaged over a period of minutes, a common problem with the silicon vidicon-based scanning system is a persistent background drift, or random change in the detector dark current level. Acquisition cycles typically consist of accumulating the required number of shots and storing data, disabling the laser trigger and accumulating an equal number of background scans. The two curves are then subtracted to extract the signal. Over this period of time, the background level generally will have drifted by a fraction of the total signal height, or even much more than the signal height in the case of very weak signals which are frequently encountered. The background level doubles for every 7°C increase in the diode array temperature and it is difficult to control the temperature of the array accurately enough to prevent this problem. Cooling the detector head to -40°C results in a highly nonlinear intensity response to pulsed signals, so this is not an acceptable solution to the problem, and background drift is encountered even when the detector is cooled because of heating from the readout beam.

A solution to this problem is to subtract a background signal immediately after each fluorescence signal acquisition and repeat until all signals have been acquired. This mode of scanning is not available on the

OMA-II model optical multichannel analyzer (12) as supplied. The OMA-II can be operated in a fully user-programmable mode ("open-system") using a Forth-based operating system. In this mode, any desired scan pattern and acquisition routine may be specified.

Forth (13), a programming language designed for real time control of peripherals and data processing, allows direct machine language access to the computer. We have programmed an alternate background subtraction routine which starts a scan, fires the laser, then moves 500 channels of data to an accumulator file in random access memory. It then starts another scan, disables the laser trigger, and subtracts the background scan from the accumulator file. This process is interleaved with a display routine which shows the running average, and is repeated until the required number of shots has been accumulated. This is implemented without hardware modifications on the OMA-II by connecting the "external event start" signal through DC relay #1 contacts and triggering the laser with this signal. The relay is alternately closed and opened under software control in between acquisition of data and backgrounds. The DC relay #2 is connected to an audio device (sonalert) which is activated after the acquisition cycle is completed, thus signaling the operator. By writing the data accumulation and display routines in assembler, the entire process runs easily between laser shots at 1 Hz. In fact, operation at 1 Hz is presently limited only by vidicon readout linearity characteristics, since it is necessary to take 20 scans to achieve reasonable intensity linearity.

With the use of the alternate background subtraction mode, the background drift problem is eliminated, regardless of the length of the averaging operation. The system operates as a lock-in amplifier, constantly subtracting background in the process of acquiring signals. This allows the recording of transients which are a fraction of the instrumental background level without fear of loss of information. Direct comparison of data to theoretical models is facilitated by the high signal-to-noise ratio and lack of background and temporal drift which can thus be achieved.

Applications

The system described above has been used in a variety of applications. In several cases, detection of extremely weak signals was made possible by averaging up to 800 shots. We have made the first measurement of fluorescence on the picosecond time scale from an amorphous semiconductor: As_2S_3 (14, 15), as discussed later. We have recently investigated the fluorescence kinetics of cis- and trans-polyacetylene (16). In these cases, detection of fluorescence with quantum efficiencies below 10^{-6} on very fast timescales was greatly facilitated by signal averaging.

In biological physics studies, we have measured the excitation intensity dependence of chlorophyll a/b fluorescence (17), anisotropy decay times of tryptophan in various environments (18), energy transfer in spinach chloroplasts (19), and decay kinetics of hematoporphyrin derivative (20).

In chemistry studies, we have measured fluorescence decay of phthalazine in various solvents (21), depolarization decay times of rhodamine 6G in various solvents (22), and torsional dynamics of DNA (23).

Three specific examples are discussed which illustrate the capabilities of the jitter-free signal averaging streak camera.

Fluorescence Response of Color Center

Vibrational relaxation of color centers has been thought to occur in less than 10 picoseconds. Recently, the response time for formation of gain after optical pumping has been determined for F centers in KCl(24), and F_A centers in KCl:Li (25). Until now there have been no direct measurements of the fluorescence rise time of F or M centers in alkali halides. In Fig. 1, we show a measurement of the fluorescence response of the M center in NaF. Thirty shots of the scattered excitation pulse (a) are compared with thirty shots of the fluorescence rise (b). The three calculated curves represent the fluorescence response assuming three-level kinetics with rise times of $\tau=0, 3$ and 12 psec. These curves have been calculated on an open system OMA-II using the excitation pulse (a) as the driving term for the differential equations. The best fit occurs for $\tau=0$ psec, but the accuracy of this data is ± 1 psec. The vibrational relaxation time of the M center in NaF is therefore < 1 psec. Thus, it is possible to determine response times down to a small fraction of the excitation pulse width by signal averaging with low jitter.

It is critical in these experiments that the laser pulse profile remain constant and free of satellite pulses in order to obtain accuracy of ~ 1 picosecond. The active-passive modelocked Nd^{3+} :YAG oscillator used in this experiment satisfies these requirements, but a purely passively modelocked oscillator does not. In particular, the modelocked Nd:Glass laser which was used in many early experiments produced pulses of duration in the range 5-10 picoseconds. These short pulses were obtained at the expense of pulse width and energy stability as well as high incidence of satellite pulses. Although the jitter-free streak camera system discussed here is in principle applicable to Nd:Glass systems of this kind, the timing accuracy and ultimate risetime measurement capability would be better for the case of a Nd:YAG system with 20 picosecond highly reproducible pulses.

Averaging of Very Weak Signals

The extensive signal averaging capability afforded by the technique described here makes possible some experiments where data from a single or even 10 or 20 shots would not be interpretable. In Fig. 2, we show a measurement of fluorescence of amorphous As_2S_3 (14, 15) excited below the bandgap by the Nd:YAG second harmonic at 532 nm. A single shot (a) contains discrete events which are representative of individual photoelectron events at the photocathode. On very high gain (10^7), these events are clearly visible and far above the OMA noise level. In (b), we

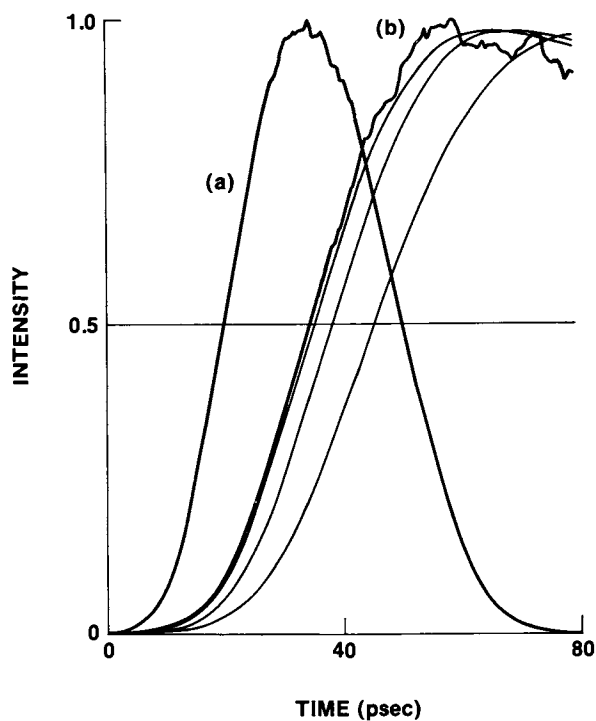


Figure 1. The absolute fluorescence timing. Rise of fluorescence of M center in NaF. Curve a shows 30 shots of excitation pulse scattered by a thin (300 μm) crystal, and Curve b shows 30 shots of fluorescence rise. Calculated curves show solution to differential equations assuming response times of $\tau = 0$ ps, 3 ps, and 12 ps. These results imply a rapid relaxation process with $\tau < 1$ ps.

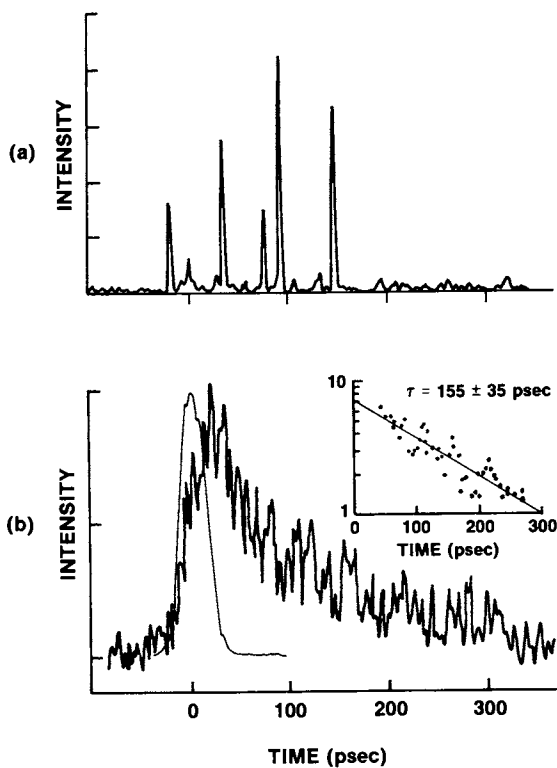


Figure 2. The averaging of very weak signals. Luminescence of amorphous As_7S_3 at 154 K. Comparison of 1 shot (a) and an average of 300 shots (b). Time constant of decay is determined to be 155 ± 35 ps (inset). Scattered excitation pulse defines $t = 0$.

show the result of a 300 shot summation with the scattered excitation pulse at $t=0$. A semi-log inset shows the determination of the decay time. This measurement was taken at 154 °K, and subsequent runs allowed a detailed determination of the temperature dependence of the nonradiative contribution to the decay time. A risetime of < 10 ps was found. Long-term timing stability of several hours is critical in extended temperature cycling experiments.

This represents a measurement in the limit of vanishing signal, where single photoelectron events are individually resolved and recorded. In this regime, the method of marker pulse overlapping becomes impossible to use because the marker pulse is generally made very intense to accurately define the time origin for averaging. The high intensity marker pulse interferes with the recording of the weak signal because of electron scattering in the image converter tube and cross-talk in the multichannel array. The ability to signal average in the single-photoelectron range should enable many studies which are not possible with limited numbers of shots.

Fluorescence Depolarization Measurements

Fluorescence depolarization time courses contain information about rotational diffusion (26). The main difficulty with streak camera measurements of time-resolved fluorescence depolarization is limited signal-to-noise ratio of single shot records. The fluorescence anisotropy parameter is defined as :

$$r(t) = \frac{I_{\parallel}(t) - I_{\perp}(t)}{I_{\parallel}(t) + 2I_{\perp}(t)} \quad (1)$$

where $I_{\parallel}(t)$ is the time dependent intensity in the polarization parallel to the excitation polarization and $I_{\perp}(t)$ is the intensity in the polarization perpendicular to the excitation polarization. This quantity is very sensitive to noise in the measurement of $I_{\parallel}(t)$ and $I_{\perp}(t)$, and hence signal averaging can greatly increase the quality of these measurements.

Several problems were encountered in early fluorescence depolarization work. Since the $I_{\parallel}(t)$ and $I_{\perp}(t)$ were acquired on separate shots in the presence of large laser energy fluctuations, the data had to be arbitrarily scaled to either match tails at late time or early times. Using two-track detection, where $I_{\parallel}(t)$ and $I_{\perp}(t)$ were measured simultaneously for each shot, the fluorescence depolarization of Rhodamine B was measured with high accuracy in a large range of solvent viscosities and ionic concentrations (22). The two-track technique eliminates the problem of shot-to-shot energy fluctuations in the determination of the depolarization factor, and the high signal-to-noise ratio available with signal averaging allows greater sensitivity to detail.

Another problem with single shot recordings of this sort is that the high current density caused by an intense signal of long duration (such as that obtained with a nanosecond fluorescence lifetime) causes a distur-

tion of the waveform which is intensity-dependent. This distortion can be seen with single shot events and is effectively impossible to compensate for. In any streak camera experiment requiring high signal-to-noise ratio, a signal averaging technique should be used with single-shot intensities well below the level of distortions. In addition, the high excitation intensities required for samples in single shot experiments may give rise to other unwanted effects such as saturation and stimulated emission.

Fluorescence anisotropy of N-acetyl-tryptophanamide has been measured (18) in various environments. This experiment was particularly difficult because it required excitation at the fourth harmonic (266 nm) with limited energy (2 μ J) and detection in the UV at 340 nm. Fig. 3 shows the result of increasing viscosity on the decay time of the anisotropy calculated using Eq. 1. In order to obtain these results, 400 traces of $I_{\parallel}(t)$ and $I_{\perp}(t)$ were averaged.

Our streak camera with a fused-silica lens was found to have less than 5% of intrinsic anisotropy for fluorescence collection, and this is taken into account when calculating $r(t)$ by using both vertical and horizontal excitations. When such a correction is taken into account, we find that ultraviolet time-dependent anisotropy values can be measured to within $\sim 0.5\%$ upon averaging up to 400 shots.

Conclusion

The jitter-free operation of a streak camera increases the precision of measurement over single-shot fluorescence records. With this increased precision, detailed comparison of data with dynamic models is made feasible. The low-light level signal enhancement afforded by signal averaging requires careful attention to background offsets. Operation of the OMA-II in a Forth-based open system provides the necessary flexibility to meet these requirements. Data acquisition routines can be designed according to the experiment at hand. The LSI-11 processor in the OMA-II can be utilized to its full potential by writing time-critical routines in assembly code. This system allows for general data acquisition and theoretical modeling routines on the same machine, thus eliminating data transfer to other computers which may be slow or inconvenient.

Acknowledgment

The authors would like to thank R. Boni, R. Frankel, C. Pruitt, W. Seka, D. Baker and J. Jarvis for their assistance, and to C. Bowe for help with the manuscript.

This work was partially supported by the following sponsors: General Electric Company, Northeast Utilities, New York State Energy Research and Development Authority, The Standard Oil Company (SOHIO), The University of Rochester, and Empire State Electric Energy Research Corporation, and NSF grant #PCM-80-18488. Such support does not imply endorsement of the content by any of the above parties.

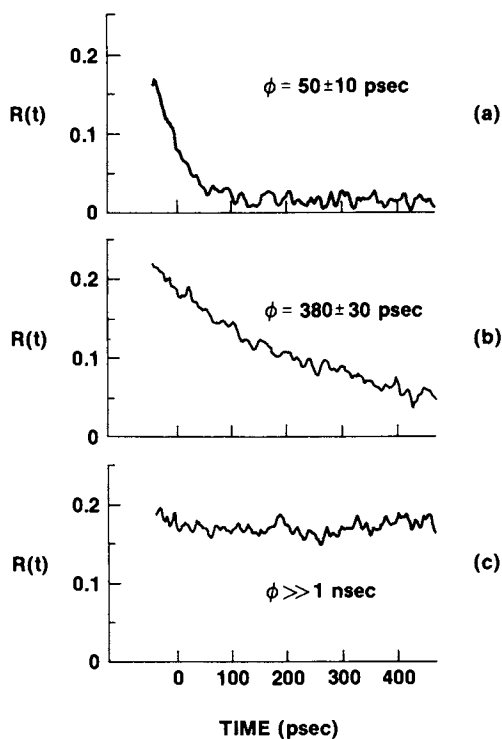


Figure 3. Examples of UV-fluorescence anisotropy decay. Anisotropy decay of fluorescence of N-acetyl-tryptophanamide with excitation at 266 nm and detection at 340 nm. Solvent viscosity dependence is investigated with 0% glycerol (a), 50% glycerol (b), and 97% glycerol (c). The scattered excitation pulse defines $t = 0$. To obtain this signal-to-noise ratio, 400 shots were averaged.

Literature Cited

1. Huston, A.E.; Walters, F., Advan. Electron. Electron Phys. 1962, 16, 249.
2. Bradley, D.J.; New, G.H.C., Proc. IEEE, 1974, 62, 313.
3. Fleming, G.R., Morris, J.M., and Robinson, G.W. Aust. J. Chem. 1977, 30, 2337-52.
4. Campillo, A.J.; Shapiro, S.L., IEEE Journal Quantum Elect., Special Issue on Pico. Phen., 1983, QE-19, 585.
5. Campillo, A.J.; Shapiro, S.L., Swenberg, C.E., Chem. Phys. Lett., 1977, 52, 11.
6. Craig, B.B.; Faust, W.L., Goldberg, L.S.; and Weiss, R.G., J. Chem. Phys., 1982, 76, 5014.
7. Adams, M.C.; Sibbett, W., and Bradley, D.J., Optics Comm., 1978, 2, 273.
8. Mourou, G.; Knox, W., Appl. Phys. Lett., 1980, 36, 623.
9. Knox, W.; Mourou, G., Opt. Comm., 1981, 37, 203.
10. Mourou, G.; Knox, W., Williamson, S., Proc. of SPIE 1982, 322, 107.
11. Mourou, G.; Knox, W., Williamson, S., Laser Focus 1982, 18, 97.
12. Princeton Applied Research, Inc., Princeton, New Jersey.
13. Moore, C., Astronomy and Astrophysics, 1974, 15, 497, and Kogge, P.M., IEEE Computer, March, 1982, 22.
14. Orłowski, T.E.; Weinstein, B.A., Knox, W.H.; Nordlund, T.M., and Mourou, G., Picosecond Phenomena II, K.B. Eisenthal, R.M. Hochstrasser, W. Kaiser, and A. Lauberau, Eds., 125 (Springer-Verlag, Berlin 1982), 395.
15. Weinstein, B.A.; Orłowski, T.E., Knox, W.H., Nordlund, T.M., and Mourou, G., Phys. Rev. B., 1982, 26, 4777.
16. Andrews, J.R.; Gibson, H., Orłowski, T.E., Slade, M.L., Knox, W.H., and Wittershaus, B., Phys. Rev. B, submitted.
17. Nordlund, T.M.; Knox, W.H., Biophys. J., 1981, 36, 193.
18. Nordlund, T.M.; Podolski, D., 10th Am. Soc. Photobiology Conf., 1982, Vancouver, B.C.
19. Breton, J.; Geacintov N., Knox, R.S., Knox, W.H., Nordlund, T.M.; Waldmeyer, J, and Wittmershaus, B., in preparation.
20. Hanzlik, C.A.; Nordlund, T.M., Knox, W., Gibson, S.L., Hilf, R., to be submitted.
21. Anderson, R.W., Knox, W.H., J. Lumin. 1981, 24/25, 647.
22. Podolski, D.; Thesis, University of Rochester, to be published.
23. Magde, D.; Zappala, M., Knox, W.H., and Nordlund, T.M., submitted to J. Phys. Chem.
24. Schubert, M.; and Vogler, K., Phys. Stat. Sol., 101, 267.
25. Weisenfeld, J.M.; Mollenauer, L.F., Ippen, E.P., Phys. Rev. Lett., 1981, 47, 1668.
26. Fleming, G.R., Morris, J.M. and Robinson, G.W., Chem. Phys., 1976, 17, 91.

RECEIVED September 2, 1983

Analytical Chemistry with Spatial Resolution: Obtaining Spectral Images with Multichannel Detectors

JAMES B. CALLIS

Department of Chemistry, University of Washington, Seattle, WA 98195

ADAM P. BRUCKNER

Aerospace and Energetics Research Program, University of Washington, Seattle, WA 98195

The concept of the "chemical composition/distribution matrix" is introduced in order to facilitate the interpretation of a chemical analysis when information about the spatial distribution of the analytes is included. Methods for displaying the chemical composition matrix as a "chemical image" are discussed. Generally, the chemical content matrix is not obtained directly, but must be deduced from spectroscopic measurements at each point in space. This data set is most conveniently thought of as a "spectroscopic image." Methods for obtaining the spectroscopic image by scanning are considered. It is shown that schemes which employ imaging detectors have large time and/or signal-to-noise ratio advantages over methods using single-channel detectors. As an example of the use of an imaging detector to obtain the spectral image, we present the "Multichannel Imaging Spectrophotometer" (MIS). It is shown that a "multichannel disadvantage" limits the ability of imaging devices to detect analytes embedded in scattering media. Possible remedies for this problem are devised and data presented to support them.

As the proceedings of this symposium attest, imaging detectors have an important role to play in analytical optical spectroscopy. They have been particularly effective in solving problems of multicomponent analysis, where it is necessary to make spectroscopic measurements at multiple wavelengths. Also, the multichannel advantage of an optical array is often valuable when a chromatographic technique for separation is combined with a spectroscopic technique for fingerprinting (1,2). The recent commercial introduction of liquid chromatography detectors consisting of rapid scanning UV-VIS spectrometers employing diode arrays demonstrates the growing appreciation of the power of these techniques (3-5).

0097-6156/83/0236-0233\$06.00/0

© 1983 American Chemical Society

In Multichannel Image Detectors Volume 2; Talmi, Y.;

ACS Symposium Series; American Chemical Society: Washington, DC, 1983.

The University of Washington group has concentrated on the use of imaging detectors in fluorescence spectrophotometry (6). Our instrument, the Video Fluorometer (7), uses a unique optical concept which allows us to record in digital form a series of fluorescence spectra as a sequenced set of up to 256 excitation wavelengths in a time as short as 16.7 msec without mechanical scanning. The effect of this novel scheme is to produce an image which contains both excitation and emission spectra. To capture this image quantitatively, we use an SIT vidicon as a sensitive multichannel imaging device interfaced to a PDP 11/04 computer through a high speed frame buffer memory. The performance of the Video Fluorometer has been thoroughly tested (8,9) and a series of algorithms has been designed to allow quantitative (10,11) and qualitative (12) analysis of complex mixtures.

Recently, we have interfaced the Video Fluorometer to a liquid chromatograph so that individual components of a complex mixture could be separated and their fluorescence scanned in real time as they emerged from the column (13). We are currently constructing a second generation of video fluorometers, replacing the SIT camera with an even more sensitive intensified diode array, and incorporating a rapidly scanned nitrogen laser pumped dye laser as excitation source. This system is being interfaced to a capillary gas chromatograph via a molecular beam so that ultra-high resolution spectroscopy can be performed "on-the-fly" (14).

While applying optical imaging detectors to analytical spectroscopy, we gradually began to appreciate their potential for elucidation of those problems of multicomponent analysis where it was desired not only to identify and quantitate each component but also to specify its location in space as well, i.e. when analytical chemistry was to be performed with spatial resolution. It is our belief that analytical chemists will become increasingly concerned with this problem in the next decade (15,16) and that optical imaging detectors will play a major role in its solution.

Conceptual Framework

The desired endpoint of the task of analytical chemistry with spatial resolution is a list of the analytes present, their amounts, and the spatial locations of each. The best means for organizing such a list is in the form of a "chemical composition/distribution tensor," \bar{c} , each element of which is a vector \bar{c} of dimension $3+R$, whose first three elements refer to the specific location in space, and the remaining R elements give the amounts of each of the R distinct chemical components recognized, i.e.

$$\bar{c} = \{c_{i,j,k,m,n,\dots}\} \quad [1]$$

Here, the indices i, j, k refer to the three spatial coordinates,

and the R indices m, n, \dots enumerate the R distinct components.

The chemical composition tensor can be written conveniently as a $3+R$ by L matrix, \bar{C} , which consists of L ordered rows which are the vectors \bar{c} , and the scalar L is the total number of spatial elements. Interpretation of the chemical composition tensor as a table quickly becomes difficult for complex objects with multiple analytes. A much better representation is in the form of a "chemical image" displayed on a computer graphics terminal. For a two-dimensional object this is readily done because there is a one-to-one correspondence between the positions on the object and locations on the x,y display. Each chemical entity can be readily identified if it is encoded as a particular color with the intensity being proportional to local concentration. For three-dimensional objects, the task is more difficult. One simple method is to follow the example of computed tomography and to display the object as a series of two-dimensional slices. In cases where the distributions of specific entities are organizable as discrete subobjects, e.g. inclusions in a rock, surfaces enclosing each object may be defined, the three-dimensional scene projected on a two dimensional plane, the visible surfaces false-color encoded, and hidden objects removed. In the case where objects are embedded within other objects, one can define "clipping" planes or use semitransparent outer surfaces. Some beautiful examples of the use of these techniques for portraying the structures and interactions of biomolecules have been given by Langridge and coworkers (17).

Unfortunately, the chemical composition tensor is not a directly measurable quantity. Instead, it must be deduced from indirect data. In the first place, spectroscopic measurements will usually be used to identify and quantify the chemical substances present. There may or may not be a one-to-one relationship between the intensity at one particular wavelength and the local concentration of a particular chemical entity. In the second place, if the analysis is to be three-dimensional and non-destructive, the chosen range of electromagnetic radiation must be transmitted through the object for multiple orientations of the object. The reconstruction of three-dimensional information from a series of two-dimensional projections is not at all trivial, but we shall leave this aspect of this problem to a later date.

Of major concern in this work is the irrefutable fact that when high resolution chemical images are being sought, where a number of analytes are to be identified and quantified, huge amounts of data will be involved. For example a single two-dimensional object resolved to 256 points in both spatial domains with absorbance measured at 256 wavelengths to a precision of one part in 256 will require 16.78 Mbytes for storage. While such data storage and processing requirements will strain the capacities of present-day computers, recent advantages in optical storage techniques (such as the read/write

video disk) and inexpensive pipelined array processors give us optimism that this part of the problem is tractable. There still remains the difficulty of acquiring all of the data in a finite period of time. For example, consider the acquisition of data for the 256x256 image mentioned above using a conventional spectrometer which takes one second to obtain a 256-point spectrum from one spatial element on the object: a total of 18 hours would be needed! Clearly, multichannel detectors would be of enormous benefit in reducing the data acquisition time and/or improving the signal-to-noise ratio (SNR) for a given acquisition time.

We shall now consider several methods for acquiring spectroscopic images using optical imaging detectors. In the first method, shown schematically in Figure 1, a one-dimensional array detector is used at the output of a spectrometer to acquire all the desired spectral data simultaneously at one spatial location at a time. The spatial scanning may be achieved either by displacement of the object through a fixed measuring spot as shown in Figure 1A or by displacement of the image of the fully illuminated object through a fixed aperture before the spectrometer as shown in Figure 1B. Either of these methods will potentially yield a time advantage of N over a single-channel detector, where N is the number of spectral elements acquired. For convenience, we have shown lasers as the light sources, but incoherent sources may be used as well and indeed will be needed for absorption/reflectance imaging.

Even more efficient methods for collecting the spectral image are shown in Figure 2. In these schemes, a two-dimensional imaging detector is used to capture a spatial image of the object. In the case where the spectral measurement is absorption, reflectance, or excitation, the object is illuminated by a sequence of uniform monochromatic wavelengths produced by a tunable laser or lamp/monochromator combination, as shown in Figure 2A. One spatial image is acquired at each wavelength of interest and stored in digital or analog form. In the case where the spectral measurement is optical emission or Raman scattering, a monochromator is used as an imaging wavelength filter, and one spatial image at each wavelength of interest is obtained, as shown in Figure 2B. This scheme has been successfully used to produce Micro-Raman images of high contrast and resolution (18). In the case of fluorescence imaging, the schemes of Figures 2A and 2B can be combined to yield an instrument capable of recording both excitation and emission information on an extended object.

Obviously, the above strategies employing a two-dimensional spatial detector have a much larger multichannel advantage than schemes using a one-dimensional spectral detector. Their potential time advantage is $M \times N$, where M is the number of spatially resolved elements in the X direction and N is the number of spatially resolved elements in the Y direction. Essentially, designs based upon two-dimensional detectors can acquire a complete spectral image in the same time as a

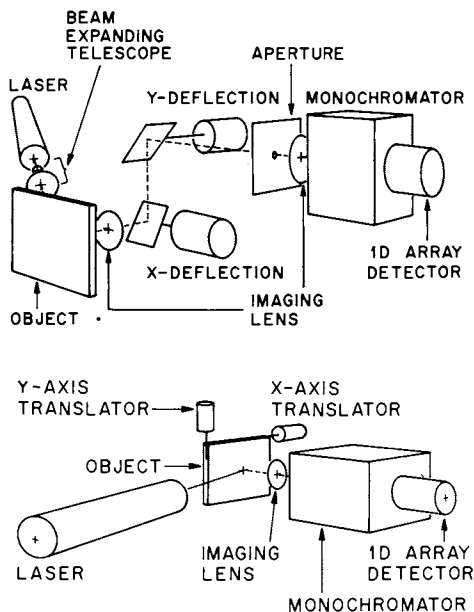


Figure 1. Schemes for using a one-dimensional array detector to acquire spectral images. Key: top, scanning of object; and bottom, scanning of image.

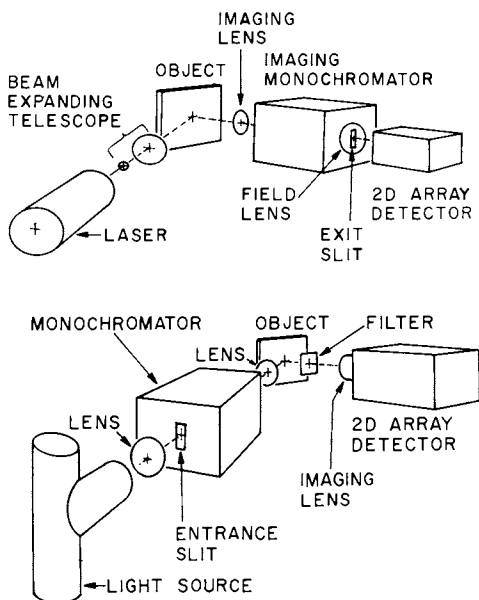


Figure 2. Schemes for using a two-dimensional array detector to acquire spectral images. Key: top, acquiring an absorption, reflectance, or excitation image; and bottom, acquiring an emission or scattering image.

conventional non-imaging spectrometer takes to scan the spectrum of a homogeneous material.

The Multichannel Imaging Spectrometer

In this section, we will describe an instrument, the "Multichannel Imaging Spectrometer" (MIS) which is capable of recording the absorption or reflectance spectrum at up to 64,000 points on an object in a time as short as two minutes. As a paradigm for spatially resolved analytical chemistry we have used MIS to analyze materials on thin-layer chromatographic plates both qualitatively and quantitatively (19). Several data analysis strategies have been devised to efficiently use the spectral data from MIS to resolve overlapping spots. A schematic of our single beam imaging spectrophotometer is given in Figure 3. A twenty-watt tungsten halogen lamp operated from a highly stable DC power supply served as the light source. Wavelength selection was accomplished with a Bausch and Lomb 1/4 meter monochromator equipped with a 600 lines/mm grating blazed for 300 nm. Slits were set to provide a spectral bandpass of 7 nm. Wavelength scanning was accomplished by means of a variable speed motor. In order to uniformly illuminate the thin-layer plate, an image of the diffraction grating was projected on to the plate by means of a lens placed at the exit slit (field stop). Light transmitted through the plate was collected by an f/0.78 CCTV lens, and focused onto the photosensitive surface of the SIT vidicon camera (Quantex QX-10). Our digital television photometry system has been previously described (8).

The camera was operated to collect a sequence of images synchronously with the scanning of the wavelength drive of the monochromator. The software for this operation was developed by Hershberger, et. al. (13) for fluorescence detection of liquid chromatographic effluents but was readily modified to serve the present need. Real-time displays of the monochromatic plate image and the absorption spectrum at two locations on the plate are available. Data consisting of a series of images taken over a selected wavelength region are stored on disk for later post-run processing, either by the PDP 11/04 or by a remote VAX 11/780.

In Figure 4 we illustrate the capability of MIS to analyze several one dimensional chromatograms simultaneously. The images are from a Whatman LHP-K plate which was spotted with various amounts of H₂TPP porphine in five separate lanes (1.1, 2.2, 3.3, 4.4 and 5.5 μg respectively, right to left in 4A). In lane 3, a mixture of H₂TPP along with ZnTPP and PdEP was spotted. The plate was then developed in a dichloromethane/cyclohexane (50:50) mixture for 3.5 min. Figure 4A shows the raw transmission image of the sample plate and a blank plate, respectively, at 420 nm. In 4B the two images of 4A are combined into an absorbance image and displayed as an isometric projection. This latter display is useful for visualizing the quantitative relationships among the absorbances of the spots. The upper trace in Figure 4C is the

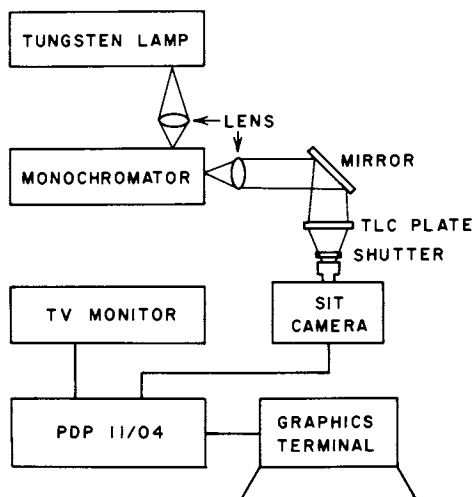


Figure 3. Block diagram of MIS.

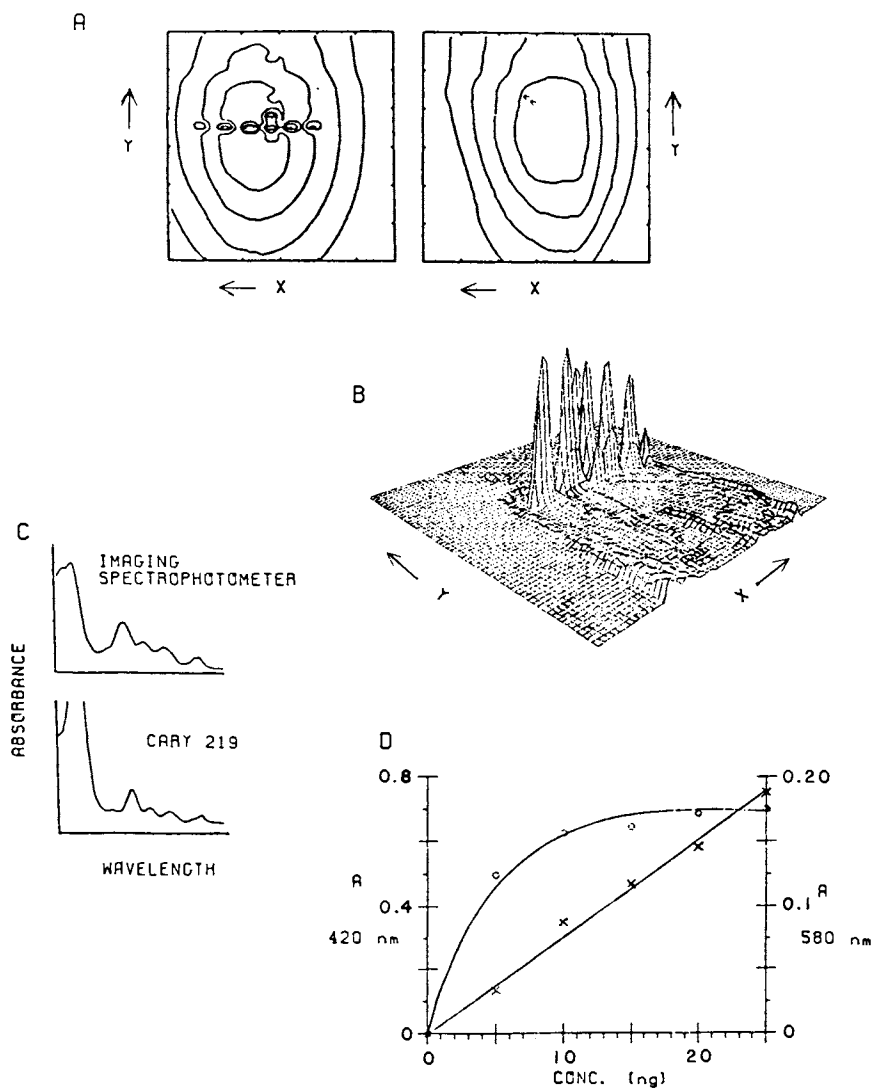


Figure 4. Use of MIS to analyze several one-dimensional chromatograms simultaneously.

spectrum of H_2TPP from the spot in lane 1. It was obtained by assembling the intensity values at a selected pixel from each of the images in the series stored on the disk. The analogy with a selected ion chromatogram of GC-MS data is obvious. The lower trace is the spectrum of the same spot obtained on a Cary 219 spectrophotometer, illustrating good agreement. Finally, Figure 4D is a plot of the integrated absorbance vs. the (known) amount of H_2TPP in each lane. At 580 nm there is an excellent linear correlation between observed absorbance and quantity of porphyrin, whereas at 420 nm a non-linear correlation is observed which exhibits a "saturation" behavior at high quantities. This latter phenomenon is attributed to the higher absorptivity at 420 nm leading to higher absorbances, and consequently greater photometric errors. Sources of photometric error include stray light in the single monochromator system and "glare" from scattered photons. Both of these sources would tend to reduce contrast and thus lead to underestimation of the absorbance. Independent experiments showed that good linearity could be obtained at 420 nm when smaller amounts of porphyrins were applied to the plate. For example, a linear calibration plot was obtained for 5 to 30 ng of ZnTPP.

A second data set is shown in Figure 5 and was designed to test the capabilities of the instrument for analysis in two spatial dimensions. Here, a Whatman LHP-K was spotted with a mixture of the three porphyrins H_2TPP , ZnTPP and PdEP. It was then developed for 3.5 min. with ethyl acetate, turned 90 degrees and then developed for 4.0 min. with the dichloromethane/cyclohexane mixture. Under these conditions the components are only partially resolved. The data shown in Figure 5 are several absorbance images of the plate taken at various wavelengths for a mixture of three porphyrins. Especially striking is the degree of differential enhancement of the selected (compound) spots as a function of wavelength of illumination. In 5A, the plate is imaged at 420 nm where all of the porphyrins absorb. The next three images were taken at 523 nm, 554 nm and 594 nm; H_2TPP absorbs strongly at 523 nm, PdEP at 554 nm, and ZnTPP at 594 nm. In 5B, then, the main contour peak is due to H_2TPP , while there is a weaker peak to the left of it due to weak² absorption by PdEP. Likewise in 5C the left PdEP peak is strong and the right H_2TPP peak somewhat diminished. In 5D, only the ZnTPP is seen.

Quantitative analysis of this mixture is has been carried out by using rank annihilation and least squares (20). As with the one-dimensional chromatograms, two-dimensional chromatograms can be analyzed quantitatively even when the spots are severely overlapping. Figure 6 illustrates the process of qualitative analysis of the two-dimensional chromatogram by means of "factorization" (20). The input data are shown as a "stack" of images; typical examples of which are displayed in Figure 5. The decomposition of these data into their three components is illustrated in Figure 6B-D. The absorption spectrum and the retention profiles along the x and y axes are all shown for each

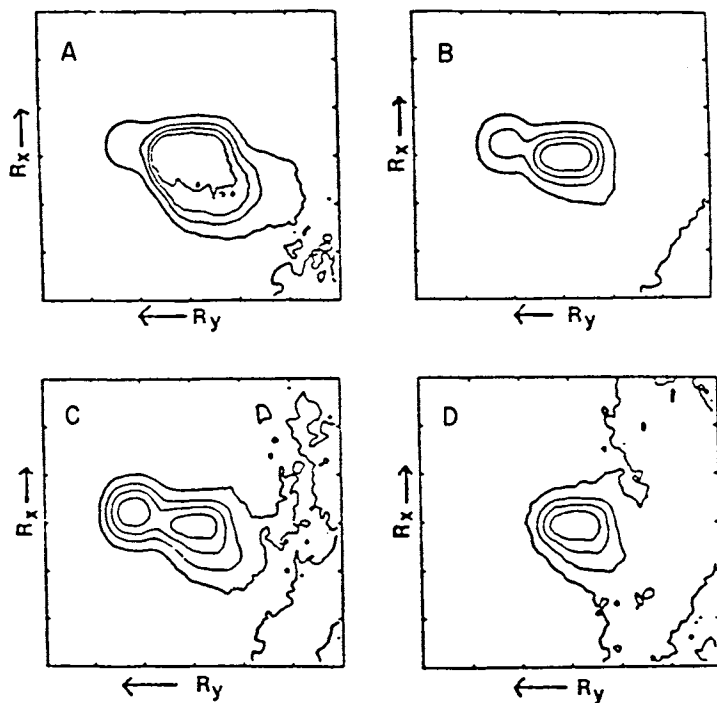


Figure 5. Two-dimensional chromatography contour plots of a mixture of H_2TPP , $ZnTPP$, and $PdEP$ at selected absorption wavelengths. Key: A, 420 nm; B, 523 nm; C, 554 nm; and D, 594 nm.

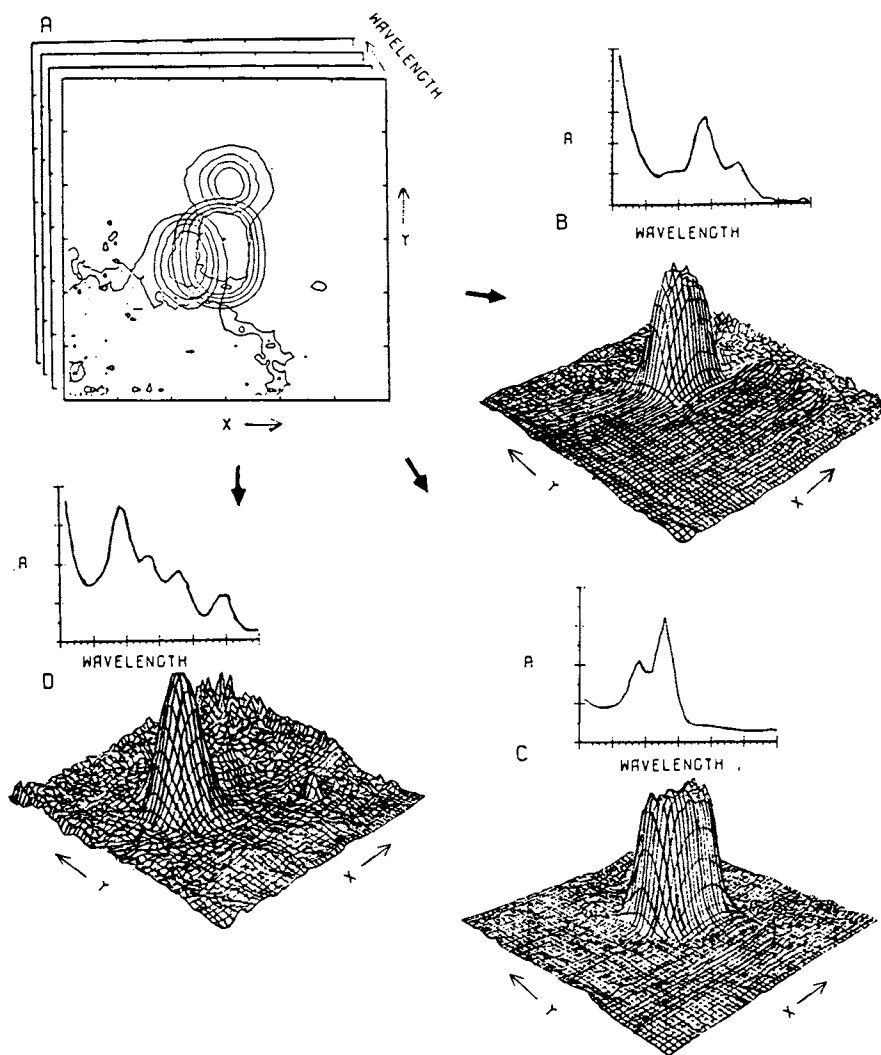


Figure 6. Three-dimensional factorization of the two-dimensional chromatogram of Figure 5. Key: A, stack of all two-dimensional chromatography images as a function of wavelength; and B-D, individual spatial-spectral components (B = PdEP; C = H₂TTP; and D = ZnTTP); each three-dimensional plot is the spatial representation of the associated compound (spectrum).

of the three components. The spectra shown superimposed nearly exactly with those of the pure components.

Imaging spectrophotometry of thin-layer plates is yet another example of the benefit of using a "hyphenated" method (21) for multicomponent analysis, i.e. a separation technique coupled with a spectroscopic technique. Our instrument compares favorably with the GC-MS in that the operator has great flexibility for display and analysis of the data: plotting the absorption spectrum of a selected spot is analagous to plotting the mass spectrum of a selected GC peak, while displaying the transmission image of the plate at a selected wavelength is analgous to displaying a selected ion chromatogram. Although the resolution of capillary GC is much higher than that of conventional one dimensional TLC, the great flexibility inherent in and the ease of implementation of two-dimensional chromatography may in some cases provide a compelling reason to prefer TLC with absorbance detection, especially when the low cost per analysis, parallel processing advantage and reliability of the instrumentation are taken into account.

Detection of Objects Embedded in Scattering Media: The Multichannel Disadvantage.

In the conceptualization section we showed that imaging schemes using two-dimensional detectors have the greatest multichannel advantage. At the same time they also have a "multichannel disadvantage" when three-dimensional imaging is performed on scattering objects. Consider the problem of detecting an absorbing object embedded in a clear and scattering medium as shown in Figures 7A and B. As can be seen, an opaque medium scatters the light beam multiple times, so that in effect the photons diffuse through the medium. Under these circumstances, light can scatter around the object of interest and reduce contrast. Moreover, the spreading of the beam due to diffusion causes loss of resolution.

We now propose two schemes for reducing the stray light. In the first one we construct the image point by point, as shown in Figure 8A, and relegate our multichannel detector (not shown) to acquisition of the spectrum. This scheme is particularly effective when the light source is coherent. As Ishimaru (22) has shown, the presence of scatterers acts to degrade the quality of the beam. However, the unscattered light remains coherent and can be focused to a diffraction-limited spot. A spatial filter placed before the detector will serve to block a major fraction of the scattered light while transmitting nearly all of the coherent light. Figure 8A shows a simple scheme for coherent imaging.

In a preliminary experiment, we have compared coherent and incoherent imaging of a strongly absorbing object suspended in a highly scattering medium. As a test object, we have used a 2-mm wide, flat metal plate (totally absorbing) suspended in a 10-mm wide cuvet containing a diluted solution of milk. When the cuvet

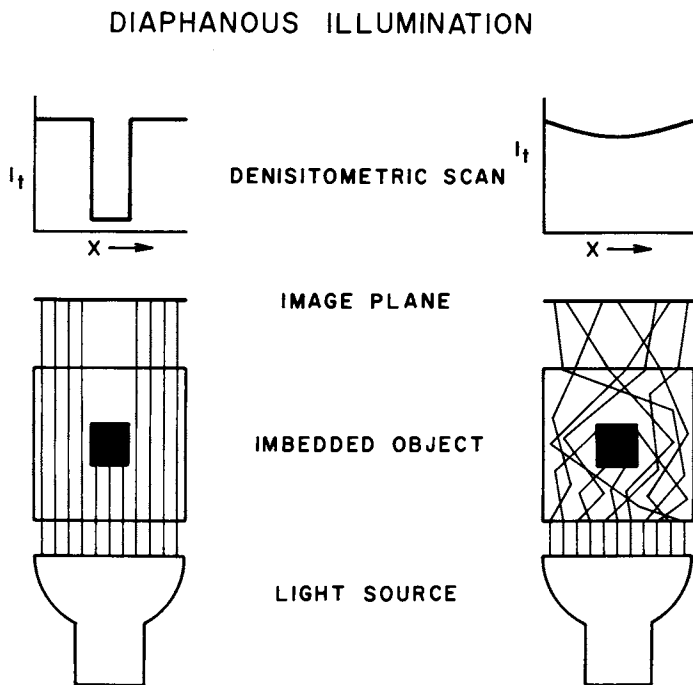


Figure 7. Comparison of images of absorbing objects embedded in a nonscattering medium (left) or a scattering medium (right).

was illuminated by a diffuse light source, one could see no evidence of the metal plate by eye. However, when the transilluminated cuvet was viewed with a silicon target vidicon, the plate was barely distinguishable as a diffuse, low contrast object when the contrast control on the monitor was set to its maximum. The apparatus for performing coherent and non-coherent imaging is shown in Figure 8A. Figure 8B gives the results of scans across the cuvet with and without the spatial filter. The considerably improved contrast and resolution for coherent imaging is obvious.

Our second scheme for overcoming the multichannel disadvantage involves temporal discrimination. Essentially, the object is illuminated with a very short pulse of light (a one-picosecond duration pulse is required to achieve millimeter scale resolution). The diffusely scattered light will travel a much longer path length than the coherent (unscattered) light (23); the latter is simply attenuated. Scattered and unscattered radiation are resolved by placing a picosecond light gate in front of an imaging detector and opening it when the unscattered pulse is expected. The feasibility of this technique of "range-gating" for detection of objects in scattering media has been carried out with an apparatus shown in Figure 9. The mode-locked Nd:glass laser produces an output train of approximately 100 infrared pulses ($\lambda=1.06\mu$), each about 10 psec in duration, spaced 7 nsec apart and carrying a power density of several hundred megawatts. This train of pulses is directed through a harmonic generating crystal, where about 10% of the infrared output is frequency doubled to 0.53μ green light. These green pulses are therefore synchronized to the infrared ones.

The infrared and green pulses are subsequently separated by a dichroic beam splitter. The infrared pulses travel directly to the ultrafast optical kerr effect shutter (24) while the green pulses are diverted through an optical delay line which consists of one movable and two fixed prisms. The shutter consists of a cell of carbon disulfide placed between two crossed polarizers, P_1 and P_2 . The infrared pulses induce a short-lived birefringence in the CS_2 as they travel through the cell, causing the otherwise opaque combination of crossed polarizers to transmit light for a time interval of about 10 psec. A camera or two-dimensional array detector records the desired light signal gated by the shutter. The green pulses are directed through an optical delay line consisting of one moveable and two fixed prisms and are then aimed by another prism towards the target, which consists of a 1 cm diameter bull's-eye drawn in white ink on black paper. In front of this target is interposed the obscuring medium. In this case, a cell containing a 20-mm thickness of diluted milk was placed 3 cm in front of the target. The optical delay line was adjusted to synchronize the simultaneous arrival at the shutter of the Nth echo from the target and the (N+1)th infrared gating pulse. By this technique the green backscattered echo from the obscuring medium was blocked from the camera because it arrived at the shutter before

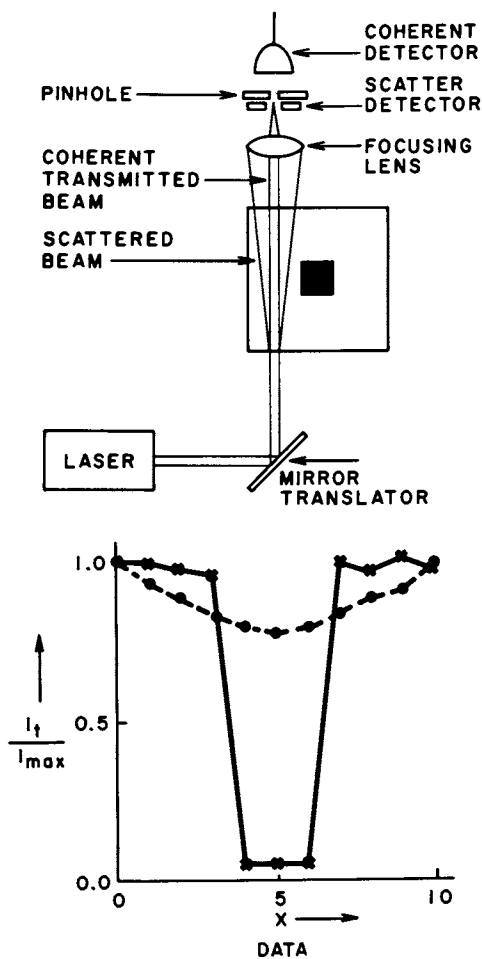


Figure 8. Scheme for coherent light imaging. Key: top, apparatus; and bottom, results. Key to bottom: x, coherent; and ●, incoherent.

the infrared gating pulse. As a result, a photographic image of only the target was recorded by the camera.

The results are shown in Figure 10. A close-up side view of the target and water cell is shown in Figure 10A. Under direct frontal laser illumination without range-gating, the result is as shown in Figure 10B. The very strong backscatter from the milky water completely obscures the target. Figure 10C shows the results of range-gating. The target image exhibits remarkable clarity and contrast, and its quality is virtually the same as that of unobstructed photographs of the target. This image clarity is result of the separation of the coherent echo signal from the incoherent diffuse scattered light generated by the target echo on its traversal of the obscuring cell. The propagation of picosecond pulses in diffuse media is the subject of ongoing investigations at the University of Washington (24-27). Multichannel detectors have become an integral part of our diagnostic approach to obtaining time-resolved signatures of pulse-broadening in diffuse media (28).

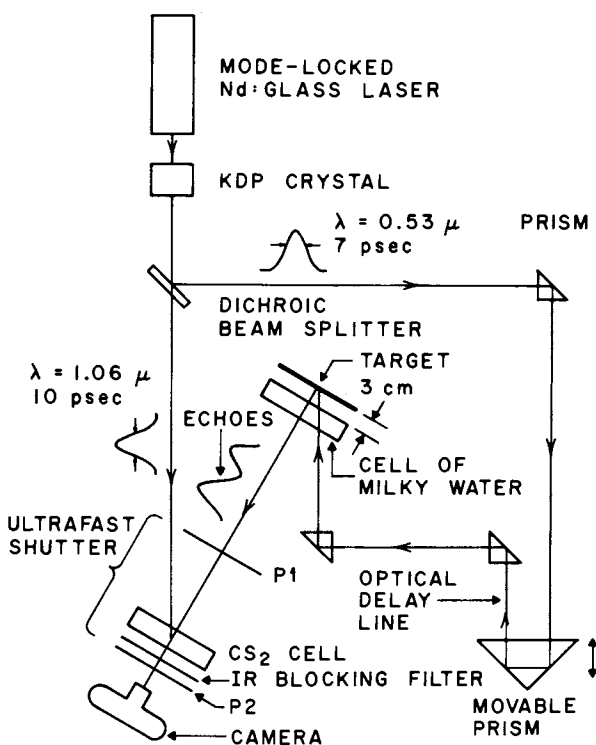


Figure 9. Scheme of overall experimental setup for range-gated imaging through diffuse media.

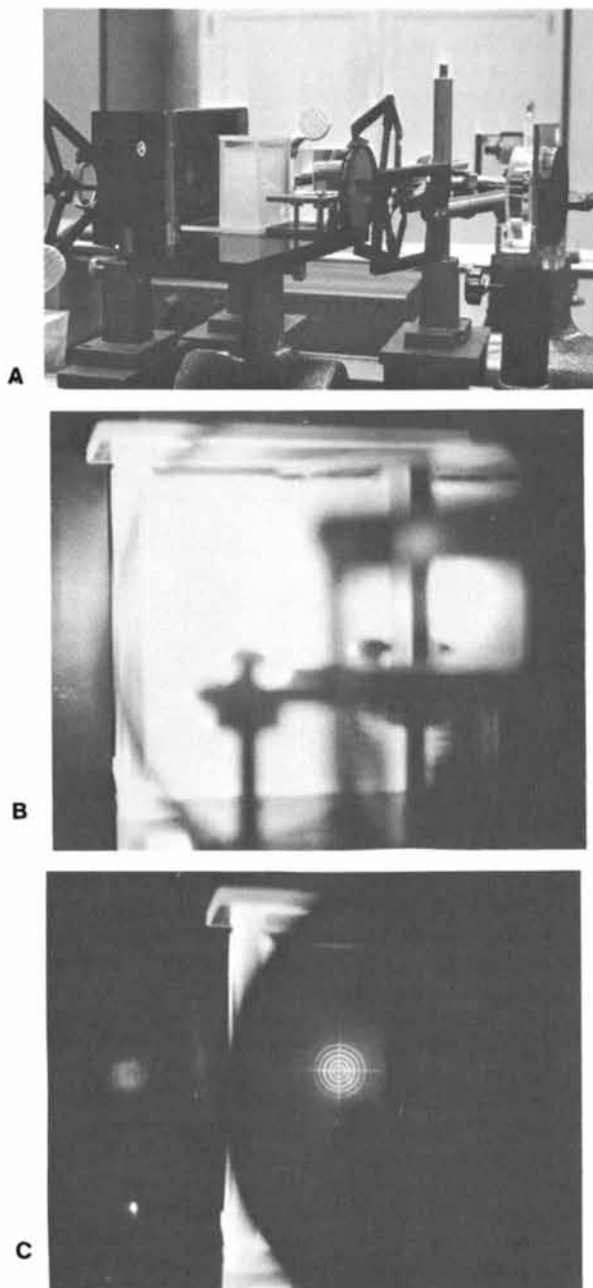


Figure 10. (A) Close-up side view of the target and water cell. (B) Results under direct frontal laser illumination without range gating. (C) Results of range gating.

Conclusions

Over the next decade, analytical chemists will have to become increasingly concerned with the acquisition and interpretation of chemical images. These in turn must be obtained from multidimensional spectral images, and it is here that multichannel detectors can play a major role in decreasing the data acquisition time and/or improving the signal-to-noise ratio. The preliminary data presented in this paper and elsewhere (19,29) show that multichannel detectors can fulfill their promise in this role and can even handle the difficult problem of detecting and characterizing objects embedded in strongly scattering media.

We have not addressed the problem of analyzing the spectral image and transforming it into the chemical image. We only note that many of the algorithms we have used in the past (10-12,20,30) for convoluting fluorescence spectral images can be readily and efficaciously applied to this problem.

Literature Cited

1. Jademec, J.R.; Saner, W.A.; Sager, R.W., in "Multichannel Imaging Detectors"; Talmi, Y., Ed.; ACS SYMPOSIUM SERIES No. 102, American Chemical Society: Washington, D.C., 1979; pp. 113-133.
2. D'Orazio, M., Appl. Spectrosc. 1979, 33, 278-283.
3. Miller, J.C.; George, S.A.; Willis, B.G., Science 1982, 218, 241-246.
4. Jenkins, R.G.; Kowalski, B.R. in "Ultrahigh Resolution Liquid Chromatography"; Ahuja, S., Ed.; ACS SYMPOSIUM SERIES, American Chemical Society: Washington, D.C., 1983, submitted.
5. Jones, D.G., Abstracts of the Pittsburgh Conference and Exposition, 1983, p. 305.
6. Christian, G.D.; Callis, J.B.; Davidson, E.R. in "Modern Fluorescence Spectroscopy vol. 4"; Wehry, E.L., Ed.; Plenum: New York, 1981; pp. 111-165.
7. Warner, I.M.; Callis, J.B.; Davidson, E.R.; Gouterman, M.P.; Christian, G.D., Anal. Lett. 1975, 8, 655-681.
8. Johnson, D.W.; Gladden, J.A.; Callis, J.B.; Christian, G.D., Rev. Sci. Inst. 1979, 50, 118-126.
9. Warner, I.M.; Fogarty, M.P.; Shelly, D.C., Anal. Chim. Acta, 1979, 109, 361-372.
10. Warner, I.M.; Davidson, E.R.; Christian, G.D., Anal. Chem. 1977, 49, 2155-2159.
11. Ho, C.N.; Christian, G.D.; Davidson, E.R., Anal. Chem. 1978, 50, 1108-1113; ibid., Anal. Chem. 1980, 52, 1071-1079; ibid., Anal. Chem. 1981, 53, 92-98.
12. Warner, I.M.; Christian, G.D.; Davidson, E.R.; Callis, J.B., Anal. Chem. 1977, 49, 564-573.

13. Hershberger, L.W.; Callis, J.B.; Christian, G.D., Anal. Chem. **1981**, 53, 971-975.
14. Hayes, J.M.; Small, G.J., Anal. Chem. **1982**, 54, 1204-1206.
15. Drummer, D.M.; Morrison, G.H., Anal. Chem. **1980**, 52, 2147-2152.
16. Vandeginste, B.G.M.; Kowalski, B.R., Anal. Chem. **1983**, 55, 557-564.
17. Langridge, R.; Ferrin, T.E.; Kuntz, I.D.; Connolly, M.L., Science, **1981**, 211, 661-663.
18. Delhaye, M.; Dhamelincourt, P., J. Raman Spectroscopy **1975**, 3, 33-43.
19. Gianelli, M.L.; Burns, D.H.; Callis, J.B.; Christian, G.D.; Andersen, N.H., Anal. Chem., submitted, 1983.
20. Appellof, C.J.; Davidson, E. R., Anal. Chim. Acta, **1983**, 146, 9-14.
21. Hirschfeld, T.A., Anal. Chem. **1980**, 52, 297A-312A.
22. Ishimaru, A., "Wave Propagation and Scattering in Random Media, vol. 1"; Academic: New York, 1978; pp. 301-306.
23. Ishimaru, A., op.cit., pp. 313-325.
24. Duguay, M.A.; Hansen, J.W., Appl. Phys. Lett. **1969**, 15, 192-194.
25. Ishimaru, A., J. Opt. Soc. Am. **1978**, 68, 1045-1050.
26. Shimizu, K.; Ishimaru, A.; Reynolds, L.O.; Bruckner, A.P.; Appl. Opt. **1979**, 18, 3484-3488.
27. Shimizu, K.; Ishimaru, A., Opt. Lett. **1980**, 5, 205-207.
28. Kuga, Y.; Ishimaru, A.; Bruckner, A.P.; J. Opt. Soc. Am., submitted 1983.
29. Geary, J.C.; Latham, D.W., "Solid State Imagers for Astronomy"; Proc. SPIE, Vol. 290, SPIE: Bellingham, Washington, 1981.
30. Appellof, C.J.; Davidson, E.R., Anal. Chem. **1981**, 53, 2053-2056.

RECEIVED June 23, 1983

Detection of Extreme UV and Soft X-Rays with Microchannel Plates: A Review

OSWALD H. W. SIEGMUND and ROGER F. MALINA

Space Sciences Laboratory, University of California, Berkeley, CA 94720

Microchannel plates are becoming widely used in spectroscopy and two dimensional imaging at EUV (100 - 1000 Å) and soft X-ray wavelengths (10 - 100 Å) for astronomy and microscopy. Although bare microchannel plates have low sensitivity (5% - 10% quantum detection efficiency) in this spectral region, use of photocathodes can increase substantially (to 30%-40%) microchannel plate performance. This, combined with the high spatial resolution ($<50\mu\text{m}$), fast time response ($<300\text{ ps}$), and large effective area (up to 100 mm diameter) achievable with microchannel plates make the latter a very attractive and versatile tool. We discuss the properties of microchannel plates, photocathode materials, and various microchannel plate detector readout schemes that have been used for soft X-ray and EUV detection.

Microchannel plate (MCP) detectors have been used in recent years as windowless X-ray and EUV detectors for astrophysical instrumentation. Successful applications have included the High Resolution Imager on the Einstein satellite (1), the EUV spectrometers on Voyager (2) and the airglow spectrometer on the P78-1 spacecraft (3). MCP's have been selected as the detectors for NASA's upcoming Extreme Ultraviolet Explorer (EUVE) satellite (4); this report was prepared as a part of the development for the EUVE satellite.

Microchannel plates (MCP's) are thin glass wafers composed of a large number ($>10^5$) of tubes or channels (Figure 1), the inner surfaces of which have a high secondary electron emission coefficient. Each glass channel in the array is used as an independent photomultiplier. Fabrication of MCP's is accomplished by several stages of drawing and stacking of glass-filled lead glass tubes to produce a boule. This boule is then sliced into wafers of the desired thickness and diameter. After the glass cores are etched out, the active surfaces of the MCP are produced by reduction of the glass surface at high temperature (250°C - 450°C) in a hydrogen atmosphere.

MCP's can be made in a variety of geometries, although normally they are in the form of rectangular or circular flat wafers whose thickness is 40 to 120 times the diameter of the glass tubes. A number of manufacturers now sell MCP's either mounted or unmounted; the most readily available are 1 inch diameter MCP's with 40:1 channel length to diameter (L/d) ratio manufactured for military night vision devices. Some

manufacturers (5, 6) will, however, cut MCP's to special requirements. Commonly-used channel diameters fall in the range 12.5 μm to 40 μm . For specialized applications, MCP's with spherical or cylindrical concave surfaces have also been made (5, 6), primarily to match the focal plane of spectrometers or grazing incidence mirrors. The channel orientation relative to the MCP front surface can also be specified. Although the channels are usually normal to the plate surface, they can be made at slant angles (typically 10°–20° to normal), and MCP's with curved channels are now available.

In operation, a high potential (~ 1000 V) is applied between the faces of the MCP, each of which is coated with a thin layer of metal to provide an electrode. Depending on the application, experimenters can use the front face negative with the rear face at a smaller negative voltage, or the front face grounded with the rear face at high positive potential. When radiation strikes the inner surface of a channel, there is a probability that an electron will be ejected. This probability is high (9, 10) for ionized particles ($>60\%$), but is comparatively low (5%-10%) for soft X-rays and EUV radiation. Electrons which are ejected from the channel walls are accelerated down the channel by the applied electric field, resulting in collisions with the wall, which produce further secondary electrons. This process leads to an electron avalanche travelling down the channel. The gain (electrons per detected photon) of single MCP's is typically 10^3 to 10^5 . Higher gains are normally achieved by cascading two or more MCP's in series, or using curved channel MCP's.

Quantum Detection Efficiency

Under typical operating conditions (high negative HV on MCP front surface), the sensitive area of an MCP is limited to the open channel area (typically $\sim 60\%$), since electrons emitted by radiation hitting the interchannel web are not collected. One way of increasing the open area is to funnel (6, 11, 12) the input end of the channels, although practical limitations restrict the maximum open area to $\sim 80\%$. However, it is also possible to recover the electrons from the interchannel web by using a small positive potential (13) on the front of the MCP or by placing a grid at high negative potential (14, 15) close to the front of the MCP to deflect electrons back into the channels. It is also worth noting that investigations (16) have shown that there is a dependence of the sensitivity on the polarization of the incident radiation.

A summary of the data on the quantum detection efficiency (QDE) of bare MCP's is given in Figure 2, where we define the 'QDE' as the probability of an incident photon giving rise to an output electron pulse from the MCP. The studies of Fraser (17) and Parkes *et al.* (18) were made without a deflecting grid, while the detectors of Martin *et al.* (15) and Taylor *et al.* (14) included an electron deflecting grid which increased the efficiency by approximately 30% over a bare MCP. The angle of incidence of the detected photons relative to the channel walls is an important factor in determining the QDE. This angle is indicated in Figure 2.

Typical QDE response curves as a function of photon incidence angle are given in Figure 3. The sharp drop in QDE below $\sim 5^\circ \rightarrow 10^\circ$ grazing angle is explained by the increase of channel wall reflectivity at low grazing angles (19). Although the peak QDE is reached at $\sim 10^\circ$ to the channel wall for XUV photons, the peak angle gradually increases to $\sim 15^\circ$ for EUV photons. At progressively higher angles of incidence, the depth of penetration of the incoming radiation into the MCP material increases; thus, the probability of secondary electrons escaping reduces and results in lower QDE.

Taking into account the angular factor, the QDE as a function of wavelength shows a slow increase in QDE as photon energies decrease from soft X-rays to EUV followed by a drop-off in QDE above 1200 Å. This is caused by the decreasing absorption depth of incident photons (19) as the wavelength increases, resulting in higher secondary electron ejection probability, followed by a cutoff which is determined by the work function of the MCP material.

Regarding the nature of the active surface composition of the bare MCP's, detailed investigations have been made by *Panitz et al.* (13) and *Siddiqui* (20). These show that, although the MCP faces are coated with an electrode material (Ni, Cr, nichrome), there is a thin (100 Å) top surface layer rich in potassium (20) that has been transported up from the underlying glass. The inner surfaces of the channels also have a surface layer which is rich in alkali (primarily K) metals (oxides), Si, and SiO₂ (13, 20). These surface layers, in addition to the composition of the bulk glass (PbO + SiO₂, predominantly), determine the QDE (19). Improvements in the QDE may, however, be obtained by the use of photocathode materials deposited on the MCP surface, which will be discussed later in this paper.

MCP Gain and Pulse Height Distribution

The gain and pulse height distribution of MCP's have been studied by many authors (21-27). Single straight channel MCP's may be operated up to gains of 10^4 - 10^5 (12, 21-23) and give negative exponential output pulse height distributions (12, 21, 22, 25). [A number of authors have developed models for the gain characteristics of MCP's (12, 26, 27).] The MCP gain increases rapidly with applied voltage (12, 23, 26, 27) up to 10^4 - 10^5 , and then begins to level off. This 'saturation' of the gain (at high gains) occurs because the charge density in the output end of the channel is high enough to initiate space charge effects. The resulting charge build-up on the channel walls lowers the accelerating field and reduces the kinetic energy of the electrons. This, in turn, causes a reduction in the secondary electron yield and hence, limits the gain. The maximum gain achievable at fixed applied voltage and channel length over diameter ratio (L/d) has been shown (21, 27) to be proportional to the channel diameter and is in the range 10^5 - 10^6 for common MCP geometries. Normally, however, straight channel MCP's cannot be operated at these high gains because of ion feedback effects. Positive ions are produced by collisions of electrons with residual gas molecules (at pressures $>10^{-6}$ torr) in the channels and gas molecules released from the channel walls during multiplication (22, 23, 28). The ions travel back up the channel and may strike the channel wall near the MCP input face, releasing electrons, which results in a secondary electron avalanche and afterpulsing.

The problem of ion feedback has been circumvented in a number of ways. First, if the MCP's are baked in vacuum, 'scrubbed' by running them at high current, and not reexposed to air, the problem of desorbed gas from the channel walls is greatly reduced. Good results are achieved in this way for sealed tube devices. At high gains, however, the baking and scrubbing are insufficient to suppress ion feedback, so various geometrical modifications of MCP's have been devised.

One method is to use MCP's with curved channels ((L/d) typically in the range 80:1 \rightarrow 140:1), so that ions strike the channel walls closer to their point of origin than in a straight channel MCP. This reduces the size of the secondary electron pulses associated with ion feedback to acceptable levels, allowing gains of up to 2×10^6 to be used. At these high gains, the pulse height distribution is peaked with a Gaussian type shape and a FWHM on the order of 30% - 60% (30-32, 34). The narrow pulse height

distribution is a consequence of the limiting of the gain when operated in the 'saturated' mode, as described previously.

Ion feedback may also be reduced by using a tandem (V) or triple (Z) stacking arrangement of MCP's. These configurations are oriented such that there is an angle of about $15^\circ - 20^\circ$ between the channels at the stack interfaces. Ions generated at the stack output face cannot proceed past this bend, and thus produce only small secondary electron pulses. Tandem and Z arrangements have operational gains as high as $10^7 - 10^8$ (1, 28, 33), with a gain/voltage curve shape similar to that of single MCP's (Figure 4). A pair of 40:1 L/d MCP's separated by $25 \mu\text{m} - 150 \mu\text{m}$ is a commonly used tandem configuration (23, 28).

The pulse height distributions for a tandem of two 40:1 L/d MCP's in this arrangement are poor (100% - 200% FWHM) (23, 28, 31) compared to curved channel MCP's. However, by increasing the L/d ratio of each of the MCP's to 80:1, or greater, and using each MCP in a near saturated mode, pulse height distributions of 30% - 50% FWHM have been achieved (1, 25, 27, 33). Figure 5 demonstrates the progressive narrowing of the pulse height distribution as the MCP gain is increased for a tandem of two 80:1 (5) MCP's placed back to back (no gap). Recent results (27) also indicate that reducing the channel diameter improves the pulse height distribution.

The configuration of the interface between the two MCP's of a tandem is an important factor in determining the gain/pulse height performance. For a back to back tandem pair of MCP's, electrons from the first MCP can enter only a maximum of 3 channels (35) in the second MCP, assuming flat MCP surfaces. If a small gap between the MCP's is introduced, the electrons from the first MCP can spread into many more channels of the second plate. This results in an increase of the gain, since more channels contribute; however, the pulse height distribution is degraded because the channels of the second plate are not as highly saturated. If a field is applied across the gap (23, 27, 36) between the MCP's, the gain drops and pulse height FWHM is found to improve. This results because the electrons from the first plate are accelerated into fewer channels of the second MCP. The configuration used in any application depends on the desired gain/pulse height characteristics.

It should be noted that the gain of MCP's is not constant with accumulated dosage. Lifetests (1, 12, 25, 29) of MCP's have shown that there is an initial sharp drop in the gain, associated with outgassing of the channel walls, followed by a plateau region of stable operation. The behavior of MCP parameters after re-exposure to air (37, 38) indicates reversible increases in gain attributable to adsorption of gas in the channels. For this reason, it is advisable to 'scrub' (or 'burn in') MCP's until the plateau region is reached before use. Another frequently-used technique is to bake out (29) MCP's in vacuum; however, this can cause an additional permanent drop of the MCP gain. It has been suggested (13) that, in addition to driving off adsorbed gases and water vapour, the bake causes desorption of the alkali metals which are responsible for the secondary emission properties of the MCP. Desorption of alkali metals under electron bombardment may also play a part in determining the overall lifetime of MCP's, although there is, at present, insufficient information to characterize MCP lifetime properties completely.

Unlike conventional photomultiplier tubes, MCP's can be subjected to high magnetic fields (>100 G) without significant changes in gain and pulse height distribution (39). This is attributable to the small size and length of the MCP channels and the high electric fields within the channels. Magnetic fields are, however, a more serious concern in the readout system located behind the MCP.

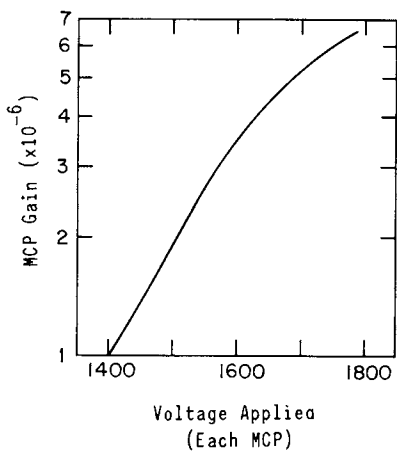


Figure 4. Gain/voltage curve for a tandem pair of 80:1 L/d MCPs with $d = 12.5 \mu\text{m}$.

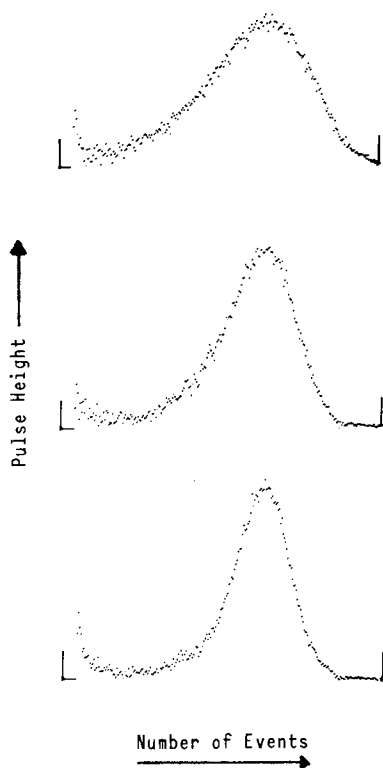


Figure 5. Pulse height distribution of a tandem pair of MCPs each having $L/d = 80.1$ and $d = 12.5 \mu\text{m}$. Conditions (top): gain, 10^6 ; and FWHM, 58%. Conditions (middle): gain, 1.9×10^6 ; and FWHM, 41%. Conditions (bottom): gain, 4.6×10^6 ; and FWHM, 32%.

Noise characteristics

The number of background noise events (18, 23, 29) from both single and tandem MCP's is generally very low (< 1 count/cm²/sec), but this can still be a significant limitation in applications such as X-ray and EUV astronomy, where very low count rates are experienced. Lower thresholds must be carefully chosen to exclude the low gain exponential tail responsible for a large fraction of the background counts. Most manufacturers now produce MCP's which have, on average, dark count rates of < 0.5 counts/sec/cm², and we have found that selected plates can have rates as low as 0.1 - 0.2 counts/sec/cm². Investigation (1) of the sources of background events suggests that, at sea level, cosmic ray events, intrinsic radioactivity, and thermionic emission contribute less than 5% to the overall background rate. It has been suggested (1) that defects in the MCP channel walls are responsible for the background events through field emission. This correlates with the non-saturated pulse height distributions obtained for background events using a tandem, indicating that background events are generated all along the channel walls (1).

Other noise phenomena which may impair the performance of MCP's include 'switched on' channels, 'hot spots', 'dead' channels, and field emission from mounting hardware. Due to improved selection and production techniques, the incidence of 'dead' channels and 'switched on' channels is now relatively low. However, hot spots, producing relatively large numbers of spurious events, are a more common occurrence. Currently this effect is thought to be associated with dust or damage on the front surface of MCP's. Certainly our experiences suggest that, if care is taken with cleanliness and handling of MCP's, the occurrence of hot spots can be kept very low.

Time Response and Count Rate Performance

A single event electron pulse emerging from a MCP can be extremely short (< 1 ns) in duration (23, 30, 40-42). Due to the high fields and short distances, the transit time of the electrons through a MCP is calculated to be on the order of 250 ps (40:1 L/d MCP) and the transit time spread to be about 50 ps (42). Experimental results with MCP photomultiplier tubes (PMT's) indicate (23, 30, 40, 41) that pulse widths of 200 - 300 ps can be achieved with single MCP's. Fast MCP PMT's with Z MCP configurations have longer (23, 40, 41) pulse widths (300 - 500 ps), due to the extra length of the channels. Slowing-down effects, caused by the reduction of electron energies in the saturated mode also contribute to this.

The recovery time of a single channel after an event is determined by the rate at which the extracted charge can be replaced. For a typical 1 mm thick MCP of resistance 300 m Ω , the channel recovery time τ_c is of the order 20 ms (21, 23), where $\tau_c \approx R_c C_c$ (R_c and C_c are the effective channel resistance and capacitance, respectively). So, the maximum event rate per channel is ~ 50 counts/sec, and if this rate is exceeded, the channel does not recover fully between events and the gain drops as a consequence. Since an MCP has on the order of 10^5 - 10^6 channels, the overall counting rate can be very high ($> 10^6$ counts/sec), provided no channel experiences more than ~ 50 counts/sec. Some manufacturers (5, 6) provide MCP's with low channel resistance to reduce the channel time constant in applications which require high localized counting rates.

For a tandem MCP configuration, a number of channels of the second MCP are excited by a single event in the front MCP. Therefore, neighboring channels of the first MCP will, in effect, cause some of the same channels of the second MCP to be

excited. So, although the recovery time for a single event is similar to that for a single MCP, the overall counting rate for the tandem is lower, by a factor equivalent to the number of channels which a single event excites in the second MCP.

Photocathode Materials

Photocathode materials are used routinely to enhance the detection efficiency of MCP's at soft X-ray and EUV wavelengths. Unlike detectors with optical photocathodes, most MCP detectors for this wavelength range operate in a 'windowless' mode, because there are no suitable window materials sufficiently strong to hold back 1 atm. Since either production of photocathodes *in situ* or transport of unsealed devices under ultra high vacuum is usually impractical in space instrumentation, photocathodes which are stable under exposure to air are normally selected. Since the photon energies of interest are in excess of 10 eV, photocathode materials with relatively high work functions (a few eV) can be used. Widely used materials include MgF_2 , LiF and CsI. Many other alkali halides are suitable, although some precautions need to be taken, since many of these compounds are hygroscopic.

Photocathodes may be used in two configurations, opaque (or reflection) photocathodes and transmission photocathodes. Detailed calculations of the performance of both types of photocathode may be found in the articles of *Henke* (43-45). Opaque photocathodes usually are deposited directly onto the input face of the MCP such that the photocathode material penetrates a short distance into the channels. Thus incident radiation which enters the channels strikes the photocathode material, resulting in enhanced detection efficiency. As in the case of a bare MCP, radiation striking the interchannel web is not normally detected, so electron deflection grids in front of the MCP are sometimes used to further the enhancement of detection efficiency.

Transmission photocathodes for EUV and soft X-ray applications can be deposited on very thin substrates such as parylene, polypropylene, lexan, aluminum, or even fine mesh grids. This photocathode assembly is normally used in a proximity-focussed configuration mounted close to the MCP input ($300\ \mu\text{m} \rightarrow 1000\ \mu\text{m}$). Electrons emitted from the photocathode are then accelerated to the MCP by a high electric field ($500 \rightarrow 1000\ \text{V/mm}$). One of the limitations of this configuration, however, is that the photoelectrons spread laterally in the photocathode/MCP gap, resulting in a practical limitation of $\sim 50\ \mu\text{m}$ FWHM for the position resolution (33, 46). In general, transmission photocathodes also show lower quantum yields (electrons/incident photon) than opaque photocathode configurations.

Cesium Iodide

Cesium iodide has received much attention recently as a potential photocathode material (17, 47-55) by virtue of its high quantum efficiency in the soft X-ray and EUV regions. A compilation of CsI efficiency data in the range $10\ \text{\AA} - 2000\ \text{\AA}$ for a number of different configurations is given in Figure 6. (Grazing angle of incidence is indicated). The measurements of *Fraser* (17), *Martin et al.* (15), and *McClintock* (47) were taken with opaque CsI coatings on the surface of MCP's. However, the QDE's measured by *Fraser* refer to efficiency of CsI in the channels alone, since the electrons emitted from the interchannel web were not collected. On the other hand, in the measurements of *McClintock* and *Martin et al.* electrons from the interchannel web were collected with an electric field. In the latter case (14), the channels were found to contribute little ($\sim 20\%$) to the overall quantum efficiency. This was because the CsI coating inside the channels was too thin ($< 400\ \text{\AA}$), resulting in a low photoyield.

In comparison, the measurements of *Lukirskii* (48) and *Iyesaar* (49) are of the QDE of evaporated CsI coatings on flat substrates, and not on MCP's. These show the QDE peak associated with the strong absorption (4d - 4f transition) peak of CsI at about 100 eV. This agrees with the results obtained by measurement of the photoemission current from CsI evaporated coatings (50, 51). The high yields obtained on flat substrates will be reduced proportionally by the open area of the MCP unless a deflection grid is used.

Investigations (51, 52) of the variation of quantum efficiency as a function of the CsI layer thickness show that (Figure 7) the quantum detection efficiency, for wavelengths under 100 Å, is nearly constant for layers above 1000 Å in thickness. Below 1000 Å thick, the QDE falls off, due to the increasing transmission of the photocathode layer.

The QDE is also a function of the grazing angle of incidence of the incoming radiation, as is the case for bare MCP's. The typical curve for CsI is shown in Figure 8, demonstrating that there is a peak efficiency at small angles of incidence. It has been shown that (51, 52), as for all alkali halide materials, the bulk of the photoemission is due to low energy secondary electrons, which have a narrow energy distribution that is relatively invariant with the energy of the incoming radiation (51).

It is clear from the above that improvements in the QDE of CsI coatings on MCP's should be achievable by using coatings of sufficient thickness on both the web and the channel areas and by using a collecting field above the MCP.

Some work has also been done with CsI transmission photocathodes (53, 54). *Bateman* (54) has used low density (5% relative density) CsI layers on thin aluminum substrates and has obtained high efficiencies (60%) in the X-ray region (6 - 20 keV). For work at longer wavelengths, very thin foil substrates are required. Another method has been used by *Carruthers* (53), where the CsI photocathode is deposited on a fine mesh grid (36% open area), which is placed in front of the MCP. Due to the reduction in sensitive area, however, the efficiency obtained was somewhat less than that for opaque photocathodes.

An important aspect of the performance of CsI is its stability under atmospheric conditions. Several workers (17, 50, 51, 55) have reported no degradation of QDE in the range 1 Å - 250 Å, even under exposure to humid atmosphere. There is evidence (53), however, of degradation of QDE at longer wavelengths after exposure to humid air.

Magnesium Fluoride and Lithium Fluoride

MgF₂ has been used extensively as an opaque photocathode material for the EUV and X-ray regions (1, 48, 55-59). This is due to its stability in air (55-57) and its ability to increase the quantum efficiency of bare MCP's by up to a factor of four.

Figure 9 gives a composite of the measurements of the QDE of MgF₂ at specified grazing angles of incidence. The measurements of *Lapson et al.* (56), *Likurskii et al.* (48), and *Savinov et al.* (55) were all made with single channel electron multipliers, while the measurements of *Henry et al.* (1) and *Fraser* (58) were done using MCP's. Due to the large variation in the grazing angle of incidence at which these measurements were made, it is important to note that the dependence of QDE on angle is very similar to that of CsI and bare MCP's (1, 48, 55, 57, 58). Nevertheless, it is evident that MgF₂ has two reasonably high (40% QDE) QDE peaks at ~200 Å and ~500 Å, indicating the suitability of this material for use in the EUV.

Figure 6. Quantum detection of efficiency of CsI-coated MCPs and flat samples, as a function of wavelength. Key: —, Reference 48 (10°); —, Reference 49 (20 and 23°); -- and —, Reference 17; —, Reference 15 (8°); and \circ , Reference 47.

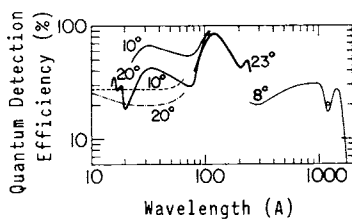
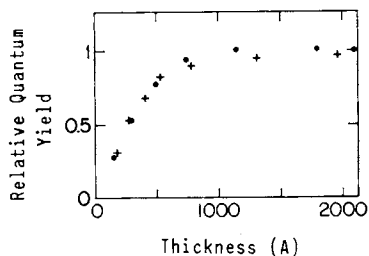


Figure 7. Relative quantum yield of CsI coatings as a function of CsI layer thickness. Key: +, $\lambda = 44 \text{ \AA}$ (51); and \bullet , $\lambda = 44 \text{ \AA}$ (52).



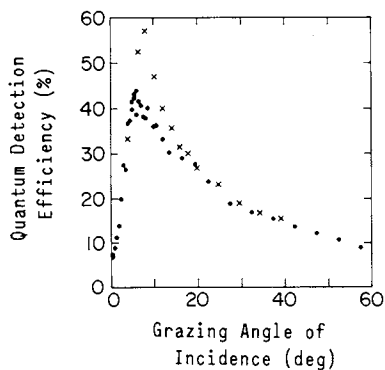


Figure 8. Quantum detection efficiency of CsI coatings as a function of grazing angle of incidence. Key: \times , $\lambda = 67 \text{ \AA}$ (48); and \bullet , $\lambda = 44 \text{ \AA}$ (17).

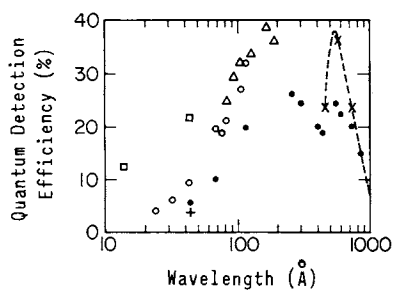


Figure 9. Quantum detection efficiency of MgF_2 coatings as a function of wavelength. Key: \times , 4.5° (60); \circ , 20° (48); $+$, 20° (17); \bullet , 45° (56); Δ , 23° (55); and \square , 6° (1).

Investigations (55, 60) of the stability of MgF_2 photocathodes under exposure to a laboratory environment show that, over relatively long periods (weeks), there is little degradation of QDE. However, *Smith et al.* (57) have observed a factor of two degradation in QDE over a period of 400 days under unspecified storage conditions.

The QDE profile of LiF as a function of wavelength is similar to that of MgF_2 (48, 55, 60), with QDE peaks in the regions of $\lambda = 200 \text{ \AA}$ (55) and $\lambda = 550 \text{ \AA}$ (60, 59). In general, the QDE of LiF is close to that of MgF_2 , except in the regions of $100 \text{ \AA} - 200 \text{ \AA}$ and $800 \text{ \AA} - 1000 \text{ \AA}$, where the LiF QDE is higher than that of MgF_2 (55, 60). LiF is not as widely used as MgF_2 because there is evidence (57, 60) to suggest that the QDE drops on exposure to laboratory air, presumably due to the hygroscopic nature of LiF. Other data (55) indicate very little degradation of QDE, however, even after 1 month in air. It has been suggested (58) that relative humidity levels may play a large part in this respect, a factor not specified in these measurements.

Other Photocathode Materials

A number of other photocathode materials have been examined (48, 50, 52, 55, 59) to determine their potential as photocathodes in the soft X-ray and EUV regions. The majority of these are alkali halides or alkali earth halides, such as KI, SrF_2 , and CaF_2 , which have, in general, significantly higher QDE than evaporated metal photocathodes (48, 52, 55, 59). Most of the alkali halides exhibit a similar dependence of QDE on grazing angle of incidence (48, 55), which is close to that of the bare MCP. Alkali halides show varying degrees of hygroscopic behavior, however, which again influences the choice of materials. A number of other materials (BeO , MgO , and CuI) which exhibit high QDE have also been considered (48, 50, 52, 55). The QDE maxima of these materials at selected wavelength bands may be found particularly useful in some applications.

MCP Image Readout Systems

In recent years, considerable effort has been made to develop high resolution distortion-free image readout systems for MCP's. The result is that there is now a large range of readout systems with varying resolution, speed, size, and image linearity characteristics. The choice of readout system is normally determined by the constraints imposed by the required application, but the comparison of the readout systems discussed here (shown in Table I) gives a general idea of the operational parameters.

Phosphor/photodetector Systems

The use of proximity-focussed phosphor screen behind an MCP is an established procedure for second generation image intensifier tubes. It is also a convenient method for examination of soft X-ray and EUV images. Electronic registration of the images can then be accomplished with a TV camera (61), photodiode arrays (62, 63, 98-103) or CCD's (62, 64, 65) coupled to the phosphor screen by lenses or fiber optic windows. Although the event spot size on the phosphor screen is normally $50 \mu\text{m} - 100 \mu\text{m}$ FWHM (63), determination of the centroid of the intensity distribution can give better resolution than this, provided the MCP channel size and pixel size are sufficiently small. For example, the event centroid position on a CCD may be found by examining the signal levels on adjacent pixels to determine the center of gravity of the charge

Table I. Demonstrated Published Performance of Position Readout Systems

Readout System	Active Area	FWHM Spatial Resolution	Pixels	Time Resolution	Max Count Rate	References
Resistive Anode	25×25 mm	~50 μm	500×500	<10 μs	>10 ⁴	(80)
Wedge and Strip	25×25 mm	<40 μm	600×600	<10 μs	>4 × 10 ⁴	(33)
Phosphor + TV	21×21 mm	<25 μm	850×850	>10 ms	10 ⁴	(61)
Phosphor + Reticon	26 mm	<40 μm	1024×1	5 ms	<10 ⁴	(63)
Phosphor + CCD	10×10 mm	~100 μm	190×244	>10 ms	>10 ⁴	(64)
Multiwire	26×26 mm	<25 μm	>1000×1000	<8 μs	>10 ⁴	(1)
Multianode, Quadrant	1×1 mm	~10 μm	100×100	<1 μs	>10 ⁵	(72)
Multianode, Array	10×10 mm	1 mm	10×10	300 ps	10 ⁸	(11)
Codacon	26 mm	25 μm	1024×1	<1 μs	10 ⁶	(47)
MAMA	10×10 mm	~20 μm	512×512	<1 μs	10 ⁶	(32)

distribution. The statistical variation of the event centroid position, for the same real event position, is much smaller than the overall event spot size.

CCD's and photodiode arrays are obtainable with dimensions on the order of 1 cm square; for larger formats, the use of tapered fiber optics gives larger effective areas which can be used at correspondingly lower spatial resolution. Alternatively, arrays of CCD's and photodiode arrays have been proposed (66). Count rates can be quite high with these devices (>10⁴ counts/sec); however, if two events fall in similar positions within one readout time frame, the centroid position will be averaged. This type of effect may be corrected by pulse amplitude rejection, provided that the MCP pulse height distribution is sufficiently narrow (<70% FWHM). Due to the strong fields and small distances for the proximity-focussed phosphor scheme, this arrangement is fairly immune to external magnetic fields. This is not true for some of the following readout schemes, however, where relatively large distances and low field strengths are used. Examples of applications of these types of detector include a photodiode system for astronomical FUV spectrophotometry (63), plasma fusion spectroscopy (99-103), and EUV spectroscopy using a CCD system for upper atmosphere studies (64, 65).

Multiwire Readout Systems

Multiwire position readout systems have been used for a number of years with proportional counter detectors (67, 68). Adaptations of this method have proved very successful in imaging applications with MCP's (1, 69-71). A typical arrangement (Figure 10) is described by Knapp (69) and consists of two planes of closely spaced wires. Each wire is 0.1 mm in diameter and individual wires are spaced at 0.2 mm intervals with a gap on the order of the wire spacing between the two planes. The wires in the two planes run orthogonal to each other to permit determination of both the x and y coordinates of an event. Resistors interconnect the wires in each plane and preamplifiers are connected to every eighth wire. Thus, a readout system of ~130 + 130 wires, for example, requires 16 + 16 amplifiers. Electron clouds emerging from

the MCP are allowed to spread over a number of wires of this 'crossed grid' readout system. The coarse event position is found by locating the preamplifier with the greatest signal and the centroid position is determined by the ratios of charge division between neighbouring preamplifiers. The large number of amplifiers required is a disadvantage in some applications.

The crossed grid readout system gives very little image distortion (70) and can be extended to relatively large areas ($>26 \times 26$ mm) without loss of spatial resolution. Resolution ($\sim 10 \mu\text{m}$ FWHM) comparable to the MCP channel diameter has been demonstrated (1) for a $130 + 130$ ($26 \text{ mm} \times 26 \text{ mm}$) multiwire system, and can be maintained up to counting rates of the order of 10^4 counts/sec. This type of crossed grid readout was successfully used for the High Resolution Imager (HRI) on the Einstein satellite (1) at soft X-ray wavelengths (0.25 - 1.5 keV) and has also been used for detection of FUV ($1000 \text{ \AA} - 2500 \text{ \AA}$) light from gas scintillation proportional counters (71).

Multinode Imaging Systems

There are a number of multinode readout systems (47, 72-78) which have been used with MCP's. One such system is the quadrant anode (72), which consists of a metal disc divided into four separate quadrants, each connected to a preamplifier. Charge clouds from the MCP are allowed to spread over an area 1 - 2 mm in diameter before striking the anode. The ratio of the charges detected by diametrically opposed quadrants then gives the x and y event positions. Due to the low noise of the anode, very high resolution ($<25 \mu\text{m}$ FWHM) can be achieved and individual MCP channels are easily resolved (72). However, this system allows imaging only of a small area, 1 - 2 mm across, close to the center of the anode, and furthermore, the images obtained are very distorted, due to the nonlinear relationship of charge division to position.

Another simple readout scheme is the discrete anode array (11, 74). This usually takes the form of a rectangular array of individual square metal anodes, each connected to an amplifier. The event pattern is determined by finding the anode onto which the charge from the MCP falls, so the position resolution is therefore limited to the individual anode size (typically $\sim 1 \text{ mm} \times 1 \text{ mm}$). Unfortunately, this kind of anode array cannot be extended usefully to give large numbers of pixels over large areas, due to the large number of connections and preamplifiers required. However, low resolution anode arrays are particularly useful for high speed devices, since the metal anodes allow extraction of charge on short timescales. Commercial optical photocathode/ MCP/ multinode devices have demonstrated <300 ps risetime with 4×4 image resolution (74), 600 ps risetime with 24×18 pixels (75), and a 10×10 anode UV sensitive (CsI photocathode) tube has been investigated by Timothy (32).

CODACON Readout System

Recently, several high resolution large area multinode readout systems have been developed (34, 47). One of these, the CODACON, consists of a large number of thin ($15 \mu\text{m}$ wide) metal strips on a $10 \mu\text{m}$ thick dielectric substrate. On the opposite side of the substrate are a number of pairs of binary code tracks (Figure 11). This arrangement is placed close ($50 \mu\text{m}$) to the output of a curved channel MCP such that an event will deposit charge onto a single metal strip. Charge is induced capacitively on the binary code tracks at the appropriate position. According to the distribution of induced charge on the binary code tracks, the differential amplifiers connected to binary

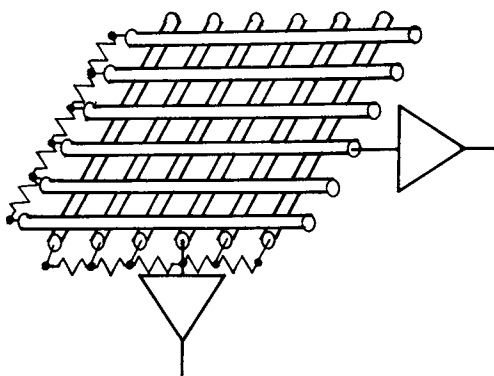


Figure 10. Scheme of a section of a multiwire position readout system.

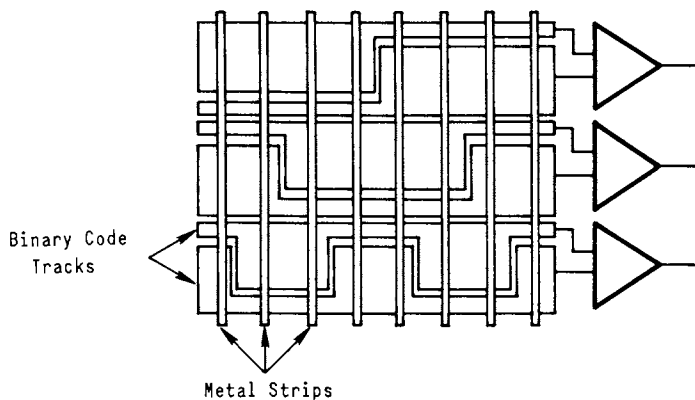


Figure 11. Scheme of a 3-bit Codacon position readout system.

code pairs will switch to the appropriate state, giving a (parallel) reverse binary position readout. Since the anode output already provides digital encoding of the event location, the processing electronics is very simple. Therefore only n amplifiers are needed for 2^n position locations in one dimension. Resolution of $\sim 25 \mu\text{m}$ FWHM has been achieved with a 1024 element linear array (26 mm long) of the type described (47). Two dimensional systems of the CODACON type have also been constructed (76) (a 32×32 pixel array was recently demonstrated to one of the authors (OS)). In this case, two sets of orthogonally-aligned metal strips are placed on top of one another such that they are insulated from each other but are both exposed to the charge from the MCP. The sets of strips extend outside the required active area to two independent sets of binary code tracks, thus giving both x and y event positions.

Image linearity with CODACON schemes is very good and extension to larger areas should be possible without loss of position resolution. Fabrication of the CODACON pattern, however, requires multilayer integrated circuit production techniques. A MCP/linear CODACON system of the type described (with a CsI photocathode on the MCP front face) has been used for FUV ($1500 \text{ \AA} - 1800 \text{ \AA}$) spectroscopy of Jupiter (47) and a two dimensional system of this type is being constructed for a similar application (76).

Multi-Anode Microchannel Plate Array

An alternative multianode readout arrangement is the Multi-Anode Microchannel plate Array (MAMA), developed by *Timothy et al.* (77). As in the case of the two dimensional CODACON, two sets of orthogonal thin ($15 - 25 \mu\text{m}$ wide) metal strips are sandwiched together, but insulated from one another, with the exposed metal left bare. This assembly is then placed close to ($50 \mu\text{m} - 100 \mu\text{m}$) the MCP output, so that charge from the MCP is allowed to spread over two or three metal strips when impinging on the array. In the case of the MAMA, however, strips in each set are connected together in a scheme similar to that illustrated in Figure 12 for a 1×32 linear array. In this fashion, 96 amplifier/discriminators are required for a 512×512 array, for example. However, unlike the CODACON, the position encoding must be carried out in the processing electronics. The coarse ($1/2$) event position is determined with the lower 4 output lines and the fine ($1/16$) event position then can be deduced using the upper 8 output lines. Precise ($1/32$) event positions then may be found by interpolation between the 2 or 3 strips involved. To ensure registration of an event on 2 or 3 strips, it is essential to keep the dynamic range of the signals low. For this reason, MAMA readouts require the narrow pulse height distributions that are available from curved channel or high L/d tandem MCP's.

A variety of MAMA arrays have been built (1×512 , 512×512 , 256×1024 , etc.) which demonstrate good resolution ($\sim 20 \mu\text{m}$ FWHM) over areas of $\sim 1 \text{ cm} \times 1 \text{ cm}$ without any detectable image distortions. The event processing time is typically $< 1 \mu\text{s}$, allowing counting rates of up to 10^6 counts/sec to be achieved with little ($< 10\%$) dead time. As in the case of the CODACON, the MAMA pattern is produced with multilayer integrated circuit techniques. A number of MAMA detectors are being built for use at optical EUV and soft X-ray wavelengths, in both ground-based (77) and rocket-launched applications (34).

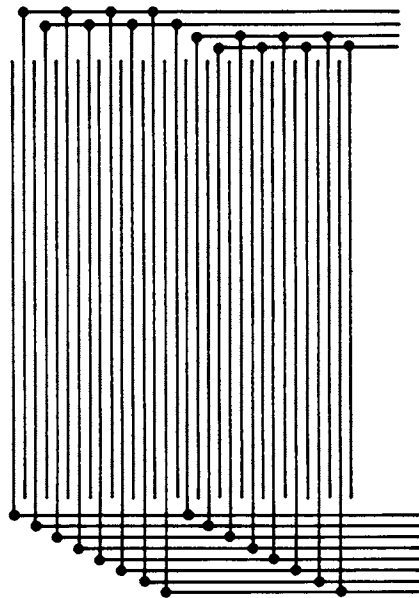


Figure 12. Scheme of a 1 x 32 Mama readout system.

Resistive Anode Position Readout Systems

Resistive anode position readout systems have been used extensively in applications with MCP's and gas proportional counters (78-91). The anode consists of a resistive coating (several 100 k Ω) applied to an insulating substrate, ensuring that the coating resistivity is uniform. A simple one dimensional readout can take the form of a rectangular sheet with contacts at opposite ends, and a simple two dimensional readout can be a square sheet with contacts at the corners. A particular advantage of resistive anode readouts is the small number of amplifiers required; only four amplifiers are required for full 2 dimensional imaging. These anodes are usually mounted close (<1 mm) behind the MCP output face.

Two methods can be used to determine event positions, charge division between the opposing contacts, or difference in pulse development times between opposing contacts. These systems are used since the diffusion of charge from the event location gives pulse amplitudes and risetimes proportional to the distance from the contact. Simple one dimensional resistive anodes have good image linearity (25, 78, 79, 81), but simple two dimensional resistive anodes display considerable image distortion due to charge reflection effects (88). This problem may be largely overcome by using a specially-terminated resistive anode ("Gear" anode) with low resistivity borders (84, 87, 89, 90). Position resolution of resistive anode detectors is limited by the signal/noise ratio, rather than the anode element dimensions, since the resistive elements display considerable thermal noise. However, by using high gain tandem MCP configurations, resolutions of $\sim 50 \mu\text{m}$ FWHM (over $\sim 25 \text{mm}$) have been achieved (80) with count rates in excess of 10^4 counts/sec. The count rate capability is limited by the combination of charge diffusion time and electronic processing time. Several types of resistive anode detector are available commercially (Hamamatsu, ITT, Surface Science Laboratories, IITL). Applications of the resistive anode scheme include soft X-ray imaging for the EXOSAT satellite (91), FUV spectroscopy of stellar and planetary objects (78, 79), and EUV spectroscopic studies of airglow (81).

Wedge and Strip Readout Systems

Although the principle of the wedge and strip anode was suggested as early as 1966 (92), only recently has interest been shown in this position readout technique for MCP's (33, 93-96). The wedge and strip anode can take a variety of forms. The most commonly used version has three electrodes (Figure 13), connected to only 3 amplifiers for full two dimensional imaging. The anodes are formed by etching the required pattern in a thin (10 μm thick) metal layer which has been deposited on an insulating substrate, using standard printed circuit board techniques. One electrode is a set of tapering wedge shapes, another is a set of varying width strips, and the third covers the area between the latter two. The insulating gaps between the electrodes are approximately 50 μm wide and the pattern repetition period is $\sim 1 \text{mm}$.

The wedge and strip anode must be placed $\sim 1 \text{cm}$ behind the MCP output, to allow the emerging charge cloud to spread over more than one repetition period of the pattern. The incident charge then is divided among the electrodes in ratios according to the electrode areas. Since the areas of the wedges vary linearly with position in one axis, and the areas of the strips vary linearly with position in the other axis, ratios of the charge seen on each of these electrodes with respect to the total charge give linear x and y event positions. (It is important to note that this type of readout system may need magnetic shielding, since a magnetic field of ~ 1 Gauss is sufficient to deflect image points by $\sim 100 \mu\text{m}$.)

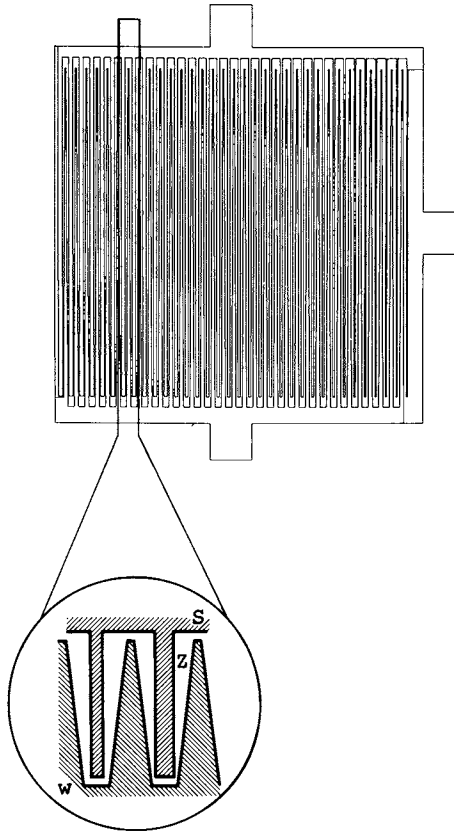


Figure 13. Scheme of a wedge and strip position sensitive anode.

Results show that the image distortion is quite low (better than for comparable resistive anode detectors) for detectors with active areas of ~ 20 mm (33, 93, 94). The position resolution is determined by the preamplifier noise levels and by statistical variations in the charge division (33, 93). Provided that the amplifier time constants are $>1 \mu\text{s}$, the resolution achievable with the wedge and strip is superior to that of the resistive anode at a given gain and anode size. Using high gain tandem MCP configurations, resolution of $<40 \mu\text{m}$ FWHM has been achieved (33) over ~ 25 mm at count rates of up to $4-5 \times 10^4$ counts/sec. Systems of this type have been used in optical detectors (33) for ground-based spectroscopy and will be used for EUV imaging and spectroscopy on the Extreme Ultraviolet Explorer Satellite (4).

Acknowledgments

We would like to thank Professor C. S. Bowyer for his support of this study. We would also like to acknowledge useful discussions with Dr. S. Murray, Dr. G. Fritz, Dr. G. Gruddace, Mr. P. Henkel, Prof. S. Rappaport, Mr. M. Barstow, Dr. K. Long, Prof. H. W. Moos, Prof. A. Davidsen, Dr. E. Eberhardt, Dr. J. G. Timothy, Mr. R. L. Bybee, Mr. R. Field, and Dr. G. Lawrence. This work was supported by NASA contract NAS5-24445 and by NASA Innovative Research Grant NGL-05-003-497.

Literature Cited

1. Henry, J. P.; Kellogg, E. M.; Briel, U. G.; Murray, S. A.; van Speybroeck, L. P.; Bjorkholm, P. J. Proc. SPIE 1977, 106, p. 163.
2. Broadfoot, A. L. et al. Space Science 1977, 21, 183.
3. Bowyer, S.; Kimble, R.; Paresce, F.; Lampton, M.; Penegor, G. Appl. Opt. 1981, 20, 477.
4. Malina, R. F.; Bowyer, S.; Lampton, M.; Finley, D.; Paresce, F.; Heetderks, H. Opt. Eng. 1982, 21, 764.
5. Mullard Ltd., Mullard House, Torrington Place, London, U.K.
6. Galileo Electro-Optics Corp., Galileo Park, Sturbridge, Mass.
7. Hamamatsu Corp., 120 Wood Avenue, Middlesex, NJ.
8. Varian, L.S.E. Div., 611 Hansen Way, Palo Alto, CA.
9. Fraser, G. W. accepted for publication in Nucl. Instrum. Meth. Sept. 1982.
10. Galanti, M.; Gott, R.; Renaud, J. F. Rev. Sci. Instrum. 1971, 42, 1818.
11. Timothy, J. G.; Mount, G. H.; Bybee, R. L. IEEE Trans. Nucl. Sci. 1981, NS-28, 689.
12. Ruggeri, D. J. IEEE Trans. Nucl. Sci. 1972, NS-19, 74.
13. Panitz, J. A.; Foesch, J. A. Rev. Sci. Instrum. 1976, 47, 44.
14. Taylor, R.; Hettrick, M.; Malina, R. F. submitted to Rev. Sci. Instrum. Nov. 1982.
15. Martin, C.; Bowyer, S. Appl. Opt. 1982, 21, 4206.
16. McConkey, J. W.; Crouch, T.; Tomc, J. Appl. Opt. 1982, 21, 1643.
17. Fraser, G. W.; Barstowe, M. A.; Whiteley, M. J.; Wells, A. accepted for publication in Nature Oct. 1982.

18. Parkes, W.; Gott, R.; Pounds, K. A. IEEE Trans. Nucl. Sci. 1972, NS-17, 360.
19. Bjorkholm, P. J.; Van Speybroeck, L. P.; Hecht, M. Proc. SPIE 1977, 106, p. 189.
20. Siddiqui, S. J. Appl. Phys. 1977, 48, 3053.
21. Loty, C. Acta Electronica 1971, 14, 107.
22. Pletneva, N. I.; Sattarov, D. K.; Semenov, E. P. Sov. J. Opt. Technol. 1976, 43, 53.
23. Wiza, J. L. Nucl. Instrum. Meth. 1979, 162, 587.
24. Chalmeton, V.; Chevalier, P. Acta Electronica 1971, 14, 99.
25. Parkes, W.; Evans, K. D.; Mathieson, E. Nucl. Instrum. Meth. 1974, 612, 151.
26. Eberhardt, E. H. Appl. Opt. 1979, 18, 1418.
27. Fraser, G. W.; Pearson, J. F.; Smith, G. C.; Lewis, J. F.; Barstowe, M. A. to be published in IEEE Trans. Nucl. Sci. 1983, NS-30.
28. Timothy, J. G.; Bybee, R. L. Rev. Sci. Instrum. 1975, 46, 1615.
29. Timothy, J. G. Rev. Sci. Instrum. 1981, 52, 1131.
30. Boutot, J. P.; Delmotte, J. C.; Miehé, J. A.; Sipp, B. Rev. Sci. Instrum. 1977, 48, 1405.
31. Henkel, P.; Roy, R.; Wiza, J. IEEE Trans. Nucl. Sci. 1978, NS-25, 548.
32. Timothy, J. G.; Mount, G. H.; Bybee, R. L. Proc. SPIE 1979, 183, p. 169.
33. Siegmund, O. H. W.; Clothier, S.; Thornton, J.; Lemen, J.; Harper, R.; Mason, I. M.; Culhane, J. L. to be published in IEEE Trans. Nucl. Sci. 1983, NS-30.
34. Timothy, J. G.; Bybee, R. L. Proc. SPIE 1981, 265, p. 93.
35. Eberhardt, E. H. IEEE Trans. Nucl. Sci. 1981, NS-28, 712.
36. Rogers, D.; Malina, R. F. Rev. Sci. Instrum. 1982, 53, 1438.
37. Rager, J. P.; Renaud, J. F. Rev. Sci. Instrum. 1974, 45, 922.
38. Rager, J. P.; Renaud, J. F.; Tezenas du Montiel, V. Rev. Sci. Instrum. 1974, 45, 927.
39. Coleman, C. I. Rev. Sci. Instrum. 1982, 53, 735.
40. Hocker, L. P.; Zagarino, P. A.; Madrid, J.; Simmons, D.; Davis, B.; Lyons, P. B. IEEE Trans. Nucl. Sci. 1979, NS-26, 356.
41. Lo, C. C.; Leskovar, B. IEEE Trans. Nucl. Sci. 1981, NS-28, 698.
42. Eberhardt, E. H. ITT Tech. Note 1980, 127.
43. Henke, B. L.; Smith, J. A.; Attwood, D. T. J. Appl. Phys. 1977, 48, 1852.
44. Henke, B. L.; Liesegang, J.; Smith, S. D. Phys. Rev. 1979, 19, 3004.
45. Henke, B. L.; Proc. SPIE 1981, 146, p. 316.
46. Eberhardt, E. H. Appl. Opt. 1977, 16, 2127.
47. McClintock, W. E.; Bazhi, C. A.; Steele, R.E.; Lawrence, G. M.; Timothy, J. G. Appl. Opt. 1982, 21, 3071.
48. Lukirskii, A. P.; Savinov, E. P.; Brytov, I. A.; Shepelev, Y. F. USSR. Acad. Sci. Bull. Phys. 1964, 128, 774.
49. Iyesaar, T. E.; Saar, M. E.; Elango, M. A. Sov. Phys. Solid. State 1978, 20, 454.
50. Saloman, E. B.; Pearlman, J. S.; Henke, B. L. Appl. Opt. 1980, 19, 749.
51. Henke, B. L.; Knauer, J. P.; Premaratne, K. & J. Appl. Phys. 1981, 52, 1509.
52. Fraser, G. W. accepted for publication in Nucl. Instrum. Meth. Sept. 1982.
53. Carruthers, G. R. Appl. Opt. 1975, 14, 1667.
54. Bateman, J. E.; Apsimon, R. J. Adv. Elec. Phys. 1979, 52, 189.

55. Savinov, E. P.; Lukirskii, A. P. Opt. Spectrosc. 1967, 23, 163.
56. Lapson, L. B.; Timothy, J. G. Appl. Opt. 1976, 15, 1218.
57. Smith, D. G.; Pounds, K. IEEE Trans. Nucl. Sci. 1968, NS-15, 541.
58. Fraser, G. W. accepted for publication in Nucl. Instrum. Meth. 1982.
59. Metzger, P. H. J. Phys. Chem. Solids. 1965, 26, 1879.
60. Lapson, L. B.; Timothy, J. G. Appl. Opt. 1973, 12, 388.
61. Boksenberg, A. "Image Processing Techniques in Astronomy"; Reidel: Dordrecht, Holland, 1975; p. 59.
62. Johnson, C. B. IEEE Trans. Nucl. Sci. 1982, NS-29, 200.
63. Hartig, G. F.; Moos, H. W.; Pembroke, R.; Bowers, C. preprint.
64. Torr, M. R.; Devlin, J. Appl. Opt. 1982, 21, 3091.
65. Torr, M. R.; Vitz, R. C. Appl. Opt. 1982, 21, 3080.
66. Starlab UV Optical Telescope Facility, A Summary Report, Vols. 1 and 2, 1979, NASA, Goddard Space Flight Center, Greenbelt, MD.
67. Bokowski, C. J.; Kopp, M. K. IEEE Trans. Nucl. Sci. 1970, NS-17, 390.
68. Charpak, G. Nature 1977, 270, 479.
69. Knapp, G. Rev. Sci. Instrum. 1978, 49, 982.
70. Kellogg, E.; Henry, P.; Murray, S.; van Speybroeck, L.; Bjorkholm, P. Rev. Sci. Instrum. 1976, 47, 282.
71. Hailey, D. J.; Hamilton, T. T.; Ku, W. H. M. Nucl. Instrum. Meth. 1981, 184, 543.
72. Lampton, M.; Malina, R. F. Rev. Sci. Instrum. 1976, 47, 1360.
73. Butcher, H. R., to appear in "SPIE Instrumentation in Astronomy"; 1983.
74. Hamamatsu, Technical Data Sheet, 1981, T82-9-10.
75. Oba, K.; Sugiyama, M.; Suzuki, Y.; Yoshimura, Y. IEEE Trans. Nucl. Sci. 1979, NS-26, 346.
76. Lawrence, G. M., personal communication, University of Colorado, Boulder, Sept. 1982.
77. Timothy, J. G.; Bybee, R. L. Proc. SPIE 1981, 279, p. 129.
78. Lawrence, G. M.; Stone, E. J. Rev. Sci. Instrum. 1975, 46, 432.
79. Weiser, H.; Vitz, R. C. Moos, H. W.; Weinstein, A. Appl. Opt. 1976, 15, 3123.
80. Firmani, C.; Ruiz, E.; Carlson, C. W.; Lampton, M.; Paresce, F. Rev. Sci. Instrum. 1982, 53, 570.
81. Carruthers, G. R.; Opal, C. B. "Instrumentation in Astronomy II"; Tuscon, 1974, p. 127.
82. Rees, D.; McWhirter, I.; Rounce, P. A.; Barlow, F. E.; Kellock, S. J. J. Phys. E. 1980, 13, 763.
83. Mathieson, E. Nucl. Instrum. Meth. 1971, 92, 441.
84. Augustyniak, W. M.; Brown, W. L.; Lie, H. P. IEEE Trans. Nucl. Sci. 1972, NS-19, 196.
85. Stumpel, J. W.; Sanford, P. W.; Goddard, H. F. J. Phys. E. 1973, 6, 397.
86. Lampton, M.; Paresce, F. Rev. Sci. Instrum. 1974, 45, 1098.
87. Lampton, M.; Carlson, C. W. Rev. Sci. Instrum. 1979, 50, 1093.
88. Siegmund, O. H. W. Ph.D. Thesis, University of London, 1981.
89. Gear, C. W. Proc. Skytop Conf. Computer Systems in Exp. Phys. USAEC conf-670301, 1969, 552.

90. Fraser, G. W.; Mathieson, E. Nucl. Instrum. Meth. 1981, 179, 591.
91. de Korte, P. A. J.; Giralt, R.; Coste, J. N.; Ernu, C.; Frindel, S.; Flamand, J.; Contet, J. J. Appl. Opt. 1981, 20, 1080.
92. Anger, H. O. ISA Trans. 1966, 5, 311.
93. Martin, C.; Jelinsky, P.; Lampton, M.; Malina, R. F.; Anger, H. O. Rev. Sci. Instrum. 1981, 52, 1067.
94. Rees, D.; McWhirter, I.; Greenaway, A. M.; Cochrane, A.; Lampton, M. submitted to J. Phys. E. 1982.
95. Grewing, M.; Barnstedt, J.; Streitenberger, R.; Wulf-Mathies, C. "Universities Annual Research Report," W. Germany, 1981.
96. Burton, W. M. submitted to J. Phys. E. Jan. 1982.
97. Malina, R. F.; Kimble, R. personal communication, University of California, Berkeley, Jan. 1983.
98. Sandel, W. R.; Broadfoot, A. L. Appl. Opt. 1976, 15, 3111.
99. Bell, R. M.; Firkenthal, M.; Moos, H. W. Rev. Sci. Instrum. 1981, 52, 1806.
100. Hodge, W. C.; Yu, T. U.; Moos, H. W. Bull. Am. Phys. Soc. 1980, 25, 999.
101. Straton, B. C.; Hodge, W. C.; Moos, H. W. Bull. Am. Phys. Soc. 1981, 26, 968.
102. Hodge, W. C.; Straton, B. C.; Moos, H. W. Bull. Am. Phys. Soc. 1981, 26, 968.
103. Fonck, R. J.; Ramsey, A. T.; Yelle, R. V. Appl. Opt. 1982, 21, 2115.

RECEIVED August 15, 1983

Multichannel Extreme UV Spectroscopy of High Temperature Plasmas

RAYMOND J. FONCK

Plasma Physics Laboratory, Princeton University, Princeton, NJ 08544

Spectroscopy of magnetically confined high temperature plasmas in the visible through X-ray spectral ranges deals primarily with the study of impurity line radiation or continuum radiation. Detailed knowledge of absolute intensities, temporal behavior, and spatial distributions of the emitted radiation is desired. As tokamak facilities become more complex, larger, and less accessible, there has been an increased emphasis on developing new instrumentation to provide such information in a minimum number of discharges. The availability of spatially-imaging detectors for use in the vacuum ultraviolet region (especially the intensified photodiode array) has generated the development of a variety of multichannel spectrometers for applications on tokamak facilities.

The measurement of extreme ultraviolet radiation (EUV) emitted from magnetically confined fusion plasmas deals principally with the study of line emissions from highly ionized impurities in the hot plasma (1). The 500-1600 Å spectral range includes the major $\Delta n = 0$ transitions of common intrinsic low-Z impurities such as carbon and oxygen, while the 100-500 Å range contains the principal lines from highly ionized metals such as Fe, Ti, and Ni. In a hot plasma with central electron temperatures on the order of several keV, the low-Z impurity radiation comes mainly from the cool plasma periphery while the metallic radiation is emitted from the hotter core region of the plasma. Measurement of these emissions can provide sensitive local diagnostics of plasma properties. Determination of the absolute intensities of spectral lines are coupled with impurity transport models (2-4) to provide estimates of total radiative power loss due to the impurities. Even relative measurements

0097-6156/83/0236-0277\$06.00/0
© 1983 American Chemical Society

under changing discharge conditions can be used to interpret the effects of plasma-wall interactions. Finally, plasma properties such as ion temperature and rotation velocities can be obtained through high resolution studies of impurity spectra.

A given fusion-grade plasma, whether it is in a tokamak, magnetic mirror, or other magnetic confinement device, will in general contain several impurity species, and all ion stages of a given atomic species will be present somewhere in the discharge. This of course leads to very complex spectra which must be measured and analyzed. For example, Figure 1 shows an EUV spectrum obtained from the PDX tokamak, and the prominent lines of O, C, Fe, and Ti ions are indicated. The large background at short wavelengths is due principally to unresolved lines from several ion stages of the impurities. Measurements of the time histories of the absolute intensities of the designated spectral lines in Figure 1 during the transient plasma discharge would be the minimum amount of information needed for a semi-quantitative idea of impurity radiated power. To obtain more detailed information, such as the transport of impurities across the magnetic field lines in the tokamak, both spatial and temporal distributions of these lines and several others would have to be measured.

Clearly, this becomes a formidable task requiring a large number of reproducible discharges when done with conventional monochromators. As fusion experiments become more expensive and less accessible to the experimenter, reliable multichannel spectrometers are becoming essential to obtain appropriate information on discharge conditions. Even more important than the detailed studies of impurities alluded to above is the ability to give immediate feedback on impurity behavior and content under rapidly changing conditions. In the largest magnetic confinement devices, such as the TFTR tokamak, this "machine monitor" mode of operation will be an indispensable aid to guide the variation of discharge operation.

In this paper, we discuss the requirements for multichannel EUV detectors for studies in controlled thermonuclear research (CTR) plasmas. The emphasis is on obtaining spectra from tokamak experiments, but considerations for magnetic mirrors are similar. We mention several types of detectors used in the 20 to 1700 Å range in CTR, but only the most common, the intensified photodiode array, will be discussed in detail. These detectors are usually placed at the focal surface of an EUV spectrometer, which can range from a conventional normal or grazing incidence system with a single spherical diffraction grating to more exotic optical systems designed to perform specific measurements. Examples of both types of uses will be given.

General Considerations

There are several criteria which are used to evaluate multichannel detectors for use in CTR. Some of those are:

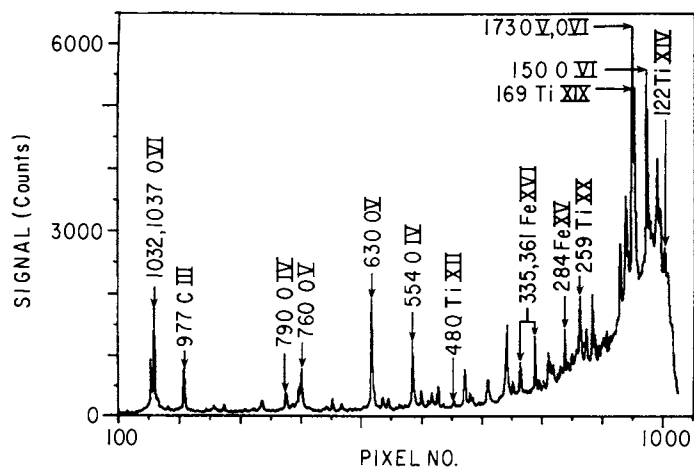


Figure 1. Extreme UV (EUV) spectrum, from the PDX tokamak, showing prominent impurity emission lines. (Reproduced with permission from Ref. 12. Copyright 1982, Appl. Optics.)

- (A) Sensitivity
- (B) Stability
- (C) Uniformity
- (D) Spatial Resolution
- (E) Dynamic Range
- (F) Time Resolution
- (G) Susceptibility to harsh electromagnetic environments
- (H) Storage space requirements
- (I) Radiation hardness

Several of these properties are interrelated, and the importance of a given feature depends in large part on the proposed application. We concentrate here on applications to broad spectral band monitoring of CTR plasmas to provide qualitative and quantitative survey spectra.

The spectral range of interest is typically anywhere from 20 to 1500 Å for general impurity monitoring, and a detector must have good sensitivity over at least a large fraction of that range. Since absolute intensity measurements are routinely required, the stability of a detector's response over long periods is especially crucial for minimizing the required maintenance and recalibration efforts. This requirement becomes more important as tokamak facilities become larger and less accessible. For a given spectrometer, the spatial resolution of the detector determines, in large part, the ultimate spectral resolution of the system consistent with the spectrometer apertures being large enough to admit a detectable light flux. In addition to resolution as specified by the full width at half maximum (FWHM) of a spectral line profile, the contrast afforded by the detector (i.e., how fast the wings of the line profile drop away from the line center) is an important factor in determining the ability to detect weak lines in close proximity to very strong lines. Typical line intensities range from 10^{12} to 10^{15} photons/cm²·s·sr and experience on several tokamaks indicate that spectrometer slits with at least 20 to 50 μm widths are required for reasonable signal-to-noise ratios. Hence detectors with FWHM < 50 μm are desirable to obtain 2 to 3 detector resolution elements within the instrumental line profile. Transient events in hot plasmas can occur on time scales of ~ 0.1 ms [e.g., impurity spectra produced by laser ablation injection (5), or excitation of impurity spectra by pulsed diagnostics neutral beams (6)] while for routine monitoring of impurities, a time resolution of ~ 10 ms is sufficient. Finally, CTR experiments present noisy electrical and magnetic environments for operation of sensitive imaging detectors, and care is required to provide appropriate shielding and isolation. Steady state and transient magnetic fields on the order of 1 kG are present in diagnostic areas, and large electromagnetic pulses are present near the machines (some of the larger perturbations being due to faults or abrupt terminations of

several MW neutral beam sources or to the presence of several MW radiofrequency sources for heating the plasma). The near future will see CTR plasmas which emit large levels of energetic neutrons, and detectors must be hardened for radiation noise and damage.

The generic one-dimensional imaging device used for EUV plasma spectroscopy employs a microchannel plate (MCP) (7) image intensifier/converter placed at the focal surface of the spectrometer. This provides an imaging device which converts EUV photons to electrons and amplifies the electron current with gains of 10^3 to 10^6 . These detectors have a very fast time response (8, 9) and are easily available from several commercial sources. The main disadvantages to the MCP seem to be the available dynamic range, especially at high gain, and to a lesser extent, the achievable spatial resolution in a typical MCP proximity focussed intensifier. Both of these areas of concern are presently being addressed and improved upon by the MCP vendors.

The conversion of the electron signal out the back of the MCP to a useful signal is achieved via two approaches: 1) the electron current is read directly with some sort of multi-anode structure, which allows operation in either a pulse-counting or analog current measurement mode; and 2) the electrons are accelerated into a phosphor to produce visible photons which are then detected by a multichannel visible light detector. The latter approach is almost always used in an analog mode for broad band magnetic fusion spectroscopy. We give most of our attention to this second approach because it is the most widely used and offers the greatest flexibility in a given detector.

Several visible detectors have been used in CTR research as the encoding device behind an MCP for EUV spectroscopy. These have included a gated Vidicon (10), a CID camera (11), and most commonly, a self scanning photodiode array (PDA) (12, 13). The self scanning PDA has achieved widespread use and has shown itself to be a very useful and flexible detector. It is discussed in some detail in the next section.

Intensified Photodiode Array

An intensified photodiode array (IPDA) detector for one-dimensional spatial imaging in the EUV is shown in Figure 2. This type of detector was originally described by Riegler and Moore (14). It consists of a microchannel plate whose output is optically coupled to a self scanning photodiode array. An incident photon produces a photoelectron which is subsequently amplified by the MCP. The exiting electrons are proximity focussed onto a phosphor layer which converts the electron energy to visible photons. Proximity focussing is accomplished by applying a 5 kV potential across the small gap (~ 1 mm) between the back of the MCP and the phosphor. P-20 phosphor is typically used for maximum signal and good matching to the photodiode array

response. This phosphor is coated on the face of a fiber optic image conduit which is optically contacted to the PDA.

The photodiode array most commonly used is the Reticon 1024SF which has 1024 pixels on 25 μm centers. Each pixel is 2.5 mm high, which gives an aspect ratio (height to width) of 100:1 and is well suited for acting as an exit slit for a grating spectrometer. The large pixel size allows a large dynamic range (maximum signal/readout noise) in a single scan. These features make the intensified photodiode array a very attractive detector for simultaneous observation of intense and weak emissions.

Requiring at least 2 pixels per resolution element gives a maximum of 512 resolution elements across the array. Readout times of the PDA can vary greatly depending on the driving electronics, and scan integration times from 1 to 50 msec are readily achievable. The PDA has virtually no image lag on successive scans, which is an important feature when observing rapidly varying spectra. Since the effective spectral range is determined by the photocathode material on the MCP and the PDA responds only to the phosphor output, the IPDA can serve as a general detector ranging from the soft X-ray to the far visible. The response of an IPDA with a CuI photocathode is shown in Figure 3.

Another attractive feature of the PDA is the flexibility in readout pattern available with single detector. By selectively collecting data from predetermined pixels or groups of pixels, time resolution can be increased and required memory space can be minimized.

The resolution of the IPDA detector is determined chiefly by spreading of the electron cloud as it exits the back of the MCP and is accelerated towards the phosphor. Ignoring space charge effects, which are unimportant for a single MCP run at a gain of 10^4 or less, (15) simple orbit theory gives the charge spreading due to a point source of electrons in the channel to be

$$Y = 2 \sin(2\theta) \frac{Us}{v_{ph}} \left(\sqrt{1 + \frac{v_{ph}}{U} \cos 2\theta} - 1 \right) \quad (1)$$

In Eq. (1), Y is the diameter of the electron cloud at the phosphor surface, θ is the effective angle at which an electron is emitted relative to the MCP channel axis, s is the separation between the phosphor surface and the MCP, U is the mean electron energy at the end of the channel, and v_{ph} is the potential difference between phosphor and MCP. Although this description grossly oversimplifies the actual physical processes occurring at the MCP-phosphor interface, it provides a remarkably good semi-quantitative estimate of the net detector resolution. Figure (4) shows the measured FWHM of a spectral line profile measured with an IPDA on the output planes of two VUV spectrometers with similar instrumental functions. The solid line is given by Eq. (1) with a 50 μm offset added to account for the channel-to-channel separation of the MCP (15 μm) and the spectrometer resolution due

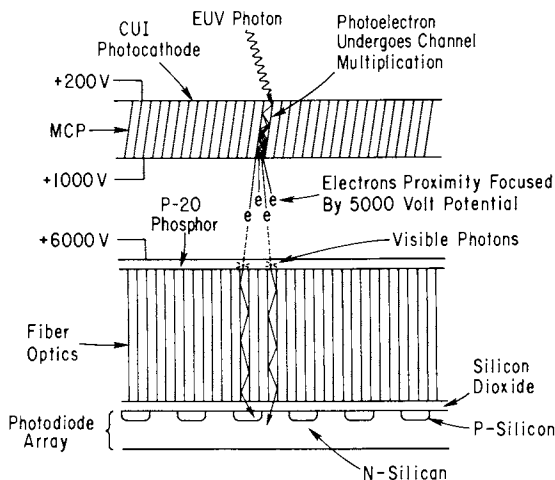


Figure 2. Intensified photodiode array detector for one-dimensional UV spatial imaging. (Reproduced with permission from Ref. 13. Copyright 1981, American Institute of Physics.)

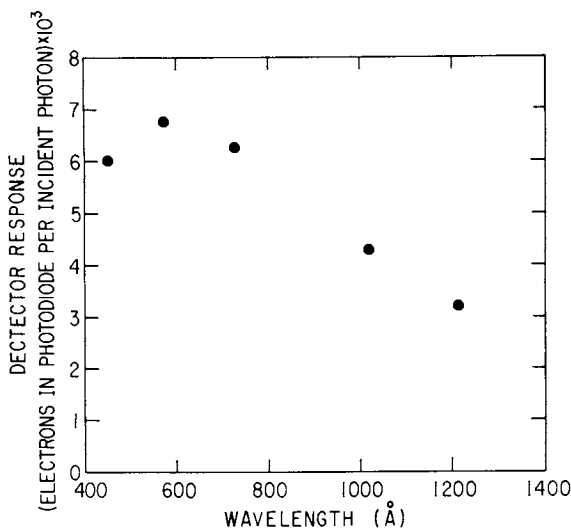


Figure 3. IPDA detector response for an MCP with a CuI photocathode. Ordinate is in units of electrons produced in the photodiode array per photon incident on the MCP. (Reproduced with permission from Ref. 13. Copyright 1981, American Institute of Physics.)

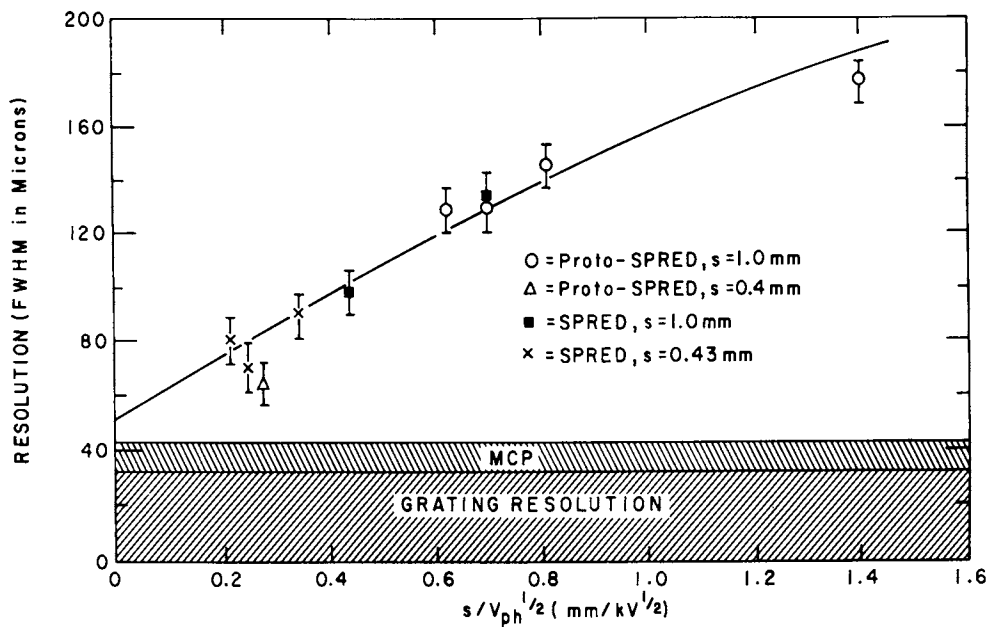


Figure 4. Resolution obtained with an IPDA as a function of intensifier parameters.

Solid line is from Equation 1 with $U = 30$ V and $\theta = 10.5^\circ$ plus an offset of $50 \mu\text{m}$. The grating resolution used for the two spectrometers is noted. The Proto-SPRED spectrometer is shown in Figure 10, and the SPRED spectrometer is shown in Figure 12. The area marked MCP reflects the channel-to-channel spacing of the MCP. (Reproduced with permission from Ref. 12. Copyright 1982, Appl. Optics.)

to the finite slit width ($\sim 30 \mu\text{m}$). The values of $U = 30 \text{ eV}$ and $\theta = 10.5^\circ$ used for the fit to the data are typical for a single stage MCP intensifier (16).

In practice, the detector resolution is limited by the value of s , the MCP-phosphor separation, since electrical breakdown eventually occurs if V_{ph} is kept at a reasonably high value of $\sim 5 \text{ kV}$. Values of s down to 0.4 mm are possible with $V_{\text{ph}} = 5 \text{ kV}$ if sufficient precautions are taken to ensure a clean vacuum and that the phosphor and MCP surfaces are sufficiently smooth.

Although a FWHM of $40 \mu\text{m}$ or less is achievable with the IPDA, the line profile obtained with this detector is not optimal for quantitative spectroscopy of dense spectra. Figure 5 shows the line profile (at 304 \AA) obtained with an IPDA on a grazing incidence spectrometer. The solid line is a least squares best fit of the data to a convolution of the PDA response function (a trapezoid of base width $37.5 \mu\text{m}$ and top width $12.5 \mu\text{m}$) and a Lorentzian function. The fact that a Lorentzian gives a good description of the line profile from the intensifier indicates that the wings of the instrumental function decrease rather slowly as one moves away from the line center. This presents severe problems when trying to separate weak lines from nearby strong lines (c.f. Figure 1). In effect, the intensified PDA suffers from relatively poor contrast and, in many cases, this property can be its chief defect.

The time response of the IPDA is usually determined by the decay time of the phosphorescence of the phosphor layer. For P-20 phosphor, it usually takes about 2 ms for the output to decay to 10% of the initial value. A typical decay characteristic for an MCP intensifier is shown in Figure 6. The decay is not exponential. Faster decays can be obtained using other phosphors, but phosphor efficiency and optimal matching to the PDA response may then be compromised.

The major sources of noise in the detector are dark current shot noise and readout noise (17). A PDA has a fixed pattern noise level due to transient signals being coupled to the video lines by external stray capacitances and a noise level due to uncertainty in resetting each diode during the readout process. Dark current noise can be made negligible by cooling the PDA (a typical temperature for operation is -20°C using a Peltier thermoelectric cooler). The fixed pattern noise level can be eliminated by subtracting a dark scan from the data scan, as shown in Figure 7. With careful circuit design, the residual noise level can be reduced to ~ 1000 electron-hole pairs in a controlled environment.

The output of a pixel of the PDA is linear up to at least 2×10^4 times greater than its noise level, and comparison of the ratio between weak and strong spectral lines using the IPDA indicates that the MCP/intensifier output also is linear to $\pm 5\%$ over this same range. Thus, the dynamic range in a single scan can be as high as $10^4:1$, which is very useful since spectra from

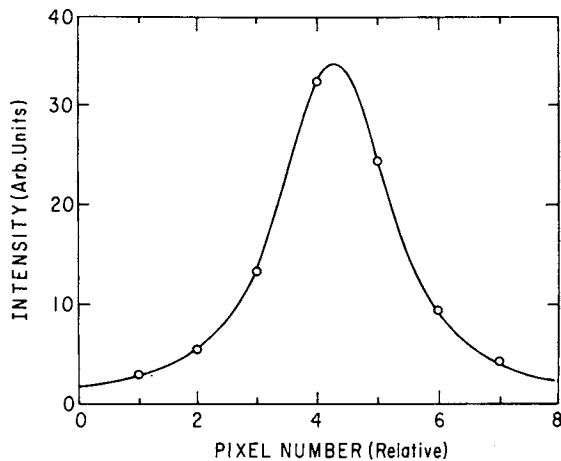


Figure 5. Line profile obtained with an IPDA detector system.

Key: ○, signals from individual pixels; and —, the best fit of data to a convolution of a Lorentzian function with the PDA response function and the entrance slit width. FWHM of the fitted Lorentzian is 1.84 pixels. (Reproduced with permission from Ref. 12. Copyright 1982, Appl. Optics.)

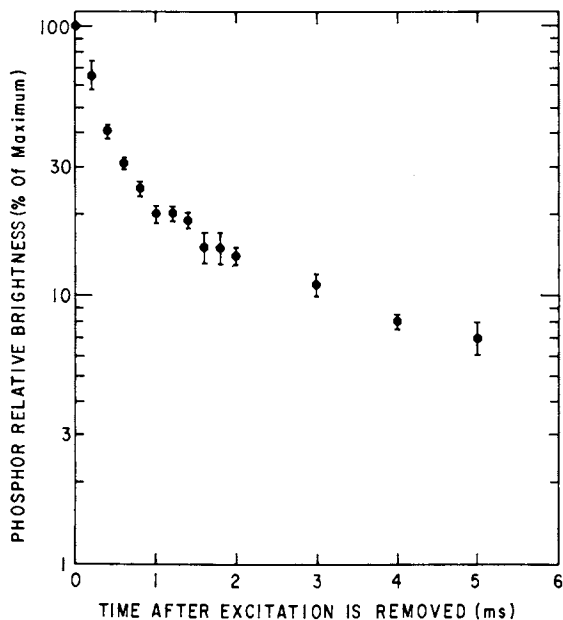


Figure 6. Decay characteristic of an intensifier phosphor output when a steady source is stopped at $t = 0$. The intensifier had P-20 phosphor. (Reproduced with permission from Ref. 12. Copyright 1982, Appl. Optics.)

plasmas can have both weak and strong lines of interest in a given discharge.

The readout and data storage electronics for the IPDA can be quite varied, and two systems presently in use on tokamaks are mentioned here. Figure 8 shows a block diagram of the electronics used in an IPDA system in use at the Princeton University Plasma Physics Laboratory (PPPL) on the PDX and PLT tokamaks. The PDA is controlled by an optical multichannel analyzer system from EG&G Princeton Applied Research Corporation. This system, whose performance is described in some detail by Talmi and Simpson (17) allows a great deal of flexibility in the output format of the PDA data. The entire 1024 pixels or selected portions thereof can be read (full or partial spectrographic modes of operation); alternately, adjacent pixels can be grouped to a common datum readout and other spectral regions skipped to allow observation of specific spectral lines (polychromatic mode). Minimum scan time for a full spectrographic readout is 16 ms while up to six or seven isolated spectral lines (i.e., pixel groups) can be sampled at a 1 kHz clock rate in the polychromator mode. The PARC 1412 detector head and PARC 1218 PDA controller module are interfaced to a mainframe computer system via a CAMAC interface system. The data is read directly into dual port memory modules which act as buffers for temporary data storage. The output register supplies programming commands to specify the PDA readout pattern, and the programmable clock provides a sequence of trigger pulses, each of which initiates a scan of the PDA. The programmable clock allows varying scan integration times for importance sampling during a tokamak discharge (duration ~ 1 sec) and hence helps minimize local memory requirements. The local CAMAC crate is fiber optically coupled to the serial CAMAC highway to eliminate ground loops and noise pickup. The CAMAC system is controlled by a PDP-11 on PDX and PLT. This interface system provides a relatively simple and cheap method of interfacing a PDA detector system to an existing data acquisition system with several separate diagnostic systems controlled by a single computer.

An alternate approach using a dedicated desktop computer has been developed by the Johns Hopkins University spectroscopy group (13). A block diagram of their system is shown in Figure 9. The Reticon Evaluation Circuit Board (RC1024S) is used for the scanning circuitry. The digitized (12-bit) data are transmitted to the remote data processor and control unit and held in a buffer memory access. The data is stored on flexible disk and can be processed and displayed on graphical output between plasma shots. This system has the advantages of a dedicated computer system and easy mobility, while largest disadvantages seem to be cost and lack of general availability. The system shown in Figure 9 reads out a full scan every 3.7 ms. This increased time resolution comes out at the expense of dynamic range (i.e., 12-bit data versus 14-bit data output from the PARC electronics).

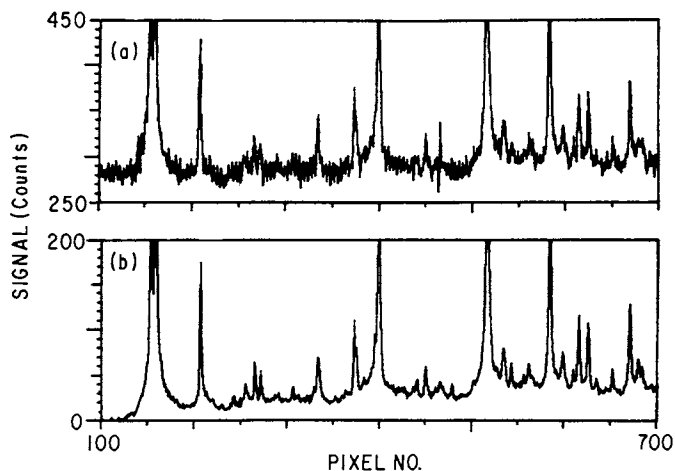


Figure 7. Example of fixed background compensation. Key: a, raw data from an IPDA on a grazing incidence spectrometer; and b, data in (a) with a dark scan subtracted. Spectrum obtained on the PDX tokamak. (Reproduced with permission from Ref. 12. Copyright 1982, Appl. Optics.)

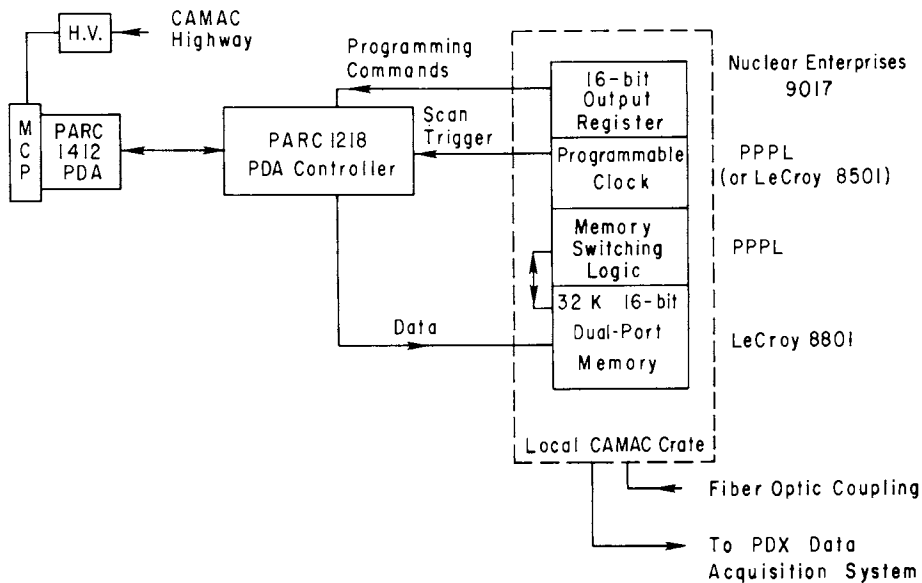


Figure 8. Block diagram of electronics used to couple the PARC photodiode array readout electronics to a local data acquisition system. (Reproduced with permission from Ref. 12. Copyright 1982, Appl. Optics.)

Applications of the IPDA

The application of IPDA's to spectroscopy of fusion plasma is a relatively new phenomenon and we mention here a few of the conventional and unconventional EUV spectrometer systems made possible by the availability of these detectors.

The simplest application of the IPDA is to place it at the output focal surface of a typical vacuum ultraviolet monochromator. Such a system is shown in Figure 10 and has been employed on the PDX tokamak (18). The spectrometer is a 0.2 m focal length normal incidence spectrometer which is readily available commercially (e.g., Action Research Corporation, Model VM-502). The orientation of the detector as shown results in substantial defocussing on the edges of the detector plane, but this can be minimized by proper orientation of the detector along the tangential focal surface or by operating at higher f/number and hence large depth of focus. This simple system allows coverage of $\sim 900 \text{ \AA}$ in first order of diffraction with $\sim 3 \text{ \AA}$ resolution. Rotation of the grating allows coverage of the 300-1700 \AA spectral range. The holographic gratings employed in the spectrometer provide a sufficiently broad blaze that increased resolution is available with reasonable efficiencies by working in higher orders of diffraction. This spectrometer system has been used to provide a monitor of general machine and impurity conditions. A sample of spectra obtained from the PDX tokamak is given in Figure 11. The spectrum labelled Diverted corresponds to discharges bounded by a magnetic divertor system on PDX which is employed to remove the contact between the hot plasma and a material surface to a remote burial chamber, thus minimizing the production and influx of metallic impurities in the discharge. The second scan corresponds to a discharge with a conventional metallic (titanium) rail limiter in the main plasma chamber to provide the plasma-surface contact point. The reduction of metallic impurities and increased fueling requirements (evidenced by increased hydrogen emissions) in diverted discharges is immediately obvious from these two spectra.

A much more sophisticated and versatile normal incidence time-resolving spectrograph is described by Bell, Finkenthal, and Moos (13). They employ a normal incidence spectrometer with seven separate diffraction gratings and an IPDA detector system in place of the exit slit on the Rowland circle. The gratings are blazed and coated to give maximum efficiency in different wavelength intervals. A pre-slit is employed to illuminate a single grating at a time. This system has been employed on the Alcator A and TFR-600 tokamaks. The wavelength range is 300-200 \AA and the resolution varies between 0.7 to 4 \AA .

Since many important spectral lines from hot plasmas are emitted at very short wavelengths ($< 300 \text{ \AA}$), the IPDA has been increasingly used in grazing incidence spectrometer systems on tokamak facilities. Hodge *et al.* (19) have placed an IPDA tangent

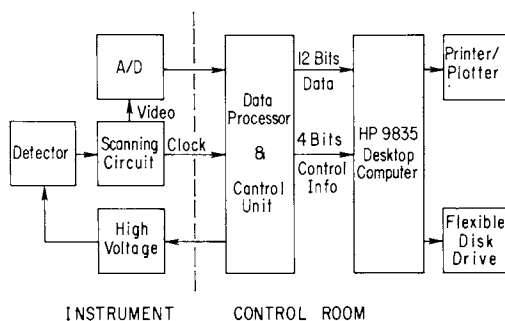


Figure 9. Block diagram of a self-contained electronics control system for an IPDA detector. Components to the left of the dashed line are incorporated into the detector package on the spectrometer, and those to the right are located in the tomamak control room. (Reproduced with permission from Ref. 13. Copyright 1981, American Institute of Physics.)

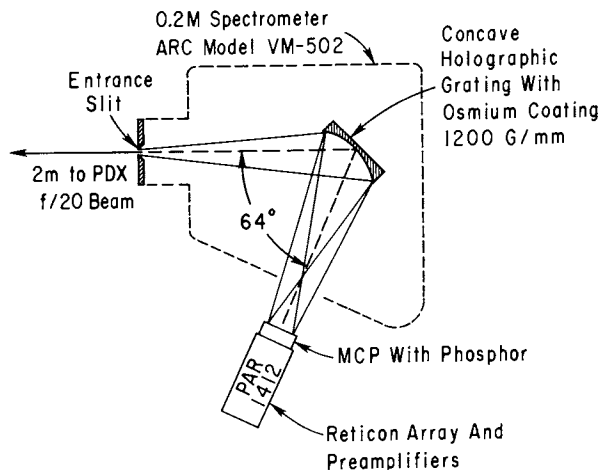


Figure 10. Simple visible UV spectrometer system with an IPDA detector attached. Accessible spectral range is 300–1700 Å.

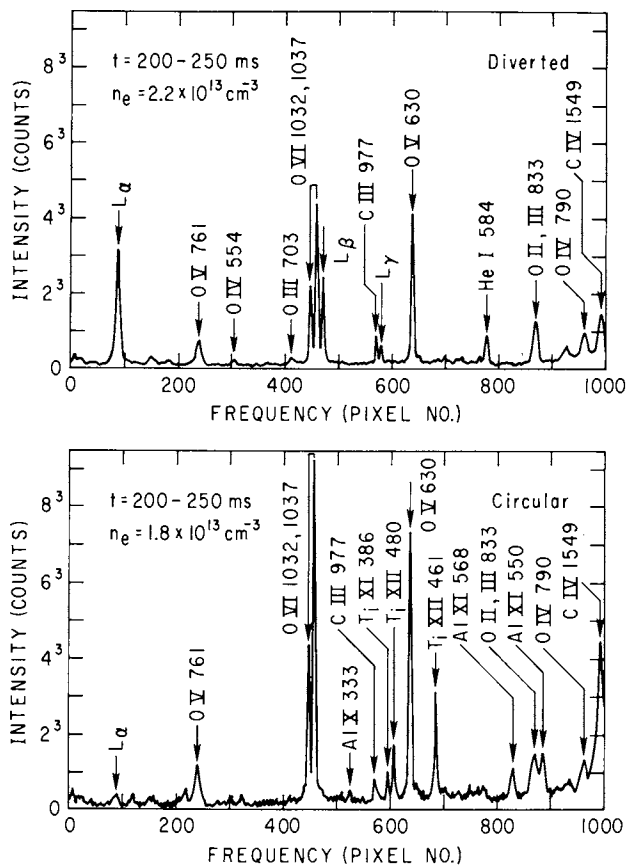


Figure 11. Spectra obtained from the PDX tokamak with the normal incidence spectrometer system shown in Figure 10. Integration times are 50 ms for each scan. Most of the lines observed are with higher orders of diffraction.

to the Rowland circle on a 1-meter focal length grazing incidence spectrometer ($\alpha = 88^\circ$) in order to observe spectra in the 20 to 300 Å range from the PLT tokamak. A desirable feature while working at such grazing angles of incidence on the detector plane is that an electron collection field be employed or the MCP must be funneled to provide a decent detection efficiency (20). A general impurity monitor for tokamak plasmas has been developed by the author and co-workers by employing a Type IV toroidal diffraction grating in a grazing incidence spectrometer ($\alpha = 71^\circ$) (12). The gratings are aberration-corrected to give a flat focal surface which matches the input face of an IPDA. A schematic of such a system is shown in Figure 12. This spectrometer provides spectra over the 100-1100 Å range with 2 Å resolution. A full spectrum such as shown in Figure 1 is recorded every 20 ms.

The flexibility and utility of these spectrometers with IPDA detectors is quite obvious. Figure 13 shows a time evolution of low wavelength spectra from the PDX plasma using the spectrometer in Figure 12. Only one half of five of the full thirty-five recorded scans are shown here. The abrupt appearance of the TiXI and XII lines and a group of lines at 200-300 Å in scan 13 is indicative of an influx of titanium into the discharge. Within 20 msec, these ions have diffused into the hot plasma core and ionized up to produce strong TiXIX and XX lines. Before these atoms leave the plasma, another burst of Ti influx occurs in scan 15. Throughout these random bursts of Ti influx, it is noted that the oxygen radiation is unaffected. This wealth of information is obtained in a single shot, while a standard monochromator would have required a large number of reproducible discharges to produce similar information.

Operation in the polychromatic mode allows the determination of the time evolution of individual ion species. Figure 14 shows polychromatic data obtained with the spectrometer of Figure 12 on the PDX tokamak. For this data, several groups of pixels, ranging in sizes from 4 to 8 pixels and each covering a spectral line of interest, were sampled with a 2 msec integration time. The sudden rise in the ScXI and ScXVII lines is due to a short burst of scandium influx induced via laser ablation of a thin Sc film from a glass slide. As Sc moves into the discharge it ionizes upward until it reaches a terminal stage of ScXVIII or XIX in the center of the discharge. The subsequent decay of these central ions is due to the loss of Sc from the discharge and is a measure of the impurity confinement time. The fact that the OVI radiation remains unchanged throughout this process indicates that the injection process is nonperturbing. Again, the number of discharges required to get the salient data is significantly reduced by using the IPDA/spectrometer system instead of conventional monochromators.

Discussion

A notable multichannel spectrometer which does not use an IPDA is the SIDS (Spatial Imaging Detector System) spectrometer

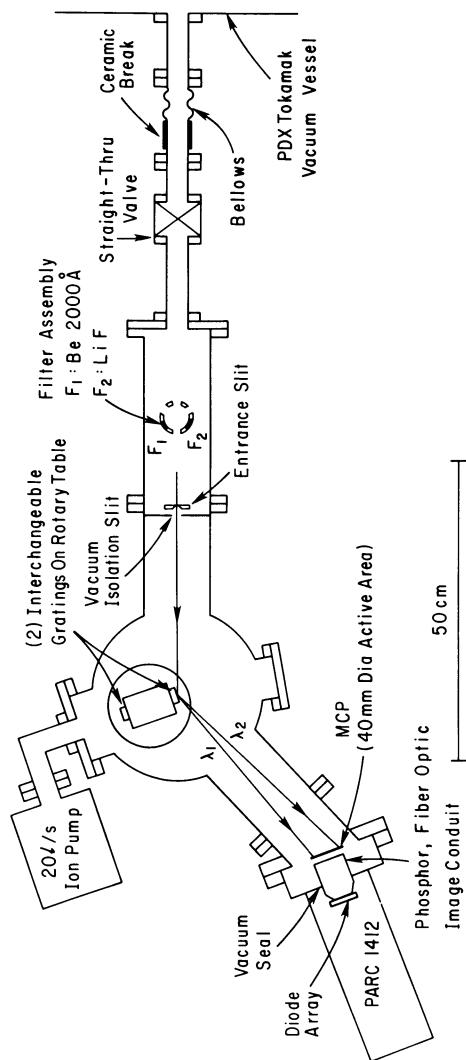


Figure 12. Optical schematic representation of an aberration-corrected toroidal diffraction grating spectrometer designed for use with an IPDA detector system. (Reproduced with permission from Ref. 12. Copyright 1982, Appl. Optics.)

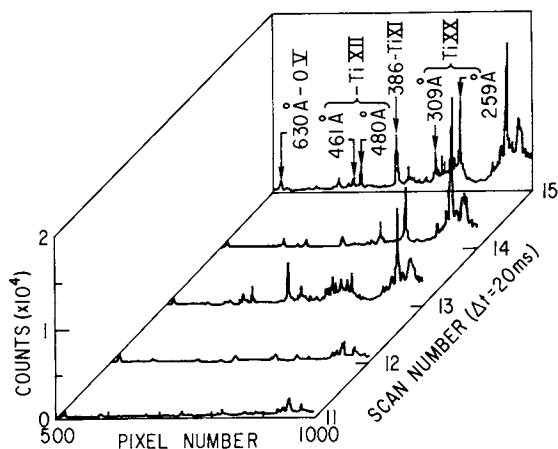


Figure 13. Time evolution of low-wavelength spectra showing bursting of titanium radiation in a PDX discharge. (Reproduced with permission from Ref. 12. Copyright 1982, Appl. Optics.)

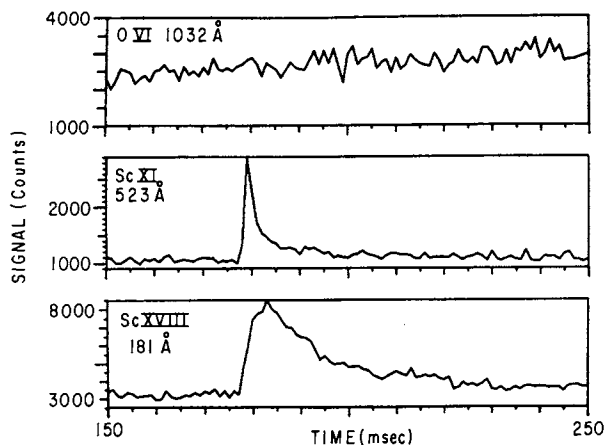


Figure 14. Polychromatic output of the spectrometer in Figure 12 showing the time evolution of Sc spectral lines arising from laser blowoff injection of Sc in a tokamak discharge. Integration time is 2 ms. (Reproduced with permission from Ref. 12. Copyright 1982, Appl. Optics.)

system developed by Richards *et al.* (21). This system uses a discrete anode array behind a high gain MCP combination to provide a photon counting detector with 19 separate channels. Placing this detector behind the exit slit of a conventional normal incidence EUV spectrometer allows one-dimensional images of the plasma to be recorded at a given wavelength with relatively high time resolution (~ 0.1 msec). This system has been used extensively on the Alcator tokamaks and on the TMX magnetic mirror experiment.

The above discussion is presented merely to give an idea of the types of EUV detectors and their applications in use on present fusion plasma experiments. It is by no means an exhaustive list of possibilities. Indeed, several different detectors are in use or being planned in future experiments. Resistive anode encoders will probably see more use in fusion experiments as they become commercially available. However, the low count rates available ($\sim 10^5$ to 10^6 sec⁻¹) will result in these detectors being used mostly for line profile studies (e.g., ion temperature measurements via Doppler broadening measurements). Intensified CCD arrays (back-illuminated or otherwise), vidicon or CID systems, lens-coupled intensifiers, and anode detectors have all seen some use on tokamak experiments or are planned for the near future, but have not been widely used as yet. However, in terms of availability, pixel format, dynamic range, insensitivity to magnetic fields, compact package, and moderate cost, the IPDA remains the most versatile multichannel EUV detector for plasma spectroscopy.

An interesting development of the IPDA has recently been reported by Benjamin *et al.* (22). They use a high gain ($\sim 10^7$) MCP combination coupled with a rapid readout of the PDA to allow detection of individual photons. Centroiding of the photon pulse allows spatial resolutions less than the pixel width. Also, a P-46 phosphor is used for fast time response. This system may be quite useful for line profile measurements in the EUV, where low counting rates can be tolerated.

Improvements in the IPDA would be desirable in the areas of resolution and contrast. The high wings in the line profiles from some intensifiers should be eliminated if possible, perhaps by adjusting the end spoiling depth of the MCP or tailoring the phosphor thickness to reduce light scattering in the phosphor. Finally, a large problem looming on the horizon for the use of these detectors in fusion research is the performance and reliability expected in high radiation environments. Even in the relatively protected areas near the next generation of fusion experiments (e.g. TFTR, JET, JT-60), fast neutrons (14 MeV) and the resultant gamma rays will provide a fairly hostile environment. Considerations of noise, degradation and damage to the PDA, and deterioration or coloring of the fiber optics will have to be addressed in the near future.

Acknowledgments

The author acknowledges useful conversations with Drs. R. Bell and W. Moos of Johns Hopkins University and Dr. A. Ramsey of the Princeton University Plasma Physics Laboratory. Also, the helpful comments and suggestions of the referee are greatly appreciated. This work was supported by the Department of Energy, Contract No. DE-AC02-CHO-3073.

Literature Cited

1. Equipe TFR, Nucl. Fusion 1975, 15, 1053.
2. R.A. Hulse, Nucl. Tech./Fusion 1983 3, 259.
3. R.C. Isler, E.C. Crume, and H.C. Howe, Nucl. Fusion 1979, 19, 727.
4. R.J. Hawryluk, S. Suckewer, and S.P. Hirschman, Nucl. Fusion 1979, 19, 607.
5. S.A. Cohen, J.L. Cecchi, and E.S. Marmor, Phys. Rev. Lett. 1975, 35, 1507.
6. R.J. Fonck, M. Finkenthal, R.J. Goldston, D.L. Herndon, R.A. Hulse, R. Kaita, and D.D. Meyerhofer, Phys. Rev. Lett. 1982, 49, 737.
7. J.L. Wiza, Nucl. Instrum. and Meth. 1979, 162, 587.
8. L.P. Hocker, P.Z. Zagarino, J. Madrid, D. Simmons, B. Davis, and P.B. Lyons, Proc. of the IEEE, Trans. Nucl. Sci. 1979, NS-26, 356.
9. C.C. Lo and B. Leskovar, Proc. of the IEEE, Trans. Nucl. Sci. 1981, NS-28, 698.
10. R.J. Groebner and R.N. Dexter, Plasma Phys. 1980, 23, 693.
11. J.R. Roberts and T.L. Pittman, Bull. Am. Phys. Soc. 1980, 25, 690.
12. R.J. Fonck, A.T. Ramsey, and R.V. Yelle, Appl. Optics 1981, 21 2115.
13. R.E. Bell, M. Finkenthal, and H.W. Moos, Rev. Sci. Instrum. 1981, 52, 1806.
14. G.R. Riegler and K.A. Moore, Proc. of the IEEE Trans. Nucl. Sci. 1973, NS-20, 102.
15. R. Hutter, in "Focusing of Charged Particles," A Septier, Ed; Academic: New York, 1967, Vol. II.
16. J.G. Timothy and R.L. Bybee, Appl. Optics 1975, 14, 1632.
17. Y. Talmi and R.W. Simpson, Appl. Optics 1401, 19, 1401.
18. A.T. Ramsey, R.J. Fonck, and R.V. Yelle, Bull. Am. Phys. Soc. 1980, 25, 938.
19. W.L. Hodge, B.C. Stratton, and H.W. Moos, Bull. Am. Phys. Soc. 1982, 27, 284.
20. P. Jelinsky, R.F. Malina, and H. Gould, to be published.
21. R.K. Richards, H.W. Moos, and S.L. Allen, Rev. Sci. Instrum. 1980, 51, 1.
22. R. Benjamin, R. Zimmerman, and H.W. Moos, Bull. Am. Phys. Soc. 1982, 27, 824.

RECEIVED June 28, 1983

Spectrometers for Rocket, Balloon, and Spacecraft Experiments

AKIYOSHI MATSUZAKI, YOSHIHARU NAKAMURA, and TOMIZO ITOH

The Institute of Space and Astronautical Science, Komaba, Meguro, Tokyo 153, Japan

While photometers using band-pass filters have long been the most popular optical instruments for aeronomic studies, mainly due to their simplicities, we can imagine that more exact and new experimental data could become available from variable spectral measurements. Yet, in spite of this promise, very few such experiments have been made. Especially, no variable spectral window spectrometers have been available for rocket experiments; fast scanning of a spectrum is required in order to measure it without being affected by rocket motion. Moreover the spectrometer must be designed to get the satisfactory experimental results under various adverse conditions and restrictions, e.g., shock of launching, dimensions and data transmission limitations, etc.. In recent years, we have developed new types of spectrometers based on multichannel spectroscopy using image sensors for rocket, balloon, and spacecraft experiments.

This article reports on new instrumentation for measuring spectra in rocket, balloon, and spacecraft observations. In the past, most optical measurements, performed in aeronomic optical experiments, were obtained with bandpass filter photometers. However, there are many advantages to measurements of whole spectra, i.e., more informative data can be obtained. For example, least-squares curve fitting techniques can be used to obtain more accurate interpretations, rotational and vibrational temperatures can be calculated and dynamic molecular processes can be studied.

Table I, shows the spectrometers recently developed by the authors. All are based on the principle of multichannel spectroscopy utilizing image devices as sensors (1). In these spectrometers, a spectrum is scanned rapidly electronically, typically in 10 ms. Spectral data can be readily available in a digitized form, the sensitivity of these image devices is generally better than

0097-6156/83/0236-0297\$07.50/0
© 1983 American Chemical Society

Table I.

List of the spectrometers developed by the authors for rocket, balloon, and satellite experiments.

No. on board	wavelength region	Detectors	purpose of experiment
1. rocket	near IR (680-900nm)	photodiode array	Simultaneous measurement of H ₂ O and O ₂ concentrations and temperature.
2. rocket	near IR (755-770nm)	image intensified photodiode array	The rotational temperature of the O ₂ (³ Σ _g ⁻) molecule.
3 balloon	near IR (670-870nm)	charge coupled device (CCD)	The stratospheric aerosol extinction.
4. balloon	IR (2-5μm)	pyroelectric vidicon	Simultaneous measurement of H ₂ O, CO ₂ , and CH ₄ concentrations.
5. satellite	IR (1.6-2.4μm) (2.8-4.8μm) (8.8-10.2μm)	solid-state pyroelectric array sensor	Simultaneous measurement of H ₂ O, CO ₂ , CH ₄ , and O ₃ concentrations.

that of any existing photographic emulsions and linearity is satisfactory over a wide dynamic range (2).

This paper will concentrate on the unique requirements of aeronomic spectroscopy and on the application of image devices to these measurements. Spectrometer 1, Table I, was developed for rocket experiments intended to measure the NIR absorption spectra of H₂O and O₂ molecules in the middle atmosphere. A photodiode array was used as the spectrometric sensor. With this spectrometer we were able to measure the NIR solar radiation spectrum with an altitude resolution better than 2 km. Spectrometer 2, Table I, was basically of the same design as spectrometer 1, except that an image intensifier was optically coupled to the diode array to permit low light-level measurements. The resolution of this spectrometer was adequate for measurements of rotational profiles of the A-band absorption spectra of O₂ molecules. We were able to measure the rotational temperature of oxygen molecules, in the stratosphere and the lower mesosphere with an accuracy of + 1.5°, and a spatial resolution better than 2 km. These experiments provided the basis for study of the dynamic processes of atmospheric molecules. Spectrometer 3, Table I, provided yet another instrumental approach for balloon experiments intended to measure the extinction of solar radiation by stratospheric aerosol. Spectrometer 4, Table I, based on the use of a pyroelectric vidicon image device, was developed to measure the strong absorption bands of non-isonuclear molecules (2-5 μm range). Recently we have developed spectrometer 5, Table I, based on the use of a self-scanned solid state pyroelectric array sensor. The main advantages of this sensor, over the pyroelectric vidicon, are its improved sensitivity and reduced channel-to-channel cross-talk.

We will first discuss studies performed with spectrometers 1 and 2, then with spectrometer 3 and finally spectrometers 4 and 5. In the spectral measurements, data processing is of essential importance. Because, a large amount of experimental data must be quickly and accurately transmitted, a PCM (pulse code modulation) telemetry is indispensable, and will be also discussed.

1. Rocket-borne Spectrometer for the Study of Dynamic Molecular Processes in the Atmosphere

In the rocket experiments, the NIR absorption spectra of various atmospheric constituents were measured. Using the solar light as the primary light source its extinction due to absorption and scattering by the atmospheric constituents was measured (3). This method allows measurements of absorption spectra with a contamination-free and long optical path. However, because of the complex and rapid motion of the rocket it is difficult to continuously utilize the solar light. A rocket motion can be roughly considered as comprising three basic motions: spin around the rocket axis, precession of the longitudinal axis, and change of

the trajectory azimuth. With S-310 type rocket, used in this study, the period of spin motion is approx. 1/3 Hz, in the first 50 seconds following launch, and approx. 1 Hz thereafter. The period and amplitude of the precession are approx. 4 minute and 25°, as a whole angle, respectively. Changes in the trajectory azimuth depend on the rocket altitude and is affected by wind and other factors such as the position of the mass center of the rocket etc.. To successfully utilize a spectrometer based on the solar occultation method we had to resolve two essential problems: (1) How can the period of constant incidence of solar light be prolonged? (2) How rapidly can a spectrum be measured? Another important problem that had to be solved was the development of a mechanical support for the spectrometer to counteract the violent vibrations and acceleration of the rocket.

Spectrometer 1 is based on a linear self-scanned image sensor, capable of providing a 10 ms per spectrum, scan time. This spectrometer was borne by the S-310-8 rocket, which was launched from Kagoshima Space Center (131°04'45"E, 31°15'00"N) at 17:47 JST (Japan Standard time, 135°E) on February 2, 1980. The spectrometer, that measured the NIR absorption of atmospheric constituents such as O₂ and H₂O, was according to our knowledge the first rocket-borne² multichannel spectrometer capable of measuring spectra with an altitude resolution better than 2 km. The schematic diagram of the spectrometer is shown in Figure 1. The solar light entered the spectrometer input slit through a window which was opened on the rocket wall. The optical system, consisting of lenses, a diffuser, and a random-type optical fiber coupler, transmitted a uniform solar light into the spectrometer with a field of view of 50°, Figure 2. The dispersion spectrometer used was a Jobin Yvon H-10IR monochromator (f=100 mm, F/3.5, with a grating of 600 g/mm). The grating and mirror holders were specially reinforced. A linear photodiode array, Matsushita MEL 1024KV, 1024 elements, was used.

The video signals from the diode array were digitized (8-bits) temporarily stored in memory and then transmitted to ground by the PCM telemetry system. The transmitted data, received and decoded by the PCM telemetry ground system, were acquired by a microcomputer-based data processing system utilizing a DMA controlled floppy diskette as a master storage device. Because the rocket spun at the rate of 1-3 Hz, the period of solar light incidence was rather short, 139 ms and 46 ms, for 1 and 3 Hz respectively, whereas the scan time was 10 ms per spectrum.

To achieve maximum efficiency, measurements of spectral data were initiated by a trigger signal from a reference detector. Following triggering, two spectra were selected and transmitted to ground at a 25.6 kbaud rate. The field angles and the direction of the field were identical for the diode array and the optical trigger. Following this transmission, the sequence was started again, according to the time diagram shown in Figure 3, and so on. Although eight spectra could be measured in the READ mode only

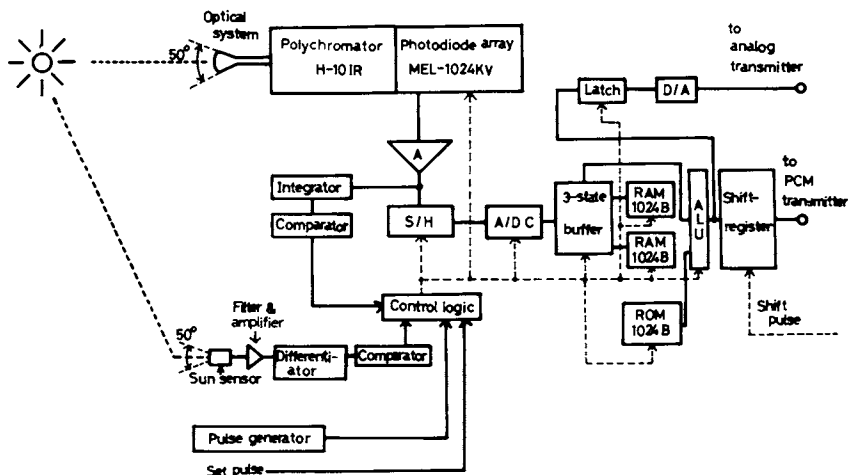


Figure 1. Schematic diagram of the rocket-borne NIR spectrometer. Key: A, amplifier; S/H, sample and hold; A/D C, analog-to-digital converter; D/A, digital-to-analog converter; and ALU, arithmetical logic unit. (Reproduced with permission from Ref. 3. Copyright 1981, American Institute of Physics.)

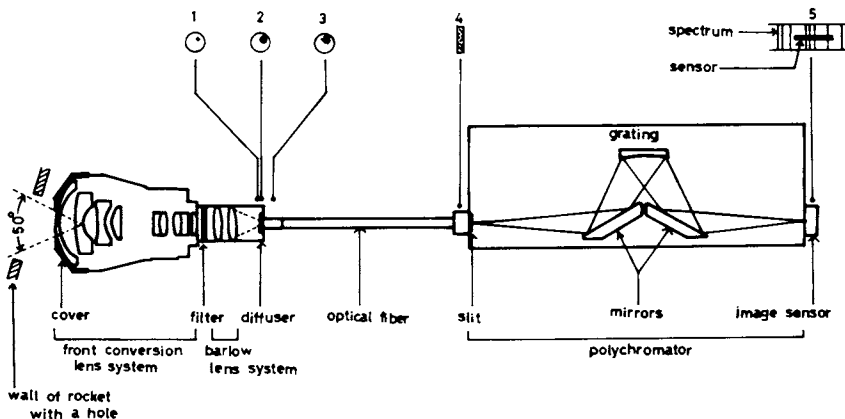


Figure 2. The optical system of the spectrometer and the image patterns of the solar light at the focal point of lens (1), at the diffuser (2), at the entrance of fiber (3), at the exit of fiber (4), and at the surface of the sensor (5). (Reproduced with permission from Ref. 3. Copyright 1981, American Institute of Physics.)

two were transmitted in order to obtain the desirable altitude resolution of better than 2 km. The second spectrum was automatically stored in memory. To qualify as a good spectrum i.e., to be transmitted to ground, the integrated signal intensity of each spectrum was compared with a preset value. This intensity value was predetermined based on ground intensity measurements and also from scattering extinction values calculated from air mass and scattering cross-section values of the atmosphere. When the measured integrated intensity surpassed this preset value, it was automatically stored. This procedure is performed again until a "good" spectrum is stored. By this discrimination we can select the spectrum which was measured under constant intensity of solar light. Since the second "good" spectrum was considered most probably "good" it was automatically selected. Moreover, to protect against malfunction of the trigger system, it was possible to store spectra whose integrated signal surpassed the present threshold level even without it.

It is important that the trigger signal is not affected by spurious noise signals, and therefore it must be carefully shielded. The variation in the rocket spin period and the intensity variation of the solar light intensity on the trigger sensor can cause jitter in the trigger time. To eliminate this jitter, a differential amplifier was used in the trigger-control electronic circuit.

Figure 4 is an example of spectra measured with the spectrometer 1 system in the S-310-8 rocket experiment. The A-band absorption spectra of oxygen molecules, which originate from the ${}^1\Sigma_g^+(v'=0) \leftarrow {}^3\Sigma_g^-(v''=0)$ and ${}^1\Sigma_g^+(v'=1) \leftarrow {}^3\Sigma_g^-(v''=0)$ transitions (4), have been observed at 763 and 692 nm, respectively. The rotational bands (3,0,1) and (2,1,1) of water vapors have also been observed at 720 and 820 nm, respectively (5).

Measurements of the rotational and vibrational temperatures of atmospheric molecules provide direct information on the molecular processes in the upper atmosphere. These temperatures are obtained from high resolution vibrational and rotational spectral profiles.

Spectrometer 2 was used to measure the rotational profile of the A-band absorption spectrum of oxygen molecules. The resolution of the spectrometer, approx. 1.2 cm^{-1} , was adequate to determine the rotational temperature with an accuracy of $\pm 1.5^\circ$. The measurement of the absorption spectrum was based on the solar occultation method. The basic instrumentation is similar to that used in the S-310-8 rocket experiment. To obtain the necessary spectral resolution of 1.2 cm^{-1} , the monochromator used had a focal length of 400 mm and it utilized a grating with 2000 g/mm. The image sensor comprised a microchannel plate (MCP) image intensifier (proximity focused, ITT type F-4769) optically coupled to a 1024 element self-scanned photodiode array (RL-1024SF). To ensure a uniform solar light illumination, within the 50° field of view, a diffused plate was used as a light scatterer

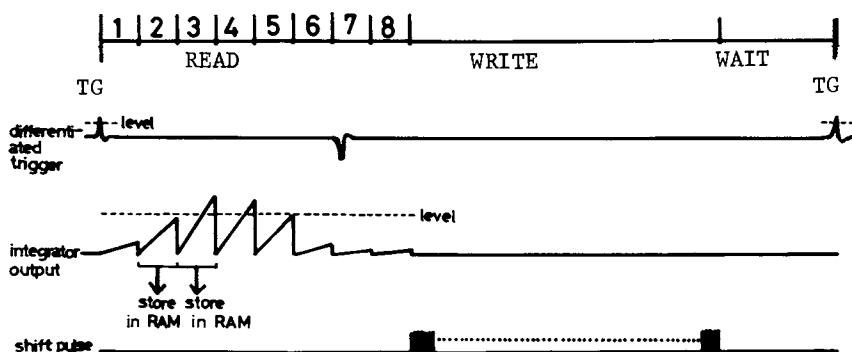


Figure 3. The time sequence of the rocket-borne spectrometer. (Reproduced with permission from Ref. 3. Copyright 1981, American Institute of Physics.)

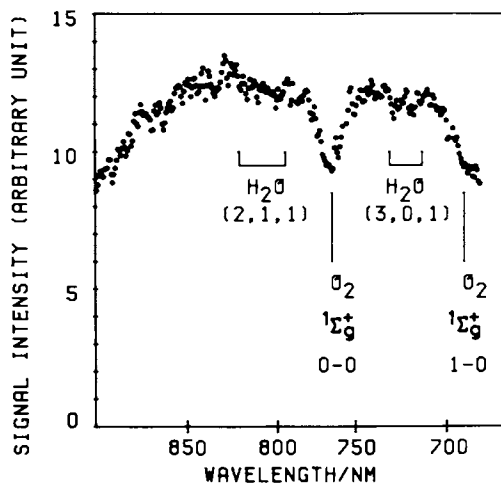


Figure 4. The NIR spectrum of the solar radiation measured by the S-310-8 rocket experiment. (Reproduced with permission from Ref. 3. Copyright 1981, American Institute of Physics.)

and a lens system with an iris were added. Figure 5a shows the schematic diagram of the spectrometer system and Figure 5b shows its photograph. The dimensions of the spectrometer were 260 mm (diameter) x 365 mm length. Its weight was 20 kg. This spectrometer was S-310-11 rocket borne. The rocket was launched from KSC at 18:38 JST on September 7, 1981. The zenith angle of the sun was 92° at the time of launch. Figure 5c shows a photograph of the spectrometer set in the nose cone of the rocket. Figure 6 shows the S-310-11 rocket and its launch.

The first valid spectrum was measured 16 seconds after launch and two spectra were transmitted each second thereafter. An example of the spectra measured, is given in Figure 7. "Spectrum 1" shows the rotational profile of the A-band absorption spectrum of O₂ molecules. This absorption band is very intense at low altitudes and decreases at higher altitudes. In "spectrum 2", measured at an altitude of 190 km, the absorption spectrum of O₂ has practically disappeared and the Fraunhofer lines of the solar radiation are seen clearly instead. From such spectra, the absorption intensity (i.e. absorbance) at each wavelength can be obtained using the Beer-Lambert law, $\ln(I_0/I) = nql$, where I_0 and I are the incident and transmitted spectral values, q the cross-section and n the density. The pathlength is l . Because atmospheric molecules and aerosols quench the solar light according to the relationship of wavelength and scattering set by Rayleigh and Mie scattering, the I_0 values are expected to be different at different altitudes; the I_0 value must be evaluated for each spectrum. As mentioned in a previous study (6), the plot of $[\ln\{I_1(\lambda)/I_1(\lambda_1)\} - \ln\{I_h(\lambda)/I_h(\lambda_1)\}]$ as a function of $(\lambda_1^{-4} - \lambda^{-4})$ gives an excellent approximation of the linearity in the wavelength region where the absorption extinction is negligible. In the above expression, I is the signal intensity and the subscripts l and h correspond to spectra measured at low and high altitudes. λ_1 is a definitive wavelength, where the absorption coefficient is negligible. In this case, 755 nm was chosen as λ_1 . Good linearity was obtained by using the least squares method in the wavelength regions of 754.5 to 758.5 nm and 768.0 to 769.0 nm, Figure 8. Similar linearities were confirmed for all other spectra measured in this experiment. The subtraction of the $[\ln\{I_1(\lambda)/I_1(\lambda_1)\} - \ln\{I_h(\lambda)/I_h(\lambda_1)\}]$ value from the extrapolated linearity gives the absorbance at each wavelength, Figure 9.

In order to obtain the rotational temperature, we need to calculate the theoretical spectra at various temperatures. The theoretical basis for calculating the absorption of the atmospheric O₂ band has been developed by Schlapp (7), Tinkham and Strandberg (8), Watson (9), and Tilford et al. (10). The detailed spectroscopic assignment has been made by Babcock and Herzberg (4): The O₂ A-band has the following four branches, R_R , R_Q , P_Q , and P_P , where P , Q , and R correspond to $\Delta J = -1, 0, +1$, respectively and where the superscript R and P correspond to $\Delta K = +1$ and $\Delta K = -1$, respectively. The detailed procedure for the theoretical

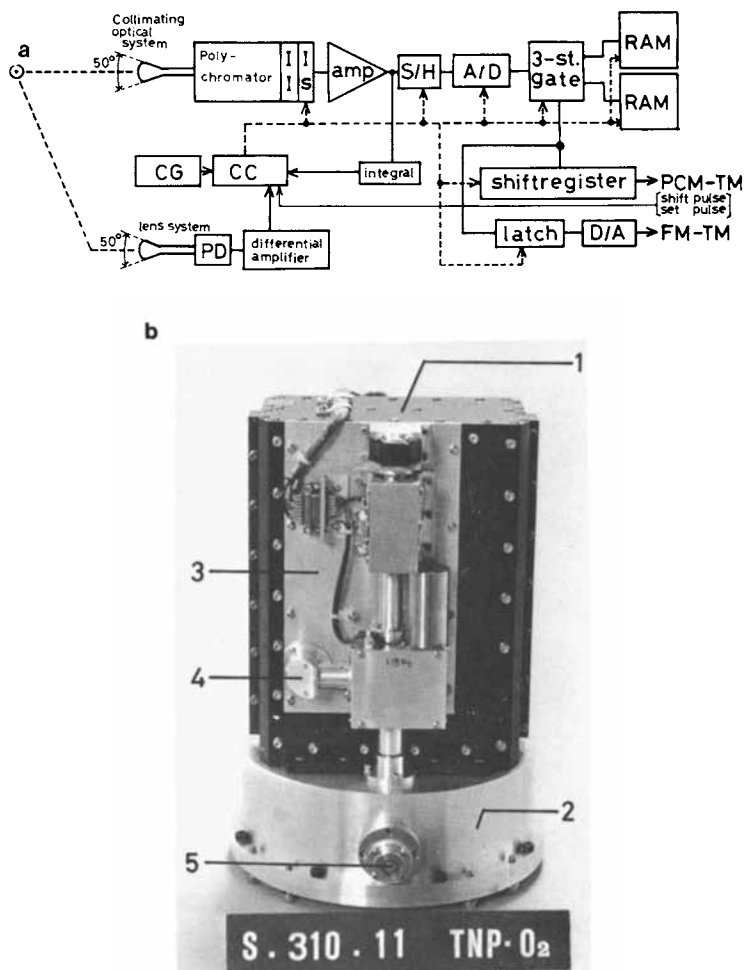


Figure 5. (a) A schematic diagram of the rocket-borne spectrometer designed for measuring the rotational profile of the A-band absorption spectrum of O_2 molecules. Key: II, image intensifier; IS, photodiode array; CG, clock generator; CC, clock controller; and PD, photodiode. (Reproduced with permission from Ref. 11. Copyright 1983, American Geophysical Union.)

(b) A photograph of the rocket-borne spectrometer. Key: 1, polychromator; 2, airtight chamber; 3, electronics; 4, position of the entrance slit of the polychromator; and 5, entrance of the optical system that introduces the solar light into the polychromator.

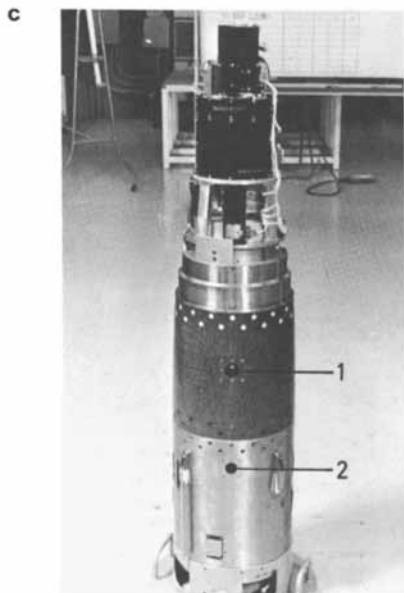


Figure 5. (c) The spectrometer, set in the nose cone of the rocket. Key: 1, entrance window for the polychromator; and 2, entrance window for the triggering optical system.



Figure 6a. Photograph of the S-310-11 rocket.



Figure 6b. Photograph of the S-310 rocket launch.

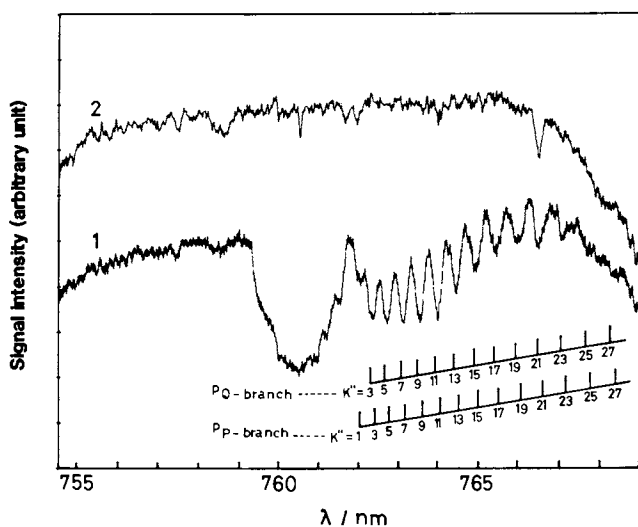


Figure 7. Examples of the solar radiation spectra measured in the S-310-11 rocket experiment. Key: 1, measured at 24.8 km; and 2, 190 km. (Reproduced with permission from Ref. 11. Copyright 1981, American Geophysical Union.)

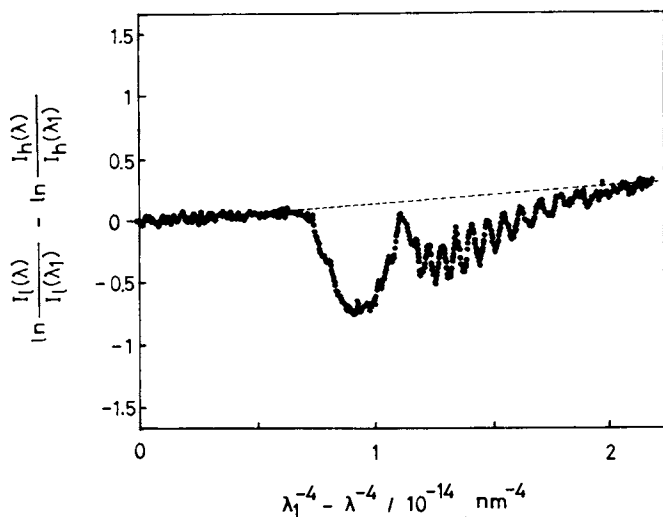


Figure 8. Plot of the $[\ln\{I_1(\lambda)/I_1(\lambda_1)\} - \ln\{I_2(\lambda)/I_2(\lambda_1)\}]$ value as a function of the $(\lambda_1^{-4} - \lambda^{-4})$ value. Here, $I_1(\lambda)$ and $I_2(\lambda)$ are the signal intensities of Spectra 1 and 2 of Figure 7, respectively, at a wavelength $\lambda = 755$ nm. (Reproduced with permission from Ref. 11. Copyright 1983, American Geophysical Union.)

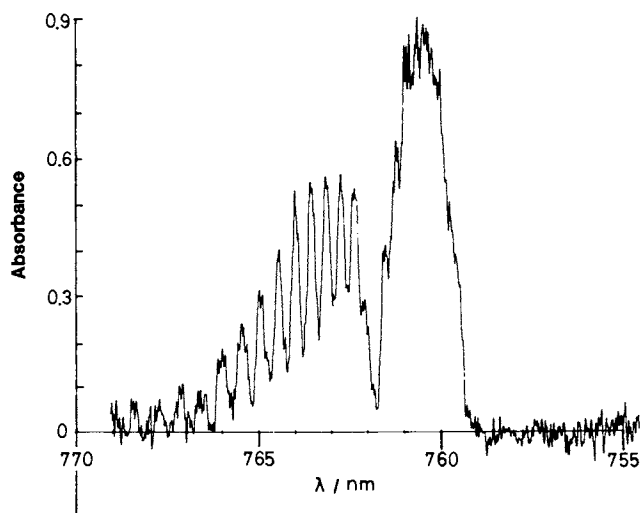


Figure 9. The absorbance spectrum obtained from the plot in Figure 8. (Reproduced with permission from Ref. 11. Copyright 1983, American Geophysical Union.)

calculation has been previously described (11). An example of the spectra obtained from these theoretical calculations is shown in Figure 10. To achieve a best fit between the observed and calculated spectra the absorptions of their peaks were compared. An example to such a comparison, for a temperature of 220 K is shown in Figure 11. The better the calculated spectrum reproduces the experimental one the more closely the various peaks aligned with the linear relationship curve. Similar plots were produced for various temperatures and standard deviation values i.e., $\sigma = \sqrt{\sum_i (f_i - f)^2}$, where $(f_i - f)$ are the deviations from the linearity, were calculated by using the least squares method. Evaluated standard deviations as function of temperature are shown in Figure 12. From the minimum value of standard deviation, the rotational temperature of "spectrum 1" in Figure 2 is calculated to be 218 ± 1.5 K.

The temperature obtained here is for the tangential height of 21 km and agrees with that of the U.S. Standard Atmospheric Supplements, 1966, as compiled in the "Handbook of Geophysics and Space Environments". This means, that this altitude, the $O_2(^3\Sigma_g^-)$ molecules are in thermal equilibrium with ground state N_2 molecules; the collisional deactivation is faster than activation of oxygen photochemical processes (12). Thus, we were able to confirm that the present spectrometer measures the effective spectrum necessary to determine rotational temperatures with a satisfactory accuracy. The rotational temperatures of the $O_2(^3\Sigma_g^-)$ molecule, at other altitudes were similarly obtained. The final report will be presented elsewhere (13).

2. Stratospheric Aerosol Measurements Using the CCD-Based Spectrometer

Balloon experiments can be effective for studies of photochemical reactions of stratospheric molecules. Spectrometer 3, Table I, was used to obtain altitude profiles of scattering coefficients of stratospheric aerosols. The spectrometer is shown schematically in Figure 13. Correct solar light illumination of the spectrometer was controlled by combination of azimuth and zenith controllers. A Jobin Yvon H20IR monochromator (F/3.5, $f=200$ mm, 600g/mm grating) without its exit slit was used as the polychromator. Wavelength calibration was performed using a He-Ne laser and a Hg lamp as reference sources. The multichannel imager was a 2048-element linear self-scanned charge-coupled device, NEC model μ PD 792. Video signal was digitized (8 bit converter), temporarily stored in memory and then transmitted to ground, at a rate of one spectrum per second, by an FM (frequency modulation) analog telemeter. The scanning rate of the CCD was 204.8 elements/ms. The balloon borne spectrometer, balloon B₁₅-100, was launched from the Sanriku Balloon Center (SBC, 39° 09.5' N, 141° 49.5' E) at 6:30 a.m. JST on May 31, 1979. The balloon altitude was 22 km when it was in level flight. The experiment

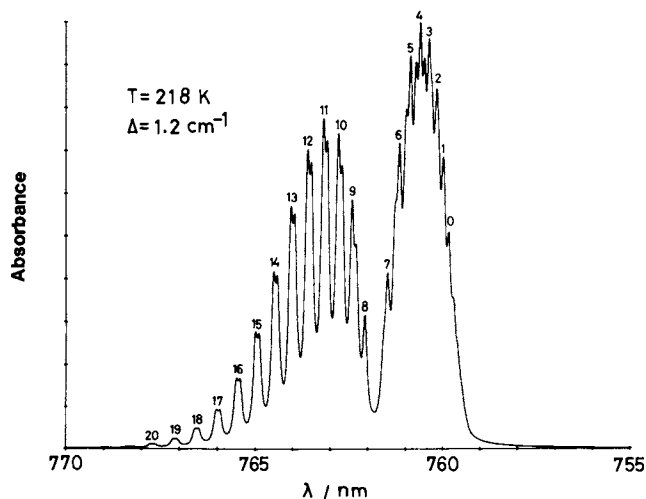


Figure 10. Example of the spectrum obtained by the theoretical calculation. (Reproduced with permission from Ref. 11. Copyright 1983, American Geophysical Union.)

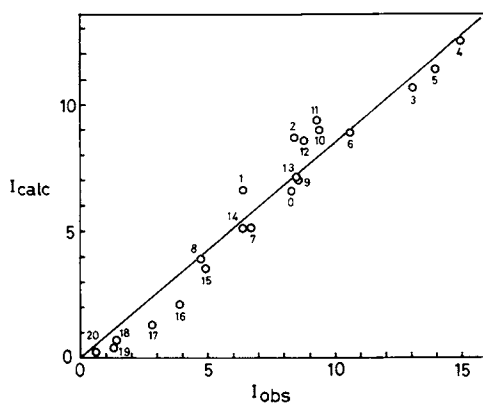


Figure 11. The relationship of the peak intensities obtained from the experimental and the calculated spectra (220 K), I_{obs} and I_{calc} , respectively. The numbers in this figure correspond to those in Figure 10. (Reproduced with permission from Ref. 11. Copyright 1983, American Geophysical Union.)

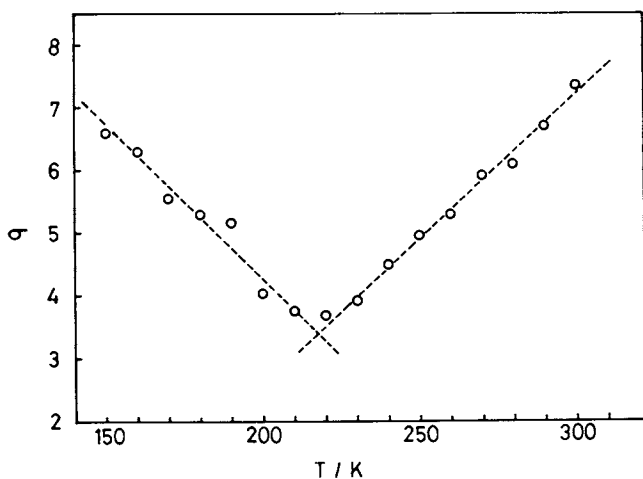


Figure 12. The standard deviation σ for the plot in Figure 11, as a function of temperature. (Reproduced with permission from Ref. 11. Copyright 1983, American Geophysical Union.)

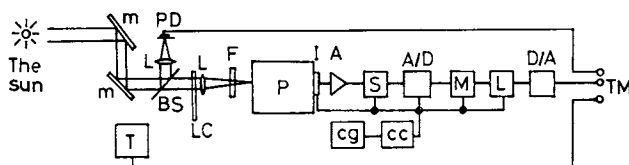


Figure 13. The schematic diagram of the balloon-borne spectrometer. Key: M, mirrors for introducing the solar light correctly into the polychromator; BS, beam splitter; LC, light-intensity controller; L, focusing lenses; F, filter for removing higher-order dispersed light; P, polychromator; I, CCD; A, amplifier; S, sample and holder; A/D, analog-to-digital converter; M, memory (RAM); L, latch; D/A, digital-to-analog converter; cg, clock generator; cc, clock controller; PD, photodiode for monitoring light intensity; T, thermocouple for monitoring temperature; and TM, FM analog transmitter. (Reproduced with permission from Ref. 6. Copyright 1983, American Geophysical Union.)

was performed until sunset (at the balloon altitude). The spectral resolution of the polychromator was calculated to be 10 cm^{-1} ($100 \mu\text{m}$ slit width). Because the width of each CCD element was $14 \mu\text{m}$ ($9 \mu\text{m}$ length), it provided a nominal spatial resolution that is 7 times better ($100/14$). The input optics of the system focused a 2 mm diameter image of the solar disk on the entrance slit of the polychromator. The altitude resolution of the input optics, 30° field of view, is approx. 4 km. However, since only $9 \mu\text{m}$ (element height) of this 2 mm image are measured, the theoretical altitude resolution of the spectrometer is approx. 0.02 km ($4 \text{ km} \times 0.009/2$). Nevertheless, due to various aberrations, the actual altitude resolution was estimated at better than 0.1 km. Figure 14 shows typical spectra. It is clear that more solar light is quenched as shorter wavelengths are approached. These spectral radiations are due to scattering extinction by atmospheric molecules and aerosols. Study of these variations, as a function of the sun altitude, can produce the altitude profile of the extinction coefficients of atmospheric aerosols. Details on these calculations will be reported elsewhere (6). This profile is shown in Figure 15. It is close to the profile given in the SAM II measurements, near Alaska during 16-19 July, 1979 (14). The aerosol scattering extinction coefficients given in Elterman's model (15) were, however, three times larger than ours. This suggests that our results are closer to "background level" values, and that Elterman's model represents a period of high aerosol concentration, due to volcanic eruptions.

The results obtained in this study can be concluded as follows.

- (1) Spectra can be readily measured: accuracy of data can be increased through least-mean-squares data analysis. Consequently, the effects of absorption or scattering of solar radiation can be determined with sufficient accuracy.
- (2) Spectrum scan rate is fast: Acquired spectra are therefore free from distortions due to balloon and gondola motions and variations of the sun altitude. Good altitude resolution is obtainable and measurement signal-to-noise can be improved by summation (ensemble averaging) of consecutive spectra measured in each altitude interval.
- (3) The excellent altitude resolution achieved with this linear CCD array suggests that further improvement in resolution can be obtained with area-array CCD's.

3. IR Spectrometer for Balloon and Satellite Experiments

Because many atmospheric constituents absorb efficiently in the infrared spectral region, the development of an IR multi-channel spectrometer was important to complement our near IR spectrometers. Originally, the pyroelectric vidicon (16) was selected as the IR image devices. This imager is a thermal rather than photon detector, and as such detects only variations

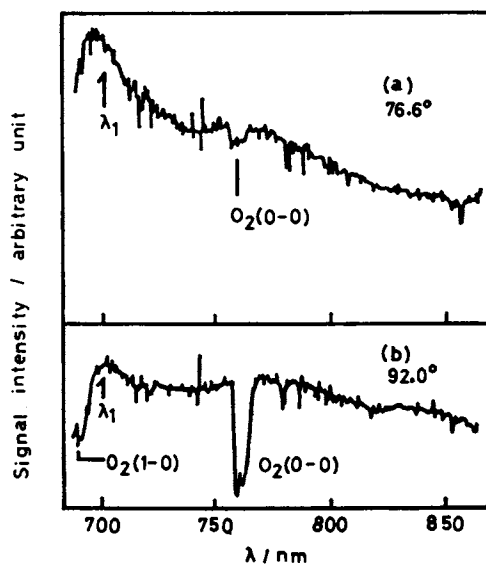


Figure 14. Solar occultation spectra measured in this balloon experiment. Solar zenith angle: a, 76.6° ; and b, 92.0° . (Reproduced with permission from Ref. 6. Copyright 1983, American Geophysical Union.)

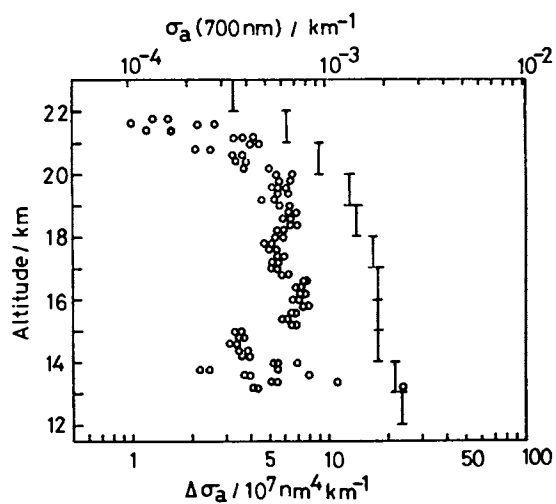


Figure 15. Altitude profile of aerosol extinction coefficient, σ_a . Key: \circ , current result; and \perp , Elmerman's model. (Reproduced with permission from Ref. 6. Copyright 1983, American Geophysical Union.)

in thermal flux. Consequently, the pyroelectric vidicon does not require cooling to reduce the background thermal noise. The performance of this detector will be discussed below. At the present time we are developing a new IR spectrometer that will use a self-scanned solid state pyroelectric array. This spectrometer will be used in satellite experiments.

3a. Balloon-borne IR Spectrometer—Pyroelectric Vidicon Sensor

A schematic diagram of the system is shown in Figure 16 a. The solar IR radiation was directed to the focusing optical system by an azimuth controller and two-axis-controlled solar tracking system. Because the pyroelectric vidicon is insensitive to cw thermal signals, the polychromator-dispersed solar radiation was chopped at a frequency of 2 Hz, prior to incidenting on it. The selected chopping frequency is compromised due to its opposite effect on sensitivity and spatial resolution. The detector produces positive signals during periods of open chopper and negative signals during periods of closed chopper. Since negative signals cannot be read out by the electron beam, the potential of the pyroelectric target is artificially raised to a positive enough pedestal potential i.e., counteract maximum negative signals during closed chopper periods. To eliminate this pedestal, the negative signal is automatically subtracted from each preceding positive signal, prior to transmission, Figure 16a, and after the video signal from the vidicon is amplified. The subtracted digitized signal is stored in memory.

Because the solar irradiance varies greatly across the IR region of interest (2 to 5 μm) a three stage polychromator was used. Each stage displays a different spectral region across the detector and thus improves its virtual dynamic range and its spectral resolution. The timing diagram is shown in Figure 17. The status of the system is indicated by the "FLAG" pulse. The spectrometer measures the spectrum in the "MEASURE" mode, and transmits data to ground during "DATA-SEND" mode. The "MEASURE" mode lasts for a single chopper period. Forty-eight horizontal lines are swept in each frame. The video signal of each line is converted to 8-bits digital data by 128 conversion pulses. Therefore, a spectrum represents an 8 bits x 128 element datum. For each spectrum, the spectral data of two lines were stored in memory, since the height of the dispersed spectrum is larger than the scanning line of the vidicon. Therefore six spectra were measured for each frame. Since the signals with the third and fourth frames were the most intense and produced the best spatial resolution, they were stored in memory, during the "MEASURE" mode. In the "DATA-SEND" mode, the six spectral records of the accumulated third frame and the six spectral records of the accumulated fourth frame, after negative subtraction, were transmitted to ground.

The average spectral resolution was approx. 50 cm^{-1} , limited by the sensitivity of the pyroelectric vidicon. The target, polyvinylidene phthalate (PVH₂), is approx. ten times less sensitive

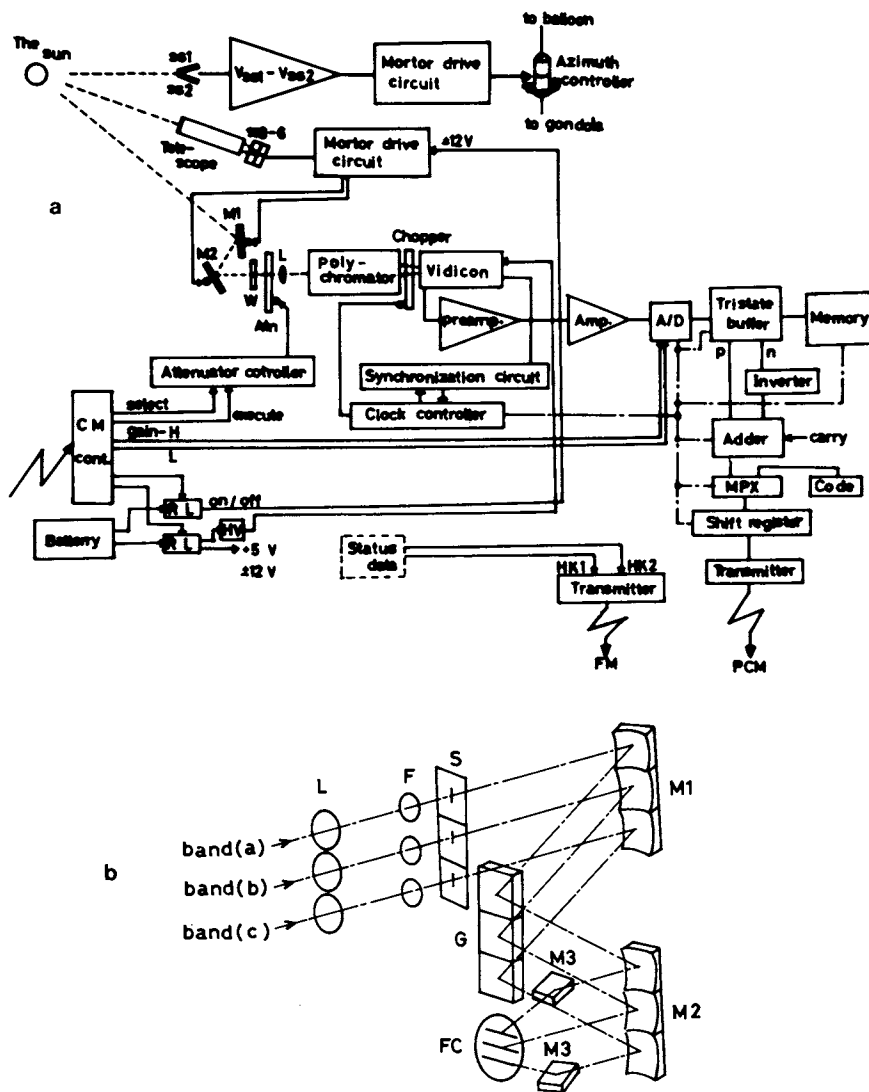


Figure 16. (a) Schematic diagram of the balloon-borne IR spectrometer. Key: SSI-6, sun sensor; W, attenuator; CM cont., command controller; RL, relay; HV, high voltage power supply; and MPX, multiplexer.

(b) The three-stage polychromator. Key: L, focusing lenses; F, cutoff filters for order separations; S, entrance slits; M1, collimating mirrors; M2, focusing mirrors; M3, flat mirrors; and FG, target of the pyroelectric vidicon. (Reproduced with permission from Ref. 17. Copyright 1982, American Institute of Physics.)

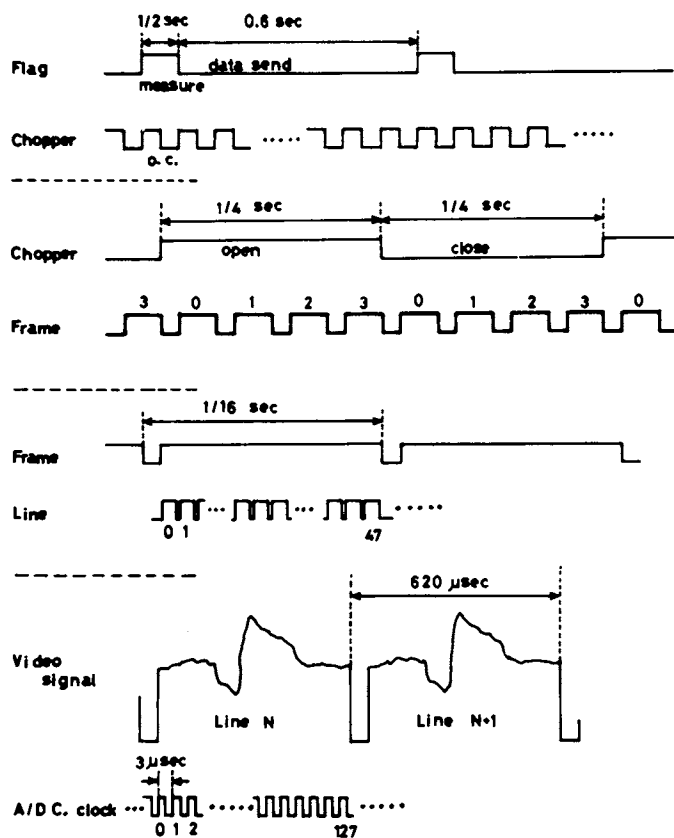


Figure 17. The timing diagram of the electronic system of the spectrometer. (Reproduced with permission from Ref. 17. Copyright 1982, American Institute of Physics.)

than the more standard triglycine sulfate (TGS) target. However, it was preferred for space experiments because the Currie point of TGS is too low, i.e., 49°C. A more detailed description of the spectrometer is given elsewhere (17).

3b. Satellite-borne IR Spectrometer — Pyroelectric Array Sensor

Very recently, a self-scanned pyroelectric array sensor, with higher sensitivity and reduced cross-talk, has become available (18, 19). Also, the pedestal level setting is far less demanding compared to the pyroelectric vidicon. We are currently developing a new IR spectrometer based on this sensor, to be used in conjunction with our satellite (EXOS-C) experiment. Using the solar occultation method, this spectrometer will measure the IR absorption spectra of atmospheric molecules such as, H₂O, CO₂, O₃, and CH₄, in the 2-10 μm wavelength region. To obtain maximum dynamic range and spectral resolution, the three-stage polychromator will again be used. Thus, the absorption spectra of H₂O will be measured in the 1.6-2.4 μm wavelength range (0.025 μm/mm), those of CO₂ and CH₄, in the 2.8-4.8 μm range (0.032 μm/mm) and those of O₃ in the 8.8-10.2 μm range (0.0448 μm/mm). In the 1.6-2.4 μm and 2.8-4.8 μm ranges the Spiricon model IR-32-42 and IR-64-42, slightly modified, will be used, respectively. These detectors, however, are not sensitive enough in the 8.8-10.2 μm range where the solar irradiance is low. In this range, a 16-element pyroelectric array sensor that has no self-scanning system will be used. Each element will be directly connected to its own preamplifier and the video signal will be measured by a lock-in amplifier. Launching of this IR-spectrometer is planned for February 1984.

4. Spectral Data Processing

Since we have to transmit a large amount of spectral data exactly and quickly in rocket, balloon, and satellite experiments, a digital data transmission method is indispensable. For example, in the spectra shown in Figure 14, which were transmitted by an FM analog telemetry, there is noise which is associated with element-to-element sensitivity radiations. If the sensitivity of each element is measured before the experiment, correction factors, for these variations, can be made and therefore correct the raw spectral data transmitted by the PCM telemetry. However, exact correction for spectra transmitted by the analog telemetry (see Figure 14) is impossible, since these rapid variations are filtered to some extent, i.e., high frequency components are lost.

Figure 18 shows the overall process of PCM telemetry. The data from a rocket-, balloon-, or satellite-borne physical instrument are edited in a PCM frame pattern with an encoder and then transmitted by the PCM telemetry to the ground. The PCM data are decoded and acquired in a computer system. In data analysis, a computer system is also used. Although data acquisition and data

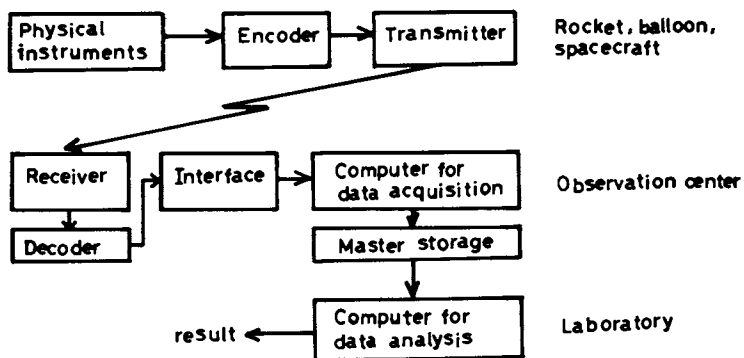


Figure 18. Overall process of PCM telemetry.

analysis are usually performed differently, their recorded data formats must be compatible. Such a computer system is prepared for satellite experiment, but not for our rocket and balloon experiments. It seems to be wasteful to use an expensive computer system for rocket and balloon experiments within the limited budget. Therefore, we constructed a microcomputer-based PCM data processing system for making data acquisition and analysis. In this system two types of 16-bit microcomputers have been used; a single-board microcomputer has been extended for high-speed data acquisition (ASSEMBLER-based) and a personal computer is used for data analysis (BASIC-based). Since the microprocessor is somewhat smaller, the required task is often beyond the capability of a single microprocessor. Therefore, it is preferred to adapt microcomputers to special tasks and use them in a multiprocessor system. The maximum rate of data acquisition is 4096 bytes of data / 986 ms. The results obtained with this PCM data-processing system indicates that the use of microcomputers is effective in the following ways: (1) the data-processing system can be connected easily to different PCM telemetry systems with a simple interface, and (2) a personal-computer-based data analysis can be made. More details on our microcomputer-based PCM data processing system has been described elsewhere (20).

5. Conclusion

The multichannel spectrometric system developed for our experiment have been proven viable and useful for a variety of spectroscopic studies. Further system design should consider the following parameters.

- (1) Sensitivity — The most sensitive imaging detector, available at the present time is an MCP image intensified photodiode array. Its sensitivity, however, is lower than that of photo-multipliers. To regain signal-to-noise, the diode array is cooled to allow for on-target signal integration. Space experiments, however, do not easily lend themselves to long integration times because of rocket motion. Better sensitivities should be obtained through the use of MCP-image intensifiers directly attached to multi-anode arrays. These detectors are used in the photon-counting readout mode. Various methods for position sensing anodes were previously reviewed (21).
- (2) Dynamic range — In aeronomic optical measurement, a wide dynamic range is usually required. For example, since the solar radiation intensity varies greatly with wavelength, a wide detector dynamic range is necessary to measure its spectrum simultaneously. Similarly, a wide dynamic range is required to measure the variations in airglow intensity with altitude. The factors that determine the upper and lower limits of the dynamic range of a light sensor are its sensitivity saturation effect and its noise, respectively. To

reduce the effect of electromagnetic and thermal noise, the sensor must be appropriately shielded and cooled. At the upper level, the signal saturation process must be carefully evaluated. In the microchannel plate (MCP) for example, the output current is limited by the maximum current supported by charges derived from the walls of the individual channels. Consequently, the amplification gain of the MCP can be greatly reduced when the incident signal is excessively large, i.e., signal saturation occurs and there is a departure from linearity in the transfer characteristics of the detector.

Eventhough, the high sensitivity and wide dynamic range achieved with the photomultiplier and other single channel detectors may not be fully achieved with multichannel detectors, such instruments perform well enough to acquire high quality data, otherwise unobtainable in rocket, balloon and spacecraft observations.

Acknowledgment

The authors indebted to the members of the S-310-8 and S-310-11 rocket experimental, the B₁₅-100 and B₃₀-38 balloon experimental, and the EXOS-C satellite project teams. English of this manuscript was reviewed by Dr. Y. Talmi of Princeton Instruments. The authors express sincere thanks for his kindness.

Literature Cited

1. "Advanced Scanner and Imaging Systems for Earth Observations", NASA Report SP-335, December, 1972.
2. Talmi, Y., "Multichannel Image Detectors", Talmi, Y., ed.; ACS SYMPOSIUM SERIES No. 102, ACS: Washington D. C., 1979; P3
3. Matsuzaki, A., Nakamura, Y., and Itoh, T., Rev. Sci. Instrum. 52 1685 (1981).
4. Babcock, H. D., and Herzberg, L., Astrophys. J. 108 167 (1948).
5. Mecke, R., Z. Phys. 81 313 (1933).
6. Matsuzaki, A., Nakamura, Y., and Itoh, T., J. Geophys. Res., in press
7. Schlapp, R., Phys. Rev., 51 342 (1937).
8. Tinkham, M., and Strandberg, M. W. P., Phys. Rev., 97 937 (1955).
9. Watson, J. K. G., Can. J. Phys., 46 1637 (1968)
10. Tilford, S. G., Vanderslice, J. T., and Wilkinson, P. G., Astrophys. J., 141 1226 (1965).
11. Matsuzaki, A., Nakamura, Y., and Itoh, T., submitted (Ann. Geophys.).
12. Chapman, S., Mem. R. Meteorol. Soc., 3 103 (1930).
13. Matsuzaki, A., Nakamura, Y., and Itoh, T., unpublished work.
14. McCormick, M. P., Chu, W. P., McMaster, L. R., Grams, G. W.,

- Herman, B. M., Pepin, T. J., Russell, P. B., and Swissler, T. J., *Geophys. Res. Lett.*, 8 3 (1981).
15. Elterman, L., *Air Force Camb. Res. Lab. Environ. Res. Rap.*, 285, AFCRL-68-0153, April, 1968.
16. Talmi, Y., *Appl. Opt.*, 17 2489 (1978).
17. Matsuzaki, A., Nakamura, Y., and Itoh, T., *Rev. Sci. Instrum.* 53 978 (1982).
18. Roundy, C. B., Application note An-10, Spiricon Inc., 1978.
19. Roundy, C. B., Supplementaly data sheet, Spiricon Inc., 1981.
20. Matsuzaki, A., Nakamura, Y., Itoh, T., and Hasebe, A., *J. Chem. Inf. Comput. Sci.*, 22 165 (1982).
21. Lampton, M., *Sci. Am.*, 245 46 (1981).

RECEIVED April 26, 1983

Author Index

- Aiello, Peter J., 57
Barbara, P. F., 183
Bruckner, Adam P., 233
Busch, Kenneth W., 1
Callis, James B., 233
Denton, M. B., 117,133
Enke, Christie G., 57
Fonck, Raymond J., 277
Forsley, L., 221
Grabau, Frederick, 75
Hilinski, E. F., 201
Ingle, Jr., James D., 155
Itoh, Tomizo, 297
Knox, W., 221
Lewis, H. A., 133
- Malina, Roger F., 253
Matsuzaki, Akiyoshi, 297
Milton, S. V., 201
Nakamura, Yoshiharu, 297
Olesik, John W., 31
Rentzepis, P. M., 201
Ryan, Mary Andrieu, 155
Siegmond, Oswald H. W., 253
Sims, G. R., 117,133
Strandjord, A. J. G., 183
Talmi, Yair, 1
Talmi, Yair, 75
Tripathi, G. N. R., 171
Walters, John P., 31

Subject Index

A

- Absolute fluorescence timing, 226f
Absorbance spectra, for albumin
 solution, 71f
Absorbance spectrometry
 multiwavelength measurement, 66f
 wide dynamic range array , 57-74
Acridine
 absorbance, 208
 absorption, 209f
 fluorescence, 212
 time-resolved fluorescence, 214f
Aluminum
 signal, 91,94
 signal integration, 93f
Analyses, spatial resolution
 conceptual framework, 234-38
 in spectral images, 233-52
Array detector
 one dimensional, 237f
 use of optical systems, 150-51
Arsenic, analytical
 calibration, 89f,90f
Astronomy
 low-light level measurements, 59
 use of charge-coupled devices, 139
Atmospheric studies, rocket-borne
 spectrometers, 299-309

- Atomic emission spectroscopy
 apparatus, 77,78-79t,80
 procedure, 77,78-79t,80
 multielement detection, 75
 SIT, 31-56
Azulene, two-photon fluorescence, 204f

B

- Background corrections, plasma
 sources, 86-94
Background spectral stripping, 84
Balloon experiments
 IR spectrometers, 312-14
 spectral data processing, 317-19
 spectrometers, 297-320
Balloon-borne IR spectrometer, 314-17
p-Benzosemiquinone anion, time-resolved
 resonance Raman spectroscopy, 179
Bias flash, in charge-injection
 devices, 123
Biological systems, picosecond
 spectroscopy, 201-20
Blood, copper and zinc analyses, 112
Blooming
 avoidance, 60
 definition, 134,135

Author Index

- Aiello, Peter J., 57
Barbara, P. F., 183
Bruckner, Adam P., 233
Busch, Kenneth W., 1
Callis, James B., 233
Denton, M. B., 117,133
Enke, Christie G., 57
Fonck, Raymond J., 277
Forsley, L., 221
Grabau, Frederick, 75
Hilinski, E. F., 201
Ingle, Jr., James D., 155
Itoh, Tomizo, 297
Knox, W., 221
Lewis, H. A., 133
Malina, Roger F., 253
Matsuzaki, Akiyoshi, 297
Milton, S. V., 201
Nakamura, Yoshiharu, 297
Olesik, John W., 31
Rentzepis, P. M., 201
Ryan, Mary Andrieu, 155
Siegmond, Oswald H. W., 253
Sims, G. R., 117,133
Strandjord, A. J. G., 183
Talmi, Yair, 1
Talmi, Yair, 75
Tripathi, G. N. R., 171
Walters, John P., 31

Subject Index

A

- Absolute fluorescence timing, 226f
Absorbance spectra, for albumin
 solution, 71f
Absorbance spectrometry
 multiwavelength measurement, 66f
 wide dynamic range array , 57-74
Acridine
 absorbance, 208
 absorption, 209f
 fluorescence, 212
 time-resolved fluorescence, 214f
Aluminum
 signal, 91,94
 signal integration, 93f
Analyses, spatial resolution
 conceptual framework, 234-38
 in spectral images, 233-52
Array detector
 one dimensional, 237f
 use of optical systems, 150-51
Arsenic, analytical
 calibration, 89f,90f
Astronomy
 low-light level measurements, 59
 use of charge-coupled devices, 139
Atmospheric studies, rocket-borne
 spectrometers, 299-309

- Atomic emission spectroscopy
 apparatus, 77,78-79t,80
 procedure, 77,78-79t,80
 multielement detection, 75
 SIT, 31-56
Azulene, two-photon fluorescence, 204f

B

- Background corrections, plasma
 sources, 86-94
Background spectral stripping, 84
Balloon experiments
 IR spectrometers, 312-14
 spectral data processing, 317-19
 spectrometers, 297-320
Balloon-borne IR spectrometer, 314-17
p-Benzosemiquinone anion, time-resolved
 resonance Raman spectroscopy, 179
Bias flash, in charge-injection
 devices, 123
Biological systems, picosecond
 spectroscopy, 201-20
Blood, copper and zinc analyses, 112
Blooming
 avoidance, 60
 definition, 134,135

- Blooming--Continued
 elimination, 125,126f
 on charge-injection devices, 149
 SIT, 35,36f
- Bromomethylnaphthalenes, two-color
 fluorescence, 212-13
- C
- CID--See Charge-injection devices
 CL--See Chemiluminescence
 CODACON readout systems, microchannel
 plates, 265-67,266f
 CTR--See Controlled thermonuclear
 reasearch plasmas
 Camera devices, types, 134
 Camera system, with charge-injection
 devices, 118
 Cereal, analysis by thiochrome rate
 method, 165
 Cesium iodide, 260-61
 quantum detection efficiency, 262f
 Charge-coupled devices, 60
 UV enhanced, 145f
 charge collection, 138f
 construction, 134
 frame-by-frame readout, 137f
 limitations, 139,142
 operation characteristics, 133-54
 pixel layout, 136f
 readout, 136f
 satellite experiments, 298t
 spectral response curves, 146f
 stratospheric aerosol
 measurements, 309,311f,312
 use by astronomers, 139
 Charge-injection devices, 60
 blooming elimination, 149
 camera system, 119f
 charge amplifier, 120
 construction, 134
 destructive readout, 149
 detection limits, 129
 detector response linearity, 121,122f
 injection mode readout, 147f
 iron solution, 127,128f
 low-light levels, noise source, 121
 manganese working curve, 129f
 mixing destructive and nondestructive
 readouts, 125
 nondestructive readout, 149
 nondestructive/destructive
 readout, 148f
 operation, 149
 operation characteristics, 133-54
 spectral response curves, 151f
 Chemical composition and distribution
 tensor, 234
 Chemical composition tensor, 235
- Chemical systems, picosecond
 spectroscopy, 201-20
 Chemiluminescence
 measurements, 156,165-66
 Chemiluminescence spectrum, 167f
 advantages, 166
 Chloranil
 absorption spectra, 218f
 photoinduced intermolecular electron
 transfer, 217
 Chloromethylnaphthalenes, two-color
 fluorescence, 212-13
 Chromatograms, one dimensional, 240f
 Clinical determinations, trace
 elements, 113
 Coherent light imaging, 247f
 Continuous source, 58
 Controlled thermonuclear reasearch
 plasmas
 evaluation criteria, 280
 spectral range, 280
 Copper iodide photocathode, intensified
 photodiode array, 283f
 Coumarin 520, upconverted emission
 spectra, 194f
 Crossed-grating echelle
 spectrometer, 153f
 Crosstalk, SIT, 35
- D
- DCP--See Direct current plasma
 DMA--See Direct memory access
 Dark charge, 20
 Dark charge level, intensified silicon
 photodiode detector, 19f
 Dark signal characteristics, in
 intensified diode arrays, 159-60
 Data acquisition system, 65-67
 linear diode array, 66f
 Detection, definition, 20
 Detector, wide dynamic range array
 absorbance spectrometry, 57-74
 performance, 67-70
 rotation spectrometry, 57-74
 Direct current plasma, 117,125,127
 Direct memory access, 67
 Direct reader, 59
 method, 134
 Discharge lag, 37
 dwell times results, 38f
 Donor arenes, photoinduced intermole-
 cular electron transfer, 217
 Double-beam picosecond laser
 system, 207f
 Dwell time, 37
 Dynamic range
 definition, 23,80

- Dynamic range--Continued
 inductively coupled plasma sources, 83f
 intensified silicon intensified target vidicon, 23
 intraspectral, 23
 memory, 23
 overall, for plasma sources, 82t
 Dynamic range
 SIT, 23
 single channel, 23
- E
- EUV--See Extreme UV
 Echelle spectrometer
 crossed-grating, 153f
 modified, 122f
 starting orders, 152f
 Echelons, 205
 Electron pulse radiolysis, 173
 Electron transfer, intermolecular
 photoinduced, 215,217
 Electronic wavelength scanning image dissector, 59
 Electrostatic image intensifier, 39
 Emission spectroscopy, limitations, 171
 Excimer formation, studies, 187
 Excited state isomerization
 scheme, 188
 studies, 187
 Experiments, range gating,
 results, 249f
 Extreme UV
 detection, 253-76
 intensified photodiode array, 281-88
 measurement, 277
 noise characteristics, 259
 phosphor/photodetector systems, 263
 photocathode materials, 260
 transmission photocathodes, 260
 Extreme UV Spectroscopy, multichannel,
 of high temperature plasmas, 277-96
- F
- Fluorescence, acridine, 212
 Fluorescence anisotropy parameter, 228
 Fluorescence depolarization
 measurements, 228
 Fluorescence intensity, vs.
 upconverted signal intensity, 197f
 Fluorescence kinetic-based
 measurements, 163-65
 instrumentation, 156
 Fluorescence measurements, intensified
 diode arrays instrumentation, 158f
 Fluorescence spectrum, 165,183
 accuracy from upconverted data, 196
 Fluorescence timing, absolute, 226f
 FortH programming language, 224
 Frame transfer, 135
 Frame-by-frame readout, 135,137f
 Fusion-grade plasma, spectra, 279f
- G
- Gated spectra, picosecond emission
 spectroscopy, 192
 Glass, determination of trace
 concentrations, 105-9
 result comparison, 106t,107t
- H
- Haloaromatic compounds,
 photodissociation, 212-13
 High temperature plasmas,
 multichannel EUV, 277-96
 Horse blood serum, copper and zinc
 determination, 112-13
 Hot spots, microchannel plates, 259
 Human urine, copper and zinc
 determination, 112-13
 Hydrogen fluoride, time-integrated
 fluorescence spectra, 189f,190f
 Hydroxyphenylbenzothiazole, excited
 state relaxation dynamics, 191,193f
- I
- ICP--See Inductively coupled plasma
 sources and Plasma sources
 IDA--See Intensified diode arrays
 IR spectrometer
 balloon experiments, 312-14
 balloon-borne, 314-17
 satellite experiments, 312-14
 satellite-borne, 317
 ISIT--See Intensified silicon
 intensified target vidicon
 ISPD--See Intensified silicon
 photodiode array detector
 Image dissectors, 59
 Image intensified photodiode array,
 satellite experiments, 298t
 Imaging spectrophotometry, thin layer
 plates, 244
 In-memory integration, 97
 Inductively coupled plasma sources
 background corrections, 86-94
 linear dynamic range, 83f

- Inductively coupled plasma sources--
 Continued
 noise features, 101
 overall dynamic range, 82t
 readout noise
 uncorrected background shifts, 87
- Inductively coupled plasma-atomic
 emission spectroscopy, 75-117
See also Inductively coupled plasma
 sources
- Initial integration time, equation, 62
- Instrument optics, 64-65
- Integration time
 automatic optimization, 61-64
 initial, equation, 62
 total, 65
- Intensified diode arrays
 applications, 162-63
 characteristics, 160
 chemiluminescence measurements, 165
 dark signal characteristics, 159-60
 detection limits, 162
 diagnostic capabilities, 165
 emission spectra, 163,164f
 fluorescence measurements,
 instrumentation, 158f
 hardware, 157,159
 light signal noise, 162
 luminescence measurements, 155-70
 signal-to-noise, 160
 software, 159
 thiochrome rate method, 163
 use for luminescence, 157
- Intensified photodiode array
 applications, 289-92
 copper iodide photocathodes, 283f
 extreme UV, 281-88
 grazing incidence spectrometer, 286f
 noise, 285
 one-dimension imaging, 281,283f
 picosecond emission spectroscopy, 18
 resolution, 282,285
 time response, 285
 tokamaks, 287
- Intensified self-scanning photodiode
 array detector, detection, 96t
- Intensified silicon intensified target
 vidicon, 3
 cost and availability, 5
 dark charge level, 19f
 distortion, 26
 dynamic range, 23
 gain, 20,21
 gating, 17
 power consumption, 10
- Intensified silicon photodiode array
 detector
 cost and availability, 5
 distortion, 26
 gain, 21
 gating, 17
- Intensified silicon photodiode array--
 Continued
 power consumption, 10
 random access capability, 15
 reliability, 8
- Intermolecular photoinduced electron
 transfer, 215,217
- Intraspectral dynamic range, 23
- Ion feedback, circumvention, 256
- J
- Jitter free deflection, 223
- Jitter free streak camera, 222-23
 applications, 224-25
 averaging weak signals, 227f
 data acquisition system, 221-32
 fluorescence response, color
 center, 225
 signal averaging, 223
 weak signal averaging, 225-28
- L
- LDA--See Linear diode arrays
- LED--See Light emitting diode
- LQD--See Limit of quantitative
 determination
- Lag, dwell times results, 38f
- Light emitting diode, 37
- Light imaging, coherent, 247f
- Light signal noise, in intensified
 diode arrays, 162
- Limit of quantitative determination, 81
- Line peak width effects, 109t
- Linear diode array, 60
 dark current reduction, 62
 data acquisition system, 66f
 data acquisition capabilities, 65
 integrating capability, 61
 microcomputer control system, 66f
 stray light interference, 70-71
- Linearity
 emission spectrometers, 197
 fluorescence, 197
- Liquid chromatography, 233,234
- Lithium fluoride, 261,263
- Low-level signals, causes, 2
- Low-light level applications, opto-
 electronic image detectors, 1-29
- Low-light level measurements
 astronomy, 59
 silicon intensified target tube, 59
- Low-light level spectroscopy, 59
- Low-light levels, charge-injection
 device noise source, 121

Luminescence measurements, with intensified diode arrays, 155-70

M

MCP--See Microchannel plate image intensifier and Microchannel plates

MIS--See Multichannel imaging spectrometer

Magnesium fluoride, 261,263
quantum detection efficiency, 262f

Memory dynamic range, 23

Methoxyphenol, radiolysis, resonance Raman spectra, 180f

Microchannel plate image intensifier, 4

Microchannel plates, 255f
CODACON readout systems, 265-67,266f
count rate performance, 259
decay, 286f
fabrication, 253
gain, 256-58
image readout systems, 263,264t
magnetic field susceptibility, 257
multianode array, 267
multianode imaging systems, 265
multiwire readout systems, 264-65
noise characteristics, 259
photocathode materials, 260
pulse height distribution, 256-58
quantum detection efficiency, 254-56
resistive anode readout, 269
strip readout, 269,271
time response, 259
wedge readout, 269,271

Modified echelle spectrometer, 122f

Modulation transfer function, pin cushion distortion, 27

Multianode microchannel plate array, 267

Multichannel, disadvantage, 244

Multichannel array detection, coupled with plasma-atomic emission spectroscopy, 75-117

Multichannel extreme UV, of high temperature plasmas, 277-96

Multichannel imaging spectrometer, 238-44,239f,240f

Multichannel parallel detector, 5
characteristics, 6t
ideal, 6t
spectrometer performance, 6,7

Multielement emission spectrometry, charge-injection devices, 117-31

Multiple detectors, types, 58

Multiple wavelength detection for overcoming limitations, 58

Multiple wavelength spectrometer, construction, 156

Multiwavelength ORD spectrometry, 70-71

Multiwavelength detector, photographic plate, 59

Multiwire position readout system, 266f

N

Naphthylmethyl radicals, two-color fluorescence spectra, 214f

Noise characteristics, microchannel plates, 259

Nondestructive readout, charge-injection devices, 123

Nondestructive/destructive readout, charge-injection devices, 148f

Nonlinear responses, 197

Nonscattering medium, images, 245f

O

OID--See Optoelectronic image devices

Objects in scattering media, detection, 244-48

On-target integration, 97

On-target signal integration, 22f

One dimensional array detector, 237f

Optical multichannel detectors, advantages and disadvantages, 206f

Optical rotation, optical system for multiwavelength measurement, 66f

Optoelectronic image devices capabilities, 76
low-light level applications, 1-29
selection, 1-29

Over-illumination, of pixels, 135

P

PDA--See Photodiode array

PMT--See Photomultiplier tube

Para-substituted phenols, time-resolved resonance Raman spectroscopy, 179

Phenoxy radicals, analysis by time-resolved resonance Raman spectroscopy, 176,177f

Phosphor/photodetector systems, 263-64

Photo starvation, causes, 2

Photocathode materials, 263
cesium iodide, 260-61
lithium fluoride, 261,263
magnesium fluoride, 261,263
microchannel plates, 260

Photocathodes, configurations, 260

- Photodiode array
 advantages and disadvantages, 206f
 construction, 134
 for satellite experiments, 298t
 multichannel detection, 194f
 response evaluation, 198f
 vs. photomultiplier
 detection, 192,195
- Photodiode detectors, comparison to
 photomultiplier, 57
- Photodissociation of haloaromatic
 compounds, 212-13
- Photographic plate, 59
- Photoinduced intermolecular electron
 transfer
 chloranil, 217
 donor arenes, 217
- Photometer, light source, 57
- Photomultiplier detection vs.
 photodiode array, 192,195
- Photomultiplier tube
 advantages and disadvantages, 206f
 comparison to photodiodes, 57
 coupled, noise features, 101
 desirable features, 133
 detection limits, 96t
- Photon shot noise, charge-injection
 devices, 123
- Photons, storage, 135
- Picosecond absorption spectroscopy,
 time-resolved, apparatus, 203f
- Picosecond emission spectroscopy
 apparatus, 185,186f
 gated spectra, 192
 with intensified photodiode
 arrays, 183-200
- Picosecond laser spectroscopy, 2
- Picosecond laser system,
 double-beam, 207f
- Picosecond photophysics, streak
 camera, 222
- Picosecond spectroscopy, 201-2
 applications, 212-17
 biological systems, 201-20
 chemical systems, 201-20
 optical detection, 202-12
 rhodopsin, 215
- Picosecond time-resolved emission
 spectrometers, 197
- Pincushion distortion, 41f
 effects, 39
 on detected spectra, 42f
- Pixels
 definition, 134
 over-illumination, 135
 super, 139
- Plasma background emission intensity,
 noise, 100f
- Plasma background subtraction
 efficiency, 85f
 on-detector integration, 86f
- Plasma emission, 47f
- Plasma sources
 background corrections, 86-94
 dynamic range, 80-81
 overall, 82t
 linear dynamic range, 83f
 linearity, 80-81
 noise features, 101
 radio frequency interference, 81
 readout noise, 81
 uncorrected background shifts, 87
- Plasma-atomic emission spectroscopy,
 inductively coupled, 75-117
- Polychromator method, 134
- Potassium analysis, super pixel
 technique, 139,140f
- Pyroelectric array sensor, 317
- Pyroelectric vidicon, satellite
 experiments, 298t
- Pyroelectric vidicon sensor, 314-17

Q

- Quantum detection efficiency
 cesium iodide, 261,262f
 definition, 254
 magnesium fluoride, 262f
 microchannel plates, 255f
- Quartz-iodine lamp, spectrum, 63f

R

- Radiation-chemical processes
 Raman cell, 175
 deoxygenation, 175-76
 time-resolved resonance Raman
 spectroscopy, 171-82
- Radio frequency interference,
 effects, 98f
- Range gated imaging, 247f
- Range gating, 246
- Readout
 frame-by-frame, 135
 mode, 135
- Resistive anode position readout
 systems, 269
- Resolution, silicon photodiode
 array, 16f
- Resonance Raman spectra
 tetrafluoro-*p*-benzosemi-
 quinone, 176,177f
p-methoxyphenol, 180f
 selective resonance enhancement, 172
- Response variations, intensified
 silicon photodiode array, 19f
- Rhodamine B, streak image, 210,211f
- Rhodopsin, picosecond spectroscopy, 215

- Rhodopsin absorption spectrum, 216f
- Rocket(s), S-310-11, 306f
- Rocket experiments
 spectral data processing, 317-19
 spectrometers, 297-320
- Rocket-borne spectrometers, 301f
 dynamic molecular atmospheric studies, 299-309
 optical system, 301f
 temperature measurement, 304
- Rotation spectrometry, wide dynamic range array detector, 57-74
- S
- SIT--See Silicon intensified target vidicon and Silicon vidicon detectors
- SPD--See Self-scanned photodiode arrays, Self-scanning photodiode array detectors, and Silicon photodiode detector
- SSANACON, 61
 See also Self-scanned anode array
- Satellite experiments,
 IR spectrometers, 312-14
 spectral data processing, 317-19
- Satellite-borne IR spectrometer, 317
- Scanning time sequence, 63f
- Scattering media
 images, 245f
 objects in , 244-48
- Selective knockdown, for blooming
 elimination, 125,126f
- Self-scanned anode array, with microchannel plate multiplier, 61
- Self-scanned photodiode arrays,
 capabilities, 76
- Self-scanning photodiode array detectors
 detection limits, 94-103,96t
 integration methods, 97
 noise characteristics, 94-103
 useful slit width, 104
- Semiquinone radicals, analysis by time-resolved resonance Raman spectroscopy, 176,177f
- Signal integration, on-target, 22f
- Signal-to-noise relationship
 with beryllium analysis, 103t
 in intensified diode arrays, 160
 with zinc analysis, 103t
- Silicon intensified target vidicon, 3,207f
 blooming, 36t
 channel-to-channel response, 43,45f
 control, 34
 cooling problems, 94
 cost and availability, 5
- Silicon intensified target--Continued
 detection limits, 96t
 distortion, 26,44f
 in low-light level measurements, 59
- Silicon photodiode arrays, 4
 characteristics, 60
 dynamic range extension, 61
- Silicon photodiode detector
 cost and availability, 5
 distortion, 27
 gain, 21
 gating, 17
 random access capability, 15
 resolution, 13,16f
 response variations, 20
 signal storage capability, 24
 simplicity, 9
 spectrometric performance, 11
- Silicon target, for storage, 35
- Silicon vidicon detectors, 3,59
- Single channel, dynamic range, 23
- Sodium analysis, super pixel technique, 139,141f
- Soft X-ray
 detection, 253-76
 phosphor/photodetector systems, 263
 photocathode materials, 260
 transmission photocathodes, 260
- Solid-state pyroelectric array sensor,
 satellite experiments, 298t
- Solution phase vibrational spectra, 172
- Spacecraft experiments,
 spectrometers, 297-320
- Spatial imaging detector system, 295
- Spatial resolution in spectral images,
 analytical chemistry, 233-52
- Spectral interferences, 84
- Spectral line
 internal standards, improvement
 in signal-to-noise, 103t
 near field radiation effect, 14f
- Spectral stripping
 misconceptions, 94
 net spectra, 88f
- Steady-state fluorescence,
 measurement, 163
- Storage devices, 3
- Stratospheric aerosol measurements,
 charge-coupled devices, 309,312
- Stray light, reduction, 244
- Streak camera, 221-22
 data acquisition, 2223-24
 jitter free, 222-23
 applications, 224-25
 averaging weak signals, 227f
 fluorescence response of color center, 225
 weak signal averaging, 225-28
 signal averaging, data acquisition system, 221-32
- Streak image, distortions, 210

Sum frequency mixing--See Upconversion
 Super pixel technique,
 chemical analysis, 139,140f

T

TPF--See Two photon fluorescence
 TRRS--See Time-resolved
 resonance Raman spectroscopy
 Temporal discrimination, 246
 Tetrafluoro-p-benzoquinone
 Raman signal decay, 176,178f
 resonance Raman spectra, 176,177f
 Thallium, analytical
 calibration, 89f,90f
 Thin layer chromatography, 238
 Thin layer plates, imaging
 spectrophotometry, 244
 Thiochrome rate method, 163
 for cereal, 165
 for urine, 165
 Three-dimensional factorization, two-
 dimensional chromatography, 243f
 Three photon fluorescence, 202
 Time dispersion, 205
 Time gating capability, 39
 Time-integrated fluorescence spectra,
 hydrogen fluoride, 189f,190f
 Time-resolved electronic absorption
 spectroscopy, limitations, 171
 Time-resolved fluorescence
 acridine, 214f
 apparatus, 186f
 Time-resolved picosecond absorption
 spectroscopy, apparatus, 203f
 Time-resolved resonance Raman
 spectroscopy
 apparatus, 173-76, 174f
 p-benzoquinone anion, 179
 excitation source, 173
 history, 172
 para-substituted phenols, 179
 phenoxy radicals, 176,177f
 radiation-chemical processes, 171-82
 semiquinone radicals, 176,177f
 Time-resolved spectra, silicon
 intensified target vidicon, 46,47f
 Tokamaks
 intensified photodiode array, 287
 polychromatic mode, 292
 Total integration time, 65
 Transient emission spectra,
 recording, 184
 Tungsten lamp, 58
 Two dimensional array detector, 237f
 Two dimensional chromatography, 242f
 three-dimensional factorization, 243f
 Two photon fluorescence,
 apparatus, 202,203f

Two-color fluorescence spectra,
 naphthylmethyl radicals, 214f
 Two-dimensional arrays, 58
 Two-photon fluorescence, azulene, 204f

U

UV fluorescence anisotropy decay, 230f
 Ultrashort spectroscopy, 2
 Upconversion
 disadvantage, 196
 fluorescence spectra, accuracy, 196
 wavelength sensitivity, 196-97
 Upconversion method, 184
 See also Fluorescence upconversion
 Upconverted emission spectra,
 coumarin 520, 194f
 Upconverted signal intensity,
 vs. fluorescence intensity, 197f
 Urine
 analysis by thiochrome rate
 method, 165
 fluorescent compound comparison, 165

V

Vanadium
 signal, 91,94
 signal integration, 93f
 Variable integration time, method, 80
 Vibrational spectra, 172
 solution phase, 172
 Video fluorometer, 233,234
 Vidicon detectors
 blooming, 25
 lag, 25
 Visual transduction process, 213,215

W

Wavelength sensitivity
 emission spectrometers, 196-97
 upconversion, 196-97
 Wavelength-resolved apparatus, 186f
 Wavelength-to-diode calibration, 104
 Weak signal averaging, streak camera,
 jitter free, 227f

X

X-Ray astronomy, noise
 characteristics, 259